Theses and Dissertations

August 2021

Theoretical and Computational Modeling of Contaminant Removal in Porous Water Filters

Aman Raizada
University of Wisconsin-Milwaukee

THEORETICAL AND COMPUTATIONAL MODELING OF

CONTAMINANT REMOVAL IN POROUS WATER FILTERS

by

Aman Raizada

A Thesis Submitted in

Partial Fulfillment of the

Requirements for the Degree of

Master of Science

in Engineering

at

The University of Wisconsin-Milwaukee

August 2021

ABSTRACT

THEORETICAL AND COMPUTATIONAL MODELING OF CONTAMINANT REMOVAL IN POROUS WATER FILTERS

by

Aman Raizada

The University of Wisconsin-Milwaukee, 2021
Under the Supervision of Professor Krishna M. Pillai
and Co-supervision of Dr. Marcia Silva

Contaminant transport in porous media is a well-researched problem across many scientific and engineering disciplines, including soil sciences, groundwater hydrology, chemical engineering, and environmental engineering. In this thesis, we attempt to tackle this multiscale transport problem using the *upscaling* approach, which leads to the development of macroscale models while considering a porous medium as an averaged continuum system.

First, we describe a volume averaging-based method for estimating flow permeability in porous media. This numerical method overcomes several challenges faced during the application of traditional permeability estimation techniques, and is able to accurately provide the *complete permeability tensor* of a porous sample in a *single* simulation. Several anisotropic unit cells are created in two- and three-dimensions based on three different parameters: (1) unit-cell size, (2) particle shape, and (3) aspect ratio of the particles inside the unit cells. The results from the volume averaging-based method show good agreement on comparison with the conventional Stokes-Darcy flow technique for the two- and three-dimensional models. We also find that the proposed method provides much faster results than the

Stokes-Darcy flow technique for 3-D unit-cell geometries.

Next, the cartridges used in commercial water filters are mostly created by packing particles or beads that can be assumed to be of mono-modal size distribution and thus create *single-scale* porous media. In this thesis, we employ the volume averaging method to upscale the phenomenon of solute transport (which include both diffusion and advection) accompanied with adsorption in such *homogeneous* porous media. Our novel contribution in this research is the development of a *micro-macro* coupling between the microscopic and macroscopic length scales, which forms the basis of our macroscale models to reflect the macroscopic behaviour of the system. Two versions of the macroscale models are proposed: (a) *complete Volume Averaged Model* (VAMc) and (b) *simplified Volume Averaged Model* (VAMs), which involve two effective transfer coefficients, namely, the total dispersion tensor and the adsorption-induced vector.

Further, in order to investigate one of the critical design parameters of a porous water filter, the 'hydraulic detention time' of the polluted water in the filter, we carry out an extensive numerical investigation of the proposed macroscale models. For this, first we nondimensionalize the pore-scale and macroscale models, which leads to surfacing of two important dimensionless numbers, namely, the *Damköhler* number and the *Péclet* number. Next, we develop a 2-D geometry of porous media made up of a chain of 100 identical unit cells for testing the above-mentioned models. The numerical simulations corresponding to the dimensionless pore-scale model, which are referred to as the Direct Numerical Simulation (DNS), and the dimensionless macroscale models, which are referred to as the Volume Averaged Model (VAM), are conducted on the chain-of-unit-cells geometry. The intrinsic average concentration predictions from the macroscale models display excellent results on comparison with the pore-scale (or DNS) outcomes. We also assess the importance of large fluid-solid interfacial area inherent in porous adsorbents by varying the porosity and number of particles inside the artificially-prepared porous-media models. The total dispersion tensor coefficient is

iii

validated and found to be in excellent agreement with the literature. Our findings reveal that an increase in the interfacial area of the models leads to higher effective transfer coefficient values.

Last, we perform adsorption experiments in an effort to evaluate the effectiveness of the proposed macroscale models. For this, three trials of column-flow experiment are conducted using an adsorbent made up of functionalized zeolite material to remove phosphorus from synthetically prepared influent. Micro-CT scans of zeolite material are used to develop a unit-cell representative of the pore space inside the actual adsorbent medium. The numerical simulations on the unit-cell provide realistic effective transfer coefficient values; however, a large difference between the concentration predictions from theory and experimental results is noted. The lack of adherence to the time-scale constraints is assessed to be the primary reason behind this discrepancy. We offer different recommendations in order to improve the experiments and accurately gauge the effectiveness of the macroscale models.

Overall, these models have the potential to improve the state-of-the-art technologies for modeling contaminant transport in porous water filters by providing useful recommendations based on numerical simulations, and may be used as a tool for the optimization of the design of porous water filters.

iv

To my family

TABLE OF CONTENTS

xi

LIST OF FIGURES

xvii

LIST OF TABLES

NOMENCLATURE

Symbol[1]	Description	Unit
A	Damköhler number (or dimensionless adsorption isotherm)	dimensionless
$A_{\beta\sigma}$	interfacial area between the β and σ phases in the REV	m^2
$A^*_{\beta\sigma}$	$= A_{\beta\sigma}/l^2$, interfacial area between the β and σ phases in the REV	dimensionless
$a_{\beta\sigma}$	the $\beta - \sigma$ interfacial area per unit volume	m^{-1}
$\mathbf{b}_\beta$	closure variable (vector) used to describe the distribution of $\tilde{c}_\beta$	m
$\mathbf{b}^*_\beta$	$= \mathbf{b}_\beta/l$ or $\mathbf{b}_\beta/(l\,Pe)$, closure variable (vector) used to describe the distribution of $\tilde{c}_\beta$	dimensionless
c_{ad}	surface concentration on the $\beta - \sigma$ interface	kg mol/m^2
c_β	point concentration of species X in the β-phase	kg mol/m^3
c^*_β	$= c_\beta/c_{in}$, point concentration of species X in the β-phase	dimensionless
$\tilde{c}_\beta$	$= c_\beta - \langle c_\beta\rangle^\beta$, spatial deviation in concentration of the β-phase	kg mol/m^3
$\langle c_\beta\rangle^\beta$	intrinsic phase average concentration in the β-phase	kg mol/m^3
$\langle c_\beta\rangle_{\beta\sigma}$	area-averaged concentration at the $\beta - \sigma$ interface	kg mol/m^3
c_{in}	constant inlet concentration of species X in the β-phase	kg mol/m^3
C	solute concentration used in the analytical solution for a finite domain	kg mol/m^3
C_0	reference concentration used in the analytical solution for a finite domain	kg mol/m^3
C_e	equilibrium concentration of phosphorus solution	mg/L
C_i	initial concentration of phosphorus solution	mg/L
D_0	constant dispersion coefficient used in the analytical solution for a finite domain	m^2/s

Da	convection transport based Damköhler number	dimensionless
$\mathcal{D}_\beta$	molecular diffusivity of the β-phase	m^2/s
$\mathbf{D}_\beta$	hydrodynamic dispersion tensor	m^2/s
$\mathbf{D}_\beta^*$	total dispersion tensor	m^2/s
$\mathbf{D}_\beta^{**}$	$= \mathbf{D}_\beta^*/\mathcal{D}_\beta$, ratio of total dispersion tensor to molecular diffusivity	dimensionless
$\mathbf{D}_{eff}$	effective diffusivity tensor	m^2/s
g	acceleration due to gravity	m/s^2
h	hydrostatic pressure head	m
$\mathbf{I}$	identity tensor	dimensionless
K	permeability of the porous medium	m^2
K_d	linear equilibrium partitioning coefficient	L/kg
K_{eq}	equilibrium coefficient for the linear isotherm (or the distribution coefficient)	m
l	length of the unit-cell	m
l_σ	characteristic length-scale associated with the average particle size (solid phase)	m
l_β	characteristic length-scale associated with the pore size (fluid phase)	m
$l_{\tilde{c}_\beta}$	characteristic length-scale for variation in $\tilde{c}_\beta$	m
$l_{\langle c_\beta \rangle^\beta}$	characteristic length-scale for variation in $\langle c_\beta \rangle^\beta$	m
$l_{\frac{\partial \langle c_\beta \rangle^\beta}{\partial t}}$	characteristic length-scale for variation in $\frac{\partial \langle c_\beta \rangle^\beta}{\partial t}$	m
l_{s_β}	characteristic length-scale for variation in s_β	m
$l_{\langle \mathbf{v}_\beta \rangle^\beta}$	characteristic length-scale for variation in $\langle \mathbf{v}_\beta \rangle^\beta$	m
l_{ϵ_β}	characteristic length-scale for variation in ϵ_β	m
$\mathbf{l}_i$	lattice vector corresponding to direction i for the repetition of unit cells	m

L	characteristic length associated with the macroscale	m
m	mass of adsorbent sample	g
$\mathbf{n}_{\beta\sigma}$	unit normal directed from β-phase to σ-phase	
N	$= L/l$, number of unit cells in the macroscale model	
P	$= P_0 - \rho_\beta gh$, hydrodynamic fluid pressure in the β-phase	N/m^2
P_0	total fluid pressure	N/m^2
P^*	$= l\,P/(\mu\,v_c)$, hydrodynamic fluid pressure in the β-phase	dimensionless
P_{in}^*	$= N$, hydrodynamic fluid pressure in the β-phase at the inlet of the DNS model	dimensionless
$\|\nabla\langle P\rangle^\beta\|$	average macroscopic pressure gradient applied across the porous domain	N/m^2
Pe	cell Péclet number	dimensionless
Pe_p	particle Péclet number	dimensionless
q_e	adsorption capacity at equilibrium	mg/g
r_o	size of the REV	m
$\mathbf{r}$	position vector	m
s_β	closure variable (scalar) used to describe the distribution of $\tilde{c}_\beta$	s/m
s_β^*	$= s_\beta/(l/D_\beta)$, closure variable (scalar) used to describe the distribution of $\tilde{c}_\beta$	dimensionless
t^*	$= t\,D_\beta/l^2$, diffusion time variable used in the dimensionless pore-scale model	dimensionless
t_{conv}^*	$= t\,v_c/l$, convection time variable used in the dimensionless pore-scale model	dimensionless
T^*	$= t\,D_\beta/L^2$, diffusion time variable used in the dimensionless upscaled models	dimensionless

T^*_{conv}	$= t\,v_c/L$, convection time variable used in the dimensionless upscaled models	dimensionless
u_0	uniform flow velocity used in the analytical solution in the finite domain	m/s
$\mathbf{u}_\beta$	adsorption-induced vector in the β-phase	dimensionless
$\mathbf{v}_\beta$	point velocity of the β-phase	m/s
$\mathbf{v}^*_\beta$	$= \mathbf{v}_\beta/v_c$, point velocity of the β-phase	dimensionless
$\langle\mathbf{v}_\beta\rangle^\beta$	intrinsic phase average velocity of the β-phase	m/s
$\tilde{\mathbf{v}}_\beta$	$= \mathbf{v}_\beta - \langle\mathbf{v}_\beta\rangle^\beta$, spatial deviation in velocity of the β-phase	m/s
$\tilde{\mathbf{v}}^*_\beta$	$= \tilde{\mathbf{v}}_\beta/v_c$, spatial deviation in velocity of the β-phase	dimensionless
$\|\langle\mathbf{v}^*_\beta\rangle^\beta\|$	$= \|\langle\mathbf{v}_\beta\rangle^\beta\|/v_c$, magnitude of the dimensionless intrinsic phase average velocity	dimensionless
v_c	characteristic velocity of the β-phase	m/s
V	volume of the REV	m^3
V_β	volume of the β-phase within an REV	m^3
V^*_β	$= V_\beta/l^3$, volume of the β-phase within an REV	dimensionless
V_l	volume of phosphorus solution	L
$\mathbf{w}$	velocity of the $\beta - \sigma$ interface	m/s
x^*	$= x/l$, x-direction coordinate used in the dimensionless pore-scale model	dimensionless
x_0	length of the finite domain used in the analytical solution	m
X^*	$= x/L$, x-direction coordinate used in the dimensionless upscaled models	dimensionless
y^*	$= y/l$, y-direction coordinate used in the dimensionless pore-scale model	dimensionless
β	fluid phase in the homogeneous porous medium	
ϵ_β	volume fraction of the β-phase	dimensionless

xxiii

μ	fluid dynamic viscosity	N·s/m^2
ϕ_β	generic variable of the β-phase	
ρ_β	fluid density	kg/m^3
σ	solid phase in the homogeneous porous medium	
τ	characteristic time for changes in $\tilde{c}_\beta$ within the REV	s
∇	differential operator operating at the length-scale l	
∇^*	$= \nabla \, l$, dimensionless differential operator operating at the length-scale l	
∇_L	differential operator operating at the length-scale L	
∇_L^*	$= \nabla_L \, L$, dimensionless differential operator operating at the length-scale L	

---

[1]List of symbols used in Chapters 3 to 5 and Appendices C to E.

ACKNOWLEDGEMENTS

CHAPTER 1

Introduction

1.1   Motivation and Objectives

Porous media studies surpass mathematics, science, and engineering. This broad and complex interdisciplinary subject is of immense theoretical and practical interest across numerous fields, such as composites manufacturing, chemical engineering, ground water hydrology, petroleum engineering, and soil mechanics [1]. It is crucial to study the physics of fluid flow through porous media in such scientific and engineering disciplines. However, the fundamental theories to explain the microscopic phenomena face a daunting challenge in precisely capturing the effect of extremely complicated solid surface geometries on fluid flow inside the porous domain. In this respect, the well-known experiment-based Darcy's law [2], mathematical analytical models of porous flows [3, 4] and various upscaling techniques [5] provide the tools to develop and solve the microscopic problem at a macroscopic scale.

An integral part of the theoretical and applied research in flow, heat, and mass transfer in porous media involves studying the effect of porosity variation and determining the anisotropic permeability and dispersion tensors [6]. These critical factors govern the fluid and mass transport in any given porous medium, which are generally multiphase, multi-species, non-laminar, and non-isothermal flows. Moreover, the medium is often anisotropic and undergoes physical transformation when subjected to external fields, such as stress, electric, gravitational, temperature gradients, among others. Hence, in order to develop accurate and efficient permeability or dispersion prediction models, it is important to carefully analyze and incorporate the pore-scale effects resulting due to the

1

irregular-shaped solid particles into the macroscopically measurable flow quantities.

Nowadays, an accurate knowledge of permeability distribution is a key parameter in dealing with advanced technological applications, such as energy harvesting devices [7], microfluidics for medical diagnosis [8], oil recovery [9], liquid composite molding [10, 11], and contaminant filtration [12–14]. In such relatively slow moving flows, it is possible to determine the velocity field using the steady-state Navier-Stokes equations, and then use the average flow velocity with the applied pressure gradient to estimate the permeability of the medium. The scalar approximations in such cases may provide useful order of magnitude estimates of the permeability. However, when dealing with anisotropic porous media, more often than not they are inaccurate [15–18]. One of the solutions offered to solve this problem is employing the channel flow experiments approach. Here, three experiments must be conducted in three different orientations to determine the two-dimensional permeability tensor [19]. However, this estimation process requires six experiments in six different orientations when practised in three dimensions, and thus becomes quite complicated [20]. This difficult situation is even further complicated if the principal permeability directions are a priori unknown. These directions are easy to figure out in simple systems such as a bank of parallel aligned fibers [21, 22]. However, for most real systems (with either the fibers distributed randomly, or the fibers in the form of tows of continuous filaments woven or stitched in intricate repetitive patterns), such directions are not obvious. Even in filtration materials such as polyurethane foam based porous adsorbents [12], where the cell structure is not necessarily consistent, the use of traditional methods to evaluate the flow parameters related to permeability have limited capabilities. Hence, based on the importance of finding permeability of a medium, it is critical to develop a technique which not only facilitates in obtaining accurate permeability *tensors*, but is also simple to implement and time-efficient.

Next, among various water treatment technologies available, the adsorption-based filtration technique involving porous media is most widely employed because it is cost-

2

effective, highly efficient, and easy to operate [23,24]. For this reason, the need to develop accurate mathematical models for providing deep insight into the adsorption process, which involves capturing of dissolved metal ions such as As(III) and As(V) onto the *active* surface of the solid particles, is a research priority. Contaminant transport in porous media is a well-researched problem across many scientific and engineering disciplines, including soil sciences, groundwater hydrology, chemical engineering, and environmental engineering. In general, this multiscale transport phenomenon can be studied by the use of either the pore-scale or the Darcy-scale models. Although significant strides have been made both in pore-scale modeling and computational capabilities [25, 26], the complex pore microstructures still pose a computational challenge in applying the pore-scale simulations in a real-world porous medium [27]. Thus, there is a need to work on an efficient approach which leads to the development of accurate macroscale models while considering a porous medium as an averaged continuum system, and thereby reduce the computational complexities involved in the models.

Hence, in response to the above-mentioned problems, this thesis focuses on proposing a novel contaminant transport modeling method based on the volume averaging theory in porous media. Additionally, it also discusses the Whitaker's closure formulation based method for estimating flow permeability in porous media.

These translate into the following objectives for the thesis:

1. **Development of a permeability estimation method for porous media:** Traditional permeability estimation techniques such as the Stokes-Darcy flow method [19] require three channel flow experiments in two-dimensions and six experiments in three-dimensions (very difficult to perform) for determining the complete permeability tensor of a porous medium. Hence, our goal is to find permeability using a closure formulation method which is derived from the volume averaging theory, and compare it with the results obtained from the Stokes-Darcy flow method. Chapter 2 of the thesis is focused on achieving this goal.

3

2. **Modeling contaminant transport in porous media:** By modeling the contaminant transport problem in porous media using the volume averaging theory, our goal is to propose macroscale models that can accurately describe the macroscopic behaviour of the system while accounting for the pore microstructure and adsorption reactions occurring at the microscopic scale. Chapter 3 of the thesis explains the theoretical developments involved in the formulation of these macroscale models.

3. **Validation of the proposed macroscale models:** After developing the macroscale models, our goal is to validate the models on the basis of a numerical investigation. Also, we conduct adsorption experiments, and draw a comparison between the concentration predictions from the proposed models and experimental results. Chapters 4 and 5 of the thesis are focused on the numerical validation of the macroscale models and comparison with the experiments, respectively.

1.2 Organization

The thesis has been written such that Chapter 2 can be read independent of others. Next, Chapters 3 to 5 are devoted to the common subject of macroscale modeling, and explain the theoretical, numerical, and experimental research, in that order. Overall, the document is organized as follows. Chapter 2 discusses a method for estimating flow permeability in porous media. Chapter 3 focuses on the development of volume-averaged models for contaminant transport in porous media. Chapter 4 is based on a numerical investigation of the proposed volume-averaged models. Chapter 5 presents a comparison between the predictions from the volume-averaged models and experiments.

CHAPTER 2

Permeability Estimation of Porous Media

2.1   Literature Review

The permeability of a porous medium is an important physical property that is employed to determine the flow field(s) using Darcy's law from the distributions of liquid pressure(s) during single- and multi-phase flows in porous media. Development of experimental, numerical, and theoretical methods to estimate the permeability is a field of study in itself [28–36], and finds applications in several areas of engineering and geosciences. The prediction of permeability of anisotropic porous media (e.g., a bed of packed aligned fibers) is relatively more challenging compared to that in the isotropic porous media (e.g., soil, sand, iron filings, etc.) because of the more complex representation (in the form of a 2nd order tensor) in the former [1]. In this context, it can be pointed out that porous water filters sometimes use fibers or elongated particulates (created through an extrusion-like manufacturing process). This may cause the medium to be anisotropic in nature, and therefore lead to permeability to be in the form of a tensor. Due to this, the velocity distribution and/or pressure distributions could result into three-dimensional forms in a cylindrical filter, which traditionally, is treated as a 1-D domain due to the isotropic nature of porous medium created in the filter. Hence, the work presented in this chapter is relevant in the context of modeling transport in such anisotropic water-filters.

The field of process modeling of composite materials, especially that of the polymer matrix composites, has been a significant contributor to the research of permeability estimation because of the use of fibers as reinforcements. The permeability is used for conducting mold-filling simulations to optimize mold design in the liquid composite

www.manaraa.com

molding (LCM) processes including the resin transfer molding (RTM) and the vacuum-assisted resin transfer molding (VARTM) [20, 37–42]. Though models are available for analytically predicting permeability for porous media made of fibers arranged in regular geometrical patterns [29–33, 43–51], more often than not they are inaccurate [15–18, 52]. This happens because of several factors including complex 3-D arrangement of fibers in real fabrics, inhomogeneity caused by packing of fabrics in LCM molds [46], higher permeability near the mold walls causing race tracking, gaps formed between fabric layers in a layered porous medium, and nesting [53,54]. Hence, though one can use the analytical models to get an order of magnitude estimate of the permeability, invariably one must rely on experimental measurement to determine the permeability for fibrous porous media created inside the molds [17,18].

A layer of complexity is added by the fact that the permeability is a function of the property porosity. Wherever the fibrous preform undergoes compression or expansion during mold-filling (say in VARTM [10]), one often requires multiple experiments in order to track the dependence of permeability on the porosity. Though such experiments involving simple flow geometries are easy to model mathematically [18,55–58], development of the corresponding setups is an expensive and time consuming proposition. There is also the issue of calibration of such a setup which is tied to the accuracy of the permeability value obtained from the equipment [59].

In the last couple of decades, significant research has been done to develop techniques to reconstruct the pore structure of porous media in 2-D using optical and electron microscopy (SEM, TEM, etc.) [15, 60, 61] and in 3-D using X-ray microtomography or micro-CT or μ-CT [16, 42, 62–64]. In case the 3-D reconstruction becomes expensive in terms of memory usage, disk storage, time and money, software such as GeoDict allows one to generate unit cells with the same average properties as those of a real porous medium. (For example, GeoDict has been used to generate unit cells using the porosity and average fiber-diameter for (1) a glass-fiber wick [17], and (2) fiber tows [18]). In the

6

last FPCM (Flow Processes in Composites Materials) conference at Lulea, Sweden in 2018, the issue of *directly* measuring permeability from the microstructure was raised in the workshop on Virtual Permeability Benchmark. The idea is that one develops the 2-D or 3-D pore geometry within a unit-cell and then runs flow simulations in order to get permeability results from the applied pressure and flow rate data.

The permeability estimation method of using the Stokes equation for modeling flow in a unit-cell is well known [65]. Brown [66] experimentally showed that when a fluid flows through a porous medium, the flux and the pressure gradient are linearly dependent, and that the coefficient of proportionality comprises of two terms: the first, characterizing the flowing material, is the viscosity, and the second, characterizing the porous medium, is the permeability. In other words, the Darcy's law is followed if Stokes flow is occurring between the particles of a porous medium. For isotropic media, the process of permeability estimation is quite simple: first use the Stokes equation to compute the flow rate through an isotropic unit-cell, then apply the Darcy's law to estimate the scalar permeability. However, for anisotropic porous media, the permeability is a 2nd order tensor with six unknown components and its estimation process becomes quite complicated [20]. As we shall see later, for the determination of the 2-D permeability tensor[1] with three unknown components, three Stokes flow simulations have to be conducted along three unique directions. Similarly, for the determination of the full 3-D permeability tensor in a normal porous medium, six Stokes flow simulations along six separate directions have to be conducted [19]. This difficult situation exists if the principal permeability directions are a priori <u>unknown</u>. These directions are easy to ascertain in simple systems such as a bank of parallel aligned fibers [21, 22]. However, for most real systems (with either the fibers distributed randomly, or the fibers in the form of tows of continuous filaments

---

[1]The thin fabrics woven or stitched from carbon or glass fibers are used to make preforms for the RTM or VARTM processes that are employed for making polymer-matrix composites with small wall thicknesses. The porous medium made by the compression of the preform in the RTM/VARTM mold can then be treated as a 2-D porous medium for the in-plane flow of the resin. The permeability can then be represented as a 2×2 matrix and can be characterized as a 2-D tensor [37].

woven or stitched in intricate repetitive patterns), such directions are not obvious. It is to be noted that these principal directions can be determined by studying the ellipse (in a 2-D study) and the ellipsoid (in a 3-D study) that result from conducting a liquid injection experiment at a single point with the major and minor axes of the resultant elliptical front corresponding with the principal directions [56]. Such experiments are easy to conduct for the 2-D case where a transparent flat mold can be used to observe the progress of the flow front in the 2-D plane [64, 67–70]. However, we are not aware of any satisfactory setup available that can 'see' such a front developing in the 3-D media which is often opaque (though some work has been done in the past to sense the arrival of fronts at different mold locations using grids of optical fibers or conducting wires [67]). Once these principal permeability directions are known, one can generate the full permeability tensor by conducting the Stokes flow simulations along only two principal directions in the 2-D case, or only three principal directions in the 3-D case.

In the composites processing community, there is a trend to believe that one can measure the transverse or 'Z-direction' permeability by conducting some transverse or across-the-thickness flow experiments for fiber mats or fabrics [71, 72]. Such a belief, at best, can be classified as an untested hypothesis because a stack of fabrics may very well have their three principal-permeability directions arranged in a very complex 3-D fashion– to the best of our knowledge, no one has tested the fact that the Z-direction is indeed one of the principal directions!

The volume averaging method [73–77] is often used in upscaling the flow and transport phenomena in porous media from the microscale to macroscale. Whitaker, one of the foremost proponents of this upscaling technique, employed the rigorously-derived volume averaging theorems for deriving the Darcy's law from the first principles [78]. One can use this derivation to comment on the permeability of a porous medium. Valdes-Parada et al. [52] used the volume averaging method to show that the permeability of a porous medium is influenced by its microstructure and the Carman-Kozeny equation is incapable

of estimating the permeability over a broad range of porous media configurations. Kim et al. [79] used unit cells with regular arrangement of rectangular particles in their volume-averaging study. The dimensions of these rectangular obstacles, representative of the solid phase, were varied while preserving the porosity of the model. In an attempt to predict permeability with confidence, Eidsath [80] solved the closure problem for different arrangement of arrays of cylinders and his results matched reasonably with Bergelin et al.'s [81] experimental work. Similarly, Zick et al. [65] estimated the permeability by calculating the drag force exerted on a periodic array of spheres using the Stokes flow.

In recent years, a volume averaging-based approach, to be referred to here as the closure formulation method, has been identified as a credible **numerical** technique to estimate the permeability of porous media. The closure formulation, where the macroscopic flow variables (pressure and velocity) were linked to the microscopic variations in the same flow quantities within a unit cell, was developed to close the averaged momentum equation [82]. This integro-differential formulation, where a boundary value problem expressed in terms of a set of elliptic partial differential equations (PDEs) is solved in unit cells with periodic boundary conditions, is now regularly used in the estimation of permeability [17, 18, 60, 83, 84]. For example, Barari et al. [60] used the closure formulation to estimate the permeability of porous media made from cellulose nano-fibers and sintered polymer beads and found them to be quite close to the experimentally determined values. Similarly, Zarandi et al. applied the closure formulation to determine the permeability for glass-fiber wicks [17] and fiber tows [18], which matched very well with the experiments and Stokes-flow simulations. *A significant advantage of this volume averaging-based method is that the complete permeability tensor can be determined from* **only one** *simulation.* The additional advantage of the method is the development of an effective micro-macro coupling, i.e., permeability is derived from solving the closure formulation in a unit cell of real porous media, thus incorporating the effects of detailed

9

pore-scale geometry in the resulting permeability tensor[2].

In this chapter, we seek to compare these two important numerical methods to estimate the permeability directly from the pore microstructure: (1) the *closure formulation* method, and (2) the *Stokes-Darcy* method based on numerical simulation of the creeping flow in unit cells. In the closure formulation method, the governing equations for the mapping variables (used for closing the volume-averaged momentum equation [82]) are solved after applying the periodicity conditions and the resulting fields are integrated to yield the complete permeability tensor. Hence, this first method provides a fast and relatively inexpensive way to find the in-plane permeability tensor through a **single** simulation. In the Stokes-Darcy method, 1-D channel flow numerical experiments are conducted along three different directions for the 2-D medium, and along six different orientations for the 3-D medium. For a pressure differential applied over the unit-cell, the resulting flow rate is used in the Darcy's law to obtain the effective permeability along the chosen direction. The complete permeability tensors in the 2-D and 3-D cases are obtained after significant mathematical manipulations of the three and six effective permeability values, respectively. Hence, this second method is rather long as it requires multiple flow simulations along with the subsequent tedious computations and manipulations.

Our main aim in this chapter is to rigorously test the performance of the closure formulation in predicting permeability by comparing it with the Stokes-Darcy flow method. The questions we want to be answered are: **(a)** How does the accuracy of the closure formulation compare with that of the Stokes-Darcy method for an anisotropic porous medium where the principal directions are not known? **(b)** Do we realize the advantage of much lesser number of numerical experiments, and hence significantly reduced computational time, associated with the former technique?

---

[2]The effect of microstructure is usually included in the analytical permeability models through (a) average particle/fiber diameter and (b) porosity (which is the ratio of pore volume to the total volume in an REV) [18].

2.2 Theory and Mathematical Formulation

2.2.1 Permeability estimation using the closure formulation

The closure formulation to estimate the porous medium permeability is based on the volume averaging method as proposed and practiced by Whitaker [82]. A synopsis of the method is presented in this section. The physical process under study is that of a single-phase flow in a rigid porous medium described in terms of a $\beta - \sigma$ system, where σ represents the rigid stationary solid phase and β denotes the fluid phase passing through the pore space of the porous medium. In such a flow, the volume fraction of the β phase is equal to the porosity of the porous medium, which is defined as the ratio of fluid (pore) volume inside a fixed representative elementary volume (REV) to the total volume of the REV.

As proposed by Whitaker [82], the volume averaging method can be used to rigorously derive the Darcy's law at the macroscale from the Stokes equation at the microscale. In the derivation, an intermediate volume averaged-equation contains integral terms that require the knowledge of deviation of the point velocity of fluid from its average velocity. In other words, to close the system of equations, the distribution of velocity and pressure deviations from their averages is required, which effectively splits the length scale in the problem into the local pore scale and the macroscopic lab scale. The method then puts forth a system of equations and boundary conditions called the closure formulation, so as to minimize the information loss occurring during upscaling of pressure and velocity fields. The vector, $\boldsymbol{d}_\beta$, is the transformed pressure-mapping variable while the 2$^{\text{nd}}$ order tensor, $\mathbf{D}_\beta$, is the transformed velocity-mapping variable. The basic purpose of the closure formulation is to generate the $\boldsymbol{d}_\beta$ and $\mathbf{D}_\beta$ fields within the pore region of the considered unit-cell so that they can be integrated to obtain the permeability tensor, $\mathbf{K}$, for the porous medium.

11

The closure equation that results from the Stokes equation is given as

$$-\nabla \boldsymbol{d}_\beta + \nabla^2 \mathbf{D}_\beta + \mathbf{I} = 0 \qquad (2.1)$$

and similarly, the closure equation derived from the continuity equation can be expressed as

$$\nabla \cdot \mathbf{D}_\beta = 0 \,. \qquad (2.2)$$

Note that the closure-formulation problem can be shown to be similar to the Stokes flow boundary value problem that can be solved in a unit-cell [82]. The no-slip boundary condition at the fluid-solid interface and the periodic flow conditions at the unit-cell boundaries are transformed into equivalent boundary conditions for the closure-formulation as follows:

Boundary Condition 1

$$\mathbf{D}_\beta = 0 \quad \text{at } A_{\beta\sigma} \,. \qquad (2.3)$$

Boundary Condition 2

$$\mathbf{D}_\beta \left(\mathbf{r} + l_\mathrm{i}\right) = \mathbf{D}_\beta \left(\mathbf{r}\right) \qquad (2.4)$$

$$\boldsymbol{d}_\beta \left(\mathbf{r} + l_\mathrm{i}\right) = \boldsymbol{d}_\beta \left(\mathbf{r}\right) \,. \qquad (2.5)$$

The periodicity boundary condition indicates that the opposite boundaries of the unit cells have same values for $\boldsymbol{d}_\beta$ and $\mathbf{D}_\beta$ at the corresponding points. Here, $\mathbf{r}$ represents the position vector of any point on the unit-cell boundary, while l_i is the lattice vector with $i \in (1, 2, 3)$ that expresses the spatially periodic nature of the unit-cell [60].

Once $\boldsymbol{d}_\beta$ and $\mathbf{D}_\beta$ are solved for, the permeability tensor, $\mathbf{K}$, is obtained as a result of the global averaging constraint placed over deviation in the velocity field and is estimated through

$$\mathbf{K} = \epsilon_\beta \left\langle \mathbf{D}_\beta \right\rangle^\beta \qquad (2.6)$$

12

where $\langle \mathbf{D}_\beta \rangle^\beta$ is the intrinsic phase average of the mapping variable $\mathbf{D}_\beta$, and is defined by

$$\langle \mathbf{D}_\beta \rangle^\beta = \frac{1}{V_\beta} \int_{V_\beta} \mathbf{D}_\beta \, dV \tag{2.7}$$

such that V_β is the volume of the β phase within the REV.

Note that estimation of the permeability tensor using the closure-formulation technique does not involve the use of any fluid properties (viscosity and density).

2.2.2 Permeability estimation through the Stokes-Darcy Method

The Stokes-Darcy method is essentially the traditional channel-flow experiment approach for numerically estimating the permeability, which involves setting up a 1-D flow geometry, imposing a pressure drop across the system, generating corresponding the flow rate, finding the average fluid velocity using the flow rate, and finally, calculating the effective permeability using the Darcy's law. This approach is easy for isotropic porous media and yields the permeability as a scalar quantity. However, for anisotropic porous media where the permeability is a 2nd order tensor, the 1-D (channel) flow method is not a straightforward one [19].

The most general form of the Darcy's law for anisotropic porous media (in matrix form) is

$$\begin{Bmatrix} q_1 \\ q_2 \\ q_3 \end{Bmatrix} = -\frac{1}{\mu} \begin{bmatrix} K_{11} & K_{12} & K_{13} \\ K_{21} & K_{22} & K_{23} \\ K_{31} & K_{32} & K_{33} \end{bmatrix} \begin{Bmatrix} \partial_1 P \\ \partial_2 P \\ \partial_3 P \end{Bmatrix} \tag{2.8}$$

where q_i with $i \in (1, 2, 3)$ represent the Darcy velocity components, K_{ij} are the components of the permeability tensor, μ is the dynamic viscosity of the fluid, and $\partial_i P$ is the pressure gradient along i-direction of the chosen coordinate system.

In the 1-D flow experiments where the liquid is forced through a flat rectangular mold with layers of fabrics as a preform that is sandwiched between the top and bottom

13

mold plates, the side walls are assumed to be impermeable and effective permeabilities are evaluated along chosen directions. Next, we adopt the permeability measurement framework put forth by Weitzenböck et al. [19] to determine the permeability tensor components based on complex non-linear combinations of effective permeabilities. Appendices A and B list those permeability expressions for the 3-D and 2-D cases, respectively.

2.2.2.1 2-D permeability estimation

As explained in Appendix B, the results from the unidirectional flow experiments along three different in-plane directions are used to decipher the complete 2-D tensor. The principal permeability components K_1, K_2 and θ are expressed in terms of the effective permeabilities K_I, K_{II} and K_{III} along the chosen flow directions I, II and III (see Fig. 2.8), respectively, as

$$K_1 = K_I \left(\frac{A - D}{A - \frac{D}{cos2\theta}} \right) \tag{2.9}$$

$$K_2 = K_{III} \left(\frac{A + D}{A + \frac{D}{cos2\theta}} \right) \tag{2.10}$$

$$\theta = \frac{1}{2} \tan^{-1} \left(\frac{A}{D} - \frac{A^2 - D^2}{K_{II} \cdot D} \right) \tag{2.11}$$

such that $A = \left(\frac{K_I + K_{III}}{2} \right)$ and $D = \left(\frac{K_I - K_{III}}{2} \right)$. Finally, the permeability tensor, $\mathbf{K}$, with its components K_{xx}, K_{yy} and K_{xy}, are derived from these principal values (Eqs. (2.9-2.11)) as per Eqs. (B.15-B.17).

2.2.2.2 3-D permeability estimation

The 3-D permeability measurements are generally based on three simplified 1-D flow experiments along the a priori known or assumed principal directions. However, Weitzenböck et al.'s [19] approach enables the determination of the 3-D permeability tensor in case these principal directions are not known or assumed. In this case, six-independent

14

unidirectional in- and out-of-plane experimental measurements are required for obtaining the tensor.

First, the effective permeability values (K_i with $i \in (I, VI)$) are calculated using the Darcy's law by simulating pressure fields across six different orientations over the unit-cell. Next, these values are inputted into some complex expressions for permeability tensor component as given by Eqs. (A.12-A.17) in Appendix A. Finally, the principal permeabilities K_1, K_2 and K_3 along with the principal directions are obtained by performing the standard eigenvalue and eigenvector operations on the resultant permeability matrix.

2.3 Theoretical Model

This chapter aims to test the anisotropic permeability tensors obtained from the conventional Stokes-Darcy method and the closure formulation method for both the 2-D and 3-D cases. Here we endeavor to first create unit cells with solid-phase particles.

In this section, we describe the following steps:

1. Preparation of models for anisotropic 2-D and 3-D porous media.

2. Orientations of the pressure field applied across the unit cells extracted from the models.

3. Calculation of permeability after solving the fluid-flow equations inside the unit cells.

The models developed for the 2-D and 3-D porous media and the examples of unit cells extracted from them for the present study are shown in Figure 2.1. Note that the model developed for the 3-D system was smaller than that for the 2-D system; this is because of the larger memory and disk space requirements for the former.

15
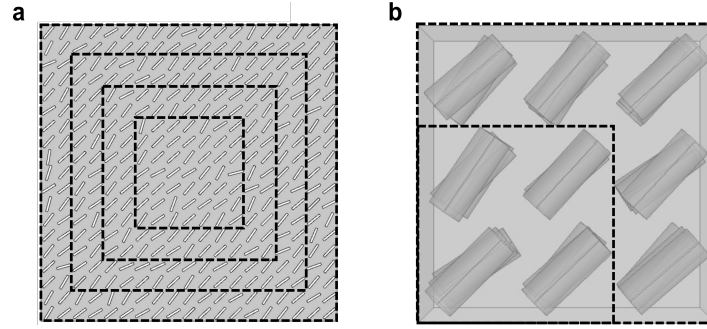
Figure 2.1: Examples of unit cells extracted from: (a) 2-D model (700 μm to 1900 μm), (b) 3-D model (200 μm and 300 μm). The unit cells used in the study are marked with black dashed lines while the REV can be approximated by the largest unit cell possible for the two cases.

2.3.1 Preparation of models for anisotropic porous media

The closure formulation technique has been tested on unit cells representing isotropic porous-media and found to give accurate results [65,79,80]. We advance these studies by further testing and evaluating this volume averaging-based method on appropriate unit cells for anisotropic porous media. Note that to create flow-related anisotropic nature in a porous medium, the solid-phase particles are expected to be elongated as well as oriented along some preferred direction. Here, we will first create an idealized model of such a medium, and then extract unit cells from it. This procedure will be followed in both the 2-D and 3-D systems.

The model development involves the following stages: **first**, preparation of angular positions of the solid-phase particles using a MATLAB-based random number generator algorithm; **next**, calculation of the coordinates of these particles within an REV encompassing the whole model, and **finally**, alteration of the particle shapes and fixing their orientations while maintaining overall porosity in the REV.

In the following sections, each of these sub-steps is further discussed in greater details.

2.3.1.1 Orientation of the particles

Anisotropic porous media properties such as permeability depend on the measurement direction. Therefore, to create anisotropy in our models, we chose to align the particles
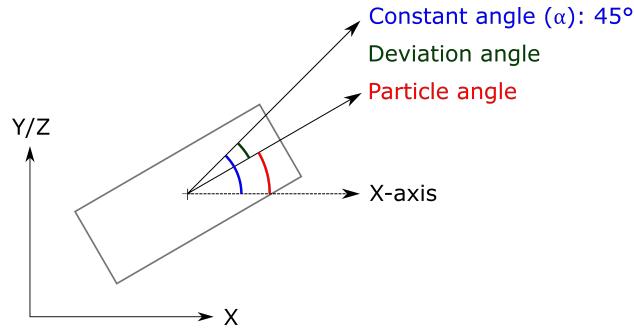
Figure 2.2: Various angles associated with the determination of particle orientation in 2-D and 3-D models.

within a pre-defined band of deviations with respect to a constant angle, as shown in Figure 2.2. We mathematically present it as

$$\text{Particle angle} = \text{Constant angle} \pm \text{Deviation angle}. \qquad (2.12)$$

We decided to use a random value for the deviation angle in order to render the particle angle stochastic in nature. This is because, in reality, similar particles are never aligned perfectly.

For both the 2-D and 3-D unit cells, the constant angle alpha, α, defined with respect to the X-axis, was assumed to be 45° and the particle angles were set using the "normrnd" function in MATLAB. This function generates a normal random number distribution based on the inputted parameters that are mean 'μ' and standard deviation 'σ'. The parametric values used in the normrnd function for the two unit cells are listed in Table 2.1. Figure 2.3 shows the Gaussian distribution of these particle angles, centered around the constant angle of 45°.

Table 2.1: Parametric values used in the calculation of particle angles.

Dimensions	Constant angle (°)	Deviation angle (°)
2-D	$\alpha = 45$	$\mu = 0$
		$\sigma = 10$
3-D	$\alpha = 45$	$\mu = 0$
		$\sigma = 10$

17

The constant angle which is defined beforehand has another objective. This provides a validation test for the principal directions calculated as the eigenvectors of the permeability tensor. If the principal directions closely match the assumed constant angle, it would verify and give credence to the principal-angle calculation method [19] for the 2-D case. Since each chosen unit-cell would have a unique permeability tensor and the resulting principal directions, the closeness of the latter to the assumed constant angle would also enable one to compare the accuracy of both the methods in predicting the permeability tensor.

2.3.1.2 Position of the particles and shape effect

The 2-D model representing anisotropic porous media is made up of a square domain interspersed with elongated particles representing the solid phase. The particles were placed equidistantly along the X- and Y-axes with 100 μm distance between them as shown in Fig. 2.4a. The corresponding 3-D model is a cube with equidistantly placed particles along the three major axes. The distance between these particles was 100 μm and they were oriented along the randomly-computed particle angles as discussed in Section 2.3.1.1. The positional details of the particles in the 3-D case are shown in Fig. 2.4b.

With such a regular placement of particles, different unit cells of varying sizes were
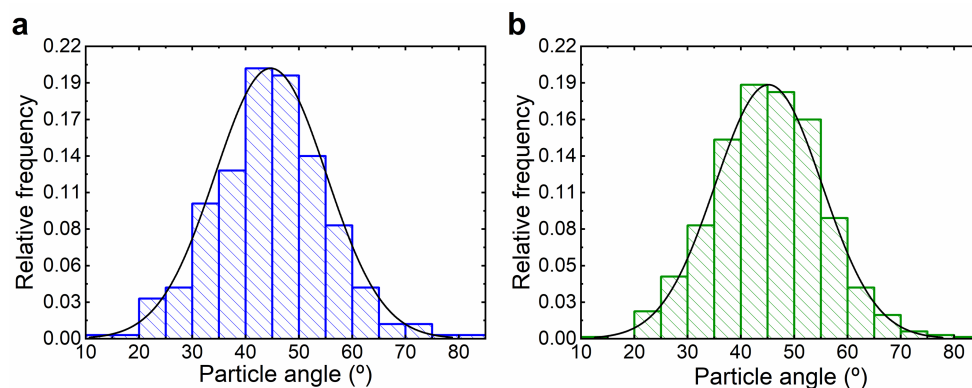
Figure 2.3: Histograms for particle angle distribution in: (a) 2-D model, (b) 3-D model.

18
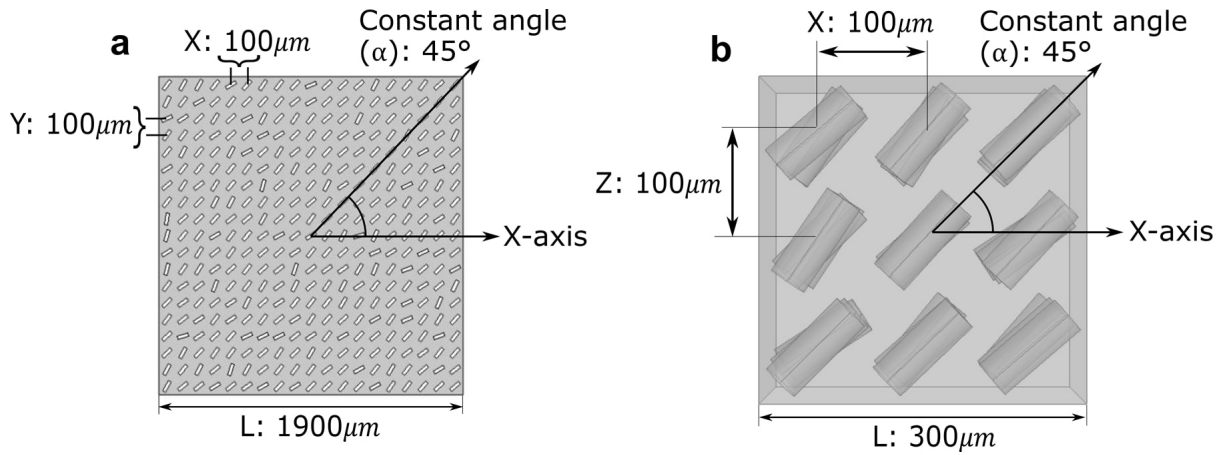
Figure 2.4: The Constant angle and the distances between particles in: (a) 2-D model, (b) 3-D model.

created/extracted from the model without violating the periodic boundary-condition needed for the closure-formulation solution, which clearly requires the opposite edges of the unit-cell to be of identical nature [81]. (We are aware that such models of real porous media constructed from micrographs rarely satisfy this criterion of periodic boundary-condition, and in such cases, permeability studies have been performed while capturing the truncated details of an actual microstructure within an assumed unit-cell [60, 81]. The use of such unit cells with artificially-enforced periodic boundaries in non-periodic microstructures leads to generation of some error, which is defined as deviation from the actual solution of the closure problem close to the REV borders [61, 82].)

As shown in Fig. 2.5a and Fig. 2.5b, elliptical and rectangular particle shapes were considered for the 2-D model while ellipsoids and cylinders were used for the 3-D models. The areas/volumes of the particles in the 2-D/3-D models were adjusted such that the overall porosity of the unit cell remains constant. This basically means setting equivalent areas for the rectangular and elliptical particles in the 2-D case (or equivalent volumes for the cylindrical and ellipsoidal particles in the 3-D case) by suitably altering their dimensions uniformly across all the particles in the models. The shape-change study led to alteration in the microstructure, which was then used to test the effectiveness of the proposed permeability-estimation methods in capturing the resultant sharp contrast in

www.manaraa.com
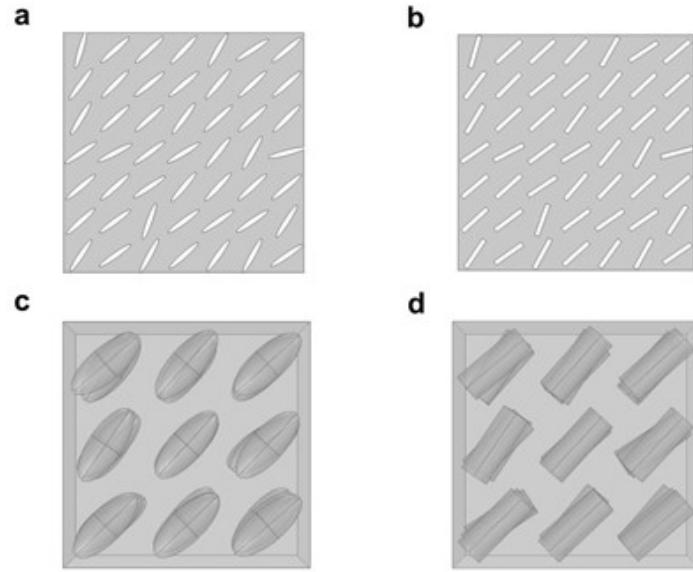
Figure 2.5: Different particle shapes used in the shape-change study: (a) ellipse and (b) rectangle for 2-D unit cells; (c) ellipsoid and (d) cylinder for 3-D unit cells, while preserving the overall REV porosity (ϵ_β). The white regions in (a) and (b) denote the solid particles, whereas the grey region is the pore phase. The dark-grey shaded objects in (c) and (d) indicate solid particles in the 3-D domain and the remaining empty portion is the pore volume.

permeability behaviour in terms of the diagonal terms vis-à-vis the non-diagonal terms.

Also, the aspect ratio (AR) of these particles was manipulated to generate anisotropy in the system from an initally existing isotropic configuration (see Fig. 2.6a and Fig. 2.6b). The aspect ratio for a 2-D ellipse model was defined as the ratio of semi-major to semi-minor axis of a particle, for a 2-D rectangle model it is the ratio of length to breadth of a particle, for a 3-D ellipsoid model it is again the ratio of semi-major to semi-minor axis of a particle (where two out of three axes are assumed to be semi-minor and of equal length), and finally, for a 3-D cylinder model it is set as the ratio of length to diameter of a particle.

2.3.2 Orientations of the pressure field to conduct Stokes-Darcy flow simulations

There is an added layer of difficulty associated with the Stokes-Darcy method of finding the permeability tensor. As previously stated, Weitzenböck et al. [19] have shown that the 3-D permeability tensor can be derived from the channel flow data with the help of
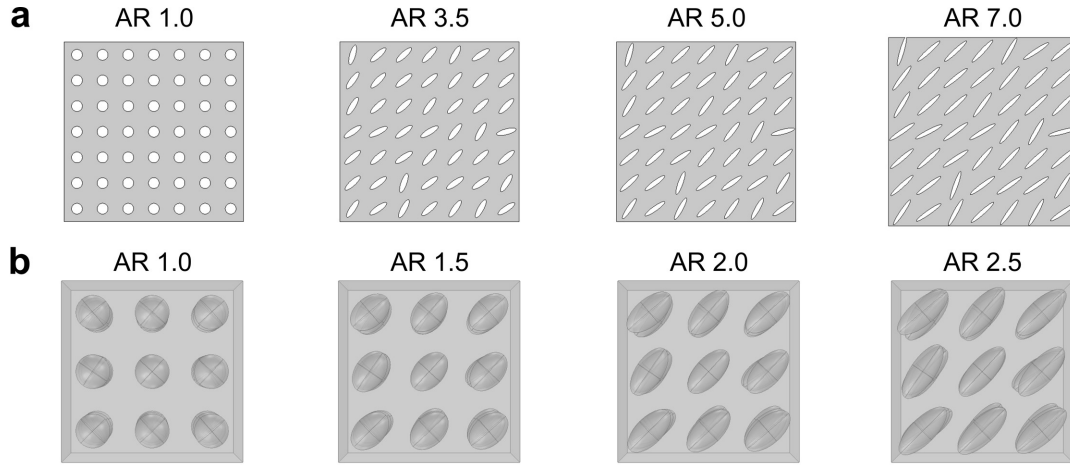
Figure 2.6: Different aspect ratios (AR) used in the shape-change study: (a) 2-D models, with AR ranging from 1.0 to 7.0; (b) 3-D models, with AR ranging from 1.0 to 2.5. Note that AR 1.0 (i.e., AR = 1.0) represents isotropic unit cells, whereas AR 7.0 and AR 2.5 indicate maximum anisotropy in the 2-D and 3-D models, respectively.

at least six different unidirectional flow experiments. Similarly, three independent flow experiments are required for determination of the 2-D permeability tensor. Along all these required flow directions, one must find ways of imposing pressure gradients in the considered 2-D and 3-D models numerically, and that can be challenging.

It is important to note that the six different flow experiments performed in the 3-D case need to consider both *in-plane* and *out-of-plane* experiments. This is because after determining three directional (effective) permeabilities in a plane, any further measurements in the same plane would prove ineffective in deciphering the complete tensor [19]. Therefore, if a channel flow experiment is conducted to measure permeability in the X-Y-Z coordinate system along the X-axis, two more of the effective permeabilities can be obtained from the X-Y plane; however, the remaining three experiments have to be conducted in the out-of-plane space to account for the required permeability values in the X-Z and Y-Z planes. This is achieved by conducting 1-D channel flow experiments across the system along different orientations as shown in Fig. 2.7.

As shown in Fig. 2.8, in the 2-D case, the pressure gradient is applied along three directions: first, along the X-axis (direction *I*); second, at an angle 45° to the X-

21
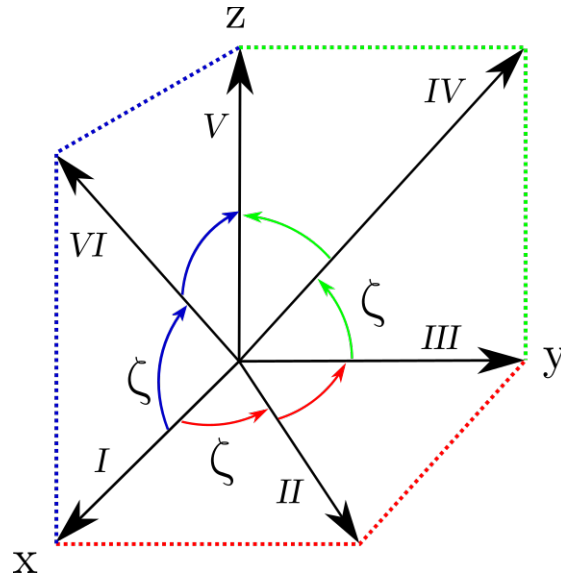
Figure 2.7: The various measurement directions in the laboratory frame of reference considered for 1-D channel flow experiments to obtain the 3-D permeability tensor. The magnitude of angle ζ is 45°.

axis (direction II), and finally, along the Y-axis (direction III). These three effective permeability values are used to calculate the principal permeability components as given by Eqs. (2.9-2.11). Generally, one should first calculate the angle of orientation (θ) and then use it to obtain K_1 and K_2. Further, the permeability tensor components are found using their correlation with the principal permeability tensor through a passive rotation of the latter about the Z-axis by angle θ, which is measured from direction I towards direction 1. The final expressions for the tensor components are given in Eqs. (B.15-B.17).

It is also worth mentioning here about the models which were treated as exceptions to the above-mentioned procedure. For the case of AR 1.0, when the models are isotropic, only a single Stokes-Darcy flow simulation is performed to capture the permeability of the medium. Here, the 2-D rectangle unit cells with AR 1.0 (unlike their ellipse counterparts which are perfectly circular for this case and the resulting porous medium is isotropic) are assumed to be very close to the isotropic state with minimal deviations occurring due to variation in the particle angles. The permeability results pertaining to these exceptions are further discussed in Section 2.4.3.1.
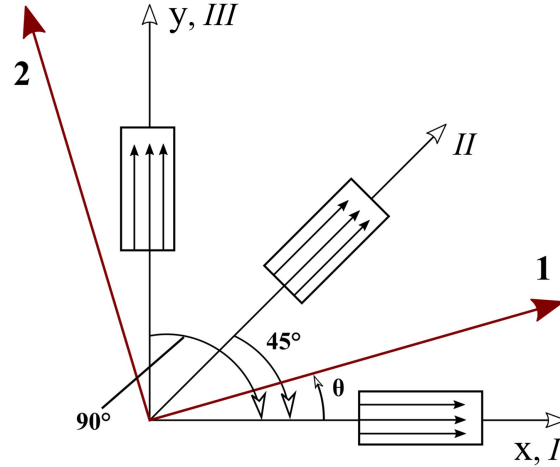
Figure 2.8: I, II and III denote the three directions of the 1-D (channel) flow experiment for the 2-D case. 1 and 2 are the principal directions of the permeability tensor. The angle θ defines the flow direction vis-à-vis the principal direction 1.

In the 3-D case, the first channel flow experiment is conducted along the X-axis (see Fig. 2.7) to obtain the first effective permeability value (K_I). The next measurement direction (i.e., the direction of imposed pressure gradient) is chosen along the angle ζ (equal to 45°) with respect to the X-axis in the X-Y plane of the laboratory frame of reference. Consequently, one needs to relate the permeability components pertaining to the second effective permeability value with the first, and this is done by passively rotating the first measurement direction about the Z-axis by angle ζ. The second effective permeability value (K_{II}) is obtained after feeding the rotated tensor component expressions into the unidirectional effective permeability equation (refer to Appendix A for more details). Following the same procedure, K_{III} is calculated by further rotation of the measurement direction about the Z-axis by 45° (which makes the measurement direction parallel to the Y-axis, as shown in Fig. 2.7). Next, K_V is obtained by rotating the measurement direction I about the Y-axis by $-90°$, which results in measurement along the Z-axis in the laboratory frame of reference. The measurement direction IV (to find K_{IV}), which lies in the Y-Z plane, is obtained after successive rotations of direction I about the Z- and X-axis by 90° and 45°, respectively, whereas the rotation of direction
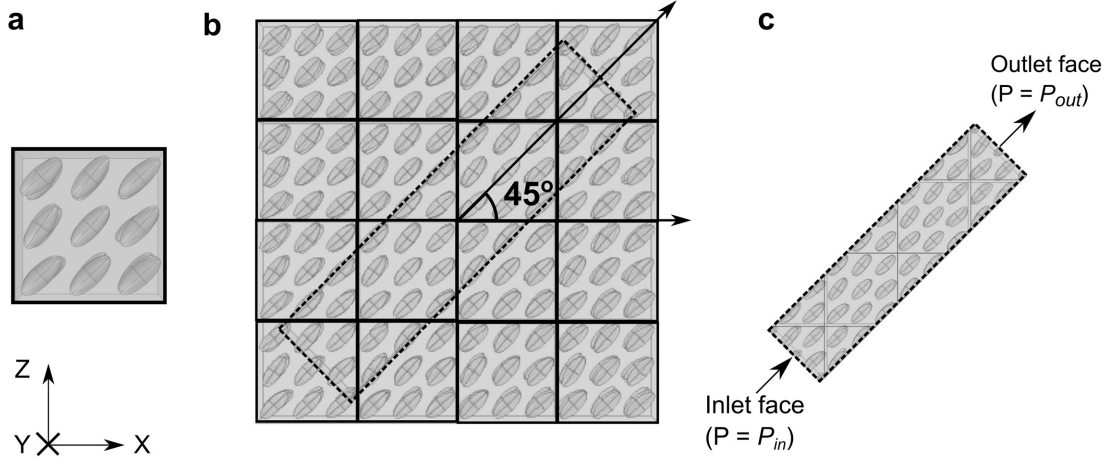
Figure 2.9: Steps involved in the preparation of a sample 3-D model for measuring the effective permeability K_{VI} in the X-Z plane, where (a) shows the X-Z view of the sample unit-cell, and (b) shows an array of the sample unit-cell replicates (all marked by solid black lines), and the diagonally-positioned long and narrow flow domain (marked by the broken black line) drawn for the measurement of K_{VI}. Finally, (c) shows the inlet and outlet faces of the newly created domain corresponding to the enforced pressure gradient along the direction VI. (Note that × in the coordinate system icon indicates the Y-axis pointing into-the-plane.)

I about the Y-axis by $-45°$ results in measurement direction VI, which leads to K_{VI} residing in the X-Z plane. Finally, these six directional permeabilities are reformulated in terms of the 3-D permeability tensor components using Eqs. (A.12-A.17) given in Appendix A.

(Note that these components are different from those presented in Appendix B of [19]. This is because Weitzenböck et al.'s [19] permeability estimation method in the 3-D case proposes incorrect rotation angles for the measurement direction I for measurement of the effective permeabilities, K_V and K_{VI}. We have offered modifications for the same and formulated the correct expressions for the tensor components in the 3-D case, as given in Appendix A.)

As done in the 2-D case, only a single Stokes-Darcy simulation is required to solve the permeability tensor for the 3-D unit cells with AR 1.0 ellipsoids (or spheres) representing an isotropic porous medium. However, two simulations are needed to accurately capture the permeability tensor for 3-D unit cells representing isotropic porous media with AR 1.0 cylinders: one, along the X- or Z-axis, and the other, along the Y-axis. The reason

24

behind the extra simulation is that although the 3-D cylinder unit cells with AR 1.0 cylinders were seemingly close to achieving a scalar permeability tensor, the shape of the particle along with variation in particle angles caused a slight deviation from the isotropic state (see K_{yy} component in the 3-D cylinder unit-cell tensors with AR 1.0 in Table 2.11) and hence it became necessary to account for these effects using another simulation in the direction orthogonal to the X-Z plane. (Note that the particle angles for 3-D models are only set in the X-Z plane, and therefore the susceptibility to permeability change is maximum when considering the area projected by the particles onto this plane.) Hereafter, keeping in mind the above caveat, the 3-D cylinder unit cells with AR 1.0 are reasonably close to be treated as isotropic models. A summary of the concerned pressure gradient directions for both 2-D and 3-D models is given in Table 2.2.

At this stage, some comment on how the permeability along a non-cardinal direction is measured is in order. Fig. 2.9 illustrates the steps followed for creating a sample flow domain for measurement of K_{VI}. The steps are described as follows. First, we switch to the X-Z view of the sample unit-cell, as shown in Fig. 2.9a. Next, we create an array of the sample-unit cell's replicates in the X- and Z-directions, as illustrated by the unit-cells marked by solid black lines in Fig. 2.9b. A long and narrow domain (highlighted by the broken black line in Fig. 2.9b), which is rotated about the Y-axis by $45°$, is also carved out from this cluster of unit cells. Finally, the pressure boundary conditions are imposed along the direction VI across the inlet and outlet faces of this newly created flow domain, as depicted in Fig. 2.9c. A similar strategy is implemented for effective permeability measurements along the other pressure-gradient directions. Note that the reason behind creation of a long and narrow domain is that the unidirectional flow approximation produces more accurate results for higher aspect-ratio flow regions, as demonstrated by Tan et al. [11].

The applied pressure-gradient directions for our anisotropic models are listed in Table 2.2. With the help of the permeability expressions developed by Weitzenböck et al. [19]

Table 2.2: Pressure gradient directions for 2-D and 3-D models.

Model type	Effective permeability	Direction of pressure gradient[3]
2-D, 3-D	K_I	along X-axis
2-D, 3-D	K_{II}	45° between X- and Y-axis
2-D, 3-D	K_{III}	along Y-axis
3-D	K_{IV}	45° between Y- and Z-axis
3-D	K_V	along Z-axis
3-D	K_{VI}	45° between Z- and X-axis

for ζ equal to 45°, we estimated the 2-D and 3-D permeability tensors using the method described in Appendices B and A, respectively.

2.3.3 Numerical simulation methods for estimation of permeability tensor

Researchers have evaluated permeability of porous media made of fibres/particles [30, 46, 47, 85] while validating them with the theoretical models based on idealized geometrical arrangements of fibres/particles [31, 45, 86]. Most of this research is focused on estimation of 2-D permeability; however, we are unaware of any anisotropic porous media studies assessing the validation of a complete 3-D permeability tensor. The decreasing cost of computational power has given us an opportunity to numerically test our models using the Stokes-Darcy flow and closure formulation methods.

2.3.3.1 Stokes-Darcy simulation

In this method, the continuity and Navier-Stokes governing equations for Newtonian flows are solved inside the unit cells. The slow movement of fluid through the pores leads us to assume that the Reynolds number for the particles in this case would be less than 1, hence, justifying the application of the Creeping flow physics in COMSOL Multiphysics, a finite element-based solver. To resemble the 1-D channel flow set up, symmetry boundary conditions are imposed on the opposite edges/faces of the 2-D/3-D models resembling

---

[3]The pressure gradient directions are as per the laboratory frame of reference.

26

rectangle/rectangular box, respectively. The effective permeability, K_i with $i \in (I, VI)$, can be calculated by imposing pressure differentials along different directions in 2-D/3-D models as discussed in Section 2.3.2 and then using the Darcy's law. It is given by

$$K_{eff} = \frac{\mu \, Q \, L}{(P_{in} - P_{out}) \, A} \tag{2.13}$$

where μ is the dynamic viscosity of the fluid, Q/A (= flow rate/cross-sectional area) is the specific discharge, P_{in} is the input pressure, P_{out} is the output pressure, and L is the REV length across the chosen flow direction.

The physical parameter values used in our Stokes-Darcy flow simulations are listed in Table 2.3. Finally, the effective permeability values are used to evaluate the full 2-D/3-D permeability tensors using the procedures described in Section 2.2.2.

2.3.3.2 Closure formulation simulation

As discussed in Section 2.2.1, the transformed form of the pore-level momentum and continuity equations for the closure formulation are given by Eqs. (2.1-2.2), respectively. $\mathbf{D}_\beta$ is a 2$^{\text{nd}}$ order tensor and is the mapping variable overseeing the variation in the velocity field within the unit-cell. Similarly, the vector $\boldsymbol{d}_\beta$ is the mapping variable which predicts pressure variation within the pore region of the unit-cell. The Coefficient form of PDE, a mathematical module available in COMSOL, is selected for the purpose of modeling these equations. Eqs. (2.1) and (2.2) are applied throughout the fluid domain of the unit cells. Boundary Condition 1 (given by Eq. (2.3)) is essentially a 'No-slip' condition, which is imposed on the fluid-solid interface area, $A_{\beta\sigma}$. Boundary Condition 2 (given by

Table 2.3: Physical parameter values used for Stokes-Darcy flow simulations.

Physical parameter	Value	Description
μ	0.001 Pa·s	Dynamic viscosity
P_{in}	1 Pa	Inlet pressure
P_{out}	0 Pa	Outlet pressure

27
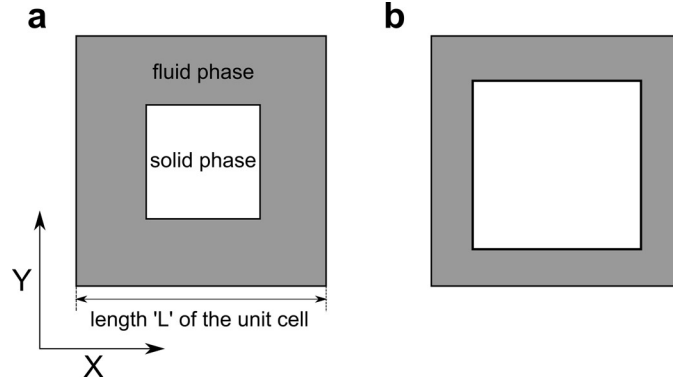
Figure 2.10: Unit cells of an idealized 2-D porous medium considered by Lasseux et al. with the porosities of (a) 75% and (b) 50% [87].

Eqs. (2.4-2.5)) calls for periodicity of the pressure and velocity fields and is imposed on the opposite edges/faces of the 2-D/3-D unit cells, respectively. This procedure leads to the development of six coupled equations in the 2-D case and twelve coupled equations in the 3-D case. After solving these equations, the product of the intrinsic phase-averaged $\mathbf{D}_\beta$ and porosity, ϵ_β, would give the permeability tensor, $\mathbf{K}$, through the use of Eq. (2.6).

2.4   Results and discussion

2.4.1   Initial validation of the permeability estimation methods

For validating the closure-formulation method and gauging its accuracy for estimating the permeability, we chose to compare our results with those of a study performed by Lasseux et al. [87] on an idealized isotropic porous medium. As shown in Fig. 2.10, square-shaped obstacles (considered to be solid phase) placed at the center of the larger square-shaped unit cells (with side-length L) were considered for validation. The two models described in parts (a) and (b) of the figure have the porosities of 0.75 and 0.50, respectively. Further, the governing equations and boundary conditions given in Eqs. (2.1-2.5) were solved within the computational domain (i.e., in the vacant or 'pore' part of the unit-cell) using COMSOL, and the resultant permeability was normalized with the side-length 'L' of the unit cell to order to generate $\mathbf{K}^*$.

28

Table 2.4 shows excellent agreement between the permeability results obtained from our closure-formulation simulation and those of Lasseux et al.'s [87]. Achievement of such a good match validates our simulation. It also strengthens our confidence in using this technique for further analysis.

Note that the validation of the Stokes-Darcy flow method, i.e., the channel-flow experimental approach, for estimating the permeability tensor is presented elsewhere [19]. Here, we aim to validate our permeability results by comparing them with the predictions of a few theoretical models for permeability. The following prominent theoretical models have been selected for this purpose: the Gebart model for flow transverse to parallel fibers, the Bruschke & Advani model for flow across the parallel fibers (using the square unit-cell), and the Kozeny-Carman model for flow through a packed bed of solids ([17]). For validation, we chose to test these models on an ellipse unit-cell with AR 1.0 (i.e., representing a transversely isotropic porous medium) where the porosity (ϵ_β) is 86% and the mean radius of a particle is 21.11 µm. The results from both the permeability estimation methods (i.e., the closure-formulation and the Stokes-Darcy flow methods) and those calculated from the analytical expressions corresponding to the theoretical models are presented in Table 2.5. A remarkable degree of closeness can be observed between the permeability values predicted by the different permeability estimation models. It should be noted that the theoretical models have various built-in constraints and are often considered useful for providing good ballpark estimates of permeability values for porous-media samples [17]. But, in this study we observe a very good agreement between

Table 2.4: Comparison of the closure-formulation result of Lasseux et al. [87] and that of the present work for the 2-D isotropic porous-medium shown in Fig. 2.10 in terms of the dimensionless permeability $\mathbf{K}^*$.

Porosity	Dimensionless permeability $\mathbf{K}^*(= \frac{\mathbf{K}}{\mathrm{L}^2})$	
	Lasseux et al.'s results	Present work's results
50%	0.002386	0.002375
75%	0.013023	0.013014

Table 2.5: Comparing the permeability values obtained from the numerical simulation methods under study with those from the theoretical models [17] for an ellipse unit-cell with AR 1.0. The unit-cell has porosity (ϵ_β) of 86% and the mean radius of a particle is 21.11 µm (Unit: $\times 10^{-10} \, \text{m}^2$).

Numerical simulation methods		Theoretical models		
Stokes-Darcy flow	Closure-formulation	Gebart	Bruschke & Advani	Kozeny-Carman
3.01	2.99	3.06	2.52	3.21

the permeability results obtained from these theoretical models, and our Stokes-Darcy flow and closure-formulation approaches, which further validates the accuracy of our numerical simulations.

2.4.2 Mesh independence study

A mesh independence study was performed to evaluate the sensitivity of the permeability results to mesh refinement. In COMSOL, the pore-region computational domains were progressively subjected to three refinement levels: start with a coarse mesh, follow it with a normal mesh, and conclude with a fine mesh. The permeability values for flow along X, Y and Z axes were compared for both 2-D and 3-D models and found to converge in the fine mesh setting. Therefore, we finally used the fine mesh size for our models to make permeability estimations.

For CFD simulation, COMSOL's mesh generator discretized the pore domains of 2-D

Table 2.6: Mesh details for the sample 2-D and 3-D unit cells.

Model type	Element type	Number of elements		
		Coarse	Normal	Fine
	Triangular	19001	20476	33325
2-D	Quadrilateral	727	747	1451
(L = 1900 µm)	Edge	3219	3278	4751
	Vertex	1448	1448	1448
	Tetrahedral	10277	30721	42168
3-D	Triangular	2744	5402	6516
(L = 300 µm)	Edge	720	1092	1128
	Vertex	170	170	170

unit cells with triangular and quadrilateral elements, and the pore domains of 3-D unit cells with tetrahedral and triangular elements. The 2-D specimen selected for this purpose is a unit-cell of length 1900 μm composed of rectangular particles with AR 3.5. The 3-D sample is a unit-cell of length 300 μm comprising ellipsoidal particles with AR 1.0. The mesh details for these specimens are listed in Table 2.6. The permeability variables for flow along the major axes, X, Y and Z, are compared and tabulated in Table 2.7 for different mesh sizes. For the closure-formulation method, they consist of K_{11}, K_{22} and K_{33}, whereas for the Stokes-Darcy method, they are K_I, K_{III} and K_V. Fig. 2.11 shows the convergence of permeability values for the selected mesh sizes. The relative error criterion, ε, is set as

$$\varepsilon = \left| \frac{K^{Fine} - K}{K^{Fine}} \right| . \tag{2.14}$$

The solution with the maximum mesh refinement (fine mesh in this case) is considered as the reference and the corresponding errors are reported in Table 2.8.

We clearly observe from Fig. 2.11 that the permeability values are nearly equal despite an increase in the number of elements corresponding to different mesh types. Also, Table 2.8 suggests that the relative error, ε, mostly decreases from the coarse mesh to normal mesh, and the maximum error amongst the permeability variables corresponding to the normal mesh is 0.72% (corresponding to K_{11} in 3-D case), which still falls within

Table 2.7: Permeability values for flow along major axes for different mesh sizes.

Model type	Mesh type	Permeability variables ($\times 10^{-10}\,\mathrm{m^2}$)					
		K_{11}	K_{22}	K_{33}	K_I	K_{III}	K_V
	Coarse	5.11	5.11	5.09	5.39	5.40	5.39
3-D	Normal	5.11	5.13	5.12	5.41	5.43	5.41
	Fine	5.14	5.14	5.14	5.42	5.43	5.42
	Coarse	1.95	1.88	–	1.70	1.66	–
2-D	Normal	1.91	1.87	–	1.70	1.66	–
	Fine	1.91	1.88	–	1.70	1.67	–
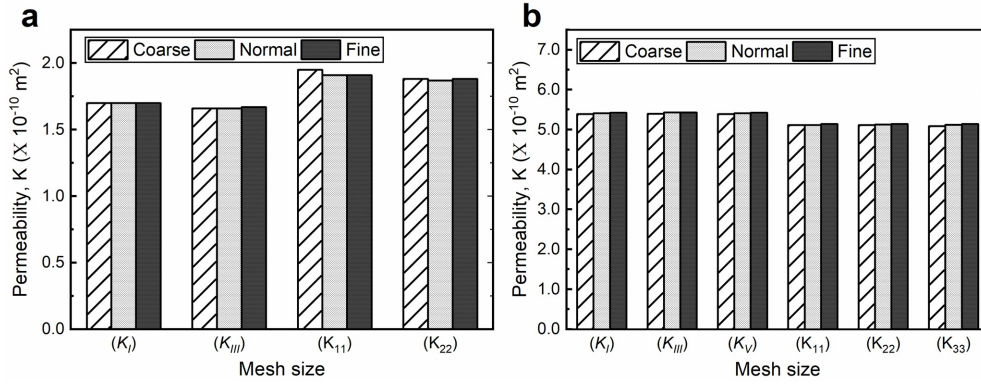
Figure 2.11: Mesh independence study comparing the permeability values from the Stokes-Darcy (K_I, K_{III} and K_V) method and the closure-formulation (K_{11}, K_{22} and K_{33}) method for (a) 2-D case, (b) 3-D case, and corresponding to the coarse, normal and fine mesh sizes.

an error band of 1%. This confirms the accuracy of our numerical solutions and helps in establishing the mesh independence of our results.

2.4.3 Comparison of the permeability tensors

After establishing the accuracy of our numerical simulations, we present the results for the calculated permeability tensors in Table 2.9 and Table 2.11. The important parameters considered in this investigation are the aspect ratio (AR) of the particles, particle shape, and the unit-cell size. The next two sections comprise of comparative studies between the permeability tensors obtained from the closure-formulation and Stokes-Darcy methods for unit cells of different sizes. Finally, we compare the computational (CPU) times

Table 2.8: Relative error corresponding to the chosen permeability variables for different mesh sizes.

Model type	Mesh type	Relative error, ε, in the considered permeability variables (%)					
		K_{11}	K_{22}	K_{33}	K_I	K_{III}	K_V
	Coarse	0.58	0.61	1.07	0.59	0.60	0.60
3-D	Normal	0.72	0.37	0.39	0.15	0.14	0.14
	Fine	–	–	–	–	–	–
	Coarse	1.70	0.24	–	0.14	0.75	–
2-D	Normal	0.00	0.21	–	0.06	0.60	–
	Fine	–	–	–	–	–	–

32

pertaining to both the methods and establish the superiority of the closure-formulation method in this matter.

2.4.3.1   2-D models

The permeability results corresponding to variations in the unit-cell size, aspect ratio (AR), particle shape, and the estimation methods are presented in Table 2.9. The off-diagonal terms which are 3~6 orders-of-magnitude lower than the diagonal components have been considered as numerical errors and equated to zero.

We begin by observing the effect of unit-cell size on the permeability tensors. It is generally accepted that a larger unit-cell is more suitable for simulation since it would encompass more microstructural details and the periodicity condition would progressively generate smaller contribution from the border regions of the unit-cell (hence lead to smaller overall errors) [61]. In the present study also, we expected the permeability values for different-sized unit cells of a given porosity and aspect ratio (containing evenly positioned solid particles aligned within a specified angular band) to experience only small variations. This fact was confirmed by comparing our results for different unit-cell with similar ARs. For example, if we consider all the 2-D (ellipse) unit cells with AR 5.0 in Table 2.9, then it can be noted that the permeability tensors are reasonably close across the different-sized unit cells corresponding to both the methods. The resultant difference between such tensors can most notably be attributed to the variance in the particle angles associated with different unit cells, which, albeit small, remains noticeable.

Next, we investigate the effect of variation in AR on permeability tensors. If we observe unit cells of a particular size (e.g., the 2-D ellipse unit cells of size 1500 μm), then we note from Table 2.9 that with the increase in AR, the diagonal permeability values reduce whereas the off-diagonal terms increase. The permeability tensors corresponding to unit-cell size ranging from L = 700 μm to 1900 μm consistently follow the aforementioned pattern across the variation in AR. In this scenario, as the particles become more elongated,

33
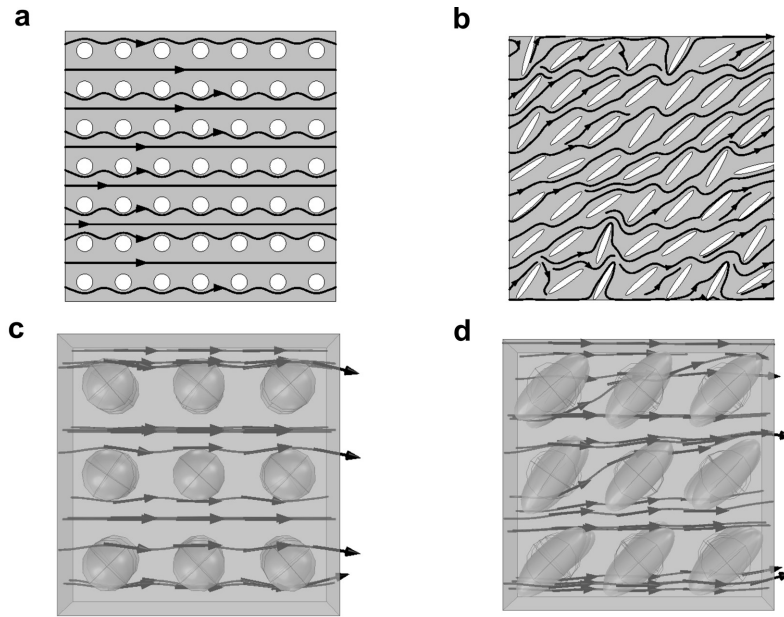
Figure 2.12: A sample of streamlines (shown by black arrow lines) representing fluid flow inside the unit-cell for (a) 2-D ellipse model with AR = 1.0, (b) 2-D ellipse model with AR = 7.0, (c) 3-D ellipsoid model with AR = 1.0, and (d) 3-D ellipsoid model with AR = 2.5.

the flow streamlines bend around them and majorly get diverted along the constant direction (α) (see Fig. 2.12b). This alteration/elongation of flow paths along the major axes of particles results in anisotropy, and is characterized by permeability reduction along the major axes (the diagonal terms), which is countered by an increase along the particle-orientation direction (the off-diagonal terms).

Let us compare the effect of the two methods on the increase in anisotropy. For AR changing from 1.0 to 7.0, the average permeability drops across the main diagonal elements by 29%-44% for the rectangular particles and by 46%-55% for the elliptical ones. On the other hand, for AR 7.0, the average difference between the off-diagonal and main diagonal terms reduces to 39%-49% for the rectangular particles and 35%-35% for the elliptical ones compared to the almost two orders-of-magnitude difference for AR 1.0! (Note that the former number in % corresponds to the Stokes-Darcy result while the latter to the closure-formulation one.)

34

Table 2.9: Computed permeability tensors for 2-D models corresponding to different: 1) unit-cell sizes, 2) aspect ratios (AR), 3) particle shapes, and 4) permeability estimation methods. The porosity across the unit cells is 0.86 and the geometrical mean radius of an elliptical particle is $21.11\,\mu$m.

Unit-cell size (μm)	Aspect ratio (AR)	Particle shape	Permeability tensor ($\times 10^{-10}\,\mathrm{m}^2$)	
			Stokes-Darcy flow	Closure-formulation
700	1.0	Rectangle	$\begin{bmatrix} 2.36 & 0.00 \\ 0.00 & 2.36 \end{bmatrix}$	$\begin{bmatrix} 2.45 & 0.01 \\ 0.00 & 2.45 \end{bmatrix}$
		Ellipse	$\begin{bmatrix} 3.03 & 0.00 \\ 0.00 & 3.03 \end{bmatrix}$	$\begin{bmatrix} 2.99 & 0.00 \\ 0.00 & 2.99 \end{bmatrix}$
	3.5	Rectangle	$\begin{bmatrix} 2.04 & 0.75 \\ 0.75 & 1.94 \end{bmatrix}$	$\begin{bmatrix} 1.91 & 0.46 \\ 0.46 & 1.87 \end{bmatrix}$
		Ellipse	$\begin{bmatrix} 2.33 & 0.86 \\ 0.86 & 2.22 \end{bmatrix}$	$\begin{bmatrix} 2.08 & 0.71 \\ 0.76 & 2.07 \end{bmatrix}$
	5.0	Rectangle	$\begin{bmatrix} 1.80 & 0.81 \\ 0.81 & 1.69 \end{bmatrix}$	$\begin{bmatrix} 1.62 & 0.56 \\ 0.58 & 1.59 \end{bmatrix}$
		Ellipse	$\begin{bmatrix} 1.99 & 0.96 \\ 0.96 & 1.85 \end{bmatrix}$	$\begin{bmatrix} 1.76 & 0.85 \\ 0.78 & 1.63 \end{bmatrix}$
	7.0	Rectangle	$\begin{bmatrix} 1.73 & 1.01 \\ 1.01 & 1.53 \end{bmatrix}$	$\begin{bmatrix} 1.38 & 0.68 \\ 0.68 & 1.33 \end{bmatrix}$
		Ellipse	$\begin{bmatrix} 1.64 & 0.98 \\ 0.98 & 1.47 \end{bmatrix}$	$\begin{bmatrix} 1.37 & 0.73 \\ 0.87 & 1.33 \end{bmatrix}$
	1.0	Rectangle	$\begin{bmatrix} 2.33 & 0.00 \\ 0.00 & 2.33 \end{bmatrix}$	$\begin{bmatrix} 2.47 & 0.00 \\ 0.00 & 2.48 \end{bmatrix}$
		Ellipse	$\begin{bmatrix} 3.01 & 0.00 \\ 0.00 & 3.01 \end{bmatrix}$	$\begin{bmatrix} 3.00 & 0.00 \\ 0.00 & 3.00 \end{bmatrix}$
		Rectangle	$\begin{bmatrix} 2.09 & 0.90 \\ 0.90 & 2.11 \end{bmatrix}$	$\begin{bmatrix} 1.88 & 0.50 \\ 0.49 & 1.92 \end{bmatrix}$

1100	3.5	Ellipse	$\begin{bmatrix} 2.33 & 0.93 \\ 0.93 & 2.35 \end{bmatrix}$		$\begin{bmatrix} 2.13 & 0.72 \\ 0.74 & 2.16 \end{bmatrix}$	
		Rectangle	$\begin{bmatrix} 1.86 & 0.93 \\ 0.93 & 1.86 \end{bmatrix}$		$\begin{bmatrix} 1.67 & 0.60 \\ 0.63 & 1.67 \end{bmatrix}$	
	5.0	Ellipse	$\begin{bmatrix} 2.01 & 1.04 \\ 1.04 & 2.02 \end{bmatrix}$		$\begin{bmatrix} 1.72 & 0.85 \\ 0.82 & 1.75 \end{bmatrix}$	
		Rectangle	$\begin{bmatrix} 1.71 & 1.06 \\ 1.06 & 1.70 \end{bmatrix}$		$\begin{bmatrix} 1.39 & 0.74 \\ 0.74 & 1.43 \end{bmatrix}$	
	7.0	Ellipse	$\begin{bmatrix} 1.66 & 1.07 \\ 1.07 & 1.65 \end{bmatrix}$		$\begin{bmatrix} 1.37 & 0.85 \\ 0.93 & 1.33 \end{bmatrix}$	
1500	1.0	Rectangle	$\begin{bmatrix} 2.31 & 0.00 \\ 0.00 & 2.31 \end{bmatrix}$		$\begin{bmatrix} 2.47 & 0.00 \\ 0.00 & 2.48 \end{bmatrix}$	
		Ellipse	$\begin{bmatrix} 3.01 & 0.00 \\ 0.00 & 3.01 \end{bmatrix}$		$\begin{bmatrix} 2.99 & 0.00 \\ 0.00 & 2.99 \end{bmatrix}$	
	3.5	Rectangle	$\begin{bmatrix} 2.05 & 0.77 \\ 0.77 & 1.97 \end{bmatrix}$		$\begin{bmatrix} 1.93 & 0.49 \\ 0.49 & 1.87 \end{bmatrix}$	
		Ellipse	$\begin{bmatrix} 2.42 & 0.95 \\ 0.95 & 2.30 \end{bmatrix}$		$\begin{bmatrix} 2.18 & 0.73 \\ 0.73 & 2.09 \end{bmatrix}$	
	5.0	Rectangle	$\begin{bmatrix} 1.81 & 0.81 \\ 0.81 & 1.72 \end{bmatrix}$		$\begin{bmatrix} 1.68 & 0.60 \\ 0.60 & 1.61 \end{bmatrix}$	
		Ellipse	$\begin{bmatrix} 2.10 & 1.06 \\ 1.06 & 1.97 \end{bmatrix}$		$\begin{bmatrix} 1.77 & 0.81 \\ 0.82 & 1.69 \end{bmatrix}$	
	7.0	Rectangle	$\begin{bmatrix} 1.71 & 1.02 \\ 1.02 & 1.63 \end{bmatrix}$		$\begin{bmatrix} 1.42 & 0.73 \\ 0.71 & 1.38 \end{bmatrix}$	
		Ellipse	$\begin{bmatrix} 1.75 & 1.12 \\ 1.12 & 1.66 \end{bmatrix}$		$\begin{bmatrix} 1.37 & 0.89 \\ 0.87 & 1.31 \end{bmatrix}$	

1900				
1.0	Rectangle	$\begin{bmatrix} 2.29 & 0.00 \\ 0.00 & 2.29 \end{bmatrix}$	$\begin{bmatrix} 2.49 & 0.00 \\ 0.00 & 2.50 \end{bmatrix}$	
	Ellipse	$\begin{bmatrix} 3.00 & 0.00 \\ 0.00 & 3.00 \end{bmatrix}$	$\begin{bmatrix} 2.99 & 0.00 \\ 0.00 & 2.99 \end{bmatrix}$	
3.5	Rectangle	$\begin{bmatrix} 1.97 & 0.73 \\ 0.73 & 1.94 \end{bmatrix}$	$\begin{bmatrix} 1.91 & 0.48 \\ 0.48 & 1.87 \end{bmatrix}$	
	Ellipse	$\begin{bmatrix} 2.35 & 0.89 \\ 0.89 & 2.29 \end{bmatrix}$	$\begin{bmatrix} 2.15 & 0.72 \\ 0.71 & 2.10 \end{bmatrix}$	
5.0	Rectangle	$\begin{bmatrix} 1.87 & 0.93 \\ 0.93 & 1.83 \end{bmatrix}$	$\begin{bmatrix} 1.63 & 0.59 \\ 0.59 & 1.59 \end{bmatrix}$	
	Ellipse	$\begin{bmatrix} 1.99 & 0.96 \\ 0.96 & 1.93 \end{bmatrix}$	$\begin{bmatrix} 1.75 & 0.80 \\ 0.80 & 1.69 \end{bmatrix}$	
7.0	Rectangle	$\begin{bmatrix} 1.60 & 0.94 \\ 0.94 & 1.59 \end{bmatrix}$	$\begin{bmatrix} 1.41 & 0.69 \\ 0.71 & 1.37 \end{bmatrix}$	
	Ellipse	$\begin{bmatrix} 1.58 & 0.95 \\ 0.95 & 1.55 \end{bmatrix}$	$\begin{bmatrix} 1.37 & 0.88 \\ 0.87 & 1.34 \end{bmatrix}$	

Besides the AR study, the study of the change in particle shape (in Table 2.9) provides interesting insights as well. For AR equal to 1.0, the rectangle is a square and the ellipse is a circle; however, due to minor fluctuation in particle angles as described in Section 2.3.1.1, the angular position of all the squares in the unit-cell tend not to be absolutely along 45° whereas the circles remain unresponsive to this variation. This difference is confirmed by the simulation results where a distinction can be made between the rectangular- and elliptical-particle values for AR 1.0. As predicted by both the methods, the permeability components for the circles (i.e., ellipse AR 1.0) for different unit-cell sizes are strikingly close, whereas minor but noticeable difference exists in the square's (i.e., rectangle AR 1.0) case. Numerical results from both the methods show,

37

that overall, the permeability values are higher for the elliptical obstacles as compared to their rectangular counterparts. The reason behind this can be the smooth shape of the former which facilitates fluid flow around them, unlike the latter case where sharp corners are expected to inhibit smooth flow. However, as the AR increases, the permeability values along the major axes to decrease. We proffer a kinematical explanation for this change—this reduction can be correlated with the aligning of streamlines around the solid particles with the particle-orientation directions, as seen in Fig. 2.12a and Fig. 2.12b. In other words, the fluid finds it easier to flow along the particles as compared to along the major axes.

We would seek a correlation between the permeability and the surface area of the particle, which can be represented by its perimeter. In this study, the perimeter of the rectangular particles was greater than that of the elliptical ones for AR 1.0, but upon transitioning towards higher aspect ratios, we eventually reached and crossed a unique aspect-ratio value lying between AR 5.0 and 7.0, after which the ellipse's perimeter became dominant of the two. Since an increase in a particle's surface-area/perimeter leads to lengthening of flow streamlines around it, an accumulation of this effect across all the particles eventually lowers the permeability of the medium. Therefore, we expected to observe higher permeability for the elliptical models with lower aspect ratios, but we also anticipated them to show lower permeability values for higher aspect ratios (e.g., AR 7.0) when compared to their rectangular counterparts. As can be noted in Table 2.9, the simple closure-formulation method proved highly consistent in capturing this effect of change in microstructural details across all unit cells and gave accurate results. However, one out of four pairs of such unit cells with AR 7.0 (unit cells with size $1500\,\mu$m), which were solved using the Stokes-Darcy flow method, failed to show this aspect.

Before the assessment and analysis of the principal permeabilities, it is essential to verify that the assumed major flow directions (i.e., X, Y and Z axes) did not coincide with the principal directions, i.e., there was a significant offset between the principal and

38
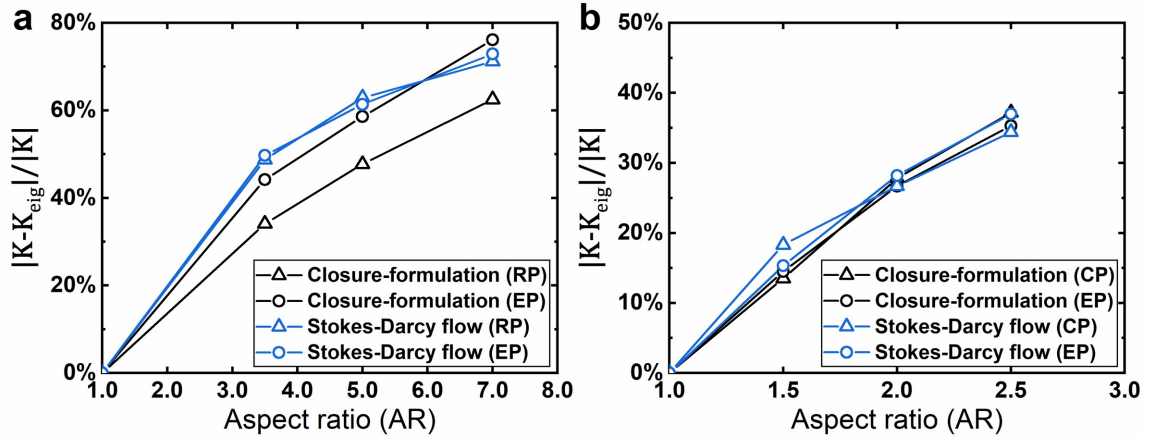
Figure 2.13: Normalized difference between the computed permeability tensor ($\mathbf{K}$) and the corresponding principal permeability tensor ($\mathbf{K}_{eig}$), obtained using the Closure-formulation and Stokes-Darcy flow methods, for (a) 2-D unit-cell (size 1900 µm) and (b) 3-D unit-cell (size 300 µm). For the 2-D unit cells in (a) RP indicates Rectangular Particles and EP indicates Elliptical Particles. For the 3-D unit cells in (b) CP represents Cylindrical Particles and EP represents Ellipsoidal Particles.

laboratory coordinate systems. This is done by demonstrating a large relative difference between the tensors $\mathbf{K}$ and $\mathbf{K}_{eig}(= \mathrm{diag}(K_1, K_2, K_3))$, obtained from both the permeability estimation methods for the largest unit-cell (size 1900 µm) across different AR for both the rectangular and elliptical particle models. Note that the standard Euclidean norm (i.e. $\sqrt{\sum_{ij} A_{ij}^2}$) of a tensor ($|A|$) is used for the scalar estimate of the difference between the two tensors. When the AR is increased from 1.0 to 7.0, Fig. 2.13a illustrates that this difference increases from 0% to 71%-63% for the 2-D rectangular-particle models and from 0% to 73%-76% for the 2-D elliptical-particle models. (Note that the former number in % corresponds to the Stokes-Darcy result while the latter to the closure-formulation one.) Of course, for AR 1.0, the system tends to be isotropic and hence $\mathbf{K} = \mathbf{K}_{eig}$ in that case. But, as the model progressively turns anisotropic, these permeability tensors become more distinct and the designed particle configuration resulted in a wide difference between the aforementioned coordinate systems.

Table 2.10 lists the principal permeability components and the anisotropy ratio for the largest unit-cell (size 1900 µm) for both the particle shapes and the solution methods. K_1 and K_2 are the maximum and minimum principal permeabilities. Similar to the

39

observations reported by Weitzenböck et al. [19], the range of measured effective permeabilities were found to be bounded by these principal permeability values. (Note that the permeability of isotropic media is independent of any special measurement direction and therefore searching for principal angles is irrelevant in such cases. It is for this reason the principal angle columns for the isotropic models have been marked as *NA* or 'Not Applicable' in Table 2.10.) Our initial assignment of the Constant angle (see Table 2.1) for producing anisotropy in the medium is reliably verified by the principal angle (θ_1) column (measured with respect to the X-axis) in Table 2.10 as the latter, despite the scatter in particle orientations, is found to be very close to the former. The second principal angle (θ_2) meant to point towards the direction of minimum permeability (K_2) is expected to be approximately at 135° with respect to the X-axis. The angle θ_2 is found using the Stokes-Darcy flow method by adding an additional angle of 90° to θ_1.

(For obtaining the principal angle results from the closure-formulation method, we used the standard procedure for finding the angle between two-vectors based on their dot-product. Here, we first find the principal components of the calculated permeability tensor using the regular eigenvector and eigenvalue operations on the matrix, and then compute the principal angles (θ_1 and θ_2) by finding the dot-product between the obtained eigenvectors of the permeability tensor and a unit-vector along the X-axis. Therefore, the dot-products obtained through this method provide the principal angles with respect to the X-axis.)

It is important to point out that the closure-formulation method successfully and quite accurately produced the expected principal angle results, θ_1 and θ_2, for all the studied aspect ratios, and that too without needing any physical-parameter inputs. Hence, this technique may prove to be valuable for researchers seeking a simple and effective way to decipher the principal directions of an anisotropic porous sample without actual experimentation. Finally, we see almost three-to-four fold increase in the Anisotropy ratio

---

[4]*NA* stands for Not Applicable.

40

Table 2.10: Principal permeability components (K_1, K_2, θ_1, and θ_2) and the Anisotropy ratio (A_k) for the 2-D unit-cell (size 1900 μm) across different aspect ratios for both the permeability estimation methods. All principal angles are measured with respect to the X-axis. (Units: Principal Permeability ($\times 10^{-10}\,\text{m}^2$) and Principal angle (°).)

Aspect ratio (AR)	Permeability method	Particle shape	Principal Permeability		Principal angles		Anisotropy ratio
			K_1	K_2	θ_1	θ_2	A_k
1.0	Stokes-Darcy flow	Rectangle	2.29	2.29	NA^4	NA^4	1.00
		Ellipse	3.00	3.00	NA^4	NA^4	1.00
	Closure-formulation	Rectangle	2.50	2.49	NA^4	NA^4	1.00
		Ellipse	2.99	2.99	NA^4	NA^4	1.00
3.5	Stokes-Darcy flow	Rectangle	2.69	1.23	44.4	134.4	2.19
		Ellipse	3.21	1.43	44.1	134.1	2.24
	Closure-formulation	Rectangle	2.38	1.41	43.8	133.9	1.69
		Ellipse	2.84	1.41	43.9	134.1	2.01
5.0	Stokes-Darcy flow	Rectangle	2.79	0.92	44.4	134.4	3.03
		Ellipse	2.92	1.00	44.1	134.1	2.92
	Closure-formulation	Rectangle	2.20	1.02	44.0	134.1	2.16
		Ellipse	2.52	0.92	44.1	133.8	2.74
7.0	Stokes-Darcy flow	Rectangle	2.53	0.66	44.8	134.8	3.83
		Ellipse	2.52	0.62	44.6	134.6	4.06
	Closure-formulation	Rectangle	2.09	0.69	44.4	133.9	3.03
		Ellipse	2.23	0.48	44.5	134.6	4.65

($A_k = \frac{K_1}{K_2}$) [53,88] on increasing AR from 1.0 to 7.0, which clearly indicates a generation of anisotropy through particle elongation in the models in contrast to their initial isotropic states.

After a thorough investigation of variation in permeability in the 2-D models, we gain more confidence in the closure-formulation method and proceed to inspect the results for 3-D models along similar lines.

2.4.3.2 3-D models

The 3-D permeability results corresponding to different parameters including the unit-cell size, aspect ratio (AR), particle shape, and the estimation methods are tabulated in Table 2.11. Similar to the 2-D case, the off-diagonal terms, which are significantly smaller

than the diagonal terms, are treated as numerical errors and equated to zero.

At this point, it is important to note that since the particles in the 3-D models are only inclined in the X-Z plane, therefore much of the permeability change across different AR values is expected to be observed in this plane's tensor component (K_{xz}), whereas trivial changes are anticipated in the remaining off-diagonal components, K_{xy} and K_{yz}.

We first investigate the variation in permeability with changes in unit-cell size. As shown in Table 2.11, when the unit-cell size is varied from $L = 200\,\mu m$ to $300\,\mu m$, the permeability tensors for the pairs of unit-cells with similar ARs were found to be reasonably close for both the methods. For example, if we examine the 3-D cylinder unit cells of sizes $200\,\mu m$ and $300\,\mu m$ with AR 1.0 in Table 2.11, then the permeability tensors predicted by both the methods are fairly close. However, the minor differences between such 3-D tensors can be ascribed to the variance in the particle angles associated with different unit cells and the presence of a third dimension which offers the fluid more space to flow around the obstacles (unlike the 2-D models where the fluid flow is restricted to two dimensions).

Next, we inspect the evolution in permeability with variation in aspect ratio of the particles. As the AR increases, the particles become stretched along 45° direction from the X-axis in the X-Z plane. Consequently, this leads to alignment and lengthening of streamlines around the particles along this direction which results in an increased permeability component, K_{xz}, similar to the K_{xy} component in the 2-D case (see parts (c) and (d) of Fig. 2.12). Hence, due to increased fluid flow in this direction, this angle is understood to point towards the direction of maximum permeability in the model. Employing the principle of orthogonality of the principal directions of the permeability tensor, the other principal directions can also be guessed: one, perpendicular to this direction in the same plane, i.e. roughly at 135° from the X-axis in the X-Z plane; and the other, orthogonal to this plane (i.e., along the Y-axis). Later, we shall see that the former indicates lower of the two principal permeabilities lying in the X-Z plane, whereas

Table 2.11: The permeability tensors computed for 3-D models corresponding to different: 1) unit-cell sizes, 2) aspect ratio (AR), 3) particle shape, and 4) permeability estimation methods. The porosity across the unit cells is 0.90 and the radius of an ellipsoid particle for the AR 1.0 case is 28.79 μm.

Unit-cell size (μm)	Aspect ratio (AR)	Particle shape	Permeability tensor ($\times 10^{-10}\,\mathrm{m}^2$)	
			Stokes-Darcy flow	Closure-formulation
	1.0	Cylinder	$\begin{bmatrix} 4.33 & 0.00 & 0.00 \\ 0.00 & 4.50 & 0.00 \\ 0.00 & 0.00 & 4.33 \end{bmatrix}$	$\begin{bmatrix} 4.24 & 0.00 & 0.00 \\ 0.00 & 4.38 & 0.00 \\ 0.00 & 0.00 & 4.25 \end{bmatrix}$
		Ellipsoid	$\begin{bmatrix} 5.24 & 0.00 & 0.00 \\ 0.00 & 5.24 & 0.00 \\ 0.00 & 0.00 & 5.24 \end{bmatrix}$	$\begin{bmatrix} 5.10 & 0.00 & 0.00 \\ 0.00 & 5.11 & 0.00 \\ 0.00 & 0.00 & 5.10 \end{bmatrix}$
	1.5	Cylinder	$\begin{bmatrix} 4.47 & 0.02 & 0.52 \\ 0.02 & 3.82 & 0.00 \\ 0.52 & 0.00 & 4.50 \end{bmatrix}$	$\begin{bmatrix} 4.43 & 0.00 & 0.12 \\ 0.00 & 3.70 & 0.00 \\ 0.11 & 0.00 & 4.45 \end{bmatrix}$
		Ellipsoid	$\begin{bmatrix} 5.43 & 0.00 & 0.51 \\ 0.00 & 4.47 & 0.00 \\ 0.51 & 0.00 & 5.46 \end{bmatrix}$	$\begin{bmatrix} 5.26 & 0.00 & 0.30 \\ 0.00 & 4.30 & 0.00 \\ 0.30 & 0.00 & 5.28 \end{bmatrix}$
	2.0	Cylinder	$\begin{bmatrix} 4.53 & 0.02 & 0.61 \\ 0.02 & 3.36 & 0.00 \\ 0.61 & 0.00 & 4.57 \end{bmatrix}$	$\begin{bmatrix} 4.53 & 0.00 & 0.22 \\ 0.00 & 3.09 & 0.00 \\ 0.23 & 0.00 & 4.57 \end{bmatrix}$
		Ellipsoid	$\begin{bmatrix} 5.35 & 0.00 & 0.76 \\ 0.00 & 3.77 & 0.02 \\ 0.76 & 0.02 & 5.39 \end{bmatrix}$	$\begin{bmatrix} 5.20 & 0.00 & 0.47 \\ 0.00 & 3.58 & 0.00 \\ 0.46 & 0.00 & 5.23 \end{bmatrix}$
		Cylinder	$\begin{bmatrix} 4.61 & 0.00 & 0.78 \\ 0.00 & 3.04 & 0.00 \\ 0.78 & 0.00 & 4.65 \end{bmatrix}$	$\begin{bmatrix} 4.73 & 0.02 & 0.37 \\ 0.02 & 2.56 & 0.01 \\ 0.37 & 0.14 & 4.67 \end{bmatrix}$

43

	2.5	Ellipsoid	$\begin{bmatrix} 5.27 & 0.04 & 0.97 \\ 0.04 & 3.28 & 0.00 \\ 0.97 & 0.00 & 5.32 \end{bmatrix}$	$\begin{bmatrix} 5.12 & 0.02 & 0.57 \\ 0.00 & 2.98 & 0.00 \\ 0.59 & 0.00 & 5.18 \end{bmatrix}$
300	1.0	Cylinder	$\begin{bmatrix} 4.31 & 0.00 & 0.00 \\ 0.00 & 4.46 & 0.00 \\ 0.00 & 0.00 & 4.31 \end{bmatrix}$	$\begin{bmatrix} 4.23 & 0.00 & 0.00 \\ 0.00 & 4.38 & 0.00 \\ 0.01 & 0.00 & 4.23 \end{bmatrix}$
		Ellipsoid	$\begin{bmatrix} 5.38 & 0.00 & 0.00 \\ 0.00 & 5.38 & 0.00 \\ 0.00 & 0.00 & 5.38 \end{bmatrix}$	$\begin{bmatrix} 5.14 & 0.00 & 0.00 \\ 0.00 & 5.14 & 0.00 \\ 0.00 & 0.00 & 5.14 \end{bmatrix}$
	1.5	Cylinder	$\begin{bmatrix} 4.54 & 0.02 & 0.65 \\ 0.02 & 3.79 & 0.01 \\ 0.65 & 0.01 & 4.57 \end{bmatrix}$	$\begin{bmatrix} 4.43 & 0.00 & 0.12 \\ 0.00 & 3.70 & 0.00 \\ 0.11 & 0.00 & 4.44 \end{bmatrix}$
		Ellipsoid	$\begin{bmatrix} 5.43 & 0.00 & 0.41 \\ 0.00 & 4.45 & 0.00 \\ 0.41 & 0.00 & 5.46 \end{bmatrix}$	$\begin{bmatrix} 5.25 & 0.00 & 0.29 \\ 0.00 & 4.33 & 0.00 \\ 0.29 & 0.00 & 5.27 \end{bmatrix}$
	2.0	Cylinder	$\begin{bmatrix} 4.63 & 0.05 & 0.70 \\ 0.05 & 3.27 & 0.04 \\ 0.70 & 0.04 & 4.66 \end{bmatrix}$	$\begin{bmatrix} 4.51 & 0.01 & 0.17 \\ 0.00 & 3.09 & 0.00 \\ 0.21 & 0.02 & 4.58 \end{bmatrix}$
		Ellipsoid	$\begin{bmatrix} 5.40 & 0.00 & 0.86 \\ 0.00 & 3.72 & 0.00 \\ 0.86 & 0.00 & 5.43 \end{bmatrix}$	$\begin{bmatrix} 5.23 & 0.00 & 0.47 \\ 0.00 & 3.58 & 0.00 \\ 0.45 & 0.33 & 5.25 \end{bmatrix}$
	2.5	Cylinder	$\begin{bmatrix} 4.70 & 0.02 & 0.78 \\ 0.02 & 2.88 & 0.00 \\ 0.78 & 0.00 & 4.74 \end{bmatrix}$	$\begin{bmatrix} 4.59 & 0.06 & 0.34 \\ 0.00 & 2.63 & 0.01 \\ 0.35 & 0.12 & 4.59 \end{bmatrix}$
		Ellipsoid	$\begin{bmatrix} 5.33 & 0.00 & 1.07 \\ 0.00 & 3.17 & 0.00 \\ 1.07 & 0.00 & 5.37 \end{bmatrix}$	$\begin{bmatrix} 4.99 & 0.06 & 0.64 \\ 0.00 & 3.02 & 0.02 \\ 0.57 & 0.03 & 5.11 \end{bmatrix}$

the latter works out to be the lowest of all the principal permeabilities. Also, with the increase in AR, the particle surface-area also increases (especially the particle area projected onto the X-Z plane), which results in greater obstruction to fluid flow along the Y-axis direction, and therefore a declining trend in the permeability component K_{yy} is rightly witnessed. Note that both the permeability estimation methods display this anticipated trend unambiguously. In the present study, permeability is expected to increase more along 45° from the X-axis in the X-Z plane, i.e., the K_{xz} and K_{zx} components of the tensor, when compared to the other off-diagonal terms, are expected to be higher. This can be inferred from the flow directions shown in Fig. 2.14, where during the measurement of effective permeabilities K_{II} and K_{IV}, the fluid flow path is observed to be heavily impeded by the obstacles which results in lower permeability values for these directions. However, in the case of K_{VI}, the fluid flows along the direction of the elongated obstacles (i.e., Constant angle 'α') which is the path of least resistance for the fluid and thus it leads to an increased permeability value for K_{xz} relative to the other off-diagonal components. Both the permeability estimation methods produce results that agree with this observation. It should also be noted that the closure-formulation method successfully reflected the trends (in the permeability tensor values for components K_{xx} and K_{zz}) as produced by the Stokes-Darcy flow method across different AR for both particle shapes. For example, an increasing trend is noted in the K_{xx} component value for the cylindrical particle model across AR 1.0 to 2.5 for the 3-D unit cells of size 300 µm based on the Stokes-Darcy method. The closure-formulation method successfully displayed a similar trend in its permeability tensor values for the component K_{11}. This is an important outcome which improves one's confidence in the ability of this latter volume-averaging-method based technique for permeability estimation of anisotropic porous samples based only on microstructural information.

When the AR is changed from 1.0 to 2.5, the average permeability along the Y-axis direction, i.e. the K_{yy} component, is noted to decrease by 34%-41% for the cylindrical-
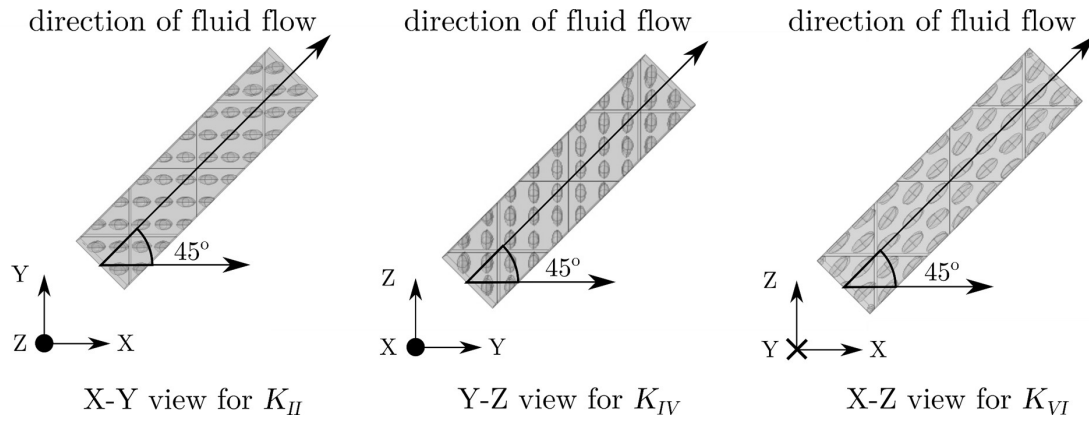
Figure 2.14: Fluid flow directions for measurement of effective permeabilities K_{II}, K_{IV} and K_{VI}. Note that the flow paths are severely impeded by the presence of obstacles in the first two cases, thereby leading to reduced effective permeability values in these two directions, whereas the path of least resistance for fluid flow is offered in the case of K_{VI} which eventually leads to a relatively higher permeability value for the tensor component K_{xz}. (The $\bullet$ in the coordinate system icon represents the z/x-axis pointing out-of-plane whereas $\times$ indicates the y-axis pointing into-the-plane.)

and by 39%-41% for the ellipsoidal-particle models. Also, for AR 2.5, the average value of the off-diagonal component K_{xz} is found to increase to 19%-9% and 22%-14% of the main diagonal terms for cylindrical and ellipsoidal particle models, respectively. (Note that the first % value correspond to the Stokes-Darcy result, while the second one to the closure-formulation one.)

We now explore the numerical results corresponding to the two particle shapes used in this study. From Table 2.11, it is clear that both the methods predict higher permeability values for the ellipsoidal obstacles as compared to their cylindrical counterparts. Based on the geometrical characteristics, the smooth shape of an ellipsoid facilitates fluid flow, whereas the sharp edges of a cylindrical particle hinder streamlined flow. This can be the reason behind the permeability difference observed between these two differently shaped particle models. Also, the permeability values for the ellipsoidal particle models remained higher than the cylindrical ones across the entire aspect ratio range under study. This can be explained based on similar reasoning provided for the pattern of permeability differences observed between the 2-D ellipse and rectangle particle models. The surface areas for both the cylindrical and ellipsoidal particles continues to grow with increasing

46

Table 2.12: Principal permeability components (K_1, K_2, K_3, θ_1, θ_2 and θ_3) and the Anisotropy ratio (A_k) for the 3-D unit-cell (size 300 μm) across different aspect ratios for both the permeability estimation methods. All principal angles are measured with respect to the X-axis. (Units: Principal Permeability ($\times 10^{-10}\,\mathrm{m}^2$) and Principal angle (°).)

Aspect ratio (AR)	Permeability method	Particle shape	Principal Permeability			Principal angles			Anisotropy ratio
			K_1	K_2	K_3	θ_1	θ_2	θ_3	A_k
1.0	Stokes-Darcy flow	Cylinder	4.46	4.31	4.31	NA^5	NA^5	NA^5	0.99
		Ellipsoid	5.38	5.38	5.38	NA^5	NA^5	NA^5	1.00
	Closure-formulation	Cylinder	4.38	4.23	4.23	NA^5	NA^5	NA^5	0.98
		Ellipsoid	5.14	5.14	5.14	NA^5	NA^5	NA^5	1.00
1.5	Stokes-Darcy flow	Cylinder	5.20	3.91	3.79	45.7	135.5	92.8	0.84
		Ellipsoid	5.86	5.03	4.45	46.0	136.0	90.0	0.82
	Closure-formulation	Cylinder	4.55	4.32	3.70	45.0	137.5	90.0	0.83
		Ellipsoid	5.55	4.97	4.33	46.0	136.0	90.0	0.82
2.0	Stokes-Darcy flow	Cylinder	5.34	3.95	3.27	45.6	135.6	88.7	0.71
		Ellipsoid	6.28	4.55	3.72	45.5	135.5	90.0	0.70
	Closure-formulation	Cylinder	4.74	4.35	3.09	53.0	137.2	90.5	0.68
		Ellipsoid	5.70	4.78	3.58	45.2	136.1	90.0	0.69
2.5	Stokes-Darcy flow	Cylinder	5.50	3.94	2.88	45.6	135.7	90.7	0.62
		Ellipsoid	6.42	4.28	3.17	45.6	135.5	90.0	0.60
	Closure-formulation	Cylinder	4.93	4.25	2.63	45.6	134.4	88.8	0.57
		Ellipsoid	5.66	4.44	3.02	46.4	139.3	88.4	0.60

AR; however, the contact area of the cylinders continually remains greater than that of the ellipsoids for all the aspect ratios in this study. Therefore, for a pre-set porosity, the permeability of the cylindrical obstacle models continues to remain smaller than their ellipsoidal counterparts.

As illustrated in Fig. 2.13b, a significant relative difference between $\mathbf{K}$ and $\mathbf{K}_{\text{eig}}$ for the larger unit cell (size 300 μm) for both the particle shapes and permeability estimation methods suggests that the principal and laboratory coordinate systems did not overlap. When the AR is increased from 1.0 to 2.5, Fig. 2.13b shows the difference to increase from 0% to 34%-37% for 3-D cylinder particle models and from 0% to 37%-35% for 3-D ellipsoid particle models. (Note that the former number in % corresponds to the

---

[5] NA stands for Not Applicable.

Stokes–Darcy result while the latter to the closure-formulation one.)

The principal permeability components and anisotropy ratios for the larger unit cell (size 300 µm) are tabulated in Table 2.12. Out of the three principal permeabilities: K_1 represents the maximum, K_2 the intermediate and K_3 indicates the minimum permeability. Further, the corresponding principal directions are given by θ_1, θ_2 and θ_3, respectively. The principal angles in the 3-D case were obtained through the standard eigenvector operation on permeability matrices, similar to the one discussed in Section 2.4.3.1 for the 2-D models. Again, the principal angles for isotropic models have been marked as *NA* or 'Not Applicable' in Table 2.12. As pointed out beforehand, the results confirmed that the largest principal-permeability lay close to 45° to the X-axis in the X-Z plane (equal to the pre-set Constant angle 'α'), the intermediate principal-permeability value was approximately at 135° from the X-axis in the same plane, and the smallest principal-permeability value was noted to be along the Y-axis (90° to the X-axis). Overall, the principal angles obtained from the closure-formulation method were found to be quite accurate when compared to the anticipated values and to those predicted by the Stokes-Darcy flow method. Again, this suggests that this volume-averaging-method based technique can prove to be a reliable tool for not only estimating the accurate permeability tensor, but also for predicting the principal directions of anisotropic porous samples without any actual experimentation. Clavaud et al. [89] have defined the Anisotropy ratio (A_k) for a 3-D permeability tensor as

$$A_k = \frac{K_{min}}{\sqrt{K_{int} \cdot K_{max}}} \tag{2.15}$$

where K_{min}, K_{int} and K_{max} are the minimum, intermediate and maximum values of the principal-permeability components, respectively. A higher A_k value suggests the porous medium to be closer to being isotropic, whereas lower values indicate highly anisotropic media. A study of Table 2.12, where the principal permeability values from both the methods are presented, suggests that with an increase in AR, the A_k values markedly

48

decrease for the 3-D models, thereby confirming the presence of higher anisotropy in configurations with elongated particles.

2.4.3.3 Comparison of CPU times for the Closure-formulation and Stokes-Darcy flow methods

This numerical study was performed using the commercial FEM software, COMSOL Multiphysics on a single Intel® Core i9-9820X powered CPU with 128 GB of physical memory. The machine allows parallel processing on its 10 cores and 20 logical processors (total threads) at 3.30 GHz microprocessor frequency with 16.5 MB shared cache per processor. COMSOL's default Windows platform setting permits the job to run on all available physical cores of the system, thus allowing shared-memory processing and promoting maximum utilization of the available resources. Next, COMSOL automatically optimizes its solver settings to robustly solve the multiphysics problems, which leads to faster convergence rates and eventual minimization of the computational times. To briefly mention, the Direct solver using the Fully Coupled algorithm was found suitable for the closure-formulation method, whereas the Algebraic Multigrid (AMG) solver executing the same algorithm was set for the Stokes-Darcy flow physics. For confirmation, the solver settings were manually permuted and compared, but the fastest solution times for the methods were obtained for COMSOL's recommended settings. Apart from the solver settings, the CPU time is strongly dependent on other parameters such as the relative tolerance, which was tightly set to 10^{-3} for obtaining accurately converged results, the mesh type, and the mesh size (discussed in Section 2.4.2).

To compare the CPU times for both the methods, it is useful to define a comparative variable, τ, as follows

$$\tau = \frac{\text{Total CPU time for the Stokes-Darcy flow method}}{\text{CPU time for the Closure-formulation method}} \qquad (2.16)$$

where the total CPU time for the Stokes-Darcy flow method is the sum of solution times

49
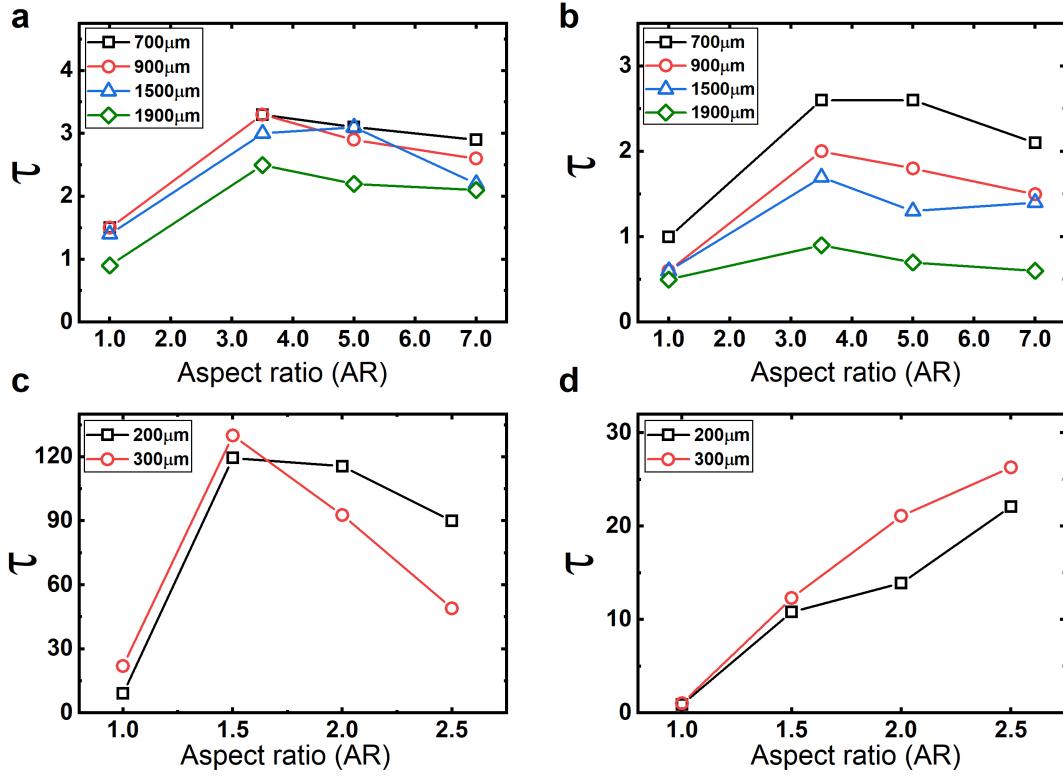
Figure 2.15: A comparison of relative CPU times using the artificial variable τ corresponding to different unit-cell sizes and aspect ratios (AR) for (a) rectangular particles, and (b) elliptical particles, in the 2-D domain; (c) cylindrical particles, and (d) ellipsoidal particles, in the 3-D domain.

for simulations in different orientations as described in Section 2.3.2. On the other hand, for the closure-formulation method, it is equal to the solution time of a single simulation for both 2-D and 3-D models.

Based on the absolute computational time data collected for the Stokes-Darcy flow method, the simulation periods corresponding to the 3-D specimens were found to be 1-2 orders-of-magnitude higher than that of the 2-D models. This is true to the expectation based on the increased mesh elements and hence higher degrees-of-freedoms ($\sim N^3$ in 3-D compared to $\sim N^2$ in 2-D) to be solved in the 3-D case. To provide an overview of the collected CPU time data and allow easy comparison, the ratio of computational times corresponding to both the methods in terms of the defined variable, τ, is plotted in Fig. 2.15.

Let us first analyze the τ for the 2-D models. As can be observed in Fig. 2.15a and Fig. 2.15b, τ is close to 1 for the majority of the 2-D isotropic unit cells studied (i.e., unit cells with AR 1.0). This value was found to be greater than 1 for most of the 2-D 'rectangle' unit-cells, whereas the results were mixed for the 2-D 'ellipse' unit-cells. Since the permeability for isotropic models was calculated using only a single Stokes-Darcy flow simulation, the τ value indicated that the closure-formulation method could produce the permeability results for such models with CPU time comparable to the Stokes-Darcy flow method. However, as the models increasingly turned anisotropic, the most important information inferred from these figures is that τ was greater than 1 for all but a few of the numerical simulations. This clearly highlights the closure-formulation's ability to provide faster permeability results for the anisotropic models. This can be explained based on the number of simulations required to solve the permeability tensor using the Stokes-Darcy flow method, which is 3 for the 2-D case, as compared to a single simulation required in the closure-formulation approach. In general, τ was found to decrease with an increase in unit-cell size and aspect ratio (AR). This can be attributed to the increase in number of elements required to mesh a larger or more asymmetric model which translates to considerably higher degrees-of-freedom to be solved in such cases. Consequently, the overall computational time increased for both the Stokes-Darcy flow and closure-formulation methods. However, τ was observed to be more sensitive to the increase in latter's CPU time as compared to the relatively smaller time-increments occurring in the numerator of Eq. (2.16). This probably led to an overall decline in the τ value with the increase in unit cell size or AR or a combination of both.

The importance of computational-time savings became clearly evident when investigating the 3-D models where greater number of simulations were required to evaluate the permeability tensor using the Stokes-Darcy flow method. The CPU-time comparison data for the 3-D models comprised of cylindrical and ellipsoidal-shaped particles is presented in Fig. 2.15c and Fig. 2.15d, respectively. It can be seen that τ shows a higher and increased

range between 1 to 130 for the considered particle shapes and unit-cell sizes, suggesting drastically lesser CPU time associated with the usage of the closure-formulation method.

As previously pointed out for the 2-D models as well, the lowest τ values were observed for the isotropic unit cells where a smaller number of simulations were involved to find the permeability tensor. Next, with the increase in unit-cell size and aspect ratio (AR), the number of mesh elements required to discretize the 3-D unit cells also increased, thus leading to inflated CPU times for both the permeability estimation methods. However, in the 3-D case, the computational time involved in the Stokes-Darcy flow simulations was noted to be significantly higher. This was caused by (a) increased CPU time for each pressure-gradient orientation, and (b) accounting for 6 different simulation runs, in contrast to the relatively smaller time-increment involved in a single run of the closure-formulation method. These factors evidently led to an increase in the τ value. Also, the cylindrical-particle models showed higher τ values when compared to their ellipsoidal counterparts. This is because the sharp edges of cylinder particles require more mesh elements to discretize and resolve the velocity gradients near the cylinder boundaries, which perhaps led to increased solution times when compared to the ellipsoidal particle models.

Overall, no proper trend could be inferred for τ in the 3-D case except for the fact that the closure-formulation method undoubtedly provided significantly faster computational results as compared to the widely used saturated linear flow permeability estimation technique [11, 18, 19, 53, 88, 90]. In addition, the closure-formulation method *repeatedly saved significant additional time* involved in changing the solver's boundary-condition settings for multiple orientations involved in the Stokes-Darcy flow method. As real-world objects are mostly anisotropic, this study puts forward a strong case for Whitaker's closure-formulation [81, 82] by showcasing its clear advantages in terms of saving the computational and setting-up times, and resource savings.

52

2.5   Summary and Conclusions

Permeability estimation in porous media is a vital area of study and a subject of intensive research in composites manufacturing and numerous other applications. The rise in computational power and scanning technology has enabled the researchers to estimate the permeability directly from 2-D and 3-D micrographs. In this chapter, two different computation-based, permeability-estimation methods were tested using artificially-prepared porous-media models. First of these methods included the Stokes-Darcy flow method that uses the Darcy's law to extract the permeability tensor from the 1-D Stokes flow simulations along the prepared unit cells in different directions. The second method is the closure formulation method that is extracted from the volume averaging method used by Whitaker [82] to upscale the Stokes equation at the micro (pore) scale to the Darcy's law at macro (lab) scale.

The closure-formulation method was validated by comparing the simulation results with Lasseux et al.'s implementation ([87]) and a good agreement was achieved, thereby establishing the accuracy of our numerical solution. Also, the results obtained from the closure-formulation and Stokes-Darcy flow methods were found to compare well with the predictions from a few established theoretical permeability models (the Gebart model, the Bruschke & Advani model, and the Kozeny-Carman model), thereby further corroborating the accuracy of the two methods.

The models for artificial porous media were synthesized from unit cells populated with rectangle-like and ellipse-like solid particles. The models were based on three different parameters: unit-cell size, particle shape, and aspect ratio of the particles. In the 2-D case, four unit-cell sizes, four aspect ratios and two particle shapes were used in the study. The Stokes-Darcy flow method used fluid properties (viscosity and density) for permeability estimation, whereas the closure-formulation method, not needing such inputs, provided highly accurate permeability results solely based on the microstructural information

available at the pore scale level. In the 3-D part of the study, two unit-cell sizes, four aspect ratios and two particle shapes were employed. Based on the permeability tensors obtained from both the methods, the closure-formulation technique produced results which were consistent with the anticipated outcomes and quite close to those predicted by the Stokes-Darcy flow method. Here, it is important to recall that achieving permeability value within the same order of magnitude is often considered creditable in any permeability-prediction study [90]. In the present work, the closure-formulation method betters this expectation by achieving much higher match with the Stokes-Darcy flow method for all but a few cases. Hence, this study offers a substantial leap over the research done with this technique till date involving relatively simple isotropic models [52, 65, 80].

Another important aspect of this study was to test if the closure-formulation method could effectively predict the principal directions of an anisotropic porous media. In both the 2-D and 3-D cases, this technique quite accurately determined the principal angles which closely matched those obtained from the Stokes-Darcy flow method. Hence, this method can prove to be an important addition to the arsenal of tools meant for estimating the principal directions of an unknown anisotropic porous sample without any experimentation.

A unique CPU-time-comparison study was performed for comparing the two methods by defining a variable, τ, as the ratio of the computational time used by the Stokes-Darcy flow method to that by the closure-formulation method. Primarily due to the fact that only a single simulation involved in the closure-formulation process, the closure-formulation technique was substantially faster for a majority of the 2-D, and all of the 3-D anisotropic models. This advantage was spectacularly displayed in the 3-D case where *the permeability obtained using the closure-formulation simulations were up to 130 times faster than the one obtained using the conventional Stokes-Darcy flow method!* Overall, no definite trend for τ could be identified, which is plausible, since it is expected to heavily depend on the microstructural details of the porous models; however, the closure-

54

formulation method clearly led to large computational time savings in contrast to the widely adopted Stokes-Darcy flow method.

CHAPTER 3

Modeling Transport and Adsorption of Tracer Species. Part I: Theoretical Developments

3.1 Literature Review

[1]The presence of arsenic in water is gravely injurious to human health. Exposure to this element leads to many skin-related, gastro-intestinal, neurological, and cardiovascular problems. Upon its consumption, the carcinogenic nature of arsenic gives rise to several types of cancers, including skin, lung and bladder cancers [91]. Contamination of water by arsenic is a problem that afflicts several parts of the world. Countries in the west, including Argentina, USA and Canada, to countries in the east, including Bangladesh, India and China, are affected by the presence of arsenic [92].

The bodies of water most affected by the problem of arsenic pollution are aquifers, which are groundwater sources. The arsenic primarily present in such sources are oxy anions with primarily two different oxidation states: arsenite (As(III)) and arsenate (As(V)) [92]. Although the arsenic can naturally dissolve into these sources of water due to its presence in the surrounding bedrock, this arsenic contamination can be exacerbated, especially in areas of Asia, through numerous human activities such as mining, smelting, using coal for power generation, and using agricultural pesticides [93].

Several water filters based on a host of separate technologies are available in the market place. These include reverse osmosis (RO), activated carbon, activated alumina, anion

---

[1]The chapter has been published in the form an invited paper as following:
a) Pillai, K. M. and Raizada, A. Modeling Transport and Adsorption of Arsenic Ions in Iron-Oxide Laden Porous Media. Part I: Theoretical Developments. *Water* **2021**, *13*, 779.
The contributions of Aman Raizada include original draft preparation, review and editing of the manuscript.

exchange, and distillation. Except for RO and distillation, all other methods involve forcing contaminated water to flow through a porous medium made from particles or beads. As the water comes in contact with the walls of porous media, the dissolved arsenic ions are captured by the walls through mechanisms such as anion exchange or sorption. The high surface area of porous media comes in handy for this 'capture'. This process can be modeled with the help of a convection-diffusion equation since the extremely low concentration of arsenic in water (typically in ppb or parts-per-billion[2]) allows the tracer-type species transport equations to handle the migration and absorption of this element. As a result, the modeling of arsenic transport and capture in any off-the-shelf water filter for arsenic is quite similar to the modeling of arsenic transport and capture in groundwater. We will be taking our inspiration and methodology for solving this problem in filters from the rather well-studied problem of contamination of groundwater by arsenic (or by any other toxic heavy metal such as lead).

In the fields of environmental engineering, soil sciences, geosciences and underground hydrology, contamination of groundwater flow is a well-researched problem. The large porous bodies, made of sand or similar particulate matter lodged between layers of rocks, hold a tremendous amount of groundwater and are called aquifers. The wells are drilled into these aquifers to extract water for human consumption. These aquifers exchange water with streams, rivers and ponds and hence the contamination in these water bodies is often passed on to the aquifers. The aquifers can also be contaminated by the nuclear, chemical and other type of wastes buried underground. The contaminated water traveling through the porous aquifer can get filtered due to the ion absorption process by solid particles as well as the action of bacteria. Hence, the concentration of contaminants may change with space and time during groundwater flow. Prediction of the contamination of aquifers is a big challenge that is being addressed by scientists in several countries.

The flow of water inside aquifers is modeled using the Darcy's law, and the transport

---

[2]According to the WHO guidelines, the acceptable concentration of arsenic in safe drinking water is less than 10 ppb.

of contaminants is modeled using the convection-dispersion equation for predicting the transport and attenuation of dissolved species due to adsorption and biological activity [94]. As mentioned earlier, the physics for modeling the transport and adsorption of contaminants is exactly identical to the transport and adsorption of arsenic in a water filter. Here we will describe the work that has already been done in this area as well as the limitation of that work.

Numerous analytical solutions have been developed for modeling solute transport through fully-saturated aquifers [95–107]. However, there are some shortcomings associated with them. For example, the dispersion tensor is simplified without any justification—it is merely presented as a constitutive relation without any correlation with the pore-scale microstructure and the phenomena occurring therein [94]. Several times, the dispersion tensor is overly simplified after dropping the molecular diffusivity contribution [95, 97, 100] or simply treated as a constant [98, 102, 104].

On the other hand, several stochastic groundwater modeling techniques have been proposed to study the transport of solute in natural porous formations like aquifers with variable permeability [108–110]. Dagan [109] explained that the spatial distribution of solute in such porous structures is mostly governed by convection and the heterogeneity of permeability on a large scale. In these cases, the marginal effect of pore-scale dispersion is generally neglected owing to the smallness of the transverse dispersivity with respect to the heterogeneity scale. Aldo [110] furthered this study [109] and investigated the influence of the pore-scale dispersion mechanism in an heterogeneous aquifer under both the ergodic and nonergodic transport conditions. In the same vein, Rubin [111] presented the stochastic formulations of the advection-dispersion equation to model the transport of tracer species in heterogeneous porous media. Such mathematical models are often based on the assumptions of stationarity, ergodicity, and gaussian distribution, and seek geostatistical parameters for stochastic modeling. These approaches have earned some success in correlating different length-scales and are able to predict the results of large-

scale controlled field experiments [112,113]. However, they lack the ability to account for the influence of pore-level microstructural details in the formulation of the total dispersion tensor, which needs further development. In the proposed research described below, we will develop a more comprehensive analysis for species transport using a micro-macro coupling that can remove the above-mentioned shortcomings and lead to an important advance in this area.

The method of volume averaging is a rigorous method to upscale from the pore scale to the macroscopic lab or field scale [82, 114, 115]. The use of this method in understanding and predicting mass transport in porous media has had a long history, and a brief synopsis is presented here. One of the first attempts to understand and model diffusion and hydrodynamic dispersion in porous media can be attributed to Whitaker [77]. Gray later [116] suggested an improvement in Whitaker's formulation by suggesting the estimation of the deviations from the intrinsic phase-average (instead of the phase-average) for the concentration of the solute. Attempts were made to understand hydrodynamic dispersion in capillary tubes representing porous media, which led to the confirmation of the Taylor-Aries model [117]. Later the same ideas were applied to develop a one-equation [118] and a two-equation [119] model for solute transport accompanied with adsorption in dual length-scale heterogeneous porous media. The volume averaging method was then adapted to find the effective dispersion tensor in a heterogeneous medium, the findings of which were tested using the ensemble averaging process [120]. The two-equation model was later employed to estimate the macroscopic properties of an ideal heterogeneous porous medium and a parametric study was conducted to study the effect of the Péclet number, permeability ratio and local-scale dispersitivity on the dispersion coefficient [121].

In this chapter, we will employ the volume averaging method to upscale the phenomenon of solute transport (which include both diffusion and advection) accompanied with adsorption in *homogeneous* porous media. Such media are found in commercial water

filters where the cartridges created by packing particles or beads that can be assumed to be of mono-modal size distribution and thus create *single-scale* porous media. It may seem that the solution to this relatively simple problem should exist somewhere in the volume-averaging literature. However, our investigation revealed that bits and pieces of this problem exist piecemeal at different locations. For example, similar problems on diffusion *without* advection, and accompanied with adsorption, have been formulated as practice problems by Whitaker in his monograph (Problems 4 and 25 in Chapter 1 of [82]). Later, solving the same problem after including the advection has been presented in Problem 13 of Chapter 3 on dispersion; however, it is presented without any solution. Similarly, Plumb and Whitaker [122] presented the upscaling theory corresponding to diffusion, adsorption and advection in porous media composed of *porous* particles in Section 5 of [122]. This one-equation model approach was a multi-scale treatment that involved lower-scale averaging inside what will be our solid phase here.

One can cite some more of the similar developments in the volume averaging method that are related to the proposed formulation. Whitaker in Chapter 1 of [123] illustrated the use of the volume averaging procedure and the boundary conditions required to derive the upscaled convective-dispersion equation with nonlinear adsorption for species transport. Wood et al. [124] developed a volume-averaged macroscale transport equation for a reactive chemical species and compared the effective reaction rate obtained from the closure formulation to that from the direct numerical simulation at the microscale. Similarly, Valdès-Parada et al. [125] carried out upscaling of mass transport equations along with diffusion and convection based reaction processes in porous media. In the same vein, the work by Quintard et al. [126, 127] had some useful developments for the interfacial boundary condition for the moving-phase velocity.

Hence, we had to gather and develop all the relevant aspects of the upscaling physics for the considered practical problem of developing for arsenic water filters the upscaled governing equation and the associated closure problem. A researcher experienced in the

volume average method may find several portions of the chapter repetitions of what is available in the literature; however, we feel that all the main derivations should be presented in the chapter here in order to improve its readability and bring diverse aspects into a single presentation.

3.2 Model for solute transport

3.2.1 Mathematical Preliminaries and Definitions

The volume averaging method will be used to upscale from the microscopic space to the macroscopic one. This means that the governing equations and boundary conditions for the large-scale space will be derived from the governing equations plus boundary conditions for the small-scale space. We will start with some basic definitions.

3.2.1.1 Representative Averaging Volume

The representative elementary volume (REV) plays an important conceptual role in upscaling of porous media processes. As shown in Figure 3.1, it is often taken to be of a spherical form. Our problem is classified as the *single-phase* flow through porous media. Hence, there is a phase called β phase that flows between the stationary, non-deforming solid particles made from the σ phase and completely fills the pores. During this flow, the ions being carried by the flowing β phase (water) are also moving towards the σ phase particles and are getting adsorbed by them.

For effective volume averaging, the following constraint is required [82]:

$$\text{Average Particle Size} \quad << \quad r_o \quad << \quad \text{Size of the upscaled domain} \tag{3.1}$$

where r_o is the size of the REV.
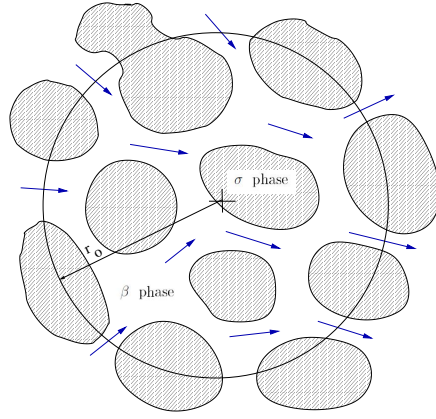
Figure 3.1: A Schematic of the Representative Elementary Volume (REV) with r_o being the radius of the sphere-shaped volume.

3.2.1.2 Phase and Intrinsic Phase Averages

The phase average $\langle \phi_\beta \rangle$ for any variable ϕ_β associated with the β phase flowing through the porous medium is defined as

$$\langle \phi_\beta \rangle = \frac{1}{V} \int_{V_\beta} \phi_\beta \, dV \tag{3.2}$$

where V is the volume of the REV. $\langle \phi_\beta \rangle$ represents the average value of any quantity within *the whole* of the REV.

On the other hand, there is an average called the intrinsic phase average, $\langle \phi_\beta \rangle^\beta$, which is the average value of any quantity *only within the β phase* of the REV. Such an average is defined as

$$\langle \phi_\beta \rangle^\beta = \frac{1}{V_\beta} \int_{V_\beta} \phi_\beta \, dV \tag{3.3}$$

where V_β represents the volume of the β phase within the REV.

As one can easily see, the relation between the two averages is

$$\langle \phi_\beta \rangle = \epsilon_\beta \langle \phi_\beta \rangle^\beta \tag{3.4}$$

62

such that ϵ_β is the volume fraction of the β phase given by the relation

$$\epsilon_\beta = \frac{V_\beta}{V}.$$ (3.5)

Note that for *single-phase flow* of the β phase through our porous medium, ϵ_β will be equal to the porosity of the porous medium, since the latter is defined as the ratio of the total pore volume within REV to the total REV volume.

3.2.1.3 Averaging Theorems

We will now present two important theorems that are used in the upscaling of transport and flow equations in porous media. A formal and easy to understand proof of these theorems can be found in [128], although similar proofs have been presented elsewhere [82, 114, 115, 129].

First Averaging Theorem

This theorem relates the phase average of a gradient or a divergence of a physical quantity to the gradient or divergence of the phase average of the quantity. As before, any variable ϕ_β associated with the β phase flowing through the porous medium will satisfy the following relationship:

$$\langle \nabla \phi_\beta \rangle = \nabla \langle \phi_\beta \rangle + \frac{1}{V} \int_{A_{\beta\sigma}} \phi_\beta \, \mathbf{n}_{\beta\sigma} \, dA$$ (3.6)

where $\mathbf{n}_{\beta\sigma}$ is the unit normal directed from β phase to σ phase, and $A_{\beta\sigma}$ is the interfacial area between the β and σ phases. In case the variable ϕ_β is a vector, then we deal with divergence of this quantity as shown below.

$$\langle \nabla \cdot \phi_\beta \rangle = \nabla \cdot \langle \phi_\beta \rangle + \frac{1}{V} \int_{A_{\beta\sigma}} \phi_\beta \cdot \mathbf{n}_{\beta\sigma} \, dA$$ (3.7)

63

Second Averaging Theorem

This theorem relates the phase average of a time derivative to the time derivative of the phase average as follows:

$$\langle \frac{\partial \phi_\beta}{\partial t} \rangle = \frac{\partial \langle \phi_\beta \rangle}{\partial t} - \frac{1}{V} \int_{A_{\beta\sigma}} \phi_\beta \, \mathbf{w} \cdot \mathbf{n}_{\beta\sigma} \, dA \tag{3.8}$$

where $\mathbf{w}$ is the velocity of the $\beta - \sigma$ interface.

3.2.2 Upscaling by Volume Averaging Method

The governing equation for solute transport within the pore space of an REV can be expressed as

$$\frac{\partial c_\beta}{\partial t} + \nabla \cdot (c_\beta \mathbf{v}_\beta) = \nabla \cdot (\mathcal{D}_\beta \nabla c_\beta) \tag{3.9}$$

where c_β is the point concentration in the β phase, $\mathbf{v}_\beta$ is the velocity of the β phase, and $\mathcal{D}_\beta$ is the molecular diffusivity of the β phase. Note that it is a tracer equation, i.e., the concentration of the transported species, c_β, in extremely small. This is a convection-diffusion type equation where velocity of the fluid β phase is given. (See [130] for a rigorous derivation of this equation.)

Let us now specify the boundary conditions needed to solve for c_β within the pore region of an REV. A flux of solute ions is created onto the $\beta - \sigma$ interface, which leads to the rate of increase in the surface concentration of the adsorbed ions. This can be expressed as $-\mathbf{n}_{\beta\sigma} \cdot \mathcal{D}_\beta \nabla c_\beta = \frac{\partial c_{ad}}{\partial t}$, where c_{ad} represents the surface concentration on the $\beta - \sigma$ interface. However, our analysis is limited to linear adsorption isotherms and local mass equilibrium exists at the $\beta - \sigma$ interface [117, 118], i.e., $c_{ad} = K_{eq} c_\beta$. Here, K_{eq} is the equilibrium coefficient (or the distribution coefficient) corresponding to the linear isotherm. On combining these two relations, the proposed boundary condition reduces to

$$\text{B.C.1}: \quad -\mathbf{n}_{\beta\sigma} \cdot \mathcal{D}_\beta \nabla c_\beta = K_{eq} \frac{\partial c_\beta}{\partial t}, \quad \text{at } A_{\beta\sigma}. \qquad (3.10)$$

It is helpful for future analysis to state here the continuity equation for the β phase as well as the associated no-slip boundary condition at the $\beta - \sigma$ interface:

$$\nabla \cdot \mathbf{v}_\beta = 0$$
$$\text{B.C.2}: \quad \mathbf{v}_\beta = 0, \quad \text{at } A_{\beta\sigma}. \qquad (3.11)$$

On taking the phase-average of Eq. (3.9), we get

$$\langle \frac{\partial c_\beta}{\partial t} \rangle + \langle \nabla \cdot (c_\beta \mathbf{v}_\beta) \rangle = \langle \nabla \cdot (\mathcal{D}_\beta \nabla c_\beta) \rangle. \qquad (3.12)$$

Let us consider the three terms of this equation one by one. On applying the second averaging theorem, the first term on the left-hand side of this equation results in

$$\langle \frac{\partial c_\beta}{\partial t} \rangle = \frac{\partial \langle c_\beta \rangle}{\partial t} - \frac{1}{V} \int_{A_{\beta\sigma}} c_\beta \, \mathbf{w} \cdot \mathbf{n}_{\beta\sigma} \, dA = \frac{\partial \langle c_\beta \rangle}{\partial t}. \qquad (3.13)$$

The integral term involving the interface velocity $\mathbf{w}$ disappears since we have taken the porous medium to be rigid (non-deforming) and stationary. On applying the first averaging theorem, the second term on the left-hand side of Eq. (3.12) develops as

$$\langle \nabla \cdot (c_\beta \mathbf{v}_\beta) \rangle = \nabla \cdot \langle c_\beta \mathbf{v}_\beta \rangle - \frac{1}{V} \int_{A_{\beta\sigma}} c_\beta \, \mathbf{v}_\beta \cdot \mathbf{n}_{\beta\sigma} \, dA = \nabla \cdot \langle c_\beta \mathbf{v}_\beta \rangle. \qquad (3.14)$$

Here the integral term disappears because of the no-slip condition described in Eq. (3.11).

Let us now look into the development of the term on the right-hand side of Eq. (3.12).

The application of the first averaging theorem leads to the following unfolding:

$$
\begin{aligned}
\langle \nabla \cdot (\mathcal{D}_\beta \nabla c_\beta) \rangle &= \nabla \cdot \langle \mathcal{D}_\beta \nabla c_\beta \rangle + \frac{1}{V} \int_{A_{\beta\sigma}} \mathcal{D}_\beta \nabla c_\beta \cdot \mathbf{n}_{\beta\sigma} \, dA \\
&= \nabla \cdot \langle \mathcal{D}_\beta \nabla c_\beta \rangle - \frac{1}{V} \int_{A_{\beta\sigma}} K_{eq} \frac{\partial c_\beta}{\partial t} \, dA \\
&= \nabla \cdot \langle \mathcal{D}_\beta \nabla c_\beta \rangle - K_{eq} \frac{\partial}{\partial t} \left[\frac{A_{\beta\sigma}}{V} \frac{1}{A_{\beta\sigma}} \int_{A_{\beta\sigma}} c_\beta \, dA \right] . \quad (3.15)
\end{aligned}
$$

Here we use B.C.1 given in Eq. (3.10) as well as the facts that (a) K_{eq} is taken as a constant within the REV, and (b) the time derivative can be taken out of the surface integral since we are dealing with a rigid (non-deforming) porous medium that ensures that the interfacial area within the REV remains unchanged. Thus, by implementing these transformations in the interfacial-flux term within the surface integral, we are able to include the effect of adsorption into the upscaled mass-transport equation.

At this stage, we introduce two definitions:

$$
\text{(I)} \qquad a_{\beta\sigma} = \frac{A_{\beta\sigma}}{V} \qquad\qquad\qquad (3.16)
$$

where $A_{\beta\sigma}$ is the net $\beta - \sigma$ interfacial area contained with the REV volume, and $a_{\beta\sigma}$ is equal to the $\beta - \sigma$ interfacial area per unit volume.

$$
\text{(II)} \qquad \langle c_\beta \rangle_{\beta\sigma} = \frac{1}{A_{\beta\sigma}} \int_{A_{\beta\sigma}} c_\beta \, dA \qquad\qquad (3.17)
$$

where $\langle c_\beta \rangle_{\beta\sigma}$ is the average concentration on the interfacial area.

Through the use of these two definitions, the term on the right-hand side of Eq. (3.11) can be expressed as

$$
\langle \nabla \cdot (\mathcal{D}_\beta \nabla c_\beta) \rangle = \nabla \cdot \langle \mathcal{D}_\beta \nabla c_\beta \rangle - K_{eq} \, a_{\beta\sigma} \frac{\partial \langle c_\beta \rangle_{\beta\sigma}}{\partial t} . \qquad (3.18)
$$

Further employment of the first averaging theorem to the first term of the right-hand side

66

leads to

$$\langle \nabla \cdot (\mathcal{D}_\beta \nabla c_\beta) \rangle = \nabla \cdot \left[\mathcal{D}_\beta \left(\nabla \langle c_\beta \rangle + \frac{1}{V} \int_{A_{\beta\sigma}} c_\beta \, \mathbf{n}_{\beta\sigma} \, dA \right) \right] - K_{eq} \, a_{\beta\sigma} \frac{\partial \langle c_\beta \rangle_{\beta\sigma}}{\partial t} \, . \quad (3.19)$$

Finally, on using equations (3.13), (3.14) and (3.19) in Eq. (3.12), we get an intermediate form of the volume-averaged solute transport equation:

$$\frac{\partial \langle c_\beta \rangle}{\partial t} + \nabla \cdot \langle c_\beta \mathbf{v}_\beta \rangle = \nabla \cdot \left[\mathcal{D}_\beta \left(\nabla \langle c_\beta \rangle + \frac{1}{V} \int_{A_{\beta\sigma}} c_\beta \, \mathbf{n}_{\beta\sigma} \, dA \right) \right] - K_{eq} \, a_{\beta\sigma} \frac{\partial \langle c_\beta \rangle_{\beta\sigma}}{\partial t} \, . \quad (3.20)$$

We will now transform this equation in terms of the intrinsic phase-average using the relation

$$\langle c_\beta \rangle = \epsilon_\beta \, \langle c_\beta \rangle^\beta \quad (3.21)$$

which is based on Eq. (3.4). This results in

$$\epsilon_\beta \frac{\partial \langle c_\beta \rangle^\beta}{\partial t} + \nabla \cdot \langle c_\beta \mathbf{v}_\beta \rangle = \nabla \cdot \left[\mathcal{D}_\beta \left(\epsilon_\beta \nabla \langle c_\beta \rangle^\beta + \langle c_\beta \rangle^\beta \, \nabla \epsilon_\beta + \frac{1}{V} \int_{A_{\beta\sigma}} c_\beta \, \mathbf{n}_{\beta\sigma} \, dA \right) \right]$$
$$- \, K_{eq} \, a_{\beta\sigma} \frac{\partial \langle c_\beta \rangle_{\beta\sigma}}{\partial t} \, . \quad (3.22)$$

Our aim is to develop an equation in terms of the macroscopic variable $\langle c_\beta \rangle^\beta$ entirely. However, we have some unknown terms in the equation which are preventing us from reaching this goal. These terms are the dispersion term $\langle c_\beta \mathbf{v}_\beta \rangle$, the surface integral term on the right-hand side, as well as the transient term involving $\langle c_\beta \rangle_{\beta\sigma}$. Hence some more work lies ahead of us.

In order to proceed further, we will take the help of the following well-known decompositions

$$c_\beta = \langle c_\beta \rangle^\beta + \tilde{c}_\beta \quad \text{and} \quad \mathbf{v}_\beta = \langle \mathbf{v}_\beta \rangle^\beta + \tilde{\mathbf{v}}_\beta \quad (3.23)$$

where $\langle c_\beta \rangle^\beta$ is the intrinsic phase-average concentration in the β phase and $\tilde{c}_\beta$ is the spatial

67

deviation in concentration of the β phase. Similarly, $\langle \mathbf{v}_\beta \rangle^\beta$ is the intrinsic phase-average velocity in the β phase and $\tilde{\mathbf{v}}_\beta$ is the spatial deviation in velocity of the β phase.

This is essentially a splitting of length scales with $\langle c_\beta \rangle^\beta$ varying over a much larger length-scale, say $l_{\langle c_\beta \rangle^\beta}$ while $\tilde{c}_\beta$ varying over the characteristic length $l_{\tilde{c}_\beta}$. Here the constraint associated with this splitting [82] is

$$l_{\tilde{c}_\beta} \; << \; r_o \; << \; l_{\langle c_\beta \rangle^\beta} \tag{3.24}$$

with r_o being the size of the REV. This constraint allows one to treat the average $\langle c_\beta \rangle^\beta$ as a constant in the volume and area integrals within the REV. A similar set of constraints and conclusions can be associated with the decomposition associated with velocity given in Eq. (3.23). Using the property of these averages to be constant within the REV, it is easy to prove the following corollary associated with the decomposition, i.e.,

$$\langle \tilde{c}_\beta \rangle \; = \; 0 \quad \text{and} \quad \langle \tilde{\mathbf{v}}_\beta \rangle \; = \; 0 \,. \tag{3.25}$$

Through the use of Eqs. (3.23) and (3.25), the dispersion term of Eq. (3.22) can be transformed as

$$
\begin{aligned}
\langle c_\beta \mathbf{v}_\beta \rangle &= \langle \langle c_\beta \rangle^\beta \langle \mathbf{v}_\beta \rangle^\beta \rangle + \langle \langle c_\beta \rangle^\beta \tilde{\mathbf{v}}_\beta \rangle + \langle \tilde{c}_\beta \langle \mathbf{v}_\beta \rangle^\beta \rangle + \langle \tilde{c}_\beta \tilde{\mathbf{v}}_\beta \rangle \\
&= \langle c_\beta \rangle^\beta \langle \mathbf{v}_\beta \rangle^\beta \epsilon_\beta + 0 + 0 + \langle \tilde{c}_\beta \tilde{\mathbf{v}}_\beta \rangle \\
&= \epsilon_\beta \langle c_\beta \rangle^\beta \langle \mathbf{v}_\beta \rangle^\beta + \epsilon_\beta \langle \tilde{c}_\beta \tilde{\mathbf{v}}_\beta \rangle^\beta \,.
\end{aligned}
\tag{3.26}
$$

In these derivations, we have also used the relation between the phase-average and the intrinsic phase-average as given by Eq. (3.21), as well as the fact that $\langle 1 \rangle = \epsilon_\beta$ which follows from the basic definitions given earlier in Eqs. (3.2) and (3.5). Using the continuity equation given in Eq. (3.11), the divergence of the dispersion term can be expressed as

$$\nabla \cdot \langle c_\beta \mathbf{v}_\beta \rangle = \epsilon_\beta \langle \mathbf{v}_\beta \rangle^\beta \cdot \nabla \langle c_\beta \rangle^\beta + \nabla \cdot \left(\epsilon_\beta \langle \tilde{c}_\beta \tilde{\mathbf{v}}_\beta \rangle^\beta \right). \tag{3.27}$$

Let us now consider the surface integral term on the right-hand side of Eq. (3.22). If we use the result $(\nabla \epsilon_\beta) = -\frac{1}{V} \int_{A_{\beta\sigma}} \mathbf{n}_{\beta\sigma} \, \tilde{c}_\beta \, dA$, which is obtained after substituting $\phi_\beta = 1$ in the first averaging theorem (Eq. (3.6)), in conjunction with the decomposition given in Eq. (3.23), we get the following result:

$$\begin{aligned}
\frac{1}{V} \int_{A_{\beta\sigma}} \mathbf{n}_{\beta\sigma} \, c_\beta \, dA &= \left(\frac{1}{V} \int_{A_{\beta\sigma}} \mathbf{n}_{\beta\sigma} \, dA \right) \langle c_\beta \rangle^\beta + \frac{1}{V} \int_{A_{\beta\sigma}} \mathbf{n}_{\beta\sigma} \, \tilde{c}_\beta \, dA \\
&= -(\nabla \epsilon_\beta) \langle c_\beta \rangle^\beta + \frac{1}{V} \int_{A_{\beta\sigma}} \mathbf{n}_{\beta\sigma} \, \tilde{c}_\beta \, dA.
\end{aligned} \tag{3.28}$$

Let us now try to exploit the developments in these last two equations in order to get closer to our goal of developing a macroscopic governing equation only in terms of the macroscopic average terms. On using the results of Eqs. (3.27) and (3.28) in Eq. (3.22), we get

$$\begin{aligned}
\epsilon_\beta \frac{\partial \langle c_\beta \rangle^\beta}{\partial t} &+ \epsilon_\beta \langle \mathbf{v}_\beta \rangle^\beta \cdot \nabla \langle c_\beta \rangle^\beta + \nabla \cdot \left(\epsilon_\beta \langle \tilde{c}_\beta \tilde{\mathbf{v}}_\beta \rangle^\beta \right) \\
&= \nabla \cdot \left[\mathcal{D}_\beta \left(\epsilon_\beta \nabla \langle c_\beta \rangle^\beta + \frac{1}{V} \int_{A_{\beta\sigma}} \mathbf{n}_{\beta\sigma} \, \tilde{c}_\beta \, dA \right) \right] - K_{eq} a_{\beta\sigma} \frac{\partial \langle c_\beta \rangle_{\beta\sigma}}{\partial t}.
\end{aligned} \tag{3.29}$$

In this equation, we can notice the mathematical representations of the different transport mechanisms involved. On the left-hand side of Eq. (3.29), the first term accounts for accumulation of the tracer species, the second term corresponds to the convective flux, and the third term captures the hydrodynamic dispersion phenomenon, which, as widely accepted [1], is the result of spatial deviations in the pore-level velocity field. Similarly, on the right-hand side of the equation, the first term represents the diffusive flux originating due to spatial gradient of the average concentration, and the macrodiffusive or non-local diffusive flux based on perturbations in the concentration field, whereas the last term accounts for the adsorptive flux onto the $\beta - \sigma$ interfacial

69

surface. It should be noted that porous media have significantly high specific interfacial area (i.e, large $A_{\beta\sigma}$ within the REV) which makes them highly effective for adsorption-based applications, and in this case, may also make the adsorptive-flux term significant even in the cases with small rates of change of average concentration.

Let us now work on the transient term on the left-hand side of Eq. (3.29). In view of the constraints expressed by Eq. (3.24), and according to [122] , it is acceptable to use the following approximations:

$$
\langle\langle c_\beta\rangle^\beta\rangle_{\beta\sigma} = \langle c_\beta\rangle^\beta \quad \text{and} \quad \langle \tilde{c}_\beta\rangle_{\beta\sigma} = 0 \,.
\tag{3.30}
$$

The use of Eq. (3.23) in the transient term along with these approximations allows one to rewrite Eq. (3.29) in a simplified form:

$$
\epsilon_\beta \left(1 + \frac{K_{eq} a_{\beta\sigma}}{\epsilon_\beta} \right) \frac{\partial \langle c_\beta\rangle^\beta}{\partial t} + \epsilon_\beta \langle \mathbf{v}_\beta\rangle^\beta \cdot \nabla \langle c_\beta\rangle^\beta
$$

$$
= \nabla \cdot \left[\epsilon_\beta \mathcal{D}_\beta \left(\nabla \langle c_\beta\rangle^\beta + \frac{1}{V_\beta} \int_{A_{\beta\sigma}} \mathbf{n}_{\beta\sigma} \, \tilde{c}_\beta \, dA \right) \right]
$$

$$
- \nabla \cdot \left(\epsilon_\beta \langle \tilde{c}_\beta \tilde{\mathbf{v}}_\beta\rangle^\beta \right) \,.
\tag{3.31}
$$

3.2.3   Seeking Closure

In order to estimate the unknown terms in Eq. (3.31) involving $\tilde{c}_\beta$, we plan to propose a set of equations for the same. Later, those equations will be transformed in order to obtain what is called the closure formulation.

We start with Eq. (3.9), where, after using the decomposition given in Eq. (3.23), we obtain:

$$
\frac{\partial \langle c_\beta\rangle^\beta}{\partial t} + \frac{\partial \tilde{c}_\beta}{\partial t} + \nabla \cdot (\langle c_\beta\rangle^\beta \langle \mathbf{v}_\beta\rangle^\beta) + \nabla \cdot (\langle c_\beta\rangle^\beta \tilde{\mathbf{v}}_\beta) + \nabla \cdot (\tilde{c}_\beta \langle \mathbf{v}_\beta\rangle^\beta) + \nabla \cdot (\tilde{c}_\beta \tilde{\mathbf{v}}_\beta)
$$

$$
= \nabla \cdot (\mathcal{D}_\beta \nabla \langle c_\beta\rangle^\beta) + \nabla \cdot (\mathcal{D}_\beta \nabla \tilde{c}_\beta) \,.
\tag{3.32}
$$

70

On dividing Eq. (3.31) with ϵ_β and rearranging the terms, we get

$$\left(1 + \frac{K_{eq}a_{\beta\sigma}}{\epsilon_\beta}\right)\frac{\partial \langle c_\beta\rangle^\beta}{\partial t} + \langle \mathbf{v}_\beta\rangle^\beta \cdot \nabla \langle c_\beta\rangle^\beta + \epsilon_\beta^{-1}\,\nabla \cdot \langle \tilde{c}_\beta \tilde{\mathbf{v}}_\beta\rangle$$

$$= \epsilon_\beta^{-1}\,\nabla \cdot (\epsilon_\beta\,\mathcal{D}_\beta\,\nabla \langle c_\beta\rangle^\beta) + \epsilon_\beta^{-1}\,\nabla \cdot \left[\mathcal{D}_\beta\left(\frac{1}{V}\int_{A_{\beta\sigma}}\mathbf{n}_{\beta\sigma}\,\tilde{c}_\beta\,dA\right)\right].$$
$$(3.33)$$

Let us look at the term $\epsilon_\beta^{-1}\,\nabla \cdot (\epsilon_\beta\,\mathcal{D}_\beta\,\nabla \langle c_\beta\rangle^\beta)$ of this equation. It is clear that this term reduces to $\nabla \cdot (\mathcal{D}_\beta \nabla \langle c_\beta\rangle^\beta)$ of Eq. (3.32) if the porous medium is assumed to be perfectly homogeneous and hence the porosity ϵ_β is constant everywhere. However, real porous media always have some little inhomogeneity associated with them. Hence, it is advisable if one develops some constraint for the applicability of this assumption of homogeneity. The expansion of the concerned term yields

$$\epsilon_\beta^{-1}\,\nabla \cdot (\epsilon_\beta\,\mathcal{D}_\beta\,\nabla \langle c_\beta\rangle^\beta) = \nabla \cdot (\mathcal{D}_\beta\,\nabla \langle c_\beta\rangle^\beta) + \epsilon_\beta^{-1}\,\nabla\epsilon_\beta \cdot \mathcal{D}_\beta\,\nabla \langle c_\beta\rangle^\beta. \qquad (3.34)$$

Our aim will be to show that the second term on the right-hand side is much smaller than the first one. After a little scaling analysis, it is easy to show that

$$\frac{O\left(\epsilon_\beta^{-1}\,\nabla\epsilon_\beta \cdot \mathcal{D}_\beta\,\nabla \langle c_\beta\rangle^\beta\right)}{O\left(\nabla \cdot (\mathcal{D}_\beta\,\nabla \langle c_\beta\rangle^\beta)\right)} = O\left(\frac{l_{\langle c_\beta\rangle^\beta}}{l_{\epsilon_\beta}}\right). \qquad (3.35)$$

Hence, if

$$l_{\langle c_\beta\rangle^\beta} \quad << \quad l_{\epsilon_\beta}, \qquad (3.36)$$

then $\epsilon_\beta^{-1}\,\nabla\epsilon_\beta \cdot \mathcal{D}_\beta\,\nabla \langle c_\beta\rangle^\beta \quad << \quad \nabla \cdot (\mathcal{D}_\beta\,\nabla \langle c_\beta\rangle^\beta)$. Eq. (3.36) implies that the length-scale over which the porosity ϵ_β is changing is much larger than the length-scale over which the intrinsic phase-average concentration $\langle c_\beta\rangle^\beta$ is changing. In such a situation, the porous medium can be said to be homogeneous in terms of the porosity, and hence Eq. (3.33)

reduces to

$$\left(1 + \frac{K_{eq}a_{\beta\sigma}}{\epsilon_\beta}\right)\frac{\partial\langle c_\beta\rangle^\beta}{\partial t} + \langle\mathbf{v}_\beta\rangle^\beta \cdot \nabla\langle c_\beta\rangle^\beta + \epsilon_\beta^{-1}\nabla\cdot\langle\tilde{c}_\beta\tilde{\mathbf{v}}_\beta\rangle$$
$$= \nabla\cdot(\mathcal{D}_\beta\nabla\langle c_\beta\rangle^\beta) + \epsilon_\beta^{-1}\nabla\cdot\left[\mathcal{D}_\beta\left(\frac{1}{V}\int_{A_{\beta\sigma}}\mathbf{n}_{\beta\sigma}\,\tilde{c}_\beta\,dA\right)\right]. \tag{3.37}$$

We will now subtract Eq. (3.37) from Eq. (3.32) to get an equation of the form:

$$\frac{\partial\tilde{c}_\beta}{\partial t} - \frac{K_{eq}a_{\beta\sigma}}{\epsilon_\beta}\frac{\partial\langle c_\beta\rangle^\beta}{\partial t} + \nabla\cdot(\langle c_\beta\rangle^\beta\langle\mathbf{v}_\beta\rangle^\beta) - \langle\mathbf{v}_\beta\rangle^\beta\cdot\nabla\langle c_\beta\rangle^\beta + \nabla\cdot(\langle c_\beta\rangle^\beta\tilde{\mathbf{v}}_\beta)$$
$$+ \nabla\cdot(\tilde{c}_\beta\langle\mathbf{v}_\beta\rangle^\beta) + \nabla\cdot(\tilde{c}_\beta\tilde{\mathbf{v}}_\beta) - \epsilon_\beta^{-1}\nabla\cdot\langle\tilde{c}_\beta\tilde{\mathbf{v}}_\beta\rangle$$
$$= \nabla\cdot(\mathcal{D}_\beta\nabla\tilde{c}_\beta) - \epsilon_\beta^{-1}\nabla\cdot\left[\mathcal{D}_\beta\left(\frac{1}{V}\int_{A_{\beta\sigma}}\mathbf{n}_{\beta\sigma}\,\tilde{c}_\beta\,dA\right)\right]. \tag{3.38}$$

Let us take the help of the point-wise continuity equation given in Eq. (3.11) to simplify this equation further. On applying the first averaging theorem to this continuity equation and applying the no-slip boundary condition on the fluid-solid interface, one obtains the macroscopic equation of continuity:

$$\nabla\cdot\langle\mathbf{v}_\beta\rangle = 0. \tag{3.39}$$

Noting the fact that $\langle\mathbf{v}_\beta\rangle = \epsilon_\beta\langle\mathbf{v}_\beta\rangle^\beta$, one can manipulate the macroscopic continuity equation to obtain

$$\nabla\cdot\langle\mathbf{v}_\beta\rangle^\beta = -\frac{1}{\epsilon_\beta}\langle\mathbf{v}_\beta\rangle^\beta\cdot\nabla\epsilon_\beta \approx 0. \tag{3.40}$$

Using a simple scaling analysis, one can convince oneself that the right-hand side of this equation will indeed tend to zero if the constraint

$$l_{\langle \mathbf{v}_\beta \rangle^\beta} \quad << \quad l_{\epsilon_\beta} \tag{3.41}$$

is valid. Note the similarity of this relation with the one given in Eq. (3.36), thus emphasizing the fact that the length-scale of variation of macroscopic quantities should be much smaller than the length-scale of variation of porosity. We can apply Eq. (3.40) to obtain the following result:

$$\nabla \cdot (\langle c_\beta \rangle^\beta \langle \mathbf{v}_\beta \rangle^\beta) = \langle \mathbf{v}_\beta \rangle^\beta \cdot \nabla \langle c_\beta \rangle^\beta + \langle c_\beta \rangle^\beta \nabla \cdot \langle \mathbf{v}_\beta \rangle^\beta \quad \approx \quad \langle \mathbf{v}_\beta \rangle^\beta \cdot \nabla \langle c_\beta \rangle^\beta . \tag{3.42}$$

Similarly, by using Eq. (3.40), one obtains the following simplification:

$$\nabla \cdot (\tilde{c}_\beta \langle \mathbf{v}_\beta \rangle^\beta) \quad \approx \quad \langle \mathbf{v}_\beta \rangle^\beta \cdot \nabla \tilde{c}_\beta . \tag{3.43}$$

Through the use of Eqs. (3.42) and (3.43), Eq. (3.38) can be rewritten as

$$\frac{\partial \tilde{c}_\beta}{\partial t} + \nabla \cdot (\tilde{c}_\beta \tilde{\mathbf{v}}_\beta) - \epsilon_\beta^{-1} \nabla \cdot \langle \tilde{c}_\beta \tilde{\mathbf{v}}_\beta \rangle + \nabla \cdot (\tilde{\mathbf{v}}_\beta \langle c_\beta \rangle^\beta) + \langle \mathbf{v}_\beta \rangle^\beta \cdot \nabla \tilde{c}_\beta$$
$$= \nabla \cdot (\mathcal{D}_\beta \nabla \tilde{c}_\beta) - \epsilon_\beta^{-1} \nabla \cdot \left[\mathcal{D}_\beta \left(\frac{1}{V} \int_{A_{\beta\sigma}} \mathbf{n}_{\beta\sigma} \tilde{c}_\beta \, dA \right) \right] + \frac{K_{eq} a_{\beta\sigma}}{\epsilon_\beta} \frac{\partial \langle c_\beta \rangle^\beta}{\partial t} . \tag{3.44}$$

From Eqs. (3.11) and (3.40), while using the decomposition given in Eq. (3.23), one can easily show that

$$\nabla \cdot \tilde{\mathbf{v}}_\beta = 0 . \tag{3.45}$$

Expanding some terms and cancelling some others on the left-hand side, while using Eq. (3.45) at one place, Eq. (3.44) can be transformed to this final form as a **governing**

73

differential equation for $\tilde{c}_\beta$:

$$\frac{\partial \tilde{c}_\beta}{\partial t} + \mathbf{v}_\beta \cdot \nabla \tilde{c}_\beta + \tilde{\mathbf{v}}_\beta \cdot \nabla \langle c_\beta \rangle^\beta - \epsilon_\beta^{-1} \nabla \cdot \langle \tilde{\mathbf{v}}_\beta \tilde{c}_\beta \rangle$$

$$= \nabla \cdot (\mathcal{D}_\beta \nabla \tilde{c}_\beta) - \epsilon_\beta^{-1} \nabla \cdot \left[\mathcal{D}_\beta \left(\frac{1}{V} \int_{A_{\beta\sigma}} \mathbf{n}_{\beta\sigma} \, \tilde{c}_\beta \, dA \right) \right] + \frac{K_{eq} \, a_{\beta\sigma}}{\epsilon_\beta} \frac{\partial \langle c_\beta \rangle^\beta}{\partial t}. \quad (3.46)$$

Here there are two terms, one $\tilde{\mathbf{v}}_\beta \cdot \nabla \langle c_\beta \rangle^\beta$ and the other $\frac{K_{eq} \, a_{\beta\sigma}}{\epsilon_\beta} \frac{\partial \langle c_\beta \rangle^\beta}{\partial t}$, which act as source terms for the creation of non-zero $\tilde{c}_\beta$ in the liquid (β) phase within the REV. Using the decomposition given in Eq. (3.23) in Eq. (3.10), one can generate the following **boundary condition**

$$\text{B.C.1}: \quad -\mathbf{n}_{\beta\sigma} \cdot \mathcal{D}_\beta \nabla \tilde{c}_\beta - K_{eq} \frac{\partial \tilde{c}_\beta}{\partial t} \quad = \quad -\mathbf{n}_{\beta\sigma} \cdot \mathcal{D}_\beta \nabla \langle c_\beta \rangle^\beta - K_{eq} \frac{\partial \langle c_\beta \rangle^\beta}{\partial t}, \quad \text{at } A_{\beta\sigma} \quad (3.47)$$

where the two terms on the right-hand side are the source terms.

We will now present a simplification of Eq. (3.46) based on an order-of-magnitude analysis. We will compare pairs of terms in order to discard the insignificant terms.

Note that

$$\frac{O\left(\mathbf{v}_\beta \cdot \nabla \tilde{c}_\beta\right)}{O\left(\epsilon_\beta^{-1} \nabla \cdot \langle \tilde{\mathbf{v}}_\beta \tilde{c}_\beta \rangle\right)} \quad = \quad O\left(\frac{L}{l_{\tilde{c}_\beta}}\right)$$

and since $L \gg l_{\tilde{c}_\beta}$

$$\implies \mathbf{v}_\beta \cdot \nabla \tilde{c}_\beta \quad \text{(Convective Transport)} \quad \gg \quad \epsilon_\beta^{-1} \nabla \cdot \langle \tilde{\mathbf{v}}_\beta \tilde{c}_\beta \rangle \quad \text{(Dispersive Transport)}$$

$$(3.48)$$

Similarly

$$\frac{O\left(\nabla \cdot (\mathcal{D}_\beta \nabla \tilde{c}_\beta)\right)}{O\left(\epsilon_\beta^{-1} \nabla \cdot \left[\mathcal{D}_\beta \left(\frac{1}{V} \int_{A_{\beta\sigma}} \mathbf{n}_{\beta\sigma} \, \tilde{c}_\beta \, dA \right) \right]\right)} \quad = \quad O\left(\frac{L}{l_{\tilde{c}_\beta}}\right)$$

and since $L >> l_{\tilde{c}_\beta}$

$$\begin{aligned} \implies &\nabla \cdot (\mathcal{D}_\beta \nabla \tilde{c}_\beta) \quad \text{(Local Diffusive Transport)}\\ &>> \quad \epsilon_\beta^{-1} \nabla \cdot \left[\mathcal{D}_\beta \left(\frac{1}{V} \int_{A_{\beta\sigma}} \mathbf{n}_{\beta\sigma}\, \tilde{c}_\beta\, dA \right) \right] \quad \text{(Non-Local Diffusive Transport)} \end{aligned} \tag{3.49}$$

Using Eqs. (3.48) and (3.49) to discard the insignificant terms in Eq. (3.46), the governing differential equation reduces to

$$\frac{\partial \tilde{c}_\beta}{\partial t} + \mathbf{v}_\beta \cdot \nabla \tilde{c}_\beta + \tilde{\mathbf{v}}_\beta \cdot \nabla \langle c_\beta \rangle^\beta = \mathcal{D}_\beta \nabla^2 \tilde{c}_\beta + \frac{K_{eq}\, a_{\beta\sigma}}{\epsilon_\beta} \frac{\partial \langle c_\beta \rangle^\beta}{\partial t} \tag{3.50}$$

after ignoring the variation in $\mathcal{D}_\beta$ within the REV. Here, $\tilde{\mathbf{v}}_\beta \cdot \nabla \langle c_\beta \rangle^\beta$ will be termed as the **convective source** while $\frac{K_{eq}\, a_{\beta\sigma}}{\epsilon_\beta} \frac{\partial \langle c_\beta \rangle^\beta}{\partial t}$ is designated as the **adsorptive source**.

While the volume-averaged species transport problem described by Eq. (3.31) has to be transient in order to handle realistic ion-transport problems through porous media, the fate of the transient term in the governing equation at the closure level, Eq. (3.50), has to be decided. We will decide this by comparing the order-of-magnitudes of the transient and the diffusive-transport terms as follows.

$$\frac{O\left(\frac{\partial \tilde{c}_\beta}{\partial t} \right)}{O\left(\mathcal{D}_\beta \nabla^2 \tilde{c}_\beta \right)} = \frac{1}{\frac{\mathcal{D}_\beta\, \tau}{l_{\tilde{c}_\beta}^2}} \tag{3.51}$$

where τ is the characteristic time for changes in $\tilde{c}_\beta$. If

$$\frac{\mathcal{D}_\beta\, \tau}{l_{\tilde{c}_\beta}^2} >> 1 \quad , \tag{3.52}$$

then $\mathcal{D}_\beta \nabla^2 \tilde{c}_\beta >> \frac{\partial \tilde{c}_\beta}{\partial t}$, and hence the transient term can be dropped.

Let us examine what it means in real practical terms. A typical value of $\mathcal{D}_\beta$ is 10^{-9} m^2/s in water-based systems while $l_{\tilde{c}_\beta} \sim 10\,\mu\text{m} = 10^{-5}\,\text{m}$ as it matches the width of the channel between particles in a typical (particulate) porous medium. In such a situation,

the condition given in Eq. (3.52) enforces that $\tau >> 0.1\,\text{s}$. Since this condition is easily satisfied in real systems, we can be sure that the *governing equations at the closure level will almost always be quasi-steady.* Hence, the final form of the governing differential equation for $\tilde{c}_\beta$ is

$$\mathbf{v}_\beta \cdot \nabla \tilde{c}_\beta \,+\, \tilde{\mathbf{v}}_\beta \cdot \nabla \langle c_\beta \rangle^\beta = \mathcal{D}_\beta \nabla^2 \tilde{c}_\beta \,+\, \frac{K_{eq}\, a_{\beta\sigma}}{\epsilon_\beta} \frac{\partial \langle c_\beta \rangle^\beta}{\partial t}\,. \tag{3.53}$$

Since the governing differential equations have been rendered quasi-steady, it is reasonable to expect the same for the associated boundary conditions given in Eq. (3.47). Let us compare the strong diffusive-transport term with the transient term and find the associated constraint through the following order-of-magnitude analysis:

$$\mathbf{n}_{\beta\sigma} \cdot \mathcal{D}_\beta \nabla \tilde{c}_\beta \quad >> \quad K_{eq} \frac{\partial \tilde{c}_\beta}{\partial t}$$
$$\Rightarrow \quad \frac{\mathcal{D}_\beta \tau}{K_{eq}\, l_{\tilde{c}_\beta}} \quad >> \quad 1\,. \tag{3.54}$$

Since this constraint is very likely to be enforced because of Eq. (3.52), Eq. (3.47) reduces to the final form of the closure-level boundary condition:

$$\text{B.C.1}: \quad -\,\mathbf{n}_{\beta\sigma} \cdot \mathcal{D}_\beta \nabla \tilde{c}_\beta \quad = \quad -\mathbf{n}_{\beta\sigma} \cdot \mathcal{D}_\beta \nabla \langle c_\beta \rangle^\beta - K_{eq} \frac{\partial \langle c_\beta \rangle^\beta}{\partial t}, \quad \text{at } A_{\beta\sigma}. \tag{3.55}$$

Note that aside from this boundary condition, one also needs a global average constraint defined as

$$\langle \tilde{c}_\beta \rangle^\beta = 0 \tag{3.56}$$

which arises from Eq. (3.25). Thus we collect Eqs. (3.53) and (3.55), and include the standard periodicity condition in order to propose the final set of equations needed to solve for the distribution of $\tilde{c}_\beta$ in the pore region of the REV, which is now in the form of a unit-cell.

Local Closure Problem:

$$\mathbf{v}_\beta \cdot \nabla \tilde{c}_\beta + \tilde{\mathbf{v}}_\beta \cdot \nabla \langle c_\beta \rangle^\beta = \mathcal{D}_\beta \nabla^2 \tilde{c}_\beta + \frac{K_{eq} a_{\beta\sigma}}{\epsilon_\beta} \frac{\partial \langle c_\beta \rangle^\beta}{\partial t} \tag{3.57}$$

$$\text{B.C.1}: \quad -\mathbf{n}_{\beta\sigma} \cdot \mathcal{D}_\beta \nabla \tilde{c}_\beta = -\mathbf{n}_{\beta\sigma} \cdot \mathcal{D}_\beta \nabla \langle c_\beta \rangle^\beta - K_{eq} \frac{\partial \langle c_\beta \rangle^\beta}{\partial t}, \quad \text{at } A_{\beta\sigma} \tag{3.58}$$

$$\text{Periodicity B.C.}: \quad \tilde{c}_\beta(\mathbf{r} + \mathbf{l}_i) = \tilde{c}_\beta(\mathbf{r}), \quad i = 1, 2, 3 \tag{3.59}$$

$$\text{Constraint}: \quad \langle \tilde{c}_\beta \rangle^\beta = 0. \tag{3.60}$$

Note that we have invoked the periodicity boundary condition here that is in line with the closure formulations proposed for other mass and momentum tranfer problems [82, 122]. When this boundary condition is applied on the boundaries of a unit-cell, it imposes the assumption that the porous medium is periodic in nature and can be recreated by the translation of the unit cell along the x-, y- and z-directions. However, as has been pointed by Whitaker [82], the influence of such a boundary condition is confined to a narrow region close to the boundary, and the accuracy of the predicted deviation field is not significantly affected.

Solving the Closure Problem using Closure Variables

We will now aim to solve for the deviation in solute concentration, $\tilde{c}_\beta$, in terms of variables that link this deviation with its sources. Note that there are two sources present in our problem: one as $\nabla \langle c_\beta \rangle^\beta$ and the other as $K_{eq} \frac{\partial \langle c_\beta \rangle^\beta}{\partial t}$. These derivatives of the macroscopic solute concentration give rise to the local deviations within in the REV. Hence, it is quite logical that we propose a representation for $\tilde{c}_\beta$ in terms of these sources:

$$\tilde{c}_\beta = \mathbf{b}_\beta \cdot \nabla \langle c_\beta \rangle^\beta + s_\beta K_{eq} \frac{\partial \langle c_\beta \rangle^\beta}{\partial t} \tag{3.61}$$

where $\mathbf{b}_\beta$ and s_β are called the closure variables that are functions of position, and hence can be thought of 'distributing' the contributions of the two sources within the β region of the unit-cell. The $\mathbf{b}_\beta$ maps $\nabla \langle c_\beta \rangle^\beta$ onto $\tilde{c}_\beta$, while the s_β maps $K_{eq} \frac{\partial \langle c_\beta \rangle^\beta}{\partial t}$ onto $\tilde{c}_\beta$.

We now use Eq. (3.61) with Eq. (3.57) and treat $\nabla \langle c_\beta \rangle^\beta$ and $\frac{\partial \langle c_\beta \rangle^\beta}{\partial t}$ as constants while doing the spacial derivatives. On collecting the coefficients of these terms, we get

$$\left[\mathbf{v}_\beta \cdot \nabla \mathbf{b}_\beta + \tilde{\mathbf{v}}_\beta - \mathcal{D}_\beta \nabla^2 \mathbf{b}_\beta \right] \cdot \nabla \langle c_\beta \rangle^\beta + \left[\mathbf{v}_\beta \cdot \nabla s_\beta - \mathcal{D}_\beta \nabla^2 s_\beta - \frac{a_{\beta\sigma}}{\epsilon_\beta} \right] K_{eq} \frac{\partial \langle c_\beta \rangle^\beta}{\partial t} = 0 . \tag{3.62}$$

Since the terms $\nabla \langle c_\beta \rangle^\beta$ and $K_{eq} \frac{\partial \langle c_\beta \rangle^\beta}{\partial t}$ are independent of each other, their coefficients have to be individually set to zero in order to satisfy Eq. (3.62). Hence, we get the governing differential equations for two different problems:

$$\text{Problem I for } \mathbf{b}_\beta : \qquad \mathbf{v}_\beta \cdot \nabla \mathbf{b}_\beta + \tilde{\mathbf{v}}_\beta = \mathcal{D}_\beta \nabla^2 \mathbf{b}_\beta \tag{3.63}$$

$$\text{Problem II for } s_\beta : \qquad \mathbf{v}_\beta \cdot \nabla s_\beta = \mathcal{D}_\beta \nabla^2 s_\beta + \frac{a_{\beta\sigma}}{\epsilon_\beta} . \tag{3.64}$$

Using this same approach, one can split the B.C.1 (Eq. (3.58)), the periodicity B.C. (Eq. (3.59)), and the global constraint (Eq. (3.60)) into two parts each–one for $\mathbf{b}_\beta$ and the other for s_β. Hence, we can generate two sets of governing equations and boundary conditions for solving the closure problem.

Problem I:

$$\mathbf{v}_\beta \cdot \nabla \mathbf{b}_\beta + \tilde{\mathbf{v}}_\beta = \mathcal{D}_\beta \nabla^2 \mathbf{b}_\beta \tag{3.65}$$

$$\text{B.C.1}: \quad - \mathbf{n}_{\beta\sigma} \cdot \nabla \mathbf{b}_\beta = \mathbf{n}_{\beta\sigma}, \quad \text{at } A_{\beta\sigma} \tag{3.66}$$

$$\text{Periodicity B.C.}: \quad \mathbf{b}_\beta(\mathbf{r} + \mathbf{l}_i) = \mathbf{b}_\beta(\mathbf{r}), \quad i = 1, 2, 3 \tag{3.67}$$

$$\text{Constraint}: \quad \langle \mathbf{b}_\beta \rangle^\beta = 0 \tag{3.68}$$

Problem II:

$$\mathbf{v}_\beta \cdot \nabla s_\beta \;=\; \mathcal{D}_\beta \nabla^2 s_\beta \;+\; \frac{a_{\beta\sigma}}{\epsilon_\beta} \tag{3.69}$$

$$\text{B.C.1}: \quad -\,\mathbf{n}_{\beta\sigma} \cdot \mathcal{D}_\beta \nabla s_\beta \;=\; 1, \quad \text{at } A_{\beta\sigma} \tag{3.70}$$

$$\text{Periodicity B.C.:} \quad s_\beta(\mathbf{r} + \mathbf{l}_i) \;=\; s_\beta(\mathbf{r}), \quad i = 1, 2, 3 \tag{3.71}$$

$$\text{Constraint}: \quad \langle s_\beta \rangle^\beta \;=\; 0\,. \tag{3.72}$$

Note that in order to solve the above sets of equations, we need the distribution of $\mathbf{v}_\beta$ within the unit-cell, which will require solving the Stokes-Flow equations in the pore-region corresponding to the β phase.

3.2.4 Developing a Conventional Form for the Macroscopic Solute Transport Equation

Now that the closure formulation can be solved in principle using any multiphysics software, we can take back the results obtained using Eq. (3.61) to Eq. (3.31) in order to solve for the distribution of $\langle c_\beta \rangle^\beta$ in the macroscopic domain. However, since the governing equation for such a distribution is of the form of a convection-dispersion equation, we will first attempt to transform Eq. (3.31) into such a form.

By employing Eq. (3.61) in the first term on the right-hand side of Eq. (3.31), we get,

after some manipulation, the following result:

$$\nabla \cdot \left[\epsilon_\beta \mathcal{D}_\beta \left(\nabla \langle c_\beta \rangle^\beta + \frac{1}{V_\beta} \int_{A_{\beta\sigma}} \mathbf{n}_{\beta\sigma} \, \tilde{c}_\beta \, dA \right) \right]$$

$$= \nabla \cdot \left[\epsilon_\beta \mathcal{D}_\beta \left(\mathbf{I} + \frac{1}{V_\beta} \int_{A_{\beta\sigma}} \mathbf{n}_{\beta\sigma} \, \mathbf{b}_\beta \, dA \right) \cdot \nabla \langle c_\beta \rangle^\beta \right]$$

$$+ \nabla \cdot \left[\frac{\mathcal{D}_\beta}{V} \left(\int_{A_{\beta\sigma}} \mathbf{n}_{\beta\sigma} \, s_\beta \, dA \right) \right] K_{eq} \frac{\partial \langle c_\beta \rangle^\beta}{\partial t}$$

$$+ \frac{\mathcal{D}_\beta}{V} \left(\int_{A_{\beta\sigma}} \mathbf{n}_{\beta\sigma} \, s_\beta \, dA \right) \cdot \nabla \left[K_{eq} \frac{\partial \langle c_\beta \rangle^\beta}{\partial t} \right] . \quad (3.73)$$

Similarly, we can transform the second term on the right-hand side of Eq. (3.31) as

$$- \nabla \cdot \left(\epsilon_\beta \langle \tilde{c}_\beta \tilde{\mathbf{v}}_\beta \rangle^\beta \right) = \nabla \cdot \left[(-\epsilon_\beta \langle \tilde{\mathbf{v}}_\beta \mathbf{b}_\beta \rangle) \cdot \nabla \langle c_\beta \rangle^\beta \right]$$

$$+ \left[\nabla \cdot (-\epsilon_\beta \langle s_\beta \tilde{\mathbf{v}}_\beta \rangle) \right] K_{eq} \frac{\partial \langle c_\beta \rangle^\beta}{\partial t} - \epsilon_\beta \langle s_\beta \tilde{\mathbf{v}}_\beta \rangle \cdot \nabla \left[K_{eq} \frac{\partial \langle c_\beta \rangle^\beta}{\partial t} \right] . \quad (3.74)$$

On using Eqs. (3.73) and (3.74) on the right-hand side of Eq. (3.31) and on manipulating the terms, one can get this penultimate form:

$$\epsilon_\beta \frac{\partial \langle c_\beta \rangle^\beta}{\partial t} + \epsilon_\beta \langle \mathbf{v}_\beta \rangle^\beta \cdot \nabla \langle c_\beta \rangle^\beta + \epsilon_\beta \mathbf{u}_\beta \cdot \nabla \left(K_{eq} \frac{\partial \langle c_\beta \rangle^\beta}{\partial t} \right) = \nabla \cdot \left(\epsilon_\beta \mathbf{D}_\beta^* \cdot \nabla \langle c_\beta \rangle^\beta \right)$$

$$- a_{\beta\sigma} K_{eq} \frac{\partial \langle c_\beta \rangle^\beta}{\partial t} . \quad (3.75)$$

The new terms used in this equation are as follows:

$$\mathbf{u}_\beta = \langle s_\beta \tilde{\mathbf{v}}_\beta \rangle^\beta - \frac{\mathcal{D}_\beta}{V_\beta} \int_{A_{\beta\sigma}} \mathbf{n}_{\beta\sigma} \, s_\beta \, dA \quad (3.76)$$

$$\mathbf{D}_\beta^* = \mathcal{D}_\beta \left[\mathbf{I} + \frac{1}{V_\beta} \int_{A_{\beta\sigma}} \mathbf{n}_{\beta\sigma} \, \mathbf{b}_\beta \, dA \right] - \langle \tilde{\mathbf{v}}_\beta \mathbf{b}_\beta \rangle^\beta . \quad (3.77)$$

Note that $\langle \tilde{\mathbf{v}}_\beta \mathbf{b}_\beta \rangle^\beta$ term essentially comes to existence because of the spacial fluctuations

80

in the velocity and the $\langle c_\beta \rangle^\beta$ induced concentration fields, and hence it is often called the **hydrodynamic dispersion tensor**, $\mathbf{D}_\beta$ (page 139 of [82]). Similarly the first part of the right-hand side of Eq. (3.77), borrowing on the traditional terminology, can be christened as the **effective diffusivity tensor**, $\mathbf{D}_{eff}$. As a result, the equation can be represented as

$$\mathbf{D}_\beta^* = \mathbf{D}_{eff} + \mathbf{D}_\beta \tag{3.78}$$

where

$$\mathbf{D}_{eff} = \mathcal{D}_\beta \left[\mathbf{I} + \frac{1}{V_\beta} \int_{A_{\beta\sigma}} \mathbf{n}_{\beta\sigma} \, \mathbf{b}_\beta \, dA \right] \tag{3.79}$$

and

$$\mathbf{D}_\beta = -\langle \tilde{\mathbf{v}}_\beta \mathbf{b}_\beta \rangle^\beta . \tag{3.80}$$

The term $\langle s_\beta \tilde{\mathbf{v}}_\beta \rangle^\beta$ of Eq. (3.76) is similar to the hydrodynamic dispersion tensor and becomes 'alive' because of the spacial fluctuations in the velocity and the $K_{eq} \frac{\partial \langle c_\beta \rangle^\beta}{\partial t}$ induced concentration fields. Hence, we can call it the **adsorption-induced hydrodynamic dispersion vector**. Also, the second term on the right-hand side of Eq. (3.76) is similar to the diffusivity tensor, and therefore can be called the **adsorption-induced diffusivity vector**.

If we assume that (a) the porosity, ϵ_β, is almost a constant following the constraint given in Eq. (3.36), (b) the total dispersion tensor, $\mathbf{D}_\beta^*$, is unchanging, (c) the equilibrium coefficient, K_{eq}, is a constant, then Eq. (3.75) can be presented in a much simpler form:

$$\boxed{\left(1 + \frac{a_{\beta\sigma} K_{eq}}{\epsilon_\beta} \right) \frac{\partial \langle c_\beta \rangle^\beta}{\partial t} + \langle \mathbf{v}_\beta \rangle^\beta \cdot \nabla \langle c_\beta \rangle^\beta + K_{eq} \, \mathbf{u}_\beta \cdot \nabla \left(\frac{\partial \langle c_\beta \rangle^\beta}{\partial t} \right) = \mathbf{D}_\beta^* : \nabla \nabla \langle c_\beta \rangle^\beta .}$$
$$\tag{3.81}$$

A study of this equation reveals that the third term in the left-hand side (to be called the mixed derivative term) is preventing us from attaining the form of the traditional convection-dispersion equation. Here we develop a constraint that will allow us to neglect

this mixed derivative term. For this to happen, it is obvious that the following restriction is observed:

$$K_{eq}\,\mathbf{u}_\beta \cdot \nabla \left(\frac{\partial \langle c_\beta \rangle^\beta}{\partial t} \right) << \left(1 + \frac{a_{\beta\sigma}\,K_{eq}}{\epsilon_\beta} \right) \frac{\partial \langle c_\beta \rangle^\beta}{\partial t}\,. \tag{3.82}$$

Use of the estimate given by

$$\nabla \left(\frac{\partial \langle c_\beta \rangle^\beta}{\partial t} \right) \sim \frac{1}{l_{\frac{\partial \langle c_\beta \rangle^\beta}{\partial t}}} \frac{\partial \langle c_\beta \rangle^\beta}{\partial t} \tag{3.83}$$

leads to

$$\frac{K_{eq}\,\mathbf{u}_\beta}{l_{\frac{\partial \langle c_\beta \rangle^\beta}{\partial t}}} << \left(1 + \frac{a_{\beta\sigma}\,K_{eq}}{\epsilon_\beta} \right) \tag{3.84}$$

where $l_{\frac{\partial \langle c_\beta \rangle^\beta}{\partial t}}$ is the length-scale associated with the spatial variation of $\frac{\partial \langle c_\beta \rangle^\beta}{\partial t}$. At this point, we need an estimate of $\mathbf{u}_\beta$, and one possibility is given by Eq. (3.76):

$$\mathbf{u}_\beta \sim \langle s_\beta \tilde{\mathbf{v}}_\beta \rangle^\beta \quad \implies \quad \mathbf{u}_\beta \sim s_\beta \mathbf{v}_\beta\,. \tag{3.85}$$

It would appear that the dominant source for s_β is given by Eq. (3.69). This assumption leads to

$$s_\beta \sim \frac{l_{s_\beta}}{\mathcal{D}_\beta} \tag{3.86}$$

which, in turn, leads to

$$\mathbf{u}_\beta \sim s_\beta\,\mathbf{v}_\beta \quad \implies \quad \mathbf{u}_\beta \sim \frac{\mathbf{v}_\beta\,l_{s_\beta}}{\mathcal{D}_\beta}\,. \tag{3.87}$$

Use of this result in Eq. (3.84) provides the restriction

$$\frac{K_{eq}\,\mathbf{v}_\beta}{\mathcal{D}_\beta} \frac{l_{s_\beta}}{l_{\frac{\partial \langle c_\beta \rangle^\beta}{\partial t}}} << \left(1 + \frac{a_{\beta\sigma}\,K_{eq}}{\epsilon_\beta} \right)\,. \tag{3.88}$$

82

In case this restriction is satisfied, the mixed derivative term in Eq. (3.81) can be discarded (as it is done for several applications), and the macroscopic species-transport equation acquires the form of the classical convection-dispersion equation:

$$\left(1 + \frac{a_{\beta\sigma} K_{eq}}{\epsilon_\beta}\right) \frac{\partial \langle c_\beta \rangle^\beta}{\partial t} + \langle \mathbf{v}_\beta \rangle^\beta \cdot \nabla \langle c_\beta \rangle^\beta = \mathbf{D}_\beta^* : \nabla\nabla \langle c_\beta \rangle^\beta. \tag{3.89}$$

3.3 Summary

We finally have the macroscopic equation for predicting arsenic concentrations in homogeneous, single-scale porous media. Using the rigorous volume averaging method, we have managed to derive for this purpose two versions of the final convection-dispersion equation, Eqs. (3.81) and (3.89). The important point is that the important macroscopic coefficients, the total dispersion tensor, $\mathbf{D}_\beta^*$, and the adsorption-induced vector, $\mathbf{u}_\beta$, can now be estimated using the closure formulation as described by the problems **I** and **II** listed through Eqs. (3.65) to (3.72). Since this closure formulation is to be solved in a unit-cell which is created from the microstructure of a porous medium, a mechanism is now in place for ensuring a proper *micro-macro* coupling.

It would be interesting to study differences in the predictions by the two macroscopic equations, Eqs. (3.81) and (3.89). Note that the former equation employs the two macroscopic coefficients, $\mathbf{D}_\beta^*$ and $\mathbf{u}_\beta$, and hence, one will need to solve both the closure problems, i.e., the problems **I** and **II** as listed by Eqs. (3.65) to (3.72). The former equation studies the effect of both passive solute transport and surface adsorption. However, the latter equation employs only $\mathbf{D}_\beta^*$ as the macroscopic coefficient, which accounts for the effect of passive solute transport, and hence, only closure problem **I**, as listed by Eqs. (3.65) to (3.68), needs to be solved in this case. The sequel of the current work, part II of this two-part chapter series, would numerically investigate both the macroscopic equations, Eqs. (3.81) and (3.89), and include validation studies on the effective transfer coefficients.

The arsenic filtration research recognizes that a critical design parameter of any filter is the 'hydraulic detention time' of the polluted water in the filter [14]. This means that the ratio of the adsorption rate to the macroscopic 'flow-through' rate, as captured by *Damköhler number*, is important. One can vary the macroscopic mass-transport rate by changing the pressure differential imposed over the filter, thereby altering the Darcy velocity and hence, changing the Damköhler number. This is also likely to impact *Péclet number*, which is the ratio of the advection and diffusion mass transports [131]. As suggested by previous studies [127, 132, 133], the effect of these two numbers on the crucial macroscopic coefficients, $\mathbf{D}_\beta^*$ and $\mathbf{u}_\beta$, needs to be studied.

Once we have determined the most effective macroscopic equation, whether Eq. (3.81) or Eq. (3.89), we will aim to use that equation to predict the distribution of the intrinsic phase-averaged concentration of arsenic, $\langle c_\beta \rangle^\beta$, within the porous regions of a commercial or lab-developed arsenic filter. Later we plan to predict the life of iron-based arsenic filters by comparing the predictions of the breakthrough times in long-term studies with the experimental data [13, 14]. Here, probably for the first time, the microstructure of the porous filters and the adsorption reactions going on at the microscopic scale will have a say in the macroscopic processes through the *micro-macro* coupling as captured by the closure formulation proposed in this chapter. We plan to use our experience in solving similar problems in the past [17, 134, 135].

CHAPTER 4

Modeling Transport and Adsorption of Tracer Species.
Part II: Numerical Validation

4.1 Literature Review

Arsenic (As) contamination poses a global threat because of its toxicity and carcinogenicity [136, 137]. It is a naturally occurring ubiquitous toxic metalloid which predominantly exists in two inorganic forms: pentavalent arsenate (As(V)) and trivalent arsenite (As(III)) [13, 138]. Different types of cancers and skin lesions may develop with chronic intake of arsenic-contaminated drinking waters, which are collectively referred to as arsenicosis [139–141]. Due to the widespread nature and seriousness of arsenic concentration-related health issues, several regulatory agencies, including the World Health Organization (WHO) and United States Environmental Protection Agency (US EPA), have revised the permissible contaminant limit to 10 µg/L for safe drinking water [142, 143]. High levels of arsenic concentration, as high as 3700 µg/L, have been recorded worldwide, especially in the countries of India, Bangladesh, and China [144–146]. Thus, a host of innovative arsenic removal technologies continue to be developed as this serious problem continues to draw the attention of researchers across the globe [13, 14, 137, 141, 144, 147–150].

Among various water treatment technologies available, the adsorption-based arsenic filtration technique involving porous media is most widely employed because it is cost-effective, highly efficient, and easy to operate [23, 24]. For this reason, the need to develop accurate mathematical models for providing deep insight into the adsorption process, which involves capturing of dissolved metal ions like As(III) and As(V) onto the *active* surface of the solid particles, is a research priority.

Contaminant transport in porous media is a well-researched problem across many scientific and engineering disciplines, including soil sciences, groundwater hydrology, chemical engineering, and environmental engineering. In general, this multiscale transport phenomenon can be studied by the use of either the pore-scale or the Darcy-scale models. Although significant strides have been made both in pore-scale modeling and computational capabilities [25, 26], the complex pore microstructures still pose a computational challenge in applying the pore-scale simulations in a real-world porous medium [27]. On the other hand, researchers have examined this mass transfer problem using the Darcy's law and presented several convection-diffusion equation-based transportation models. Numerous analytical solutions for such solute transport models are available [94–96, 99, 104, 151]; however, they have certain limitations associated with them. Pillai and Raizada [138] described these shortcomings which included, but not limited to, oversimplification of the dispersion tensor, treating the dispersion tensor as a constant, and adopting a constitutive relation for the tensor without accounting for the pore-scale effects.

Another route to investigating this problem is to use the *upscaling* approach, which leads to the development of macroscale models while considering a porous medium as an averaged continuum system. This approach has gained considerable attention from researchers on account of its ability to correlate the pore-scale physics to the macroscopic transport equations in terms of effective medium coefficients. The upscaled models can be derived through techniques of volume averaging [82,152,153], homogenization via multiple scale expansions [154–156], pore-network models [157,158], and other approaches reviewed in ref. [5].

In this chapter, we use the method of volume averaging to upscale the governing equations applicable at microscale to develop a macroscale model. This macroscale model invokes a micro-macro coupling between different length scales and reflects the macroscopic behaviour of the system, while addressing the aforementioned drawbacks

86

pertaining to the widely-used analytical solutions. The volume-averaged model involves effective transport coefficients, such as the effective diffusivity and dispersion coefficients, which can be estimated by solving the related closure problems in a representative elementary volume (REV) of porous media. For example, Wood et al. [124] predicted the effective reaction rate for a reactive chemical species using the volume-averaged model and made comparisons with similar results obtained from exercising direct numerical simulations at microscale. Valdés-Parada et al. [125, 159] presented a comprehensive numerical investigation on the upscaling of mass transport and reaction processes in porous media, where the effective diffusion tensor was found to be influenced by the reaction rate, pore microstructure, and flow rate. Quintard et al. [118] formulated the volume-averaged transport equations for solute adsorption in a chemically and mechanically heterogeneous porous medium when the condition of large-scale mechanical equilibrium is in effect. Later, Ahmadi et al. [119] formulated a two-equation model for solute transport with adsorption in dual-length scale heterogeneous porous media. In this case, the results obtained from numerical simulations carried out on an aquifer system were observed to be in good agreement with the proposed model.

In the same vein, Whitaker [123] demonstrated the process of executing the volume averaging method on the subject of solute transport with non-linear adsorption in porous media. Similarly, Plumb and Whitaker [122] used small-scale averaging to spatially smooth the microscale governing equations for describing the process of adsorption of chemical species in a heterogeneous porous medium based on linear adsorption isotherm. Their results suggested that reasonably good theoretical estimates for dispersion can be obtained if the convective transport regime under study continues to satisfy the steady state form of the closure problem. Recently, Zhang et al. [160] used the upscaling approach to model the adsorption-diffusion process in nanoporous materials.

In summation, the majority of the above-referenced works present different types of adsorption models, while considering linear and non-linear adsorption cases, and examine

87

the influence of chemical reaction over effective transfer coefficients in the upscaled models. However, to the best of our knowledge, a comprehensive examination of results obtained from an adsorption-based volume-averaged model and its validation with *direct numerical simulations* at the *pore-scale* has not been documented so far. Also, a crucial characteristic of an adsorbent is the inherent fluid-solid interfacial area which directly influences the adsorption capacity of the porous medium. It is important to assess the effect of variation in fluid-solid interfacial area on the effective parameters. Thus, the aim of this chapter is to corroborate the previous theoretical work by Pillai and Raizada [138] and address these issues on the basis of a numerical investigation.

The chapter is organized as follows. In Sections 4.2.1 and 4.2.2, we revisit the theoretical developments proposed by us (ref. [138]) on pore-scale modeling and the volume averaging method. In Section 4.2.3, we present the nondimensionalized forms of the closure problems, effective transfer coefficients, and both the volume-averaged and pore-scale models. In Section 4.3, we discuss the results which include validation of the effective transfer coefficients, affect of change in pore microstructure on the effective coefficients, and examine the performance of the volume-averaged models with respect to the pore-scale model. Finally, in Section 4.4, we offer concluding remarks.

4.2 Model for solute transport

4.2.1 Pore scale problem

In this study, we consider a *single-phase* flow occurring through a rigid and homogeneous porous medium, as presented in Fig. 4.1. The stationary and rigid solid particles constitute the σ-phase and the incompressible fluid saturating the pores represents the β-phase. We plan to investigate the mass transport of a dilute chemical species X caused due to convection and diffusion processes, with adsorption in effect at the fluid-solid interface. The pore-level convection-diffusion momentum balance equations, and the related bound-

ary conditions for solute transport and fluid flow at the microscale, are as follows:

$$\frac{\partial c_\beta}{\partial t} + \nabla \cdot (c_\beta \mathbf{v}_\beta) = \nabla \cdot (\mathcal{D}_\beta \nabla c_\beta) \tag{4.1}$$

$$\text{B.C.1}: \quad -\mathbf{n}_{\beta\sigma} \cdot \mathcal{D}_\beta \nabla c_\beta = K_{eq} \frac{\partial c_\beta}{\partial t}, \quad \text{at } A_{\beta\sigma} \tag{4.2}$$

$$0 = -\nabla P + \mu \nabla^2 \mathbf{v}_\beta \tag{4.3}$$

$$\nabla \cdot \mathbf{v}_\beta = 0 \tag{4.4}$$

$$\text{B.C.2}: \quad \mathbf{v}_\beta = 0, \quad \text{at } A_{\beta\sigma} \tag{4.5}$$

where in Eqs. (4.1) and (4.2), c_β is the point concentration of species X in the β-phase, $\mathbf{v}_\beta$ is the velocity of the β-phase, $\mathcal{D}_\beta$ is the molecular diffusivity of the β-phase, and K_{eq} is the equilibrium or distribution coefficient for the linear isotherm. The velocity field, $\mathbf{v}_\beta$, used in Eq. (4.1) is determined by the Stokes flow equation given in Eq. (4.3). In Eq. (4.3), P is the hydrodynamic fluid pressure in the β-phase and μ is the dynamic viscosity of fluid. The continuity equation for the β-phase and the no-slip boundary condition applicable at the $\beta - \sigma$ interface ($A_{\beta\sigma}$) are given in Eqs. (4.4) and (4.5), respectively. The tracer equation (Eq. (4.1)) is based on the contraints of *constant total molar concentration* and *dilute solution* in a binary system (see ref. [130] for more details).

4.2.2 Upscaling by the Volume Averaging Method

In this section, we will first present a condensed version of discussion on the upscaling procedures and the closure problem formulation. The complete details of the derivations are given in part I [138] of this two-part chapter series. Later, we will extend the previous developments and formulate the nondimensionalized forms of the pore-scale and volume-averaged models, and the associated closure formulation.
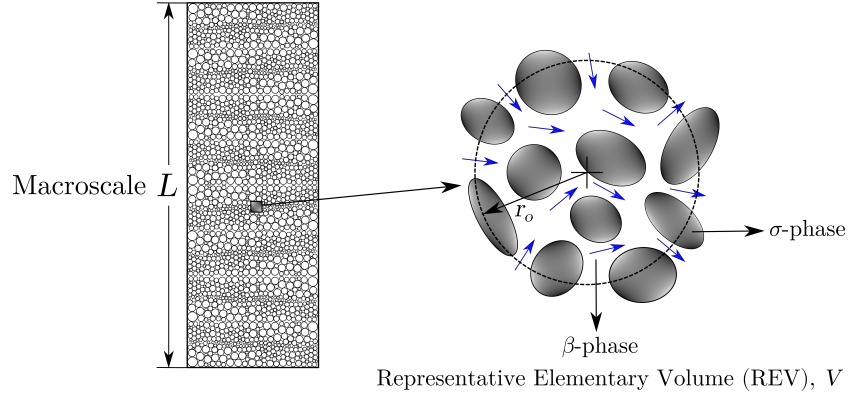
Figure 4.1: Sketch of a macroscopic region of length L and a spherical representative elementary volume (REV) of volume V with radius r_0. The REV is composed of solid (σ) and fluid (β) phases.

4.2.2.1 Upscaling procedures

In this section we will employ the method of volume averaging to upscale the aforementioned problem from the pore scale to the macroscopic one. Therefore, our objective would be to arrive at the macroscopic governing equations and boundary conditions for mass and momentum transport.

Here, the representative elementary volume (REV) for the porous medium domain, as shown in Fig. 4.1, is assumed to be in its traditional spherical form with characteristic size, r_o, and has been demonstrated to satisfy the following length-scale hierarchy [161]

$$l_\sigma \, , \, l_\beta \quad << \quad r_o \quad << \quad L \tag{4.6}$$

where the characteristic length scales, l_σ and l_β, are associated with the average particle size (solid phase) and pore diameter (fluid phase), respectively, and L corresponds to the characteristic length associated with the macroscale. This constraint (Eq. (4.6)) is considered to be crucial for the existence of the macroscale model [162]. Intuitively, one can think of this constraint as the tool for sieving out the unnecessary fluctuation details occurring at the small length-scale while still retaining the essential information related to the geometrical characteristics of the porous medium for use at the REV scale, r_o [163].

90

Next, we make use of the phase average ($\langle \phi_\beta \rangle$) and the intrinsic phase average ($\langle \phi_\beta \rangle^\beta$) operators for evaluating the average value of any variable ϕ_β within *the whole* of the REV or *only within the β-phase* of the REV, respectively. Their mathematical definitions are as follows

$$\langle \phi_\beta \rangle = \frac{1}{V} \int_{V_\beta} \phi_\beta \, dV \tag{4.7}$$

$$\langle \phi_\beta \rangle^\beta = \frac{1}{V_\beta} \int_{V_\beta} \phi_\beta \, dV \tag{4.8}$$

where V is volume of the REV and V_β is volume of the β-phase in the REV. These two averaging operators are related as

$$\langle \phi_\beta \rangle = \epsilon_\beta \langle \phi_\beta \rangle^\beta \tag{4.9}$$

where ϵ_β is the volume fraction of the β-phase within the REV, and in case of *single-phase flow* of the β-phase through the porous medium, it can be referred to as the porosity of the porous medium.

On applying the averaging operators across Eqs. (4.1) to (4.5), one comes across few terms in the resultant point differential equations which are evaluated by using the following spatial and temporal averaging theorems [78, 128, 164]

$$\langle \nabla c_\beta \rangle = \nabla \langle c_\beta \rangle + \frac{1}{V} \int_{A_{\beta\sigma}} c_\beta \, \mathbf{n}_{\beta\sigma} \, dA \tag{4.10}$$

$$\langle \frac{\partial c_\beta}{\partial t} \rangle = \frac{\partial \langle c_\beta \rangle}{\partial t} - \frac{1}{V} \int_{A_{\beta\sigma}} c_\beta \, \mathbf{w} \cdot \mathbf{n}_{\beta\sigma} \, dA \tag{4.11}$$

where $\mathbf{n}_{\beta\sigma}$ is the unit normal directed outwards from the β-phase towards the σ-phase, and $\mathbf{w}$ is the velocity of the $\beta - \sigma$ interface. Applying the necessary upscaling process (see ref. [138] for the details), we arrive at the following form of the volume-averaged

solute transport equation in terms of the preferred macroscopic variable, $\langle c_\beta \rangle^\beta$

$$\epsilon_\beta \frac{\partial \langle c_\beta \rangle^\beta}{\partial t} + \nabla \cdot \langle c_\beta \mathbf{v}_\beta \rangle$$
$$= \nabla \cdot \left[\mathcal{D}_\beta \left(\epsilon_\beta \nabla \langle c_\beta \rangle^\beta + \langle c_\beta \rangle^\beta \nabla \epsilon_\beta + \frac{1}{V} \int_{A_{\beta\sigma}} c_\beta \, \mathbf{n}_{\beta\sigma} \, dA \right) \right] - K_{eq} a_{\beta\sigma} \frac{\partial \langle c_\beta \rangle_{\beta\sigma}}{\partial t} \quad (4.12)$$

where $a_{\beta\sigma}$ is the interfacial area per unit volume, i.e., $a_{\beta\sigma} = A_{\beta\sigma}/V$. The term $\langle c_\beta \rangle_{\beta\sigma}$ represents the average concentration over the interfacial area and is defined as

$$\langle c_\beta \rangle_{\beta\sigma} = \frac{1}{A_{\beta\sigma}} \int_{A_{\beta\sigma}} c_\beta \, dA. \quad (4.13)$$

At this stage, we introduce the following length-scale decompositions proposed by Gray [116] to eliminate the pore scale variable c_β, simplify the dispersion term $\langle c_\beta \mathbf{v}_\beta \rangle$, and the transient term based on $\langle c_\beta \rangle_{\beta\sigma}$ in Eq. (4.12):

$$c_\beta = \langle c_\beta \rangle^\beta + \tilde{c}_\beta \quad \text{and} \quad \mathbf{v}_\beta = \langle \mathbf{v}_\beta \rangle^\beta + \tilde{\mathbf{v}}_\beta. \quad (4.14)$$

Here, $\tilde{c}_\beta$ and $\tilde{\mathbf{v}}_\beta$ represent the spatial deviations in the concentration and velocity variables, respectively. After substituting these pointwise defined functions (Eq. (4.14)) in Eq. (4.12) and implementing approximations for $\langle c_\beta \rangle^\beta$ and $\langle \tilde{c}_\beta \rangle_{\beta\sigma}$ as described in ref. [122], we eventually attain a simplified form of the volume-averaged solute transport equation [138]:

$$\underbrace{\epsilon_\beta \left(1 + \frac{K_{eq} a_{\beta\sigma}}{\epsilon_\beta} \right) \frac{\partial \langle c_\beta \rangle^\beta}{\partial t}}_{\text{accumulation and adsorption}} + \underbrace{\epsilon_\beta \langle \mathbf{v}_\beta \rangle^\beta \cdot \nabla \langle c_\beta \rangle^\beta}_{\text{convection}}$$
$$= \underbrace{\nabla \cdot \left[\epsilon_\beta \mathcal{D}_\beta \left(\nabla \langle c_\beta \rangle^\beta + \frac{1}{V_\beta} \int_{A_{\beta\sigma}} \mathbf{n}_{\beta\sigma} \tilde{c}_\beta \, dA \right) \right]}_{\text{diffusion and macrodiffusion}} - \underbrace{\nabla \cdot \left(\epsilon_\beta \langle \tilde{c}_\beta \tilde{\mathbf{v}}_\beta \rangle^\beta \right)}_{\text{hydrodynamic dispersion}}. \quad (4.15)$$

In this equation, one can clearly identify the distinct fluxes arising due to the different

transport mechanisms involved in the considered solute transport physics. On the left-hand side of Eq. (4.15), the first term accounts for the accumulation and adsorption of the chemical species, and the second term represents the convective transport of the fluid across the porous domain. Similarly, on the right-hand side of this equation, the first term corresponds to the sum of diffusive and macrodiffusive fluxes based on the changes in the concentration field, and the second term captures the hydrodynamic dispersion phenomenon.

4.2.2.2 *Closure problem formulation*

At this step, Eq. (4.15) is in a form equivalent to that of a convection-diffusion-source (CDS) equation applicable at the Darcy scale. However, keeping in mind that the macrodiffusion and hydrodynamic dispersion terms in this equation still depend on $\tilde{c}_\beta$ (sub-pore scale variable), we tacitly manipulate it into a more useful form by developing a local closure problem based on the method described by Crapiste et al. [165]. To accomplish this, first, a governing equation for $\tilde{c}_\beta$ is developed by using the spatial decompositions (Eq. (4.14)) in Eq. (4.1), and then the volume-averaged transport equation (Eq. (4.15)) is subtracted from the resulting pore-scale governing equation. The result is

$$\frac{\partial \tilde{c}_\beta}{\partial t} + \mathbf{v}_\beta \cdot \nabla \tilde{c}_\beta + \tilde{\mathbf{v}}_\beta \cdot \nabla \langle c_\beta \rangle^\beta - \epsilon_\beta^{-1} \nabla \cdot \langle \tilde{\mathbf{v}}_\beta \tilde{c}_\beta \rangle$$
$$= \nabla \cdot (\mathcal{D}_\beta \nabla \tilde{c}_\beta) - \epsilon_\beta^{-1} \nabla \cdot \left[\mathcal{D}_\beta \left(\frac{1}{V} \int_{A_{\beta\sigma}} \mathbf{n}_{\beta\sigma} \, \tilde{c}_\beta \, dA \right) \right] + \frac{K_{eq} \, a_{\beta\sigma}}{\epsilon_\beta} \frac{\partial \langle c_\beta \rangle^\beta}{\partial t} . \quad (4.16)$$

We identify two terms in Eq. (4.16) which may be construed as the *sources* for generating $\tilde{c}_\beta$ in the β-phase of the REV. These are designated as the adsorptive source term, $\frac{K_{eq} \, a_{\beta\sigma}}{\epsilon_\beta} \frac{\partial \langle c_\beta \rangle^\beta}{\partial t}$, and the convective source term, $\tilde{\mathbf{v}}_\beta \cdot \nabla \langle c_\beta \rangle^\beta$. Similarly, the boundary condition gets transformed as follows

$$\text{B.C.1}: \quad -\mathbf{n}_{\beta\sigma} \cdot \mathcal{D}_\beta \nabla \tilde{c}_\beta - K_{eq} \frac{\partial \tilde{c}_\beta}{\partial t} \quad = \quad -\mathbf{n}_{\beta\sigma} \cdot \mathcal{D}_\beta \nabla \langle c_\beta \rangle^\beta - K_{eq} \frac{\partial \langle c_\beta \rangle^\beta}{\partial t}, \quad \text{at } A_{\beta\sigma} \quad (4.17)$$

where the two terms on the right hand side act as the source terms.

Now, Eqs. (4.16) and (4.17) are further simplified based on order of magnitude analyses where the accumulation, macrodiffusion and hydrodynamic dispersion terms are dropped (see ref. [138] for the details), and the *governing equations at the closure level are considered to be always quasi-steady* when subjected to the following important time-scale constraint

$$\frac{\mathcal{D}_\beta \tau}{l_{\tilde{c}_\beta}{}^2} >> 1 \tag{4.18}$$

where τ is the characteristic time to note changes in $\tilde{c}_\beta$ within the REV. The final form of the local closure problem is summarized [138] as

$$\mathbf{v}_\beta \cdot \nabla \tilde{c}_\beta + \tilde{\mathbf{v}}_\beta \cdot \nabla \langle c_\beta \rangle^\beta = \mathcal{D}_\beta \nabla^2 \tilde{c}_\beta + \frac{K_{eq} a_{\beta\sigma}}{\epsilon_\beta} \frac{\partial \langle c_\beta \rangle^\beta}{\partial t} \tag{4.19a}$$

$$\text{B.C.1}: \quad -\mathbf{n}_{\beta\sigma} \cdot \mathcal{D}_\beta \nabla \tilde{c}_\beta = -\mathbf{n}_{\beta\sigma} \cdot \mathcal{D}_\beta \nabla \langle c_\beta \rangle^\beta - K_{eq} \frac{\partial \langle c_\beta \rangle^\beta}{\partial t}, \text{ at } A_{\beta\sigma} \tag{4.19b}$$

$$\text{Periodicity B.C.}: \quad \tilde{c}_\beta(\mathbf{r} + \mathbf{l}_i) = \tilde{c}_\beta(\mathbf{r}), \quad i = 1, 2, 3 \tag{4.19c}$$

$$\langle \tilde{c}_\beta \rangle^\beta = 0 \tag{4.19d}$$

where the standard periodicity condition (Eq. (4.19c)) is employed to obtain a local solution for $\tilde{c}_\beta$ in some spatially periodic representative region.

The proposed solution for the aforementioned closure problem is given by a linear combination of the source terms:

$$\tilde{c}_\beta = \mathbf{b}_\beta \cdot \nabla \langle c_\beta \rangle^\beta + s_\beta K_{eq} \frac{\partial \langle c_\beta \rangle^\beta}{\partial t} \tag{4.20}$$

where $\mathbf{b}_\beta$ (a vector field) and s_β (a scalar field) are the closure variables which are position-dependent functions. These closure variables are governed by the following boundary-value problems:

Problem I (for $\mathbf{b}_\beta$)

$$\mathbf{v}_\beta \cdot \nabla \mathbf{b}_\beta + \tilde{\mathbf{v}}_\beta = \mathcal{D}_\beta \nabla^2 \mathbf{b}_\beta \tag{4.21a}$$

$$\text{B.C.1}: \quad -\mathbf{n}_{\beta\sigma} \cdot \nabla \mathbf{b}_\beta = \mathbf{n}_{\beta\sigma}, \quad \text{at } A_{\beta\sigma} \tag{4.21b}$$

$$\text{Periodicity B.C.}: \quad \mathbf{b}_\beta(\mathbf{r} + \mathbf{l}_i) = \mathbf{b}_\beta(\mathbf{r}), \quad i = 1, 2, 3 \tag{4.21c}$$

$$\text{Constraint}: \quad \langle \mathbf{b}_\beta \rangle^\beta = 0 \tag{4.21d}$$

Problem II (for s_β)

$$\mathbf{v}_\beta \cdot \nabla s_\beta = \mathcal{D}_\beta \nabla^2 s_\beta + \frac{a_{\beta\sigma}}{\epsilon_\beta} \tag{4.22a}$$

$$\text{B.C.1}: \quad -\mathbf{n}_{\beta\sigma} \cdot \mathcal{D}_\beta \nabla s_\beta = 1, \quad \text{at } A_{\beta\sigma} \tag{4.22b}$$

$$\text{Periodicity B.C.}: \quad s_\beta(\mathbf{r} + \mathbf{l}_i) = s_\beta(\mathbf{r}), \quad i = 1, 2, 3 \tag{4.22c}$$

$$\text{Constraint}: \quad \langle s_\beta \rangle^\beta = 0. \tag{4.22d}$$

Finally, we are now in the position to resolve the distribution of $\langle c_\beta \rangle^\beta$ after substituting the solution for $\tilde{c}_\beta$ (Eq. (4.20)) in Eq. (4.15). This leads to the following closed form of the volume averaged mass transport equation [138]

$$\boxed{\left(1 + \frac{a_{\beta\sigma} K_{eq}}{\epsilon_\beta}\right) \frac{\partial \langle c_\beta \rangle^\beta}{\partial t} + \langle \mathbf{v}_\beta \rangle^\beta \cdot \nabla \langle c_\beta \rangle^\beta + K_{eq}\, \mathbf{u}_\beta \cdot \nabla \left(\frac{\partial \langle c_\beta \rangle^\beta}{\partial t}\right) = \mathbf{D}_\beta^* : \nabla\nabla \langle c_\beta \rangle^\beta}$$
$$\tag{4.23}$$

which contains the following effective transfer coefficients:

$$\mathbf{u}_\beta = \langle s_\beta \tilde{\mathbf{v}}_\beta \rangle^\beta - \frac{\mathcal{D}_\beta}{V_\beta} \int_{A_{\beta\sigma}} \mathbf{n}_{\beta\sigma}\, s_\beta\, dA \tag{4.24}$$

$$\mathbf{D}_\beta^* = \mathcal{D}_\beta \left[\mathbf{I} + \frac{1}{V_\beta} \int_{A_{\beta\sigma}} \mathbf{n}_{\beta\sigma}\, \mathbf{b}_\beta\, dA \right] - \langle \tilde{\mathbf{v}}_\beta \mathbf{b}_\beta \rangle^\beta \tag{4.25}$$

where $\mathbf{u}_\beta$ is the adsorption-induced vector and $\mathbf{D}_\beta^*$ is the total dispersion tensor. It is important to note at this point that Eq. (4.23) is only valid under certain assumptions which are: (a) the porosity, ϵ_β, is almost constant (see the constraint given in Eq. (41) in ref. [138]), (b) the total dispersion tensor, $\mathbf{D}_\beta^*$, remains unchanged, and (c) the equilibrium coefficient, K_{eq}, is a constant. In addition to these assumptions, if the restriction

$$\frac{K_{eq}\mathbf{v}_\beta}{\mathcal{D}_\beta} \frac{l_{s_\beta}}{l_{\frac{\partial \langle c_\beta \rangle^\beta}{\partial t}}} << \left(1 + \frac{a_{\beta\sigma} K_{eq}}{\epsilon_\beta} \right), \tag{4.26}$$

is satisfied as well, then the mixed derivative term in Eq. (4.23) can be dropped and the equation transforms into the standard convection-dispersion form of the macroscale conservation equation for species X:

$$\boxed{\left(1 + \frac{a_{\beta\sigma} K_{eq}}{\epsilon_\beta} \right) \frac{\partial \langle c_\beta \rangle^\beta}{\partial t} + \langle \mathbf{v}_\beta \rangle^\beta \cdot \nabla \langle c_\beta \rangle^\beta = \mathbf{D}_\beta^* : \nabla\nabla \langle c_\beta \rangle^\beta .} \tag{4.27}$$

Henceforth, we would refer to Eq. (4.23) as the *complete Volume Averaged Model* (VAMc), and to Eq. (4.27) as the *simplified Volume Averaged Model* (VAMs). In the next section, we nondimensionalize both of these models, present their modified versions, and further investigate their behaviour based on the order of magnitude estimates and Péclet number.
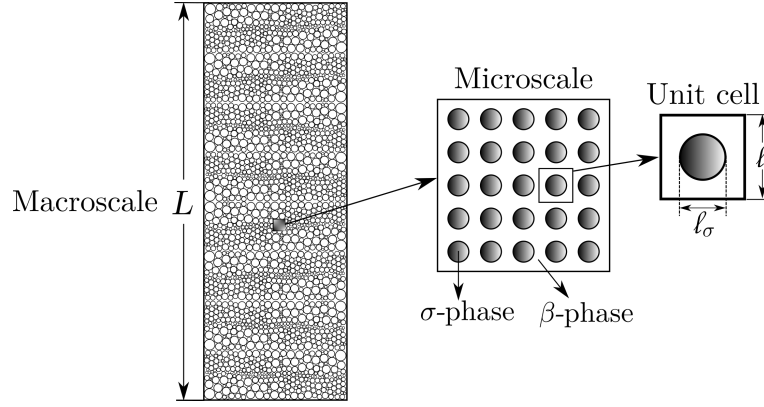
Figure 4.2: Schematic of a macroscopic region of length L assumed to be represented by a periodic arrangement of 2-D unit cells. The right-most sketch is the structure of a prototype unit cell for solving the closure problems.

4.2.3 Nondimensionalized forms

4.2.3.1 Closure problems and effective coefficients

Before proceeding with nondimensionalization of the volume-averaged models, it is important to work out the order of magnitude estimates of the closure variables and set the definition of Péclet number. The cell Péclet number [82] is defined as

$$Pe = \frac{v_c l}{\mathcal{D}_\beta} \tag{4.28}$$

where v_c is the characteristic velocity and l is the length of the unit-cell, as shown in Fig. 4.2. The macroscopic momentum equation with negligible inertia [166] and permeability $K = \mathbf{O}(l^2)$ is chosen as an estimate for the characteristic velocity v_c such that

$$v_c = \frac{l^2 \, ||\nabla \langle P \rangle^\beta||}{\mu} \tag{4.29}$$

where $||\nabla \langle P \rangle^\beta||$ is the average macroscopic pressure gradient applied across the porous domain. Here, we present a few important remarks on this dimensionless number. The Péclet number (Pe) represents the ratio of the advection rate to the dispersion rate, and therefore signifies the affect of flow rate on residence time of the solution in the system.

97

Hence, it is important to control Pe in order to optimize the *hydraulic detention time*, a critical design parameter, of a porous media-based adsorbent. If we consider the practical case of porous water filters, then the advantages of this optimization are twofold: first, it would provide enough time for the completion of chemisorption process such that any heavy metal ion, such as arsenic, can be captured with greater efficiency, and second, it would aid in the uniform consumption of adsorptive material in the filter.

Now, since both the macroscopic equations (4.23) and (4.27) directly involve K_{eq}, we would aim to work within a regulated range of K_{eq}. On the basis of experimental observations, K_{eq} (in SI unit: m) is found to satisfy the following constraint

$$K_{eq} \ll 1 \,. \tag{4.30}$$

For instance, Nikolaidis et al. [14] performed field experiments in their arsenic filtration study which resulted in the linear equilibrium partitioning coefficient, K_{d}, value of 4300 L/kg for arsenic adsorption onto the iron filings or surface binding. As shown in Appendix C, when K_{d} is normalized with the surface area of the adsorbent, it results in K_{eq} value of 1.14×10^{-4} m, which satisfies the above constraint.

It is a common practice in the volume averaging theory to use the order of magnitude estimates in order to simplify the transport equations by discarding the insignificant or *less influential* terms. This often leads to over estimation of the concerned variables, which, nonetheless, still provide accurate numerical results [82, 166]. The complete order of magnitude analyses for the closure variables $\mathbf{b}_{\beta}$ and s_{β} is described in Appendix C.2. Here, we present the resulting estimates of the closure variables and discuss the constraints associated with them.

For $\mathbf{b}_{\beta}$, we consider two different order of magnitude estimates as follows

$$\mathbf{b}_{\beta} = \mathbf{O}(l) \tag{4.31}$$

$$\mathbf{b}_\beta = \mathbf{O}(l\,Pe) \tag{4.32}$$

where the estimate in Eq. (4.31) is the result of $\mathbf{b}_\beta$'s dependence on the volume source $\tilde{\mathbf{v}}_\beta$, as can be noted in Eq. (4.21a), and the latter estimate (Eq. (4.32)) is obtained due to its dependence on the surface source $\mathbf{n}_{\beta\sigma}$ in Eq. (4.21b). The analysis also suggests that Eq. (4.32) is an overestimate of $\mathbf{b}_\beta$ since the maximum deviation in $\tilde{\mathbf{v}}_\beta$ is predicted to occur due to the no-slip condition at the fluid-solid interface, $A_{\beta\sigma}$. We deduce that the estimate given by Eq. (4.31) is suitable when $Pe \leq 1$, whereas Eq. (4.32) is appropriate for use when the constraint $Pe \gg 1$ is in place. In the following two different dimensionless closure problems for $\mathbf{b}_\beta$, $\nabla^*(= \nabla\,l)$ represents the dimensionless differential operator at the length-scale l, $\mathbf{v}_\beta^* \left(= \frac{\mathbf{v}_\beta}{v_c}\right)$ denotes the dimensionless point velocity of the β-phase, and $\mathbf{b}_\beta^* (= \frac{\mathbf{b}_\beta}{l}$ in problem **I a** and $\frac{\mathbf{b}_\beta}{l\,Pe}$ in problem **I b**) is the dimensionless vector closure variable.

Problem I a $(\mathbf{b}_\beta = \mathbf{O}(l))$

$$Pe\,\mathbf{v}_\beta^* \cdot \nabla^* \mathbf{b}_\beta^* + Pe\,\tilde{\mathbf{v}}_\beta^* = \nabla^{*2}\mathbf{b}_\beta^* \tag{4.33a}$$

$$\text{B.C.1}: \quad -\mathbf{n}_{\beta\sigma} \cdot \nabla^* \mathbf{b}_\beta^* = \mathbf{n}_{\beta\sigma}, \quad \text{at } A_{\beta\sigma} \tag{4.33b}$$

$$\text{Periodicity B.C.}: \quad \mathbf{b}_\beta^*(\mathbf{r} + \mathbf{l}_i) = \mathbf{b}_\beta^*(\mathbf{r}), \quad i = 1, 2, 3 \tag{4.33c}$$

$$\text{Constraint}: \quad \langle \mathbf{b}_\beta^* \rangle^\beta = 0 \tag{4.33d}$$

99

Problem I b ($\mathbf{b}_\beta = \mathbf{O}(l\,Pe)$)

$$Pe\,\mathbf{v}_\beta^* \cdot \nabla^* \mathbf{b}_\beta^* + \tilde{\mathbf{v}}_\beta^* = \nabla^{*2}\mathbf{b}_\beta^* \tag{4.34a}$$

$$\text{B.C.1}: \quad -\mathbf{n}_{\beta\sigma} \cdot \nabla^* \mathbf{b}_\beta^* = \frac{1}{Pe}\mathbf{n}_{\beta\sigma}, \quad \text{at } A_{\beta\sigma} \tag{4.34b}$$

$$\text{Periodicity B.C.}: \quad \mathbf{b}_\beta^*(\mathbf{r} + \mathbf{l}_i) = \mathbf{b}_\beta^*(\mathbf{r}), \quad i = 1, 2, 3 \tag{4.34c}$$

$$\text{Constraint}: \quad \langle \mathbf{b}_\beta^* \rangle^\beta = 0. \tag{4.34d}$$

For s_β, we follow the same strategy of analyzing the volume $\left(\frac{a_{\beta\sigma}}{\epsilon_\beta}\right)$ and surface (1) sources in Eqs. (4.22a) and (4.22b), respectively; however, in this case, we arrive at a unique estimate from both the equations which can be expressed as

$$s_\beta = \mathbf{O}\left(\frac{l}{\mathcal{D}_\beta}\right). \tag{4.35}$$

The order of magnitude presented in Eq. (4.35) is the result of a balancing act between the diffusive and adsorptive fluxes and is independent of Pe. Thus, this estimate is applicable across a wide range of Pe values. In addition to the variables defined for the dimensionless problems corresponding to $\mathbf{b}_\beta$, here we use $s_\beta^* \left(= \frac{s_\beta}{\frac{l}{\mathcal{D}_\beta}}\right)$ to denote the dimensionless scalar closure variable. Also, for nondimensionalization we assume that a reasonable estimate of the interfacial area per unit volume of the porous media $a_{\beta\sigma}$ is given by $\epsilon_\beta\,l^{-1}$. Thus, the dimensionless form of the closure problem associated with s_β is as follows:

Problem II a $\left(s_\beta = \mathbf{O}\left(\frac{l}{\mathcal{D}_\beta}\right)\right)$

$$Pe\, \mathbf{v}_\beta^* \cdot \nabla^* s_\beta^* \;=\; \nabla^{*2} s_\beta^* + 1 \tag{4.36a}$$

$$\text{B.C.1}: \quad -\mathbf{n}_{\beta\sigma} \cdot \nabla^* s_\beta^* \;=\; 1, \quad \text{at } A_{\beta\sigma} \tag{4.36b}$$

$$\text{Periodicity B.C.}: \quad s_\beta^*(\mathbf{r} + \mathbf{l}_i) \;=\; s_\beta^*(\mathbf{r}), \quad i = 1, 2, 3 \tag{4.36c}$$

$$\text{Constraint}: \quad \langle s_\beta^* \rangle^\beta \;=\; 0. \tag{4.36d}$$

After developing the nondimensionalized forms of the closure problems, we proceed further to formulate the dimensionless forms of the effective transfer coefficients, the adsorption-induced vector, $\mathbf{u}_\beta$, and the total dispersion tensor, $\mathbf{D}_\beta^*$. At this point, it must be noted that $\mathbf{u}_\beta$ is already a dimensionless vector; however, the two terms on the right-hand side (RHS) of Eq. (4.24) still need to be manipulated in order to obtain a pure dimensionless form of this parameter. Similar to the total dispersion tensor $\mathbf{D}_\beta^*$, this coefficient comprises of two parts, namely the adsorption-induced hydrodynamic dispersion vector and the adsorption-induced diffusivity vector. The former is the result of spatial fluctuations in the velocity field whereas the latter characterizes the surface adsorption process. After using the previously defined scaling variables and the result obtained in Eq. (4.35), $\mathbf{u}_\beta$ can be reformulated as

$$\mathbf{u}_\beta \;=\; Pe\, \langle s_\beta^* \tilde{\mathbf{v}}_\beta^* \rangle^\beta - \frac{1}{V_\beta^*} \int_{A_{\beta\sigma}^*} \mathbf{n}_{\beta\sigma}\, s_\beta^*\, dA^*, \tag{4.37}$$

which can be simplified further if we decide to estimate V_β^* according to a cubic unit-cell geometry, i.e. $V_\beta^* = \frac{V_\beta}{V\,(=l^3)}$, which is equivalent to the volume fraction or porosity (ϵ_β) of

the medium in case of a single-phase fluid flow. This allows us to rewrite $\mathbf{u}_\beta$ as

$$\mathbf{u}_\beta = Pe \, \langle s_\beta^* \tilde{\mathbf{v}}_\beta^* \rangle^\beta - \frac{1}{\epsilon_\beta} \int_{A_{\beta\sigma}^*} \mathbf{n}_{\beta\sigma} \, s_\beta^* \, dA^* . \tag{4.38}$$

When $Pe \gg 1$, the convective term in the adsorption-induced vector (first term on the RHS of Eq. (4.38)) gains much traction and contributes significantly to $\mathbf{u}_\beta$ in comparison to the other term. However, even at high Pe, one must weigh in the contribution of the second term on the RHS of Eq. (4.38) before safely neglecting it since it closely depends on the porosity and interfacial area which is usually very high for excellent porous media-based adsorbents.

Next, the dependence of the total dispersion tensor $\mathbf{D}_\beta^*$ on $\mathbf{b}_\beta$ indicates that we prepare two different dimensionless forms based on the constraints over Pe. These forms are as follows:

$$\mathbf{D}_\beta^{**} = \frac{\mathbf{D}_\beta^*}{\mathcal{D}_\beta} = \left[\mathbf{I} + \frac{1}{V_\beta^*} \int_{A_{\beta\sigma}^*} \mathbf{n}_{\beta\sigma} \, \mathbf{b}_\beta^* \, dA^* \right] - Pe \, \langle \tilde{\mathbf{v}}_\beta^* \mathbf{b}_\beta^* \rangle^\beta, \quad \text{if } \mathbf{b}_\beta = \mathbf{O}(l) \tag{4.39a}$$

$$\mathbf{D}_\beta^{**} = \frac{\mathbf{D}_\beta^*}{\mathcal{D}_\beta} = \left[\mathbf{I} + \frac{Pe}{V_\beta^*} \int_{A_{\beta\sigma}^*} \mathbf{n}_{\beta\sigma} \, \mathbf{b}_\beta^* \, dA^* \right] - Pe^2 \, \langle \tilde{\mathbf{v}}_\beta^* \mathbf{b}_\beta^* \rangle^\beta, \quad \text{if } \mathbf{b}_\beta = \mathbf{O}(l \, Pe) \tag{4.39b}$$

Similar to $\mathbf{u}_\beta$ transformation discussed in Eqs. (4.37) and (4.38), if V_β^* is assumed to be equal to ϵ_β, then the above given equations can be transformed to

$$\mathbf{D}_\beta^{**} = \frac{\mathbf{D}_\beta^*}{\mathcal{D}_\beta} = \left[\mathbf{I} + \frac{1}{\epsilon_\beta} \int_{A_{\beta\sigma}^*} \mathbf{n}_{\beta\sigma} \, \mathbf{b}_\beta^* \, dA^* \right] - Pe \, \langle \tilde{\mathbf{v}}_\beta^* \mathbf{b}_\beta^* \rangle^\beta, \quad \text{if } \mathbf{b}_\beta = \mathbf{O}(l) \tag{4.40a}$$

$$\mathbf{D}_\beta^{**} = \frac{\mathbf{D}_\beta^*}{\mathcal{D}_\beta} = \left[\mathbf{I} + \frac{Pe}{\epsilon_\beta} \int_{A_{\beta\sigma}^*} \mathbf{n}_{\beta\sigma} \, \mathbf{b}_\beta^* \, dA^* \right] - Pe^2 \, \langle \tilde{\mathbf{v}}_\beta^* \mathbf{b}_\beta^* \rangle^\beta, \quad \text{if } \mathbf{b}_\beta = \mathbf{O}(l \, Pe) \tag{4.40b}$$

As expected, Pe is found to be well-integrated with the hydrodynamic dispersion tensor term. When $Pe \leq 1$, i.e., diffusion dominates the transport processes, Eq. (4.40a) comes to the fore and $\mathbf{D}_\beta^*$ is mainly reduced to $\mathbf{D}_{eff}$, whereas when $Pe \gg 1$, Eq. (4.40b)

comes into play where Pe, through its second power, makes $\mathbf{D}_\beta$ the dominant term when compared to $\mathbf{D}_{eff}$. Note that $\mathbf{D}_\beta^*$ in Eq. (4.25) is called the total dispersion tensor which is the sum of $\mathbf{D}_{eff}$, the effective diffusivity tensor, and $\mathbf{D}_\beta$, the hydrodynamic dispersion tensor [138].

As explained in the previous chapter of this two-part chapter series, in order to compute the coefficients $\mathbf{u}_\beta$ and $\mathbf{D}_\beta^*$ for the upscaled models, first, the total mass and momentum transport equations applicable at the microscale are solved in an REV, e.g. in the unit-cell shown in Fig. 4.2, to determine the distribution of $\mathbf{v}_\beta$. Then the resulting velocity field is used to compute the solutions for the closure problems **I** and **II**, and finally, the fields of the closure variables, $\mathbf{b}_\beta$ and s_β, are employed in Eqs. (4.38) and (4.40a-4.40b) to evaluate the effective transfer coefficients.

4.2.3.2   VAMc and VAMs

After establishing the nondimensionalized forms of the closure variables and effective coefficients, we turn our attention towards formulating the dimensionless forms of VAMc and VAMs, Eqs (4.23) and (4.27) respectively. With different constraints pertaining to length-scale (Eq. (4.6)), time-scale (Eq. (4.18)) and physical parameters (Eq. (4.30)) already in place, we define the following dimensionless variables:

$$\nabla_L^* = \nabla_L\, L\,, \quad X^* = \frac{x}{L}\,, \quad T^* = \frac{t\,\mathcal{D}_\beta}{L^2}\,, \quad \mathbf{v}_\beta^* = \frac{\mathbf{v}_\beta}{v_c}\,, \text{ and } \quad c_\beta^* = \frac{c_\beta}{c_{in}}\,. \tag{4.41}$$

Here, ∇_L is the differential operator at the length-scale L, ∇_L^* is the dimensionless differential operator at the length-scale L, X^* is the x-direction coordinate nondimensionalized with the length-scale L, T^* is the dimensionless time variable corresponding to the length-scale L, c_{in} is the constant inlet concentration of species X, and c_β^* is the dimensionless point concentration of species X in the β-phase. In addition, we define the

Damköhler number [167] or the dimensionless adsorption isotherm A as follows:

$$A = \frac{K_{eq}\frac{l}{D_\beta}}{\frac{l^2}{\mathcal{D}_\beta}} \left(= \frac{K_{eq}}{l}\right) = \frac{\text{adsorption time scale}}{\text{diffusion time scale}} \,. \tag{4.42}$$

Here, based on the assumption $a_{\beta\sigma} \sim \epsilon_\beta\, l^{-1}$, the Damköhler number A can also be expressed as

$$A = \frac{a_{\beta\sigma}\, K_{eq}}{\epsilon_\beta} \tag{4.43}$$

where the parameters K_{eq}, $a_{\beta\sigma}$, and ϵ_β can be directly obtained from batch experiments and material characterization tests. Also, we assume that the macroscopic length L is equal to the length of a chain of N square unit cells (see Fig. 4.3) each of length l such that $L = N \times l$. Then, on nondimensionalizing Eq. (4.23) using the definitions given in Eq. (4.41) and performing algebraic manipulations, we arrive at the following dimensionless form of VAMc:

$$\frac{\partial \langle c_\beta^* \rangle^\beta}{\partial T^*} + \frac{Pe\,N}{1+A} \langle \mathbf{v}_\beta^* \rangle^\beta \cdot \nabla_L^* \langle c_\beta^* \rangle^\beta + \frac{A}{(1+A)\,N} \mathbf{u}_\beta \cdot \nabla_L^* \left(\frac{\partial \langle c_\beta^* \rangle^\beta}{\partial T^*} \right) = \frac{1}{1+A} \mathbf{D}_\beta^{**} : \nabla_L^* \nabla_L^* \langle c_\beta^* \rangle^\beta \,. \tag{4.44}$$

It is important to note that Pe is the Péclet number at microscale l, whereas $Pe\,N$ in Eq. (4.44) can be regarded as the Péclet number at macroscale L. Since the porous medium under consideration is assumed to be homogeneous, both the tensors, $\mathbf{D}_\beta^{**}$ and $\nabla_L^* \nabla_L^* \langle c_\beta^* \rangle^\beta$, on the RHS of Eq. (4.44) are symmetric in nature [168] and involve a double dot product between them. Furthermore, this transport equation can be expressed in its 1-D form along the x-direction as follows:

$$\frac{\partial \langle c_\beta^* \rangle^\beta}{\partial T^*} + \frac{Pe\,N}{1+A} \langle \mathbf{v}_\beta^* \rangle_x^\beta \frac{\partial \langle c_\beta^* \rangle^\beta}{\partial X^*} + \frac{A}{(1+A)\,N} \mathbf{u}_{\beta,x} \frac{\partial}{\partial X^*} \left(\frac{\partial \langle c_\beta^* \rangle^\beta}{\partial T^*} \right) = \frac{1}{1+A} \mathbf{D}_{\beta,xx}^{**} \frac{\partial^2 \langle c_\beta^* \rangle^\beta}{\partial X^{*2}}$$

$$\tag{4.45}$$
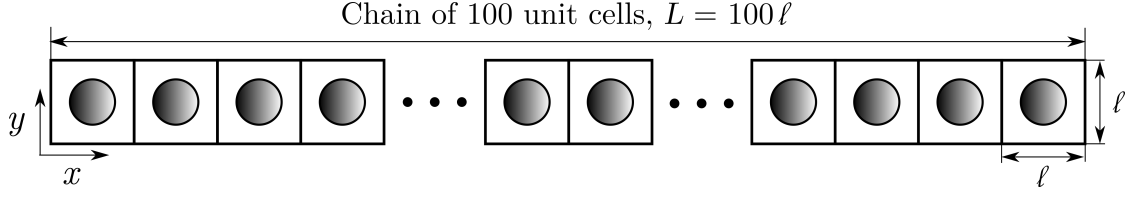
Figure 4.3: Illustration of the 2-D geometry of porous media used to conduct the direct numerical simulations (DNS). The length of the macroscopic region is assumed to be $L = 100\,l$.

where $\langle \mathbf{v}_\beta^* \rangle_x^\beta$ is the x-component of $\langle \mathbf{v}_\beta^* \rangle^\beta$, $\mathbf{u}_{\beta,x}$ is the x-component of the adsorption-induced vector $\mathbf{u}_\beta$, and $\mathbf{D}_{\beta,xx}^{**}$ is the xx-component of the $\mathbf{D}_\beta^{**}$ tensor.

The procedure to obtain the dimensionless form of VAMs is straightforward. For the macroscopic model considered in this study, the length-scale associated with the spatial variation of $\frac{\partial \langle c_\beta \rangle^\beta}{\partial t}$ is L and the spatial variation in s_β takes place at the microscopic length-scale l. Hence, while keeping in mind the dimensionless form of the restraint given in Eq. (4.26), which would be

$$\frac{A}{N}\,Pe\,\mathbf{v}_\beta^* \quad \ll \quad (1+A)\,, \tag{4.46}$$

the mixed derivative term may be dropped from Eq. (4.45) and the resulting 1-D nondimensional macroscale equation for VAMs would become

$$\frac{\partial \langle c_\beta^* \rangle^\beta}{\partial T^*} + \frac{Pe\,N}{1+A}\,\langle \mathbf{v}_\beta^* \rangle_x^\beta\,\frac{\partial \langle c_\beta^* \rangle^\beta}{\partial X^*} = \frac{1}{1+A}\,\mathbf{D}_{\beta,xx}^{**}\,\frac{\partial^2 \langle c_\beta^* \rangle^\beta}{\partial X^{*2}}\,. \tag{4.47}$$

4.2.3.3 Pore-scale model

The following subsection explains the steps involved in nondimensionalization of the pore-scale model and presents the time- and length-scale correlations between the upscaled and microscale models.

It is necessary to compare the performance of both the VAMc and VAMs models with the direct numerical simulation (DNS) results obtained at the pore-scale level. To achieve this purpose, we numerically investigate the boundary-value problem (Eqs. (4.1-4.5))

105

established at the microscale. But before proceeding, similar to the case of macroscale equations, we nondimensionalize this problem based on the following dimensionless variables:

$$\nabla^* = \nabla\, l\,,\ x^* = \frac{x}{l}\,,\ y^* = \frac{y}{l}\,,\ t^* = \frac{t\,\mathcal{D}_\beta}{l^2}\,,\ \mathbf{v}_\beta^* = \frac{\mathbf{v}_\beta}{v_c}\,,\ c_\beta^* = \frac{c_\beta}{c_{in}}\,,\ A = \frac{K_{eq}}{l}\,,\ \text{and}\ P^* = \frac{l\,P}{\mu\,v_c}\,.$$

$$(4.48)$$

Here, ∇^* is the dimensionless differential operator at the length-scale l, x^* is the x-direction coordinate nondimensionalized with the length-scale l, y^* is the y-direction coordinate nondimensionalized with the length-scale l, t^* is the dimensionless time variable corresponding to the length-scale l, and P^* denotes the dimensionless hydrodynamic fluid pressure in the β-phase. After substituting these variables in Eqs. (4.1-4.5), the dimensionless version of the problem can be summarized as follows:

$$\frac{\partial c_\beta^*}{\partial t^*} + Pe\left(\mathbf{v}_\beta^* \cdot \nabla^* c_\beta^*\right) = \nabla^{*2} c_\beta^* \tag{4.49}$$

$$\text{B.C.1}: \quad -\mathbf{n}_{\beta\sigma} \cdot \nabla^* c_\beta^* = A\,\frac{\partial c_\beta^*}{\partial t^*}, \quad \text{at } A_{\beta\sigma} \tag{4.50}$$

$$0 = -\nabla^* P^* + \nabla^{*2} \mathbf{v}_\beta^* \tag{4.51}$$

$$\nabla^* \cdot \mathbf{v}_\beta^* = 0 \tag{4.52}$$

$$\text{B.C.2}: \quad \mathbf{v}_\beta^* = 0, \quad \text{at } A_{\beta\sigma}\,. \tag{4.53}$$

Furthermore, the computational domain shown in Fig. 4.3 is subjected to the following

set of initial and (Dirichlet and Neumann type) boundary conditions:

$$c_\beta^* = 0, \quad \text{when} \quad t^* = 0 \tag{4.54a}$$

$$c_\beta^* = 1, \quad \text{at} \quad x^* = 0 \tag{4.54b}$$

$$\frac{\partial c_\beta^*}{\partial x^*} = 0, \quad \text{at} \quad x^* = \frac{L}{l} \tag{4.54c}$$

$$c_\beta^*(x^*, y^* = 0, t^*) = c_\beta^*(x^*, y^* = 1, t^*) \tag{4.54d}$$

$$P^* = P_{in}^*(= N), \quad \text{at} \quad x^* = 0 \tag{4.54e}$$

$$P^* = 0, \quad \text{at} \quad x^* = \frac{L}{l} \tag{4.54f}$$

$$\mathbf{v}_\beta^*(x^*, y^* = 0, t^*) = \mathbf{v}_\beta^*(x^*, y^* = 1, t^*) \tag{4.54g}$$

where Eqs. (4.54d) and (4.54g) represent the periodicity boundary conditions applied at the top and bottom of the DNS model, and the pressure differential applied across the domain due to the combination of Eqs. (4.54e) and (4.54f) has an effect such that each unit-cell in Fig. 4.3 is subjected to a unitary pressure gradient.

Now, since different length and time scales have been used to nondimensionalize the volume-averaged and the pore-scale models (see Eqs. (4.41) and (4.48), respectively), we need to develop suitable length- and time-scale correlations in order to draw comparisons between the two systems. For this, if a point x in the laboratory frame of reference is to be located in both the coordinate systems, then based on Eqs. (4.41) and (4.48) we deduce the following length-scale relation:

$$\nabla_L^* = N \nabla^*. \tag{4.55}$$

Similarly, in order to study the results at any given time t in the laboratory frame of reference, the following dimensionless time-scale relation should be used:

$$T^* = t^* / N^2. \tag{4.56}$$

107

An alternate nondimensionalization approach based on the characteristic time for convection at the pore-scale has been put forward in Appendix D. In this case, we define the Damköhler number Da (Eq. (D.4)) which is the ratio of adsorption to convection time scales, and accordingly propose nondimensionalized forms of the pore-scale and volume-averaged models.

4.3 Results and discussion

In this section, we focus on the following points: (a) validation of the effective transfer coefficients, (b) discuss the effects of change in porosity and number of particles on the effective transfer coefficients, and (c) examine the performance of the volume-averaged models with respect to the pore-scale model and confirm their accuracy with an analytical solution available in the literature [151].

4.3.1 Validation of the Effective Transfer Coefficients

The effective transfer coefficients defined in Eqs. (4.38) and (4.40a-4.40b) rely on the microstructural information available at the pore-scale, volume geometry, and the Péclet number. At this point, we also define the particle Péclet number Pe_p based on the particle size [82], and would present the numerical results with reference to it. Its definition and relation with the cell Péclet number is as follows

$$Pe_p = \frac{||\langle \mathbf{v}_\beta \rangle^\beta|| \, l_\sigma}{\mathcal{D}_\beta} \cdot \frac{\epsilon_\beta}{1 - \epsilon_\beta} = Pe \cdot \frac{\epsilon_\beta}{1 - \epsilon_\beta} \cdot \frac{l_\sigma}{l} \cdot ||\langle \mathbf{v}_\beta^* \rangle^\beta|| \tag{4.57}$$

where $||\langle \mathbf{v}_\beta^* \rangle^\beta||$ is the magnitude of the dimensionless intrinsic phase average velocity. Now, in order to track the evolution of the effective transfer coefficients, numerical simulations were performed across two parameters: (a) Pe_p ranging from 10^{-1} to 10^3 and (b) porosity (ϵ_β) values of 0.4 and 0.8, in the 2-D unit-cell geometry shown in Fig. 4.2. Here, it is important to mention that the numerical solutions reported in this work were obtained by using the finite element solver COMSOL Multiphysics after conducting a
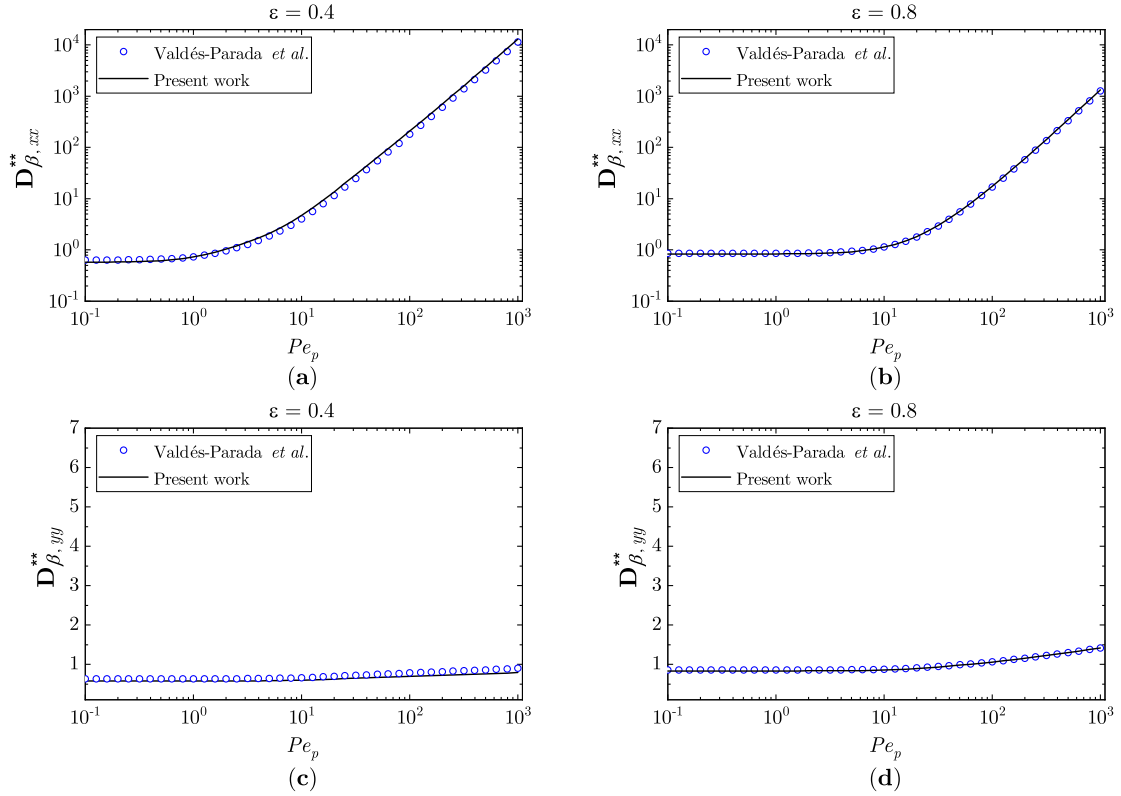
Figure 4.4: Comparison of the longitudinal (cases (a) and (b)) and lateral (cases (c) and (d)) components of the dispersion tensor $\mathbf{D}_\beta^{**}$ with the literature results [166]. The porosity values are $\epsilon_\beta = 0.4$ for the cases (a) and (c), and $\epsilon_\beta = 0.8$ for the cases (b) and (d).

mesh independence study via grid refinement [63].

Valdés Parada et al. [166] have presented upscaled models for a chemical species undergoing convective transport while sustaining a first-order heterogeneous reaction. Under prescribed length-scale contraints and after reasonable simplifications, they have shown that the closure problem for $\mathbf{b}_\beta$ (Eqs. (41) in ref. [166]) can be used to determine the total dispersion coefficient, and that this resembles to the closure problem developed by Whitaker (Eqs. (3.3-35) in ref. [82]) for passive dispersion in porous media. In the same vein, the closure problem formulated for $\mathbf{b}_\beta$ (Eqs. (4.40a-4.40b)) in the present work only includes the effect of passive solute transport in porous media, and hence, expectedly, resembles Eqs. (41) in ref. [166]. Thus, we use the data from Fig. 4 in ref. [166] to validate the dimensionless forms of the total dispersion tensor coefficients along the x- and y-directions.

109

Fig. 4.4 shows the evolution of the longitudinal and transverse components of the total dispersion tensor $\mathbf{D}_\beta^{**}$ across a range of Pe_p over two different porosity (ϵ_β) values of 0.4 and 0.8. The results from the present work, denoted by the solid black lines in Fig. 4.4, are found to be in excellent agreement with that reported in the literature [166], shown by the hollow blue circle markers. As expected, the $\mathbf{D}_{\beta,xx}^{**}$ or the longitudinal component of the $\mathbf{D}_\beta^{**}$ tensor increases with the increase in Pe_p. This observation can be directly explained from Eqs. (4.40a-4.40b) where increase in velocity (that leads to an increase in Pe_p) increases this dispersion coefficient. When $Pe \leq 1$, Eq. (4.40a) is used to find the dispersion coefficient values, whereas Eq. (4.40b) is employed when Pe exceeds 1. On the other hand, the application of unidirectional pressure drop across the regular geometry shown in Fig. 4.3, leads to reduced lateral motion of the fluid around the solid particles, which translates into a diminished $\mathbf{D}_{\beta,yy}^{**}$, the transverse component of the $\mathbf{D}_\beta^{**}$ tensor, as seen in Figs. 4.4c and 4.4d.

It can also be observed that the dispersion coefficient $\mathbf{D}_{\beta,xx}^{**}$ shows higher values for the lower porosity model ($\epsilon_\beta = 0.4$) when compared to the higher porosity case ($\epsilon_\beta = 0.8$) for $Pe_p > 1$. The effect of decrease in porosity and the consequent increase in the surface area of the particle provides the explanation for this observation according to Eqs. (4.40a-4.40b).

(a)   (b)   (c)   (d)
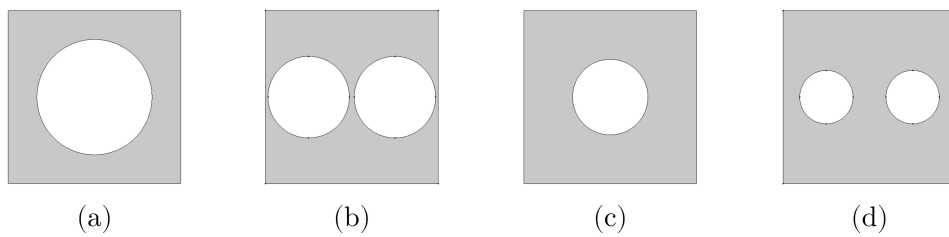
Figure 4.5: 2-D unit cells used for estimation of the effective transfer coefficents, (a) $\epsilon_\beta = 0.65$ and n = 1, (b) $\epsilon_\beta = 0.65$ and n = 2, (c) $\epsilon_\beta = 0.85$ and n = 1, and (d) $\epsilon_\beta = 0.85$ and n = 2. The descending order of the fluid-solid interfacial area in these unit cells is as follows: case (b), case (a), case (d), and case (c).

110
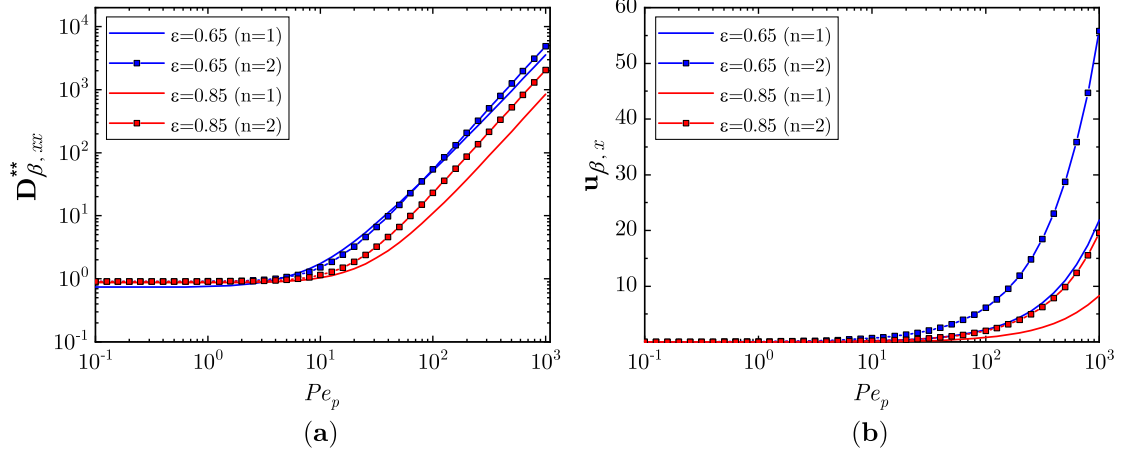
Figure 4.6: Variation in the (a) longitudinal dispersion coefficient $\mathbf{D}^{**}_{\beta,xx}$ with Pe_p and (b) x-component of the adsorption-induced vector $\mathbf{u}_\beta$ ($\mathbf{u}_{\beta,x}$) with Pe_p. Both of these coefficients are studied across two parameters: number of particles (n = 1, 2) and porosity ($\epsilon_\beta = 0.65, 0.85$), as shown in Fig. 4.5.

4.3.2 Effective Medium Coefficients

This section focuses on analyzing the effects of change in porosity (ϵ_β) and number of particles (n) on the effective medium coefficients. The hypothesis behind this exercise is to test if the increase in surface area of the particles leads to increased effective transfer coefficients. This test would help in accurately modeling strong adsorption, and hence, in general, underline the significance of high interfacial area inherent in porous adsorbents. To test this hypothesis, the 2-D unit-cell geometry shown in Fig. 4.2 is subjected to variations in both the aforementioned parameters. In principle, we consider the following four cases: (a) $\epsilon_\beta = 0.65$ and n = 1, (b) $\epsilon_\beta = 0.65$ and n = 2, (c) $\epsilon_\beta = 0.85$ and n = 1, and (d) $\epsilon_\beta = 0.85$ and n = 2. As sketched in Fig. 4.5, in cases when n = 2, the particles are equidistantly placed in a horizontal arrangement inside the unit-cell.

The results in Fig. 4.6a replicate the classical correspondence between the dimensionless longitudinal dispersion coefficient and Pe_p, as has been widely reported in the literature [82,166,169,170]. It can also be observed from this figure that $\mathbf{D}^{**}_{\beta,xx}$'s dependence on Pe_p until $\mathbf{O}(10)$, more or less follows a similar trend for all the considered cases. However,

111

as Pe_p further increases[1], the trendlines become more distinguishable and eventually the longitudinal dispersion coefficient corresponding to case (b) manifests itself as the maximum in comparison to the remaining cases. The trendlines near Pe_p of $\mathbf{O}(1000)$ line up according to the descending order of the interfacial surface area values corresponding to the different cases under study. This value is the highest for case (b), followed by case (a), and it is the lowest for case (c).

Now, let the attention be directed towards the adsorption-induced vector $\mathbf{u}_\beta$. This coefficient is attached to the mixed derivative term in Eq. (4.45), which is mostly discarded in many applications in order to convert the macroscopic species-transport equation into the conventional convection-dispersion form. To the best of our knowledge, no experimental data or theories are available for the validation of this effective medium coefficient. As pointed out by Quintard and Whitaker [126], this non-traditional term may not necessarily be negligible and it frequently appears in the non-local equilibrium models [153, 171–173]. Hence, it is important to quantify the contribution of this non-classical term to the convective transport and accordingly make an informed decision to either retain or neglect it. Fig. 4.6b depicts the evolution of this coefficient with respect to Pe_p. It can be noted that this term has an almost negligible value until Pe_p of $\mathbf{O}(10)$ for all the considered cases here, which leads to the vanishing of its product with the mixed derivative term in Eq. (4.45). However, an interesting development awaits as the convective transport regime gains prominence with Pe_p increasing to $\mathbf{O}(1000)$. When Pe_p exceeds $\mathbf{O}(10)$, $\mathbf{u}_{\beta,x}$'s value increases rapidly for all the cases under study and the trendlines become discernible. Eventually, similar to the pattern observed for $\mathbf{D}_{\beta,xx}^{**}$, the $\mathbf{u}_{\beta,x}$ trendline corresponding to the case of $\epsilon_\beta = 0.65$ and n = 2 shows the steepest ascent and displays the maximum value in comparison to the remaining cases. The order of the trendlines also remains the same as found in the analysis of $\mathbf{D}_{\beta,xx}^{**}$.

---

[1]It is important to note that for the Darcy's law to remain valid, the particle Reynolds number (Re_p) must be smaller than 1 [153]. In our numerical study, the largest Re_p was computed using the largest velocity (corresponding to $Pe_p = 1000$) and particle diameter. This led to the Re_p value of 0.15, which well satisfies the aforementioned creeping-flow constraint.

112

Again, the higher interfacial area can be deemed as the major cause behind obtaining a higher effective medium coefficient value and this can be interpreted from Eq. (4.38). In the present work, although a relatively simple periodic unit-cell, as shown in Fig. 4.2, and its modifications have been used for illustrative purposes, unit cells corresponding to real-world adsorbents are bound to be highly intricate, and thus would have much greater interfacial areas associated with them. Thus, during modeling of such cases, it is imperative to carefully gauge the contribution of non-classical terms like $\mathbf{u}_\beta$. As we shall see below, such terms may affect the accuracy of predictions of the volume-averaged models.

4.3.3 Comparison of Microscale and Macroscale simulations

In this section we compare the predictions of the volume-averaged models with the predictions of the proposed micromodels based on the DNS. To achieve this purpose, a computational domain consisting of 100 in-line unit cells each of side-length l was designed, as shown in Fig. 4.3. This model resembles a porous medium made of regularly arranged parallel cylinders with the fluid flow directed perpendicular to the cylinder axis. The nondimensionalized boundary-value problem at the pore-scale given by Eqs. (4.49-4.54g) was solved in this chosen model, whereas the upscaled equations, Eqs. (4.45) and (4.47), were solved in one-dimension along a line of unit length. These two different space-time coordinate systems were then synchronized by using the correlations given in Eqs. (4.55) and (4.56).

The simulation codes developed for the upscaled models are validated by comparing the results with that of Valdés Parada et al. [166] under specific circumstances. It can be inferred from ref. [166] that in the absence of heterogeneous first-order chemical reaction, i.e. the passive dispersion case ($\phi^2 = 0$), the macroscale model given by Eq. (48) transforms into the standard convection-dispersion transport equation. Analogously, in the present work, the volume-averaged models given by Eqs. (4.45) and (4.47), reduce to

113
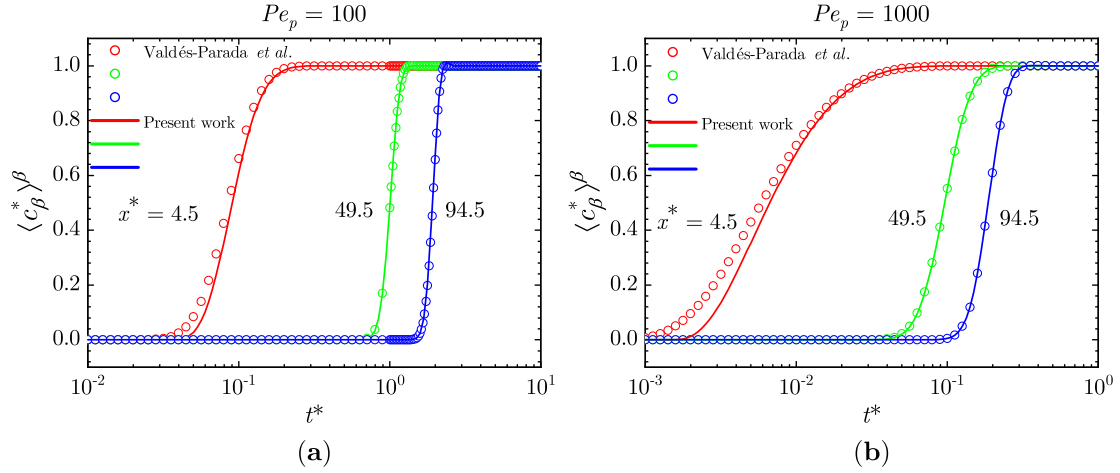
Figure 4.7: Comparison of the evolution of the intrinsic phase average concentration between the present work and the literature [166]. Assuming $\epsilon_\beta = 0.8$, case (a) corresponds to $A = 0$, $Pe_p = 100$, and case (b) corresponds to $A = 0$, $Pe_p = 1000$.

that same convection-dispersion form under the no adsorption ($A = 0$) condition. Thus, the data from Figs. 8a and 9a in ref. [166] corresponding to the no-slip boundary condition is used for validation of the code developed for the present work. It must be noted that the average concentration was tested at the following positions: (a) near the entrance, at $x^* = 4.5$, (b) near the middle, at $x^* = 49.5$, and (c) near the exit, at $x^* = 94.5$, of the computational domain shown in Fig. 4.3. As reported in Fig. 4.7, the concentration predictions made using the current code for both Pe_p of $\mathbf{O}(100)$ and $\mathbf{O}(1000)$ are in excellent agreement with the literature [166], which helps reinforce its accuracy. The minor divergence observed near the onset of the concentration profiles at position $x^* = 4.5$ maybe due to the use of compound order of magnitude estimate proposed for $\mathbf{b}_\beta$ in ref. [166]. On proceeding farther from the inlet and with increasing time, the difference between the intrinsic phase average concentration predictions occurring due to the above-mentioned estimate and our estimates in Eqs. (4.31) and (4.32) becomes barely noticeable.

Now, in order to better circumstantiate the usefulness of the upscaled models, the Damköhler number A and the convection-based Pe_p are estimated from experiments carried out for arsenic removal through the use of adsorbents. As shown in Appendix C.1, a reasonable estimate of A is 0.1 for iron filing filters in ref. [14]. Similar order of

114

magnitude estimates for artificial adsorbents can be procured from other experimental results [13, 174]. On the other hand, $Pe_p \sim 100$ based on the filtration velocity used in the arsenic adsorption experiment of [14]. In summary, assuming $\epsilon_\beta = 0.8$, the following four cases are investigated: (a) $Pe_p = 10$ and $A = 0$, (b) $Pe_p = 10$ and $A = 0.1$, (c) $Pe_p = 100$ and $A = 0$, and (d) $Pe_p = 100$ and $A = 0.1$. Here, the cases (a) and (c) correspond to the non-adsorptive or passive conditions, whereas the cases (b) and (d) conform to active adsorption on the surface of the solid particles shown in Fig. 4.3. Also, the three testing positions in the computational domain remain the same, as previously defined.

It is of some interest to introduce an analytical solution to solve the upscaled model given in Eq. (4.47). Kumar et al. [151] have proposed a one-dimensional solution for an advection-diffusion type equation with temporally dependent dispersion coefficient; however, it can easily be used to study the transport occurring in an initally solute-free finite domain with constant dispersion coefficient as well. The solution is expressed as:

$$C(x,t) \quad = \quad C_0\, A(x,t) \tag{4.58}$$

where C represents the solute concentration at position x along the longitudinal direction at time t, C_0 is a reference concentration, and

$$
\begin{aligned}
A(x,t) = {} & \frac{1}{2}\,\mathrm{erfc}\left(\frac{x - u_0 t}{2\sqrt{D_0 t}}\right) + \frac{1}{2}\exp\left(\frac{u_0 x}{D_0}\right)\mathrm{erfc}\left(\frac{x + u_0 t}{2\sqrt{D_0 t}}\right) \\
& + \frac{1}{2}\left[2 + \frac{u_0(2x_0 - x)}{D_0} + \frac{u_0^2 t}{D_0}\right] \times \exp\left(\frac{u_0 x_0}{D_0}\right)\mathrm{erfc}\left(\frac{(2x_0 - x) + u_0 t}{2\sqrt{D_0 t}}\right) \\
& - \sqrt{\frac{u_0^2 t}{\pi D_0}}\,\exp\left[\frac{u_0 x_0}{D_0} - \frac{(2x_0 - x + u_0 t)^2}{4 D_0 t}\right].
\end{aligned}
$$

Here, u_0 represents the uniform flow velocity, D_0 is the constant dispersion coefficient, and x_0 indicates the length of the finite domain. This method will provide another route to test the accuracy of VAMs vis-à-vis the most accurate, DNS results. The analytical
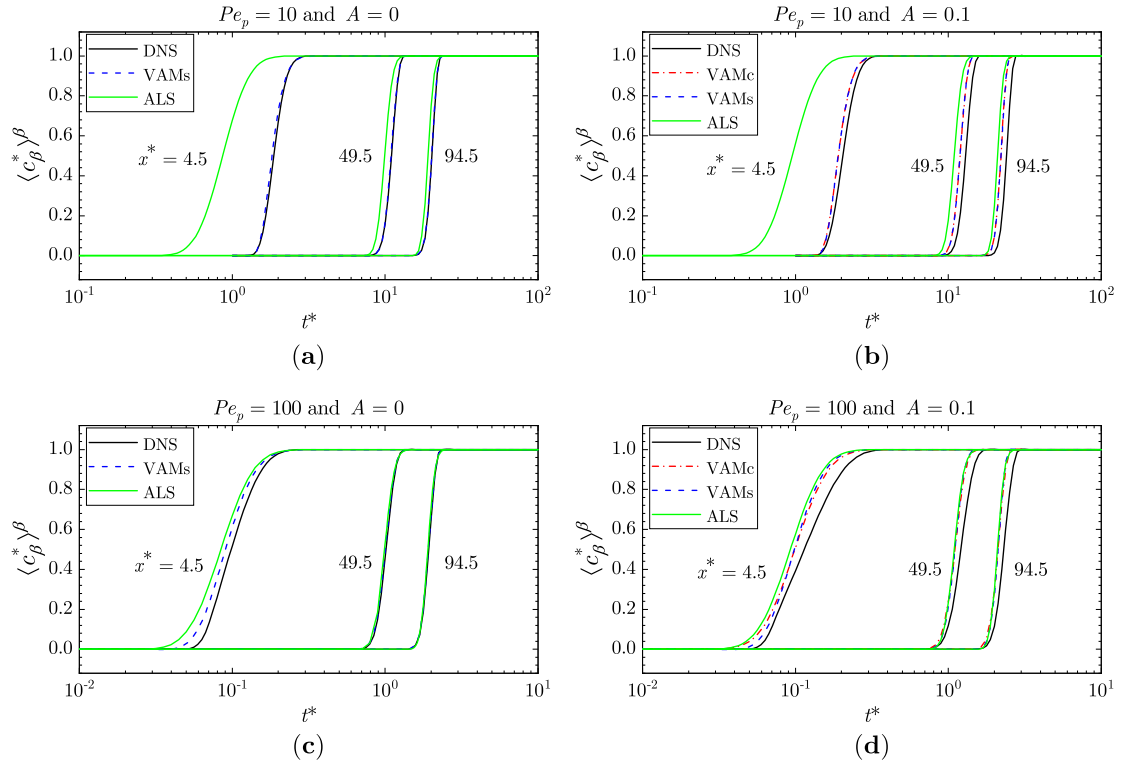
Figure 4.8: Comparison of the intrinsic phase average concentration profiles at three different locations in the macroscale model illustrated in Fig. 4.3. The predictions are made using the direct numerical simulations (DNS), volume-averaged methods (VAMc and VAMs), and analytical solution (ALS) approaches. Assuming $\epsilon_\beta = 0.8$, case (a) uses $A = 0$, $Pe_p = 10$, case (b) uses $A = 0.1$, $Pe_p = 10$, case (c) uses $A = 0$, $Pe_p = 100$, and case (d) uses $A = 0.1$, $Pe_p = 100$.

solution results are denoted by ALS in Fig. 4.8.

Fig. 4.8 compares the dimensionless intrinsic phase average concentration predictions made through the DNS, VAM, and ALS approaches. The numerical results corresponding to the DNS and VAM methods show remarkable agreement with each other. As shown in Figs. 4.8a and 4.8c, under passive condition ($A = 0$), the macroscale simulation curves simply correspond to VAMs and are observed to almost completely overlap with the DNS curves at all the three testing positions. However, in the higher Pe_p case shown in Fig. 4.8c, a marginal difference between these curves can be noticed near the inlet of the chosen domain ($x^* = 4.5$). Next, the simulation results pertaining to the adsorption condition ($A = 0.1$) for the DNS and VAM approaches are observed to be quite close, as illustrated

in Figs. 4.8b and 4.8d. This demonstrates that the procedure followed to evaluate the effective transfer coefficients is reliable and accurate with reasonable assumptions. In these cases, the difference between the VAMc and VAMs curves is hardly discernible which suggests that VAMc offers marginal improvement and can be replaced by VAMs, or in other words, VAMs is a reasonably good upscaled model for the adsorptive transport conditions considered here. This inference can be mathematically justified through the use of constraint given in Eq. (4.46), where the ratio $\frac{A}{N} Pe \, \mathbf{v}_\beta^* (= 0.05)$ is significantly smaller than $(1 + A)(= 1.10)$.

The ALS results in Fig. 4.8 help to further reinforce the accuracy of VAMs predictions. Although the concentration profiles near the inlet of the domain ($x^* = 4.5$) in cases (a) and (b) show a large variability with respect to the DNS and VAM outcomes at low Pe_p; nonetheless, this considerable difference rapidly diminishes as one progresses towards the center ($x^* = 49.5$) and exit ($x^* = 94.5$) regions. It is important to note that the predictions made by VAMs are consistent with (or mostly better than) ALS for all the cases under study.

The effect of increase in Pe_p (i.e., convection-favoured regime) on adsorption is of prime importance. Pe_p can directly be associated with the flow rate or filtration velocity through an adsorbing porous medium. As expected, when Pe_p increases from 10 to 100, the mass of liquid passing through the filter in unit time increases, and hence the adsorption process accelerates, and therefore it takes lesser time for the 'consumption' of entire adsorptive material. The result is clearly evident in Fig. 4.8 where t^* reduces from $\mathbf{O}(10)$ to $\mathbf{O}(1)$ as Pe_p increases from 10 to 100. This directly impacts the *hydraulic detention time* of the contaminant in the filter, which is an important design parameter for a filtration system [14, 160]. Hence, higher flow rates would reduce the residence time of the solution in the system which may affect the adsorption efficiency of the filter, as noted in experimental studies [175].

4.4 Conclusions

In this chapter, we continued to build on the theoretical developments put forward by Pillai and Raizada [138] and carried out a numerical investigation on the problem of mass transport and adsorption in homogeneous porous media using the volume averaging method. A brief overview of the volume averaging process is presented to upscale the boundary-value problem applicable at the microscale to macroscopic effective models. Two variants of the macroscale models are introduced: (a) *complete Volume Averaged Model* (VAMc) and (b) *simplified Volume Averaged Model* (VAMs), which involve two effective transfer coefficients, namely, the total dispersion tensor, $\mathbf{D}_\beta^*$, and the adsorption-induced vector, $\mathbf{u}_\beta$. VAMc is the original upscaled model, whereas VAMs is obtained after discarding the mixed derivative term in VAMc.

The nondimensionalized forms of the closure problems, effective coefficients, microscale, and macroscale models were formulated based on the order of magnitude estimates of closure variables $\mathbf{b}_\beta$ and s_β. The total dispersion tensor coefficient $\mathbf{D}_\beta^*$ was validated and found to be in excellent agreement with the literature [166]. The influence of the solid phase microstructure and flow rate on the effective medium coefficients was thoroughly assessed through variations across two parameters, namely, the porosity and the number of particles inside the unit-cell. The results illustrated an increase in the coefficients' values corresponding to decrease in porosity and increase in the number of particles. The resulting increase in the interfacial area inside the unit-cell was assessed to be the cause behind this outcome.

The predictive capabilities of the upscaled models were assessed by comparing the dynamics of average concentration profiles with direct numerical simulations at the pore-scale. Four investigative scenarios were considered by varying the Damköhler number (or the dimensionless adsorption isotherm) A and Pe_p values. The upscaled models, when upholding the spatial and temporal constraints, displayed excellent results on

118

comparison with the DNS. This emphasizes the effectiveness of the micro-macro coupling encapsulated in the closure formulation proposed by Pillai and Raizada [138]. VAMc was observed to offer marginal improvement over VAMs for the investigative conditions assumed in this study and this was substantiated on the basis of constraint given in Eq. (4.46). In addition, the macroscale simulations outperformed the analytical solution results for most of the cases under study, which further highlights the accuracy of the volume averaging method. For future work, the upscaled models would be employed in arsenic filtration and related research to perform experimental validation and optimize the hydraulic detention time of an adsorptive filter. Such applications could certainly corroborate their practicality and affirm the presented conclusions.

Overall, it may be concluded that the volume-averaged models present a pragmatic alternative for comprehensively studying the adsorption phenomenon in porous arsenic filters in lieu of employing direct numerical simulations at the pore-scale level, which entails a daunting challenge to surmount given the complex pore microstructures of real-world adsorbents. However, the selection of a suitable REV incorporating appropriate topographic features of the porous media, determination of the Damköhler number A, and adherence to the spatio-temporal constraints, remain the keys to accurate modeling of the adsorption of arsenic in porous filters using the upscaled models.

CHAPTER 5

Modeling Transport and Adsorption of Tracer Species. Part III: A Comparison with Experiments

5.1 Introduction

Anthropogenic activities are dramatically changing nutrient levels in many rivers, wetlands, estuaries, and coastal waters around the world [176–178]. As a direct consequence, typical eutrophication symptoms in the form of expanding hypoxic and anoxic zones, and spreading of toxic harmful algal blooms (HABs) are becoming increasingly common in waters worldwide [179]. Vollenweider in his famous critical review [180] of the eutrophication problem concluded that increases in the nutrients phosphorus and nitrogen from sources outside the lake were probably the causes of eutrophication. Other researchers [181,182] affirmed this fact and suggest phosphorus (P) losses to surface waters to be one of the major causes of eutrophication. Schindler et al. [182] reviewed several long-term phosphorus control studies at ecosystem scales and presented evidence that reduction of phosphorus is effective in controlling eutrophication (see Table 1 in [182]).

In an effort to tackle this problem, an adsorbent prepared by functionalized zeolite for removal of phosphate was developed by Silva research group at the University of Wisconsin-Milwaukee Our primary aim in this chapter is to test the volume-averaged models proposed in Chapters 3 and 4 by solving the problem of contaminant transport in this zeolite based porous adsorbent. Here, the concentration predictions from the upscaled models would be compared with the experimental results.

Overall, the chapter is organized as follows. In Section 5.2, we describe the materials and methods related to the column-flow experiment. Here, we also discuss the process of
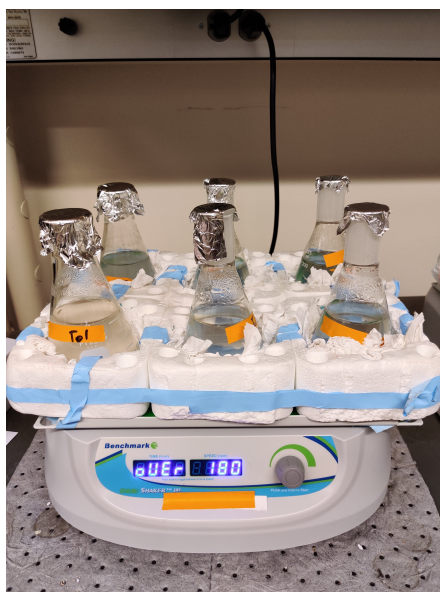
Figure 5.1: The experimental setup of the batch adsorption tests.

capturing the micro-tomographic images of the zeolite material. In Section 5.3, we provide details related to the model development, which includes REV preparation and numerical simulations. In Section 5.4, we discuss the results obtained from the column experiments and numerical simulations. Finally, in Section 5.5, we offer concluding remarks.

5.2 Materials and methods

5.2.1 Preparation of synthetic solution

All chemicals used in this study were of analytical grade. The experiment was conducted with synthetically prepared P spiked solution. To prepare the influent solution, phosphorus stock solution (Fisher Chemical) of concentration 100.0 mg/L was used to spike deionized (DI) water to the desired concentration of 50.0 mg/L. The experimental value of this concentration varied from 47.8 mg/L to 51.3 mg/L with an average value of 49.9 mg/L, and a standard deviation of 1.9 mg/L. The pH of the synthetic solution was measured using the Oakton PCTSTestr 50 and noted to be 5.8 ± 0.2.

5.2.2 Batch adsorption experiments

Batch adsorption tests were performed to evaluate the adsorption capacity of the filtration material used in this study. For this, zeolite adsorbent samples weighing 1.0 gram were placed in flasks filled with 200 mL of P spiked solution. High phosphorus concentration of 50.0 mg/L was used to allow for full evaluation of the performance and capacity of the zeolite material. As shown in Fig. 5.1, the flasks were fastened to a ORBI Benchmark Shaker plate and shaken at 180 rpm for 24 h at room temperature ($25 \pm 2°C$). After 24 h of contact time, an aliquot of 2.5 mL was sampled from each flask for residual phosphorus in the solution.

The quantity of adsorbed phosphorus, q_e (mg/g) was calculated by

$$q_e = \frac{(C_i - C_e)\,V_l}{m} \tag{5.1}$$

where C_i (mg/L) and C_e (mg/L) are the initial and equilibrium phosphorus concentration, respectively, V_l (L) is the volume of phosphorus solution, and m (g) is the mass of adsorbent sample. The adsorption capacity q_e of the adsorbent for P was determined to be 5.0 ± 0.5 mg/g and the equilibrium concentration of the sorbent C_e was assessed to be 25.5 ± 2.3 mg/L.
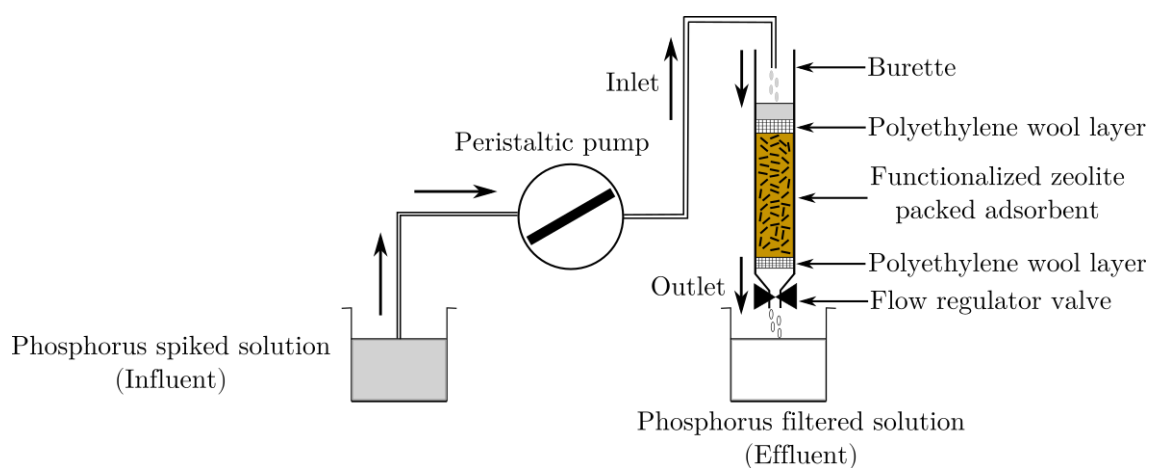
Figure 5.2: A schematic diagram of the column-flow experiment.

Figure 5.3: The experimental setup of the column-flow experiment.

5.2.3 Column-flow experiments

The performance of the zeolite absorbent was examined and quantified by conducting bench-scale column-flow experiments. A schematic diagram of the experimental setup is illustrated in Fig. 5.2. The column filter was prepared by packing 8.0 g of functionalized zeolite granules in a glass column with an inner diameter of 12 mm and a length of 275 mm. After filling up the adsorbent in the burette, the height of material was 85.3 mm. A peristaltic pump (VWR, USA), as shown in Fig. 5.3, was used to inject P spiked solution from the influent container to the functionalized zeolite particles while maintaining a flow rate close to 0.02 mL/s throughout the experiment.

Sampling for the influent samples when treated with the adsorbent was conducted at the intervals of 15 minutes over a period of 480 minutes. Effluent samples were collected directly at the bottom end of the burette. All sample collection bottles were sterile, clear polystyrene tubes. 2.5 mL aliquot of each sample was analyzed for soluble reactive phosphorus (SRP) by using the UV-VIS Spectrophotometer (Shimadzu UV-2600). For detection of P, the spectrophotometer measured the absorption of light by the sample at 885 nm wavelength.

Three trials of this experiment were conducted in order to account for the randomness
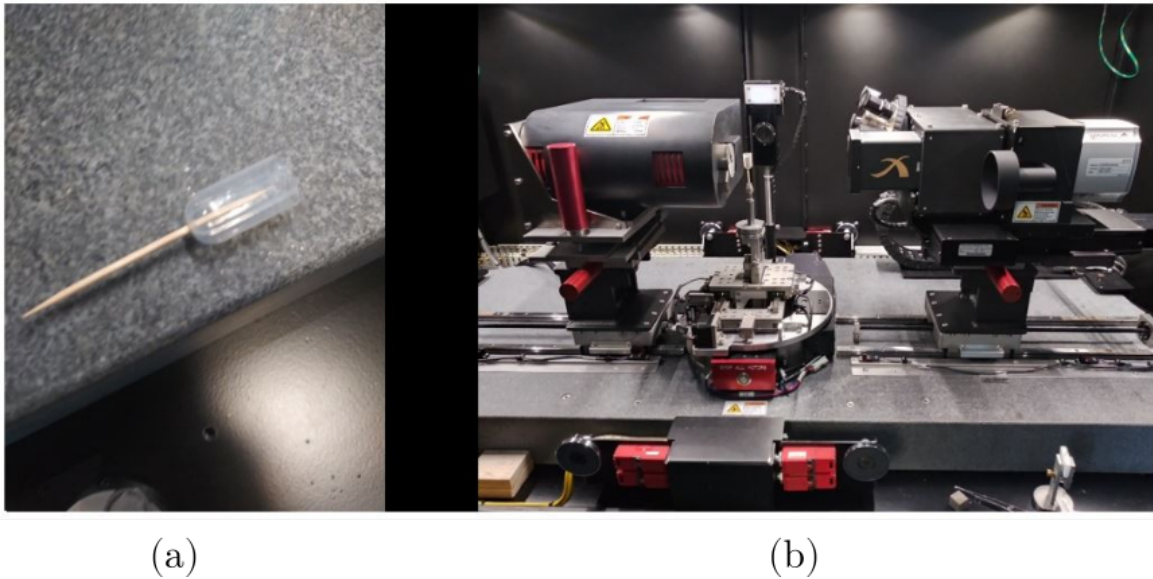
Figure 5.4: (a) An artificially prepared sample holder to store functionalized zeolite, and (b) micro-CT scanner with the sample holder secured to the mounting fixture.

and scatter in the experimental data, and to obtain more accurate average P concentration values of the effluent.

5.2.4   Micro-CT scans of functionalized zeolite

The micro-tomographic images of the zeolite adsorbent were captured using a micro-CT scanner at the Nanofabrication and Microscopy Facility, Wauwatosa, WI USA. For this, first, a sample holder for zeolite was made from the bulb of a transfer pipette and a tooth pick, as shown in Fig. 5.4a. Next, the zeolite material was filled into this apparatus, which was then secured to the ZEISS sample mount, as shown in Fig. 5.4b.

The adsorbent sample was examined using a $0.4\times$ objective with 80 kV voltage and 10W power. No filter was selected for the source and the exposure time was set to 3s accumulations with binning set to 2. The micro-CT scans in the three cartesian planes, as illustrated in Fig. 5.5, were taken at a single location in the sample. The sampling location in the sample holder and the instrument details related to the detector and source position of the scanner are given in Table 5.1.

Table 5.1: Sampling location, detector and source position information for the micro-CT scanner.

Parameter	Value
X-coordinate of the sample	368.85 µm
Y-coordinate of the sample	13.1 µm
Z-coordinate of the sample	-1.1 µm
Detector	179.475 mm
Source	-50.003 mm
Cone angle	8.66°
Fan angle	8.66°

5.3 Model development

Phosphorus is transported in the filtration material by a combination of advection and dispersion transport processes. The modeling of phosphorus adsorption by the functionalized zeolite adsorbent will help to estimate the equilibrium coefficient and investigate the design factors. Also, the linear adsorption isotherm which is based on the local mass equilibrium at the fluid-solid interface is used to model the phosphorus capturing mechanism. As discussed in Chapters 3 and 4, the proposed volume-averaged models take into account the above-mentioned physics and are able to predict the macroscopic concentration of the tracer species in the macroscopic region. A synopsis of the action steps taken to implement the upscaled models is given below:

1. The momentum equations applicable at the microscale are solved in a chosen REV

(a)   (b)   (c)
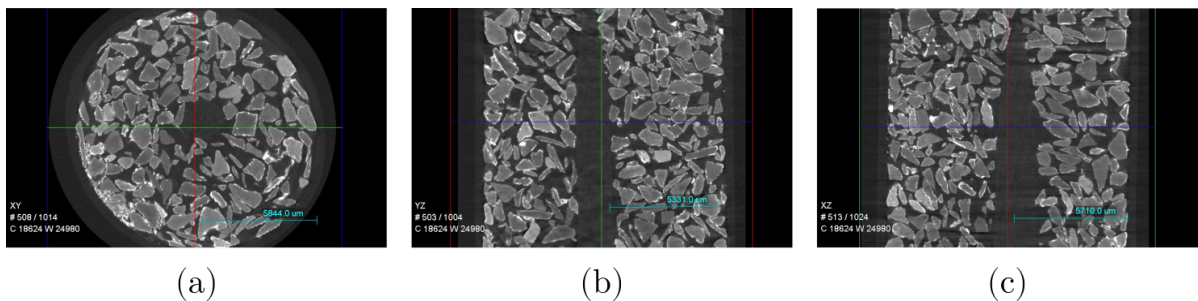
Figure 5.5: The micro-tomographic images of functionalized zeolite material in the (a) X-Y plane, (b) Y-Z plane, and (c) X-Z plane.

with suitable boundary conditions.

2. The resulting velocity field is used to compute the solutions for the closure problems **I** and **II**, as given in Eqs. (4.21a-4.21d) and (4.22a-4.22d) respectively.

3. The resulting closure fields for $\mathbf{b}_\beta$ and s_β are used to evaluate the effective transfer coefficients $\mathbf{u}_\beta$ and $\mathbf{D}_\beta^*$, as given in Eqs. (4.24) and (4.25) respectively.

4. The upscaled equations (4.23) and (4.27) incorporating the effective coefficients are solved in one-dimensional space (a line) to predict the intrinsic average concentration in the macroscale model.

It is important to note that the equilibrium coefficient K_{eq}, as used in Eqs. (4.23) and (4.27), is required for modeling the upscaled models. The general procedure to find K_{eq} is detailed in Appendix C.1.1. Based on the experimental results obtained from the batch adsorption tests, the K_d value for functionalized zeolite at the concentration of 50 mg/L was found to be 0.20 L/g. The average surface area of the adsorbent was noted to be 3.28 m^2/g in a previous study. Hence, the K_{eq} value for this adsorbent was found by calculating the ratio of K_d and the surface area of the adsorbent. It was evaluated to be 5.99×10^{-5} m. The volumetric porosity ϵ_β of the zeolite material was calculated as follows. DI water was gradually poured out from a 100 mL filled graduated cylinder into another 100 mL graduated cylinder completely filled with zeolite material. The bottom of the meniscus line for water in the zeolite filled cylinder should be exactly level with the top graduation corresponding to the 100 mL mark. At this point, we measure the amount of water that was poured into the zeolite filled column to get the volumetric porosity. The porosity was determined to be 49.6%. Apart from K_{eq} and ϵ_β, the models also require the molecular diffusivity $\mathcal{D}_\beta$ of soluble reactive phophorus (SRP). Hence, $\mathcal{D}_\beta$ of SRP was adopted from Table 1 of an experimental study in ref. [183] and taken to be 6.20×10^{-6} cm^2/s.

126
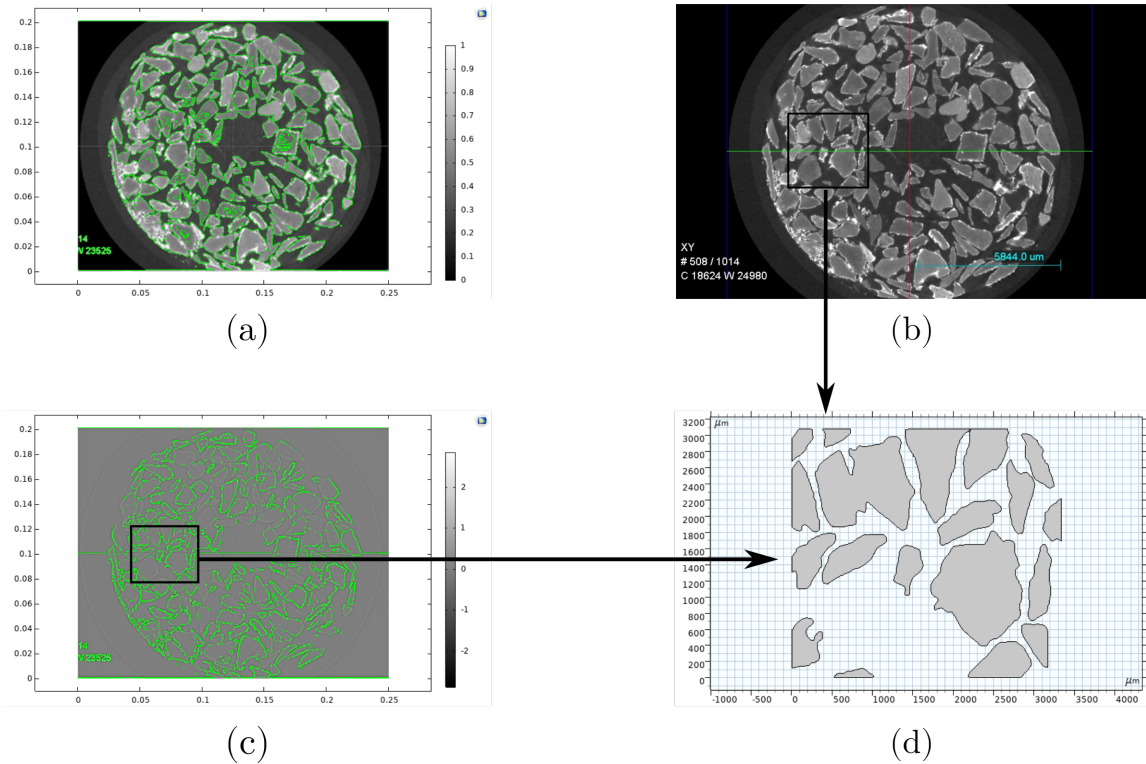
Figure 5.6: The image processing on the 2-D micrograph was done in COMSOL Multiphysics. Here, (a) shows adjustment of the contour thresholding level (marked by green lines) where the particles were separated from the dark grey background, (b) is the 2-D micrograph with chosen REV (shown by black rectangular box), (c) shows the sharpening of edges to separate the solid and void regions in the micrograph (marked by green color closed curves) based on pre-set assumptions, and (d) the solid particle matrix inside the chosen REV.

5.3.1 REV preparation

The use of porous unit cells which have a simple structure can still provide reasonable qualitative information regarding the transport phenomena that occurs at the pore-scale. However, it is better to compare the experimental findings with the predictions obtained from unit cells which are closely representative of the real-world porous samples. Therefore, in this study, we take into account unit cells whose structure is generated from the micro-CT scans of functionalized zeolite. In Fig. 5.5, we see the micro-tomographic images of zeolite material in the (a) X-Y, (b) Y-Z, and (c) X-Z planes at micron-scale resolution. The characteristic size of the adsorbent particles was 0.72 mm, as provided by the manufacturer.

127

The grayscale image corresponding to the X-Y plane, as shown in Fig. 5.5a, was converted into a binary image by performing a sequence of image processing steps in order to make it suitable for computational purposes. Here, the irregular-shaped particles in light grey color with brighter (shinier) boundaries were considered to be closer to the top of the micrograph, whereas the particles with darker (less shinier) boundaries were assumed to situated deeper into the plane or farther away from the surface of the micrograph. Thus, if a cross flow were to occur, the particles with brighter boundaries would act as the obstacles, whereas the particles with relatively dark edges would be treated as pores. Also, the dark grey color background behind the particles was invariably treated as the void space or pore space. Based on this hypothesis, the image processing capabilities of the CFD software COMSOL Multiphysics were used to alter the thresholding levels of the 2-D micrograph in order to distinguish between the solid and pore regions. The geometrical regions in the micrograph where these treatments were done are illustrated in Fig. 5.6.

The application of the volume averaging method involves setting up of a unit-cell which captures sufficient microstructural details of the actual porous medium and can be used for solving the closure problems. For this, a rectangular cross-section, as shown in Fig. 5.6b, was extracted from the micrograph and chosen to be the representative elementary volume (REV) for computational analysis. The size of the REV should follow the constraint given in Eq. (3.1). Hence, in accordance with the aforementioned constraint, we chose the length of the unit-cell l to be almost 5 times the characteristic size of the particles l_σ. It is important to remark here that finding a suitable REV size for a porous medium still remains a subject that is actively researched in the volume averaging community [184, 185]. Next, a 2-D model containing only the void region (i.e., an REV which is devoid of solid particles) was constructed by performing a sequence of boolean operations in COMSOL. Finally, the areal porosity of the developed unit-cell was estimated by finding the ratio of pore area (void region) (see Fig. 5.7a) to the total
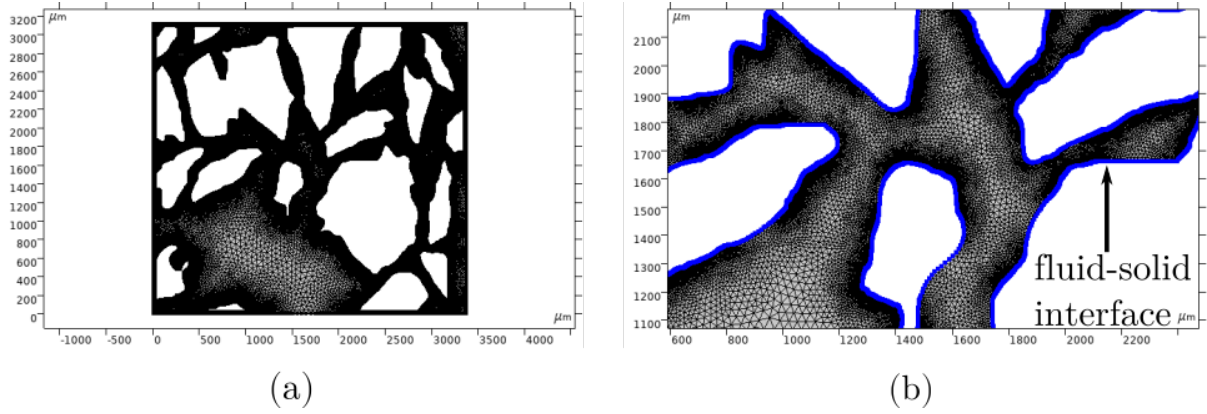
Figure 5.7: (a) The mesh model corresponding to the pore region of the REV, and (b) an example of fine mesh discretization near the fluid-solid interface (the blue color curves denote mesh elements of very small size along the fluid-solid interface).

area of the chosen REV. This important parameter was calculated to be 52.2%, which is close to the volumetric porosity of 49.6% for the functionalized zeolite material.

5.3.2 Numerical simulations

The computational domain for fluid flow, i.e. the pore region in the REV, was discretized using COMSOL's mesh generator with triangular elements. In order to evaluate the influence of mesh refinement on the solutions, the model was discretized with three meshes, namely: (a) coarse, (b) normal, and (c) fine, while the relative tolerance was tightly set to 10^{-3}. The fine mesh with 377893 triangular, 16615 edge, and 3093 vertex elements was assessed to give accurately converged results, and was thus employed for the numerical simulations. Also, the meshes were especially finely discretized near the fluid-solid interface, as shown in Fig. 5.7b, to accurately resolve the sharp gradients occurring in both the velocity and closure variable fields.

As previously mentioned, the momentum equations applicable at the microscale are solved in the REV with suitable boundary conditions. Here, the Stokes-flow equation (Eq. (4.3)) is solved in the pore region of the REV and the no-slip boundary condition (Eq. (4.5)) is applied at the $\beta - \sigma$ interface, i.e. the fluid-solid interface. It must be noted

Table 5.2: Parameters used in the numerical simulations of the closure problems and calculation of dimensionless numbers.

Parameter	Notation	Value
Density	ρ_β	1000 kg/m^3
Viscosity	μ_β	0.001 Pa·s
Pore velocity	$\|\langle \mathbf{v}_\beta \rangle^\beta \|$	3.06×10^{-4} m/s
Molecular diffusion coefficient of SRP	$\mathcal{D}_\beta$	6.2×10^{-6} cm^2/s
Specific interfacial area of the REV	$a_{\beta\sigma}$	3928 m^{-1}
Linear equilibrium partitioning coefficient	K_{d}	0.20 L/g
Equilibrium coefficient for the linear isotherm	K_{eq}	5.99×10^{-5} m
Dimensionless adsorption isotherm	$A\,(= K_{eq}\, a_{\beta\sigma}/\epsilon_\beta)$	0.45
Porosity (from REV in the micrograph)	ϵ_β	52.2%
Particle length	l_σ	0.72 mm
Hydraulic diameter	$l_\beta\,(= 4\epsilon_\beta/a_{\beta\sigma})$	0.53 mm
Unit-cell (REV)	l	3.25 mm
Macroscale model	L	85.3 mm

that the particle Reynolds number Re_p [153], which is given by

$$Re_p = \frac{\rho_\beta \,\|\langle \mathbf{v}_\beta \rangle^\beta\|\, l_\sigma}{\mu_\beta} \cdot \frac{\epsilon_\beta}{1 - \epsilon_\beta}\,, \tag{5.2}$$

must be smaller than 1 for the creeping-flow motion. Under the given experimental conditions (see Table 5.2), Re_p was found to be 0.24, which satisfies the aforementioned constraint.

Next, the computed velocity field is used in solving the closure problems **I** and **II**, as
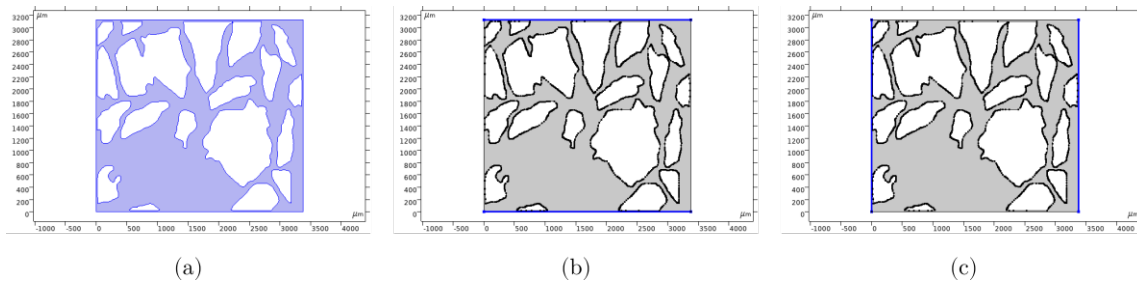
Figure 5.8: (a) The convection-diffusion based governing differential equations were solved in the pore region of the REV (blue color region), and (b) and (c) the periodicity boundary conditions were applied on the opposite edges of the unit-cell (blue color edges).

given in Eqs. (4.21a-4.21d) and (4.22a-4.22d) respectively. For the closure problems, the convection-diffusion based governing differential equations (Eqs. (4.21a) and (4.22a)) are solved in the pore region or the fluid domain of the REV, as shown in Fig. 5.8a. Note that the periodicity boundary condition cannot be directly implemented in the original porous medium due to the random distribution of the particles. However, Whitaker [82] suggested that in such cases the use of a periodic unit-cell is admissible, and the resulting errors which are confined to the borders of the unit-cell are not significant. Hence, the periodicity boundary conditions (Eqs. (4.21c) and (4.22c)) are imposed on the opposite edges of the 2-D periodic unit-cell, as illustrated in Figs. 5.8b and 5.8c.

The next step involves computation of the effective transfer coefficients $\mathbf{u}_\beta$ and $\mathbf{D}_\beta^*$. This step is completed by using the resultant closure fields for $\mathbf{b}_\beta$ and s_β in Eqs. (4.24) and (4.25) for evaluating $\mathbf{u}_\beta$ and $\mathbf{D}_\beta^*$, respectively.

Finally, the effective transfer coefficients, which establish the micro-macro coupling between the pore-scale and macroscale models, are substituted in the upscaled equations. The volume-averaged equations (4.23) and (4.27) are solved in a 1-D domain corresponding to the height of the zeolite material filled burette in the column-flow experiment. This is basically the length of the macroscale model L in Table 5.2. All the parameters used in the numerical simulations of the closure problems and macroscale models are listed in Table 5.2.

5.4   Results and discussion

The experimental data plotted in Fig. 5.9 shows the average P values (curve with black solid circles) with 95% confidence interval (shown by blue shaded region around the average P curve). It also shows the experimental data obtained from the three trials of the column experiment. The two-tailed t-test statistical analysis performed on the experimental data helped in accounting for the variations due to an ensemble of random errors that might have occurred during the experiments (refer to Appendix E for more
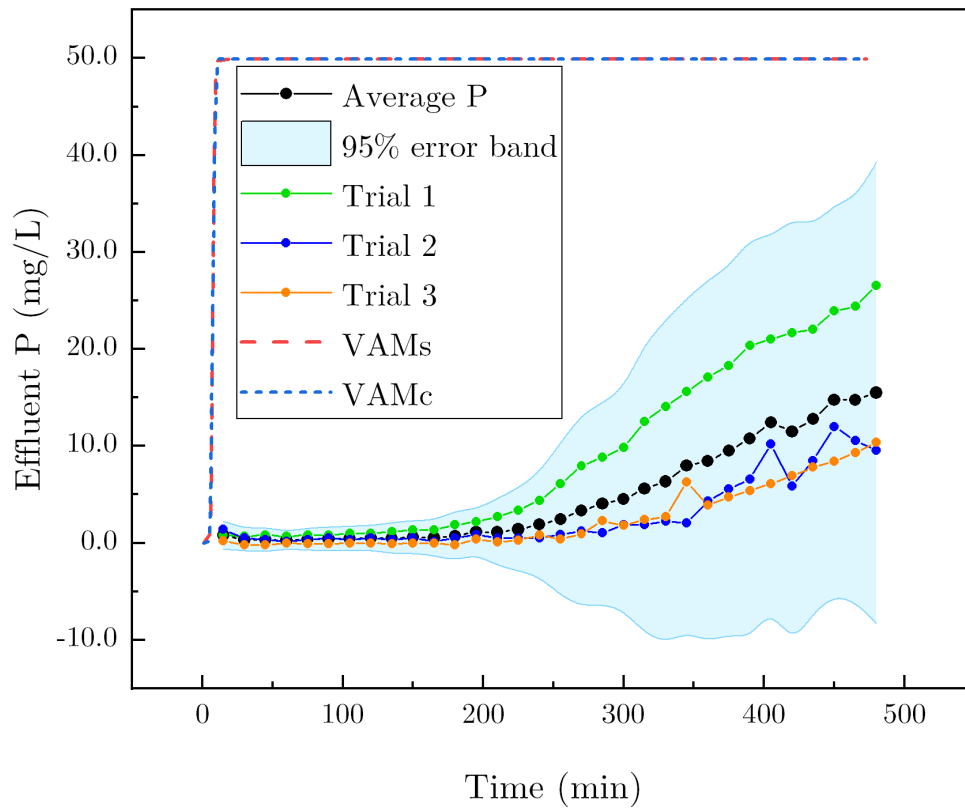
Figure 5.9: The average concentration data for the effluent recorded from the column-flow experiments and concentration predictions from the volume-averaged models, VAMs and VAMc.

details). As shown in Fig. 5.9, the functionalized zeolite was successfully able to remove the majority of phosphorus from the influent for nearly 200 minutes. After this, the number of vacant (or active) adsorption sites in the (previously used) filtration material may have started to decline, which explains the reduction in removal efficiency post 200 minutes. Near the end of 480 minutes, the effluent concentration rose to around 15 mg/L.

Next, we observe that the effluent concentration predictions from the volume-averaged models (VAMs and VAMc) show a large difference when compared to the experimental results. This observation undoubtedly raises the question in our mind– are the proposed volume-averaged models incapable of explaining the experimental results? Not exactly. Let us have a closer look at the concentration curves obtained from the upscaled models in Fig. 5.10.

In Fig. 5.10, the blue and red color curves represent VAMc and VAMs, respectively.

132

First, it is important to note that the shape of these convection-dispersion equation-based curves is in accordance with those observed in other adsorption studies [13, 14, 175]. Second, based on the parameters involved in the experiments and numerical simulations (see Table 5.2), we calculate the values of Pe_p (given in Eq. (4.57)), and the effective transfer coefficients $\mathbf{u}_\beta$ and $\mathbf{D}_\beta^{**} \left(= \mathbf{D}_\beta^*/\mathcal{D}_\beta\right)$. For $Pe_p = 388$, the value of $\mathbf{u}_\beta = 20.2$ and $\mathbf{D}_\beta^{**} = 598$. These estimates are in-line with the plots of the effective transfer values plotted in Fig. 4.6. It means that, for a given porosity, with an increase in Pe_p (here Pe_p between 100 and 1000), the values of $\mathbf{u}_\beta$ and $\mathbf{D}_\beta^{**}$ also increase by one or two orders of magnitude. Thus, the numerical simulations based on the upscaled models were able to provide realistic estimates of $\mathbf{u}_\beta$ and $\mathbf{D}_\beta^{**}$. Finally, even though the VAMc and VAMs curves remain close to each other, they are still distinguishable, which suggests that VAMc does provide some improvement over VAMs in this case. This can be explained based on the restraint given in Eq. (3.88), where the LHS of Eq. (3.88) is evaluated to be 0.2 and the RHS is 1.45. For the case under study, the term on the LHS does not remain very small or negligible with respect to the RHS of Eq. (3.88), hence, a marginal, yet observable, difference can be noted in the predictions from both the models.

Now, we must explore and throw light on the reasons behind the discrepancy observed between the experimental results and VAM predictions. We have identified four possible reasons which can help explain this inconsistence: (1) the lack of adherence to the time-scale constraints, (2) the absence of heterogeneous reaction physics in model development, (3) the simplification of the unit-cell (Fig. 5.8a) used to compute the velocity and closure variable fields, and (4) the inhomogeneity in the functionalized zeolite material properties. These are each explained in the subsequent paragraphs.

The volume averaging method models are strongly based on the development and implementation of length- and time-scale constraints, as has been described in Chapters 3 and 4. In this study, the length scales corresponding to the particle, REV, and macromodel adhere to the length-scale hierarchy proposed in Eq. (3.1). However, what is not directly
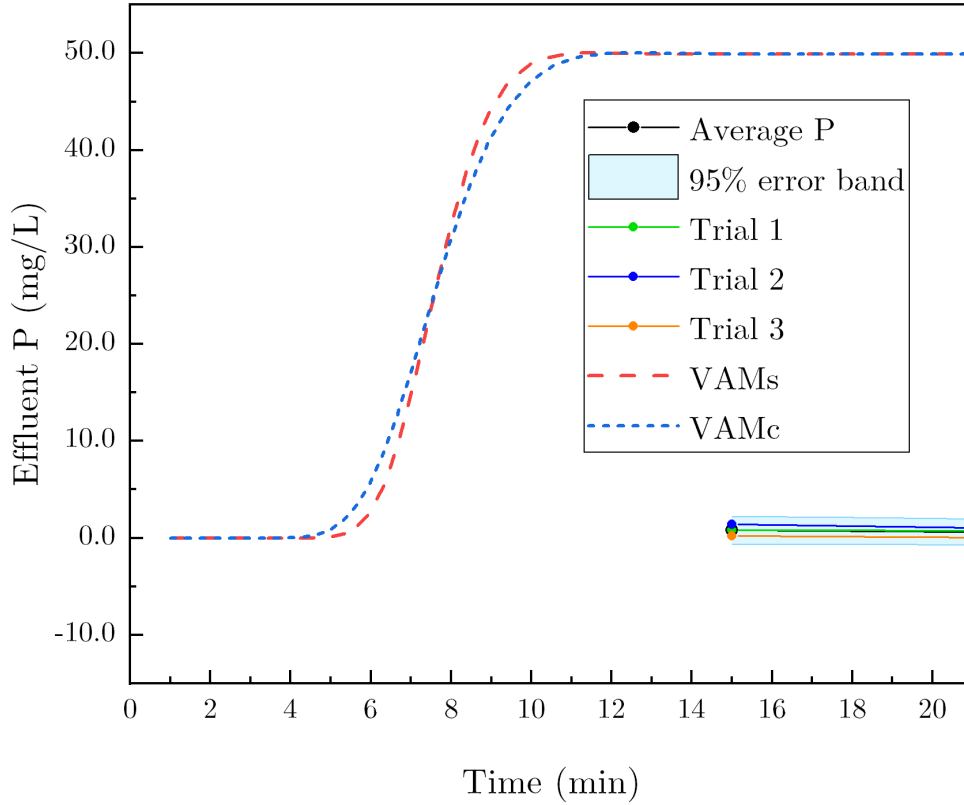
Figure 5.10: A closer view of the effluent concentration predictions obtained from the volume-averaged models, VAMs and VAMc.

evident is the effect of time-scale constraints given in Eqs. (3.52) and (3.54), which need to be satisfied in order to make the governing equations at the closure level to be almost quasi-steady. According to the length scales used in this study, the hydraulic diameter l_β can be calculated using the relation [124]

$$l_\beta = 4\frac{\epsilon_\beta}{a_{\beta\sigma}}.$$ (5.3)

Here $l_\beta = 0.53$ mm, and it is representative of the the width of the channel between the particles of the porous medium. If we consider the constraint given in Eq. (3.24), the length-scale for spatial fluctuations in $\tilde{c}_\beta$ can be taken to be the same as l_β. Thus, on using the values of l_β and $\mathcal{D}_\beta$ in the constraint given in Eq. (3.52), we get

$$\tau >> 453,$$ (5.4)

134

where τ (in s) is the characteristic time taken to note changes in $\tilde{c}_\beta$ within the REV. This condition is difficult to satisfy since the microscale diffusion time-scale $\left(= \frac{l_\beta^2}{\mathcal{D}_\beta} \right)$ involved in this study is quite large. In other words [186], it means that one must wait for much more than 453 s before the closure solution becomes quasi-steady, which is impractical. Hence, adhering to this constraint is unfeasible under the given length scales. Similarly, the constraint in Eq. (3.54) yields

$$\tau >> 51\,. \tag{5.5}$$

Therefore, Eq. (5.5) is open to a similar interpretation, as previously discussed. As pointed out by Whitaker (see Chapter 3 in [82]), such constraints, as given in Eq. (3.52), are not always adhered to in typical laboratory experiments. Hence, in such multiscale analysis, it would be interesting to formulate the set of *unsteady* closure problems in order to interpret the observations from the laboratory experiments. Although these problems have been researched [187], such analysis would require substantial computational effort which is beyond the scope of the present work. (A lab scale filtration experiment was also performed in addition to the column-flow experiments. However, similar to the column-flow experiments, a large discrepancy was noted between the predictions from the upscaled models and experimental results. For more details related to this filtration experiment, refer to Appendix E.2.)

Another route to test the effectiveness of the upscaled models would be exploring the possibility of conducting experiments with porous adsorbents which have smaller length scales associated with them, typically of the order of microns, as seen in the case of polyurethane foam-based heavy metal adsorbents. In this case, the diffusion time-scale associated with the solid particles would be smaller and therefore the time-scale constraint (Eq. (3.52)) would be easier to satisfy for the laboratory experiments.

Next, the discrepancy between the experiments and VAM also indicates that our model is perhaps incomplete. In order to develop a more accurate representation of the transport phenomena taking place at the microscale, we should also explicitly take

135

into consideration the possibility of heterogeneous reaction occurring on the fluid-solid interface. A lot of research on this subject has been done in the volume averaging community [117, 124, 125]. This addition would result in accounting for any mass transfer loss that might occur during the experiments.

Further, the use of a 3-D unit-cell of reasonable size, constructed out of a series of micro-CT scans, would be more suitable for numerical simulations. This is because such models would more accurately capture the intricate network of interconnected channels or pores within the porous material. Since the geometry of the system is of prime importance, this effort would help in obtaining accurate values of the effective transfer coefficients used in the upscaled models.

Another suggestion which would help increase the accuracy of the concentration predictions from REVs is to create unit cells of different sizes and extract them from random locations in the micro-tomographic images of all the planes. This technique would take into account the microstructural variations present across the porous domain and provide an accurate averaged data for use in the upscaled models.

Although the primary reason behind the lack of agreement between theory and observations is related to the time-scale constraints, as described above, the large error band around the mean curve (see Fig. 5.9) requires some explanation as well. The filtration material used this study was taken from a bag which was previously employed in a pilot scale filtration study. Hence, this material was neither freshly prepared nor regenerated using wash fluids prior to being used in the column-flow experiments. Although the material still had a good adsorption capacity, as was evaluated at the end of the previous filtration study, there is a strong possibility that the physical and chemical properties of the particles might have altered. This is based on the fact that the material in the bag was non-uniformly exposed to influents in the previous study. Basically, this could have resulted in inhomogeneity in the physiochemical properties of the material, which directly affected the adsorption capacity and led to a large scatter in the column-flow

experiments. Hence, in future studies, it would be advisable to use adsorption material which is freshly prepared and clean to reduce any inhomogeneity that might creep into the material properties.

5.5 Conclusions

In this chapter, we investigated the application of VAM models put forward by Pillai and Raizada [138] in order to seek a comparison between theory and experimental observations. Three trials of column-flow experiment were conducted using an adsorbent made up of functionalized zeolite material to remove phosphorus from synthetically prepared high-concentration phosphorus solution. The adsorption capacity q_e of the material was noted to be 5.0 ± 0.5 mg/g and the equilibrium concentration of the sorbent C_e was determined to be 25.5 ± 2.3 mg/L for the influent concentration of 49.9 ± 1.9 mg/L. Micro-CT scans of zeolite material were taken to develop REVs which were representative of the microstructure of the actual adsorbent medium. Unit cells with pore (or fluid) region were constructed after image processing in COMSOL Multiphysics. The Stokes flow equation was solved in the unit-cell, followed by the closure problems. Next, the effective transfer coefficients were obtained on using the closure variable fields in Eqs. (4.24) and (4.25). Finally, the effective transfer coefficients were substituted in the upscaled models (VAMs and VAMc), and both the models were solved in a 1-D domain.

The concentration predictions from the upscaled models were observed to be quite different from the experimental results. However, the upscaled models were found to give realistic effective coefficient values, and VAMc was noted to offer some improvement over VAMs. After theoretical and numerical investigations, four reasons were presented to explain the discrepancy between theory and observations. The primary reason was considered to be the lack of adherence to the time-scale constraints given in Eqs. (3.52) and (3.54). The characteristic time to achieve quasi-steady state solution for closure problems was found to be very large when compared to the diffusion time-scale related to

137

the zeolite particles. This highlighted the importance of length- and time-scale constraints involved during the development of the volume-averaged models. An alternative was suggested, where *unsteady* closure problems should be developed along with new upscaled models for explaining such laboratory experiments. The possiblity of including the physics for heterogeneous reaction in the upscaled models was highlighted. Also, the functionalized zeolite material used in the experiments was assessed to have inhomogeneity associated with it due to its prior use in another field scale experiment. This caused a large scatter in the column-flow experiment results. Different suggestions pertaining to the volume-averaged models and experiments were presented in order to improve the accuracy of VAM and to avoid the encountered pitfalls in future experiments.

Appendices

APPENDIX A

Permeability Measurement in Three Dimensions

A.1 Effective permeability in three dimensions

Effective permeability, K_{eff}, can be defined as the permeability measured along a chosen flow direction that is imposed on the fabric. In a laboratory coordinate system $(x\,y\,z)$, the Darcy velocities can be expanded in terms of the permeability tensor components, K_{ij} with $(i,\,j) \in (x,\,y,\,z)$, as follows:

$$v_x = -\frac{K_{xx}}{\mu}\frac{\partial P}{\partial x} - \frac{K_{xy}}{\mu}\frac{\partial P}{\partial y} - \frac{K_{xz}}{\mu}\frac{\partial P}{\partial z}$$

$$v_y = -\frac{K_{xy}}{\mu}\frac{\partial P}{\partial x} - \frac{K_{yy}}{\mu}\frac{\partial P}{\partial y} - \frac{K_{yz}}{\mu}\frac{\partial P}{\partial z} \tag{A.1}$$

$$v_z = -\frac{K_{xz}}{\mu}\frac{\partial P}{\partial x} - \frac{K_{yz}}{\mu}\frac{\partial P}{\partial y} - \frac{K_{zz}}{\mu}\frac{\partial P}{\partial z}$$

where v_x, v_y, and v_z are the x-, y-, and z-components of the Darcy velocity, respectively, and μ is the fluid viscosity. In the present study, we assume the fluid to flow along the x-axis direction, which in conjunction with suitable channel flow approximations (i.e., $v_y = 0$ and $v_z = 0$ in this case) in Eq. (A.1) leads to the following transformed effective permeability expression [19]:

$$K_{eff} = \frac{K_{xx}K_{yy}K_{zz} + 2K_{xy}K_{yz}K_{xz} - K_{xx}K_{yz}^2 - K_{yy}K_{xz}^2 - K_{zz}K_{xy}^2}{K_{yy}K_{zz} - K_{yz}^2}\ . \tag{A.2}$$
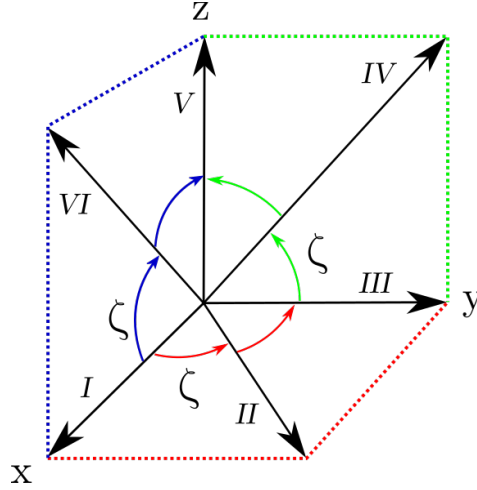
Figure A.1: The various measurement directions in the laboratory frame of reference considered for 1-D channel flow experiments to obtain the 3-D permeability tensor. The magnitude of angle ζ is 45°.

A.2 Direction of permeability measurement

Weitzenböck et al. [19] explained the need for six different experimental orientations in order to calculate the permeability tensor for a 3-D specimen. These measurement directions, as presented in Fig. A.1, need to be unique such that no more than three measurements must be made in the same plane to obtain useful permeability data.

As aforementioned, the specimen could be located using the laboratory coordinate system $(x\,y\,z)$ where the effective permeability for unidirectional flow occurring through this sample along the x-axis is given by Eq. (A.2). Further, the remaining five channel flow experiments are performed along the directions shown in Fig. A.1. In each of these five cases, the new permeability tensor components need to be related to those in the first configuration, and this is achieved through the ordered passive rotation(s) of the original permeability matrix such that it finally aligns with the new measurement direction. These rotational transformations of the tensor components are accomplished by exercising the relation

$$K' = RKR^T \tag{A.3}$$

141

where K' is the rotated permeability tensor, K is the original permeability tensor, and R is the total rotation matrix whose transpose is R^T. (Refer to Section A.6 for more details about the total rotation matrix, R.) It is important to note that the measurements for all the three in-plane diagonal directions, i.e., II, IV, and VI in Fig. A.1, are performed at an angle ζ ($= 45°$).

The first effective permeability value for flow along the x-axis is same as Eq. (A.2), i.e.,

$$K_I = \frac{K_{xx}K_{yy}K_{zz} + 2K_{xy}K_{yz}K_{xz} - K_{xx}K_{yz}^2 - K_{yy}K_{xz}^2 - K_{zz}K_{xy}^2}{K_{yy}K_{zz} - K_{yz}^2} \,. \qquad (A.4)$$

For obtaining the second effective permeability value, the experiment is performed in the same laboratory reference frame but rotated about the z-axis by angle ζ in order to coincide with direction II. The resultant rotation matrix R (equal to rotation matrix A in Section A.6 in this case) when substituted in Eq. (A.3) leads to the following rotated tensor components:

$$
\begin{aligned}
K'_{xx} &= \frac{K_{xx} + K_{yy}}{2} + K_{xy} \\
K'_{xy} &= \frac{-K_{xx} + K_{yy}}{2} \\
K'_{yy} &= \frac{K_{xx} + K_{yy}}{2} - K_{xy} \\
K'_{zz} &= K_{zz} \\
K'_{yz} &= \frac{-K_{xz} + K_{yz}}{\sqrt{2}} \\
K'_{xz} &= \frac{K_{xz} + K_{yz}}{\sqrt{2}} \,.
\end{aligned}
\qquad (A.5)
$$

These new tensor components, when substituted in Eq. (A.2), result in the following expression for effective permeability, K_{II}:

$$K_{II} = 2\,\frac{K_{xx}K_{yy}K_{zz} + 2K_{xy}K_{yz}K_{xz} - K_{xx}K_{yz}^2 - K_{yy}K_{xz}^2 - K_{zz}K_{xy}^2}{K_{xx}K_{zz} - 2K_{xy}K_{zz} + K_{yy}K_{zz} - K_{xz}^2 + 2K_{xz}K_{yz} - K_{yz}^2} \,. \qquad (A.6)$$

Next, K_{III} is obtained by rotating the measurement direction about the z-axis by $90°$ such that it aligns with the y-axis in the laboratory coordinate system, as illustrated in Fig. A.1. After completing a similar sequence of steps as exercised for deriving K_{II}, the effective permeability, K_{III}, takes the form

$$K_{III} = \frac{K_{xx}K_{yy}K_{zz} + 2K_{xy}K_{yz}K_{xz} - K_{xx}K_{yz}^2 - K_{yy}K_{xz}^2 - K_{zz}K_{xy}^2}{K_{xx}K_{zz} - K_{xz}^2} . \qquad (A.7)$$

As previously discussed, after conducting three measurements in the x-y plane, one needs to explore the out-of-plane measurements to determine the remaining three effective permeabilities. We attempt this by making the fourth measurement in the y-z plane after successive rotations of the measurement direction, first about the z-axis by $90°$ and then about the x-axis by angle ζ $(= 45°)$. In this case, the total rotation matrix modifies to $R = AC$ and the effective permeability, K_{IV}, is given by

$$K_{IV} = 2\,\frac{K_{xx}K_{yy}K_{zz} + 2K_{xy}K_{yz}K_{xz} - K_{xx}K_{yz}^2 - K_{yy}K_{xz}^2 - K_{zz}K_{xy}^2}{K_{xx}K_{yy} - 2K_{xx}K_{yz} + K_{xx}K_{zz} - K_{xy}^2 + 2K_{xy}K_{xz} - K_{xz}^2} . \qquad (A.8)$$

The effective permeability, K_V, is computed by rotating the measurement direction about the y-axis by $-90°$ such that it becomes parallel to the z-axis in the laboratory frame of reference. The total rotation matrix simplifies to $R = B$ in this case. *This step is different to the one proposed by Weitzenböck et al.* [19] *where the measurement direction is rotated by $90°$ about the y-axis*; however, the effective permeability expression for K_V comes out to be the same from both the approaches as follows:

$$K_V = \frac{K_{xx}K_{yy}K_{zz} + 2K_{xy}K_{yz}K_{xz} - K_{xx}K_{yz}^2 - K_{yy}K_{xz}^2 - K_{zz}K_{xy}^2}{K_{xx}K_{yy} - K_{xy}^2} . \qquad (A.9)$$

Finally, the effective permeability expression for K_{VI} is formulated by rotating the measurement direction about the y-axis by $-45°$ in order to match direction VI shown in Fig. A.1. Again, it is important to highlight that *Weitzenböck et al. [19] proposed a*

143

rotation of 45° about the y-axis for this step, which incorrectly causes the measurement direction to end up in the negative x-z plane, 45° below the x-axis. Thus, the resulting difference can be noted between the denominators of the permeability expressions obtained for K_{VI} from the present approach (in Eq. (A.10)) and from Weitzenböck et al.'s [19] method (in Eq. (A.11)).

$$K_{VI} = 2 \, \frac{K_{xx}K_{yy}K_{zz} + 2K_{xy}K_{yz}K_{xz} - K_{xx}K_{yz}^2 - K_{yy}K_{xz}^2 - K_{zz}K_{xy}^2}{K_{xx}K_{yy} - 2K_{yy}K_{xz} + K_{yy}K_{zz} - K_{xy}^2 + 2K_{xy}K_{yz} - K_{yz}^2} \qquad (A.10)$$

$$K_{VI} = 2 \, \frac{K_{xx}K_{yy}K_{zz} + 2K_{xy}K_{yz}K_{xz} - K_{xx}K_{yz}^2 - K_{yy}K_{xz}^2 - K_{zz}K_{xy}^2}{K_{xx}K_{yy} + 2K_{yy}K_{xz} + K_{yy}K_{zz} - K_{xy}^2 - 2K_{xy}K_{yz} - K_{yz}^2} . \qquad (A.11)$$

Hence, the permeability estimation method proposed by Weitzenböck et al. [19] *needs modification in terms of (a) correcting the formula of the effective permeability K_{VI}, and (b) correcting the derivation of the formula of the effective permeability K_V, because of the incorrect rotation matrices involved in these cases.*

A.3 Principal permeability in three dimensions

As suggested in [19], two steps are involved in calculating the principal permeability. First, the permeability tensor components are formulated in terms of the effective permeabilities given in Eqs. (A.4, A.6-A.10), and second, the principal components are computed using the standard eigenvalue and eigenvector operations on the permeability matrix. The permeability tensor component expressions obtained after accomplishing the first step are listed below:

$$\begin{aligned} K_{xx} = (K_{III}^2 K_{IV}^2 - 4K_{III}^2 K_{IV} K_V - 4K_{III}K_{IV}K_V^2 - 2K_{III}K_{IV}^2 K_V \\ + 4K_{III}^2 K_V^2 + K_{IV}^2 K_V^2) \, \frac{(K_I^2 K_{II}^2 K_{VI}^2)}{2C} \end{aligned} \qquad (A.12)$$

144

$$K_{yy} = (K_I^2 K_{VI}^2 - 4K_I^2 K_V K_{VI} - 4K_I K_V^2 K_{VI} - 2K_I K_V K_{VI}^2$$
$$+ 4K_I^2 K_V^2 + K_V^2 K_{VI}^2) \frac{(K_{II}^2 K_{III}^2 K_{IV}^2)}{2C} \qquad (A.13)$$

$$K_{zz} = (K_I^2 K_{II}^2 - 4K_I^2 K_{II} K_{III} - 4K_I K_{II} K_{III}^2 - 2K_I K_{II}^2 K_{III}$$
$$+ 4K_I^2 K_{III}^2 + K_{II}^2 K_{III}^2) \frac{(K_{IV}^2 K_V^2 K_{VI}^2)}{2C} \qquad (A.14)$$

$$K_{xy} = (2K_I K_{II} K_{III} K_{IV} K_V - K_I K_{II} K_{III} K_{IV} K_{VI} - 4K_I K_{II} K_{III} K_V^2$$
$$+ 2K_I K_{II} K_{III} K_V K_{VI} + 2K_I K_{II} K_{IV} K_V^2 - 3K_I K_{II} K_{IV} K_V K_{VI}$$
$$+ 4K_I K_{III} K_{IV} K_V K_{VI} - 3K_{II} K_{III} K_{IV} K_V K_{VI} + 2K_{II} K_{III} K_V^2 K_{VI}$$
$$- K_{II} K_{IV} K_V^2 K_{VI}) \frac{(K_I K_{II} K_{III} K_{IV} K_{VI})}{2C} \qquad (A.15)$$

$$K_{yz} = (2K_I K_{III} K_{IV} K_V K_{VI} - K_{II} K_{III} K_{IV} K_V K_{VI} - 4K_I^2 K_{III} K_{IV} K_V$$
$$+ 2K_I K_{II} K_{III} K_{IV} K_V + 2K_I^2 K_{III} K_{IV} K_{VI} - 3K_I K_{II} K_{III} K_{IV} K_{VI}$$
$$+ 4K_I K_{II} K_{III} K_V K_{VI} - 3K_I K_{II} K_{IV} K_V K_{VI} + 2K_I^2 K_{II} K_{IV} K_V$$
$$- K_I^2 K_{II} K_{IV} K_{VI}) \frac{(K_{II} K_{III} K_{IV} K_V K_{VI})}{2C} \qquad (A.16)$$

$$K_{xz} = (2K_I K_{II} K_{III} K_V K_{VI} - K_I K_{II} K_{IV} K_V K_{VI} - 4K_I K_{III}^2 K_V K_{VI}$$
$$+ 2K_I K_{III} K_{IV} K_V K_{VI} + 2K_{II} K_{III}^2 K_V K_{VI} - 3K_I K_{II} K_{III} K_{IV} K_{VI}$$
$$+ 4K_I K_{II} K_{III} K_{IV} K_V - 3K_{II} K_{III} K_{IV} K_V K_{VI} + 2K_I K_{III}^2 K_{IV} K_{VI}$$
$$- K_{II} K_{III}^2 K_{IV} K_{VI}) \frac{(K_I K_{II} K_{IV} K_V K_{VI})}{2C} \qquad (A.17)$$

145

where

$$C = K_{II}^2 K_{III}^2 K_{IV}^2 K_V K_{VI}^2 - K_{II}^2 K_{III}^2 K_{IV} K_V^2 K_{VI}^2 + K_{II}^2 K_{III} K_{IV}^2 K_V^2 K_{VI}^2$$

$$+K_I^2 K_{II}^2 K_{III} K_{IV}^2 K_{VI}^2 + 2K_I^2 K_{II}^2 K_{III} K_{IV} K_V^2 K_{VI}$$

$$-K_I^2 K_{II}^2 K_{III} K_{IV} K_V K_{VI}^2 - K_I^2 K_{II}^2 K_{IV}^2 K_V^2 K_{VI}$$

$$+K_I^2 K_{II}^2 K_{IV}^2 K_V K_{VI}^2 + 2K_I^2 K_{II} K_{III}^2 K_{IV}^2 K_V K_{VI}$$

$$-K_I^2 K_{II} K_{III}^2 K_{IV}^2 K_{VI}^2 - 4K_I^2 K_{II} K_{III}^2 K_{IV} K_V^2 K_{VI}$$

$$+2K_I^2 K_{II} K_{III}^2 K_{IV} K_V K_{VI}^2 + 2K_I^2 K_{II} K_{III} K_{IV}^2 K_V^2 K_{VI}$$

$$-3K_I^2 K_{II} K_{III} K_{IV}^2 K_V K_{VI}^2 + 2K_I^2 K_{III}^2 K_{IV}^2 K_V K_{VI}^2$$

$$-K_I K_{II}^2 K_{III}^2 K_{IV}^2 K_V K_{VI} + K_I K_{II}^2 K_{III}^2 K_{IV}^2 K_{VI}^2$$

$$+2K_I K_{II}^2 K_{III}^2 K_{IV} K_V^2 K_{VI} - 3K_I K_{II}^2 K_{III}^2 K_{IV} K_V K_{VI}^2$$

$$+2K_I K_{II}^2 K_{III}^2 K_V^2 K_{VI}^2 - 3K_I K_{II}^2 K_{III} K_{IV}^2 K_V^2 K_{VI}$$

$$+2K_I K_{II}^2 K_{III} K_{IV}^2 K_V K_{VI}^2 - 3K_I K_{II}^2 K_{III} K_{IV} K_V^2 K_{VI}^2$$

$$+K_I K_{II}^2 K_{IV}^2 K_V^2 K_{VI}^2 - 3K_I K_{II} K_{III}^2 K_{IV}^2 K_V K_{VI}^2$$

$$+2K_I K_{II} K_{III}^2 K_{IV} K_V^2 K_{VI}^2 - K_I K_{II} K_{III} K_{IV}^2 K_V^2 K_{VI}^2$$

$$2K_I^2 K_{II}^2 K_{III} K_{IV}^2 K_V - 3K_I^2 K_{II}^2 K_{III} K_{IV}^2 K_V K_{VI} \,.$$

Note that the expressions given for tensor components in Eqs. (A.12-A.17) are different from that in Appendix B of [19].

A.4 Results and discussion

A.4.1 Initial validation of the permeability estimation method

For validating the permeability estimation approach adopted in this study and estimating its accuracy, we refer to the principal permeability example published by Woerdeman et al. [20]. The validation process involves the following steps: **first**, calculate the

146

Table A.1: The permeability tensor example from Table 1 of [20].

Principal Permeability, cm^2	Rotation Angle, radians
$K_1 = 7.51 \times 10^{-7}$	$\Theta_1 = 0.3$
$K_2 = 4.58 \times 10^{-7}$	$\Theta_2 = 1.0 \times 10^{-3}$
$K_3 = 1.0 \times 10^{-7}$	$\Theta_3 = 1.2$

initial values for the tensor components by substituting the principal permeability values from Table 1 of [20] into Eqs. (A.21-A.26); **second**, substitute these calculated tensor components into Eqs. (A.4, A.6-A.10) to find the effective permeabilities, K_I to K_{VI}; **third**, again compute the tensor components, but this time by substituting the obtained effective permeability values into Eqs. (A.12-A.17); **fourth**, compare the tensor components obtained through the two different approaches involved in the first and third steps; and **finally**, determine the principal permeability values using the standard operations for finding eigenvalues of the permeability matrix, and compare them with the data of the example given in [20].

Table A.1 presents the permeability example used by Woerdeman et al. [20] to validate their permeability estimation method. Next, the tensor components computed using Eqs. (A.21-A.26) and the directional permeabilities obtained from Eqs. (A.4, A.6-A.10) are tabulated in Table A.2. For the purpose of comparison, this table also includes the effective permeability data calculated by Weitzenböck et al. (given in Table 2 of [19]). As expected, the effective permeabilities K_I to K_V match with Weitzenböck et al.'s [19] results. However, a clear deviation can be noted in the value of K_{VI}. This difference can be directly explained based on the contrast between the expressions derived for K_{VI} using both the methods (see Eqs. (A.10) and (A.11) in Section A.2).

The tensor components calculated after substituting the effective pemeabilities in Eqs. (A.12-A.17) and the resultant principal permeability values are reported in Table A.3. The tensor component values presented in Table A.3 can be seen to be in excellent agreement with those in Table A.2. Also, the computed principal permeabilities are

identical to those proposed in Woerdeman et al.'s [20] example in Table A.1. Therefore, we conclude that the derivation of the modified permeability tensor component expressions given in Eqs. (A.12-A.17) is correct.

A.4.2 Calculating permeability of a test sample

A numerical study is performed to visualize the difference between Weitzenböck et al.'s [19] and the current permeability calculation approach. In this study, the permeability is estimated for an artificial geometry featuring an inclined bank of equally-spaced parallel fibers, as illustrated by the grey colored rods in Fig. A.2. The model represents a sample volume comprising several infinitely long cylindrical fibers of radius 100 μm arranged at a regular distance from each other while being inclined at 45° to the x-axis in the x-z plane (see Figs. A.2b and A.2c).

Before carrying out the numerical simulations, the following important observations in the permeability values are anticipated based on the symmetries immanent in the model: first, the permeability tensor components should be equal for fluid flow along the x- and z-axis (i.e., $K_{xx} = K_{zz}$); second, the off-diagonal permeability components, K_{xy} and K_{yz}, should be equal; and finally, since the fibers are only inclined in the x-z plane, greater fluid flow should ensue along the axial direction of the fibers in this plane, and therefore, K_{xz} should be positive and greater than both K_{xy} and K_{yz}.

This numerical study was conducted using the commercial FEM solver, COMSOL

Table A.2: Permeability values calculated using the data in Table A.1 (in 10^{-11} m^2).

Tensor Components	Effective Permeability (present work)	Effective Permeability (Weitzenböck et al. [19])
$K_{xx} = 4.69$	$K_I = 3.76$	$K_I = 3.75$
$K_{yy} = 7.08$	$K_{II} = 3.82$	$K_{II} = 3.82$
$K_{zz} = 1.31$	$K_{III} = 6.52$	$K_{III} = 6.52$
$K_{xy} = -1.10$	$K_{IV} = 1.61$	$K_{IV} = 1.60$
$K_{yz} = -0.37$	$K_V = 1.07$	$K_V = 1.07$
$K_{xz} = -0.94$	$K_{VI} = 1.24$	$K_{VI} = 2.54$
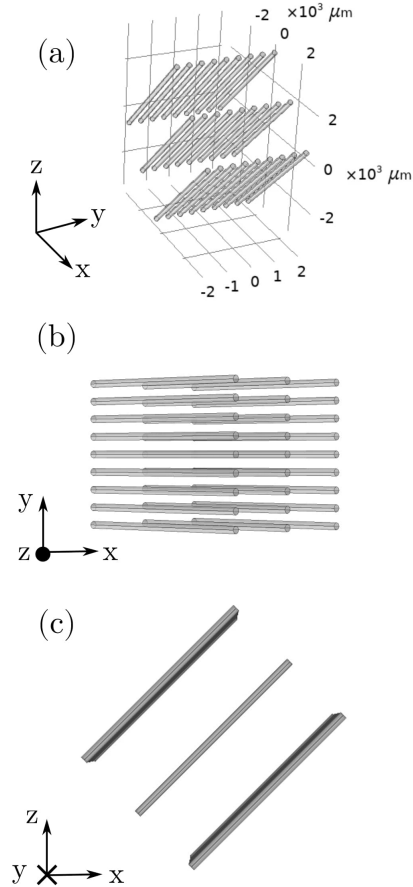
Figure A.2: Test model featuring a bank of equally-spaced parallel fibers inclined only in the x-z plane. (a) Isometric view of the model in the right-handed coordinate system (xyz). (b) x-y view of the model. (c) x-z view of the model where the fibers can be noted to be aligned at 45° to the x-axis in the x-z plane.

Multiphysics. A mesh independence study was performed for each orientation case, based on three different mesh sizes: coarse, normal, and fine. The solution corresponding to the maximum mesh refinement (i.e., the fine mesh) was considered as the reference and the relative differences in the effective permeability values were used as the convergence-test criteria. The relative error was found to be less than 1% for all the studied cases, thus confirming the mesh independence of our results. Subsequently, the fine mesh was used for numerical analysis.

After conducting unidirectional flow simulations along six different orientations, as shown in Fig. A.1, the permeability tensor results were obtained from the present approach

Table A.3: Permeability tensor components and Principal permeability calculated using data in Table A.2 (in 10^{-11} m^2).

Tensor Components	Principal Permeability
$K_{xx} = 4.69$	$K_1 = 7.51$
$K_{yy} = 7.08$	$K_2 = 4.58$
$K_{zz} = 1.31$	$K_3 = 1.0$
$K_{xy} = -1.10$	
$K_{yz} = -0.37$	
$K_{xz} = -0.94$	

by using Eqs. (A.12-A.17), and from Weitzenböck et al.'s method by employing the expressions given in Appendix B of [19]. The results are reported in Table A.4. Note that the tensor values obtained from both the approaches are different, which is expected due to the involvement of different tensor component expressions; however, they clearly displayed the aforementioned observations. The tensor components K_{xx} and K_{zz} were found to be equal. Similarly, the values for the off-diagonal terms, K_{xy} and K_{yz}, were noted to be very close. Further, the maximum permeability is reported for the tensor component K_{yy} from both the methods. However, more importantly, the tensor component K_{xz} showed a significant difference in its results. The present approach produced a positive value for K_{xz} which was greater than both K_{xy} and K_{yz}; however, Weitzenböck et al.'s [19] approach led to a **negative value** for this tensor component. This noticeable difference is further explained on the basis of the following example where

Table A.4: Permeability tensor results for the fiber model (in 10^{-8} m^2).

Tensor components obtained from	
Present approach	Weitzenböck et al. [19] approach
$K_{xx} = 8.58$	$K_{xx} = 8.36$
$K_{yy} = 10.69$	$K_{yy} = 10.42$
$K_{zz} = 8.58$	$K_{zz} = 8.37$
$K_{xy} = 1.71$	$K_{xy} = 0.74$
$K_{yz} = 1.70$	$K_{yz} = 0.74$
$K_{xz} = 3.45$	$K_{xz} = -3.13$
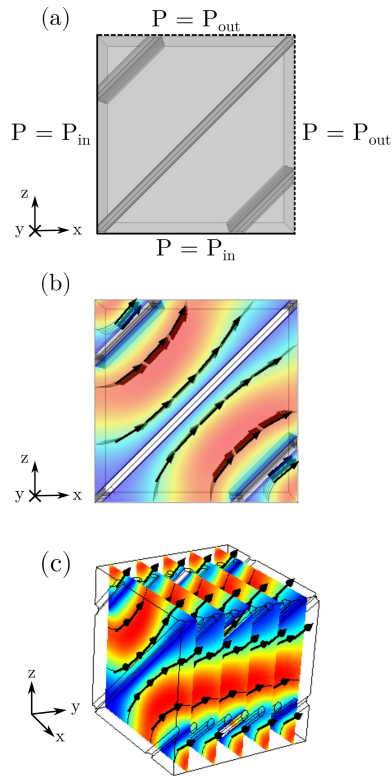
Figure A.3: A cube model encompassing segments of the inclined fibers in Fig. A.2. (a) Boundary conditions applied across the faces of the cube in the x- and z-axis directions, where P_{in} indicates pressure inlet face and P_{out} indicates pressure outlet face. (b) A sample x-z plane featuring flow streamlines denoted by black arrows. The streamlines are majorly aligned along the axial direction of the fibers (denoted by white spaces). (c) Isometric view of the cube model illustrating multiple slices of the x-z planes. The streamlines can be noted to be confined only in the x-z planes and not divert out-of plane.

the application of appropriate boundary conditions leads to the simplification of a three-dimensional flow into a two-dimensional one.

Let us consider a cubical geometry, as shown in Fig. A.3, which incorporates the set of inclined fibers used in the model of Fig. A.2. Then, the application of negative pressure gradients across the faces directed towards the x- and z-axis (see Fig. A.3a), and symmetry boundary condition across the faces along the y-axis of the cube, leads to a two-dimensional flow in three-dimensional space. This is confirmed by the characteristic streamlines depicted by black arrows in Fig. A.3b, which only traverse in the x-z planes along the axial direction of the fibers at $45°$ with respect to the x-axis. Since the pressure

gradient directions in this simplified model match with those involved in the calculations of K_I and K_V, and the resulting flow is happening along the axial direction of the fibers in the x-z plane, we conclude that the outcome of the permeability estimation approach *should result in a positive value for the tensor component K_{xz} for the model of Fig. A.2.* This confirms the correctness of our approach vis-à-vis that of Weitzenböck et al.'s [19].

A.5   Conclusions

In this appendix, we report the modifications required in Weitzenböck et al.'s [19] method for correctly estimating the permeability in three-dimensional porous media. The permeability measurement approach was thoroughly discussed in a fashion similar to the one presented in [19] to facilitate a comparison between the original and modified methods.

The theoretical errors involved during the derivation of effective permeability expressions for K_V and K_{VI} were highlighted. These perceptible errors occur due to the incorrect rotation angle(s) linked with these two cases. In the case of derivation of K_V, the measurement direction needs to be rotated about the y-axis by $-90°$ instead of the originally proposed rotation of $90°$, whereas for K_{VI}, the rotation angle should be set to $-45°$ about the y-axis in place of $45°$, as mentioned in [19]. This causes the expressions for the permeability components to be modified.

The validation of the modified permeability estimation approach was successfully carried out in a manner similar to the one given in [19] for the original method. To further elucidate the difference between the two approaches, a numerical study was conducted to estimate the permeability tensor of an artificial geometry created by an inclined bank of parallel fibers in three-dimensional space. Based on the inherent symmetries present in this model, certain key observations about the permeability tensor components were hypothesized. In contrast to the original approach, the results obtained from the new method were found to support the proposed hypotheses, thus establishing confidence in the recommended modifications.

A.6 Euler Angles and Tensor Rotation

If a proper Euler angle sequence (ABC) of passive rotations is used to locate the orientation of an arbitrary body in a laboratory coordinate system $(x\, y\, z)$, where matrix A corresponds to the rotation about the z-axis by angle γ, matrix B is the rotation about the y-axis by angle β, and matrix C represents the rotation about the x-axis by angle α, such that:

$$
A = \begin{bmatrix} \cos\gamma & \sin\gamma & 0 \\ -\sin\gamma & \cos\gamma & 0 \\ 0 & 0 & 1 \end{bmatrix}
$$

$$
B = \begin{bmatrix} \cos\beta & 0 & -\sin\beta \\ 0 & 1 & 0 \\ sin\beta & 0 & cos\beta \end{bmatrix} \tag{A.18}
$$

$$
C = \begin{bmatrix} 1 & 0 & 0 \\ 0 & \cos\alpha & \sin\alpha \\ 0 & -\sin\alpha & \cos\alpha \end{bmatrix}
$$

then the total rotation matrix, R, is a composite of the three rotations and is expressed as follows [19]:

$$
R = ABC \tag{A.19}
$$

which leads to

$$R = \begin{bmatrix} c\beta \cdot c\gamma & c\alpha \cdot s\gamma + s\alpha \cdot s\beta \cdot c\gamma & s\alpha \cdot s\gamma - c\alpha \cdot s\beta \cdot c\gamma \\ -c\beta \cdot s\gamma & c\alpha \cdot c\gamma - s\alpha \cdot s\beta \cdot s\gamma & s\alpha \cdot c\gamma + c\alpha \cdot s\beta \cdot s\gamma \\ s\beta & -s\alpha \cdot c\beta & c\alpha \cdot c\beta \end{bmatrix} \quad (A.20)$$

where c represents the cosine function (e.g., $c\beta$ is the cosine value of angle β), and similarly s represents the sine function.

When the principal permeability tensor is rotated using the rotation matrix, R, it results in the following tensor component expressions (derived using Eq. (A.3)) [19]:

$$\begin{aligned} K_{xx} = {} & K_1 \cos^2\beta \cos^2\gamma + K_2 \left(\cos\alpha \sin\gamma + \sin\alpha \sin\beta \cos\gamma\right)^2 \\ & + K_3 \left(\sin\alpha \sin\gamma - \cos\alpha \sin\beta \cos\gamma\right)^2 \end{aligned} \quad (A.21)$$

$$\begin{aligned} K_{yy} = {} & K_1 \cos^2\beta \sin^2\gamma + K_2 \left(\cos\alpha \cos\gamma - \sin\alpha \sin\beta \sin\gamma\right)^2 \\ & + K_3 \left(\sin\alpha \cos\gamma + \cos\alpha \sin\beta \sin\gamma\right)^2 \end{aligned} \quad (A.22)$$

$$K_{zz} = K_1 \sin^2\beta + K_2 \sin^2\alpha \cos^2\beta + K_3 \cos^2\alpha \cos^2\beta \quad (A.23)$$

$$\begin{aligned} K_{xy} = {} & -K_1 \cos^2\beta \cos\gamma \sin\gamma + K_2 \left(\cos\alpha \sin\gamma + \sin\alpha \sin\beta \cos\gamma\right) \\ & \left(\cos\alpha \cos\gamma - \sin\alpha \sin\beta \sin\gamma\right) \\ & + K_3 \left(\sin\alpha \sin\gamma - \cos\alpha \sin\beta \cos\gamma\right) \\ & \left(\sin\alpha \cos\gamma + \cos\alpha \sin\beta \sin\gamma\right) \end{aligned} \quad (A.24)$$

$$K_{yz} = -K_2 \left(\cos\alpha \cos\gamma - \sin\alpha \sin\beta \sin\gamma\right) \sin\alpha \cos\beta$$

$$+K_3 \left(\sin\alpha \cos\gamma + \cos\alpha \sin\beta \sin\gamma\right) \cos\alpha \cos\beta$$

$$-K_1 \sin\beta \, \cos\beta \sin\gamma \qquad\qquad (A.25)$$

$$K_{xz} = -K_2 \left(\cos\alpha \sin\gamma + \sin\alpha \sin\beta \cos\gamma\right) \sin\alpha \cos\beta$$

$$+K_3 \left(\sin\alpha \sin\gamma - \cos\alpha \sin\beta \cos\gamma\right) \cos\alpha \cos\beta$$

$$+K_1 \sin\beta \, \cos\beta \cos\gamma \qquad\qquad (A.26)$$

where K_1, K_2 and K_3 are the diagonal components of the principal permeability matrix.

APPENDIX B

Permeability Measurement in Two Dimensions

B.1 2-D permeability estimation using the 1-D channel flow

Here we present the permeability estimation method proposed by Weitzenböck et al. [19] for two-dimensional flow in porous media. For an anisotropic (thin) preform made of fabric layers laid in a flat horizontal plane, if the x- and y-axes are not the principal material directions of the porous medium, then the Darcy's law reduces to

$$\begin{Bmatrix} q_x \\ q_y \end{Bmatrix} = -\frac{1}{\mu} \begin{bmatrix} K_{xx} & K_{xy} \\ K_{yx} & K_{yy} \end{bmatrix} \begin{Bmatrix} \partial_x P \\ \partial_y P \end{Bmatrix} . \tag{B.1}$$

The unidirectional macroscopic flow domain and relevant boundary conditions in such an anisotropic medium are shown in Fig. B.1.

For long and narrow flow domains[1], we can assume that $q_y = 0$. Then it follows from Eq. (B.1) that the pressure gradient in the y-direction can be expressed as

$$\partial_y P = -\frac{K_{yx}}{K_{yy}} \partial_x P . \tag{B.2}$$

Eq. (B.1) also yields

$$q_x = -\frac{1}{\mu} \left[K_{xx} \partial_x P + K_{xy} \partial_y P \right] . \tag{B.3}$$

---

[1]A previous study has indicated that the molds with high aspect ratio (i.e., length to width ratio) yield flows that are likely to follow this assumption provided the additional conditions pertaining to the anisotropy ratio (i.e., the ratio of the major and minor permeabilities) and the permeability orientation (i.e., the angle made by the major axis of the permeability tensor with the x-axis) are satisfied [11].

156
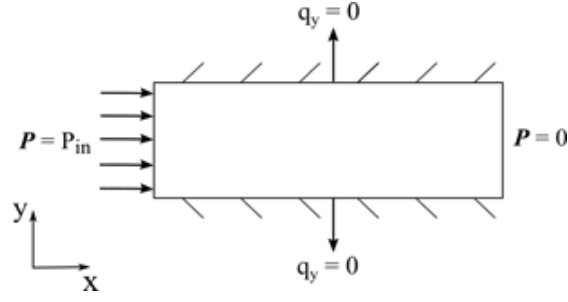
Figure B.1: A schematic of a typical macroscopic flow domain and the corresponding boundary conditions employed for the determination of the permeability tensor for a 2-D (thin) porous medium.

Substituting Eq. (B.2) in Eq. (B.3) results in

$$q_x = -\frac{1}{\mu}\left[K_{xx} - \frac{K_{yx}^2}{K_{yy}}\right]\partial_x P\,.$$ (B.4)

Now the macroscopic continuity equation states that

$$\nabla \cdot \mathbf{q} = 0$$ (B.5)

which simplifies to

$$\partial_x q_x = 0$$ (B.6)

since q_y can be assumed to be 0 in the considered flow domain. Substitution of q_x (Eq. (B.4)) in Eq. (B.6) results in the expression

$$-\frac{1}{\mu}\left[K_{xx} - \frac{K_{yx}^2}{K_{yy}}\right]\frac{\partial^2 P}{\partial x^2} = 0\,.$$ (B.7)

The permeability tensor for the assumed homogeneous porous medium can be considered to be constant, which leads to the simplification

$$\frac{\partial^2 P}{\partial x^2} = 0\,.$$ (B.8)

Eq. (B.8) is twice integrated along with the following boundary conditions

157

Boundary Condition 1:

$$P = P_{in} \quad \text{at} \quad x = 0\,. \tag{B.9}$$

Boundary Condition 2:

$$P = 0 \quad \text{at} \quad x = L\,. \tag{B.10}$$

which results in a linear distribution of the macroscopic pressure

$$P\left(x\right) = \ P_{in}\ \left(1 - \frac{x}{L}\right)\,. \tag{B.11}$$

The macroscopic Darcy velocity is obtained by substituting Eq. (B.11) in Eq. (B.4)

$$\mathrm{q_x} = \frac{Q}{A} = -\frac{1}{\mu}\left[K_{xx} - \frac{K_{yx}^{\,2}}{K_{yy}}\right]\left(\frac{-P_{in}}{L}\right)\,. \tag{B.12}$$

If we compare this with the form of Darcy's law for isotropic porous media, i.e., $q = \frac{Q}{A} = -\frac{K}{\mu}\nabla P$, the effective permeability along the 1-D flow direction can be deduced to be

$$K_{eff} = K_{xx} - \frac{K_{yx}^{\,2}}{K_{yy}} = \frac{\mu\,Q\,L}{A\,P_{in}}\,. \tag{B.13}$$

Let us now assume the principal permeability components to be K_1 and K_2, and the principal direction '1' to be at angle 'θ' with respect to the x-axis. The 2-D principal permeability tensor corresponding to the rotated coordinate system is

$$\mathbf{K} = \begin{bmatrix} \mathrm{K}_1 & 0 \\ 0 & \mathrm{K}_2 \end{bmatrix}\,. \tag{B.14}$$

Using classical manipulations [1], we can express the components of the permeability

158
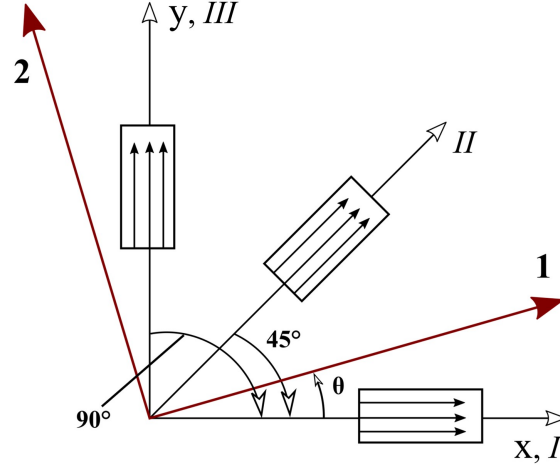
Figure B.2: I, II and III denote the three directions of the 1-D (channel) flow experiment for the 2-D case. 1 and 2 are the principal directions of the permeability tensor. The angle θ defines the flow direction vis-à-vis the principal direction 1.

tensor in terms of the principal permeability components as

$$K_{xx} = cos^2\theta \cdot \mathrm{K}_1 + sin^2\theta \cdot \mathrm{K}_2 \tag{B.15}$$

$$K_{yy} = cos^2\theta \cdot \mathrm{K}_2 + sin^2\theta \cdot \mathrm{K}_1 \tag{B.16}$$

$$K_{xy} = sin\theta \cdot cos\theta \cdot (\mathrm{K}_2 - \mathrm{K}_1) \,. \tag{B.17}$$

On substituting Eqs. (B.15-B.17) in Eq. (B.13), we get

$$K_{eff} = \frac{\mathrm{K}_1 \cdot \mathrm{K}_2}{cos^2\theta \cdot \mathrm{K}_2 + sin^2\theta \cdot \mathrm{K}_1} \,. \tag{B.18}$$

According to Weitzenböck et al. [56], three 1-D flow experiments along different directions (see Fig. B.2) are required to generate three different K_{eff} values and thus solve for the three unknowns (K_1, K_2 and θ) to determine the full in-plane (2-D) permeability tensor.

The three 1-D flow directions are: $\theta_I = \theta$, $\theta_{II} = \theta + 45°$ and $\theta_{III} = \theta + 90°$. On using these angles in Eq. (B.18), the effective permeabilities along the flow directions (K_I, K_{II}

159

and K_{III}) can be expressed in terms of principal permeability variables as

$$K_1 = K_I \left(\frac{A - D}{A - \frac{D}{cos2\theta}} \right) \tag{B.19}$$

$$K_2 = K_{III} \left(\frac{A + D}{A + \frac{D}{cos2\theta}} \right) \tag{B.20}$$

$$\theta = \frac{1}{2} \tan^{-1} \left\{ \frac{A}{D} - \frac{A^2 - D^2}{K_{II} \cdot D} \right\} \tag{B.21}$$

such that $A = \frac{K_I + K_{III}}{2}$ and $D = \frac{K_I - K_{III}}{2}$.

Finally, K_1, K_2, and θ from Eqs. (B.19-B.21), can be used to back calculate K_{xx}, K_{yy}, and K_{xy} from Eqs. (B.15-B.17), and hence the complete permeability tensor is given by

$$\mathbf{K} = \begin{bmatrix} K_{xx} & K_{xy} \\ K_{yx} & K_{yy} \end{bmatrix} . \tag{B.22}$$

APPENDIX C

Estimation of Closure Variables and Adsorption Parameters

C.1   Estimation of parameters A and Pe_p based on experimental observations

C.1.1   Estimation of the Damköhler number A

In order to obtain an order of magnitude estimate of the Damköhler number (or the dimensionless adsorption isotherm) A, which is given by Eq. (4.42), the values of K_{eq}, $a_{\beta\sigma}$, and ϵ_β need to be determined.

First, let us start with the procedure to determine K_{eq}. The K_{eq} value can be obtained from batch adsorption experiments. In general, K_{eq} (m) is related to the linear equilibrium partitioning coefficient (K_d (L/kg)) which is calculated using the ratio of the adsorption capacity at equilibrium (q_e (mg/g)) to the equilibrium concentration (C_e (mg/L)). For example, Nikolaidis et al. [14] performed field experiments in their arsenic filtration study and found K_d equal to 4300 L/kg for arsenic adsorption onto the iron filings or surface binding.

The next step involves normalization of K_d (m^3/g) with respect to the surface area (m^2/g) of the adsorbent. We continue with the same example of arsenic filtration in ref. [14]. For this case, first, the converted K_d value is equal to 4.3×10^{-3} m^3/g, and second, the surface area of the spent filter material is 37.8 m^2/g. After normalizing K_d with the surface area of the material, we estimate K_{eq} to be 1.14×10^{-4} m.

Next, the interfacial area per unit volume ($a_{\beta\sigma}$) and porosity (ϵ_β) are generally obtained from experimental studies. The porosity of the filtration material in ref. [14] is

161

given to be 0.45. Iron filings used in heavy metal filtration studies generally have effective particle size of 0.5-0.6 mm [188]. Hence, the zero-valent iron (stock number CC-1004, Connelly GPM, Inc,. Chicago, IL in ref. [14]) of size 0.6 mm (US Screen Number 30) was used to estimate the size of the filings. The characteristic length l_σ of the iron filings is 0.6 mm. Further, we assume that the characteristic length l of the porous medium is at least two times the particle size l_σ. Thus, l is estimated to be approximately 1.2 mm.

Finally, on substituting the estimates of K_{eq} and l in Eq. (4.42), A is evaluated to be 0.095. Hence, a reasonably safe estimate of A for arsenic adsorption–based filtration experiments can be assumed to be 0.1.

C.1.2 Estimation of the particle Péclet number Pe_p

In order to estimate Pe_p corresponding to filtration velocity in experiments, let us analyze the pore velocity data in the arsenic filtration study in ref. [14] and use the simplified unit-cell shown in Fig. 4.2. Note that for the estimation of Pe_p, which is given by Eq. (4.57), the values of $||\langle \mathbf{v}_\beta \rangle^\beta||$, ϵ_β, l_σ, and $\mathcal{D}_\beta$ need to be determined.

In ref. [14], the field experiments were conducted while maintaining an average flow rate of 0.5 gallons per minute in the filter columns. The pore velocity in these columns was noted to be 6.4 cm/min. The pore velocity, which is representative of the intrinsic phase-average velocity, provides a good estimate of $||\langle \mathbf{v}_\beta \rangle^\beta||$ for the filtration material. Hence, $||\langle \mathbf{v}_\beta \rangle^\beta||$ is estimated to be 1.07×10^{-3} m/s. As previously mentioned, the characteristic length l_σ of the iron filings is estimated to be 0.6 mm and the porosity of the filtration material is 0.45. A typical value of $\mathcal{D}_\beta$ for arsenic ions in aqueous phase according to experimental studies (see Table 2 in ref. [189]) is 11.6×10^{-10} m^2/s.

Thus, on substituting the estimates of $||\langle \mathbf{v}_\beta \rangle^\beta||$, ϵ_β, l_σ, and $\mathcal{D}_\beta$ in Eq. (4.57), Pe_p is evaluated to be 453. Since the flow rate involved in such adsorption–based filtration experiments is quite small, hence, a reasonably safe estimate of Pe_p can be assumed to be of $\mathbf{O}(100)$.

C.2   Order of magnitude estimates of closure variables

The order of magnitude estimate for a pore-scale variable ϕ_β is represented by $\mathbf{O}\left(\phi_\beta\right)$. As defined in Section 4.2.3.3, the reference length or characteristic length at pore-scale is chosen to be l, which is the size of unit-cell shown in Fig. 4.2. This is used to obtain the estimates for the gradient and the Laplacian of ϕ_β as follows:

$$\nabla\phi_\beta \;=\; \mathbf{O}\left(\frac{\phi_\beta}{l}\right) \quad;\quad \nabla^2\phi_\beta \;=\; \mathbf{O}\left(\frac{\phi_\beta}{l^2}\right). \tag{C.1}$$

On the basis of above definitions, the order of magnitude estimates of closure variables $\mathbf{b}_\beta$ and s_β can be ascertained from closure problems **I** and **II**. We would accomplish this by comparing the magnitudes of the *known* source terms with closure variable dependent terms in these boundary-value problems.

Let us first consider **problem I** for obtaining the estimates of $\mathbf{b}_\beta$:

$$\mathbf{v}_\beta \cdot \nabla\mathbf{b}_\beta + \tilde{\mathbf{v}}_\beta \;=\; \mathcal{D}_\beta\,\nabla^2\mathbf{b}_\beta \tag{C.2a}$$

$$\text{B.C.1}: \quad -\mathbf{n}_{\beta\sigma}\cdot\nabla\mathbf{b}_\beta \;=\; \mathbf{n}_{\beta\sigma}, \quad \text{at } A_{\beta\sigma} \tag{C.2b}$$

$$\text{Periodicity B.C.}: \quad \mathbf{b}_\beta(\mathbf{r}+\mathbf{l}_i) \;=\; \mathbf{b}_\beta(\mathbf{r}), \quad i=1,2,3 \tag{C.2c}$$

$$\text{Constraint}: \quad \langle\mathbf{b}_\beta\rangle^\beta \;=\; 0. \tag{C.2d}$$

Here, $\mathbf{b}_\beta$ is expected to depend on the volumetric source $\tilde{\mathbf{v}}_\beta$ in Eq. (C.2a). In this scenario, it is important to note that $\tilde{\mathbf{v}}_\beta$ would achieve its maximum magnitude on the solid-fluid surface due to the presence of no-slip boundary condition. This would lead to the circumstance where an upper limit can be established for $\mathbf{O}\left(\mathbf{b}_\beta\right)$ which can be used

163

in convection-dominated regimes ($Pe \gg 1$). Thus, we can proceed to write

$$- \langle \mathbf{v}_\beta \rangle^\beta = \mathcal{D}_\beta \nabla^2 \mathbf{b}_\beta, \quad \text{at } A_{\beta\sigma} \tag{C.3}$$

from which an estimate for $\mathbf{b}_\beta$ can be obtained after using the definitions in Eqs. (C.1) and (4.28) as follows

$$\mathbf{b}_\beta = \mathbf{O} \left(\frac{v_c l}{\mathcal{D}_\beta} \cdot l \right) = \mathbf{O} \left(l \, Pe \right). \tag{C.4}$$

This completes the derivation for $\mathbf{b}_\beta$ estimate based on the volumetric source in Eq. (C.2a). Further, an alternate order of magnitude estimate for $\mathbf{b}_\beta$ can be obtained after comparing the magnitude of the surface source $\mathbf{n}_{\beta\sigma}$ to $\nabla \mathbf{b}_\beta$ in the boundary condition (Eq. (C.2b)) as follows

$$\nabla \mathbf{b}_\beta = 1, \quad \text{at } A_{\beta\sigma} \tag{C.5}$$

which leads to

$$\mathbf{b}_\beta = \mathbf{O} \left(l \right). \tag{C.6}$$

This $\mathbf{b}_\beta$ estimate, which is independent of Pe, is more suitable for transport conditions when $Pe \leq 1$. Note that this estimate can also be obtained by comparing the two terms on the LHS of Eq. (C.2a).

Next, let attention be directed towards closure **problem II** for obtaining the order

164

of magnitude estimate of s_β. The problem is summarized below:

$$\mathbf{v}_\beta \cdot \nabla s_\beta \;\;=\;\; \mathcal{D}_\beta \nabla^2 s_\beta + \frac{a_{\beta\sigma}}{\epsilon_\beta} \tag{C.7a}$$

$$\text{B.C.1}: \;\; -\mathbf{n}_{\beta\sigma} \cdot \mathcal{D}_\beta \nabla s_\beta \;\;=\;\; 1, \quad \text{at } A_{\beta\sigma} \tag{C.7b}$$

$$\text{Periodicity B.C.}: \;\; s_\beta(\mathbf{r} + \mathbf{l}_i) \;\;=\;\; s_\beta(\mathbf{r}), \quad i = 1, 2, 3 \tag{C.7c}$$

$$\text{Constraint}: \;\; \langle s_\beta \rangle^\beta \;\;=\;\; 0. \tag{C.7d}$$

In this case, the gradient of the closure variable ∇s_β is observed to depend on the surface source (1) in Eq. (C.7b). With the spatial variation in s_β occurring over the length-scale l, after a simple algebraic manipulation this boundary condition yields the following estimate for s_β

$$s_\beta \;=\; \mathbf{O}\left(\frac{l}{\mathcal{D}_\beta}\right). \tag{C.8}$$

A similar estimate can be drawn by comparing the two terms on the RHS of Eq. (C.7a). Thus, for s_β, we arrive at a unique order of magnitude given in Eq. (C.8), which is independent of Pe.

It must be noted that in case of macroscopic variables, the order of magnitude analysis would be based on the characteristic length L of the macroscale model instead of the microscale length l.

APPENDIX D

An Alternate Nondimensionalization Approach

Based on the theoretical developments in Chapter 3, where the convection, diffusion, and adsorption phenomena are analyzed for upscaling, we proposed to use the characteristic time for diffusion at the pore-scale for nondimensionalization of the pore-scale and volume-averaged models in Chapter 4. However, let us explore another approach to nondimensionalize the aforementioned models based on the characteristic time for convection at the pore-scale.

D.1   Pore-scale model

For a unit-cell in the porous media model shown in Fig. D.1, the characteristic time for convection at the pore-scale is given by

$$t_{cl} = \frac{l}{v_c}\,. \tag{D.1}$$

The dimensionless variables needed to nondimensionalize the boundary-value problem (Eqs. (4.1-4.5)) are as follows:

$$\nabla^* = \nabla\, l\,,\ x^* = \frac{x}{l}\,,\ y^* = \frac{y}{l}\,,\ t_{conv}^* = \frac{t\,v_c}{l}\,,\ \mathbf{v}_\beta^* = \frac{\mathbf{v}_\beta}{v_c}\,,\ c_\beta^* = \frac{c_\beta}{c_{in}}\ ,\ \text{and}\ P^* = \frac{l\,P}{\mu\,v_c}\,. \tag{D.2}$$

Here, ∇^* is the dimensionless differential operator at the length-scale l, x^* is the x-direction coordinate nondimensionalized with the length-scale l, y^* is the y-direction coordinate nondimensionalized with the length-scale l, t_{conv}^* is the dimensionless convection time variable corresponding to the length-scale l, $\mathbf{v}_\beta^*$ denotes the dimensionless point
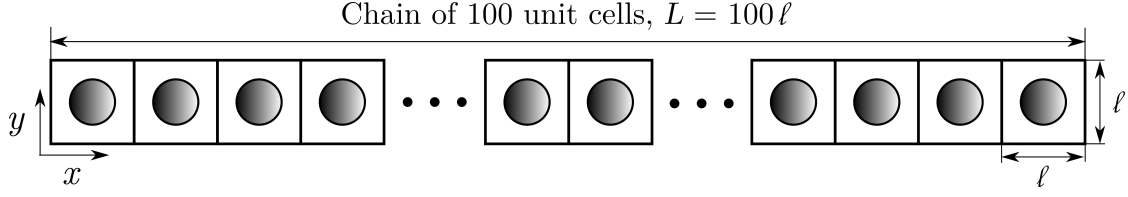
Figure D.1: Illustration of the 2-D geometry of porous media used to conduct the direct numerical simulations (DNS). The length of the macroscopic region is assumed to be $L = 100\,l$.

velocity of the β-phase, c_{in} is the constant inlet concentration of species X, c_β^* is the dimensionless point concentration of species X in the β-phase, and P^* denotes the dimensionless hydrodynamic fluid pressure in the β-phase.

In addition, we define the convection transport based Damköhler number Da as follows:

$$Da = \frac{K_{eq}\frac{l}{\mathcal{D}_\beta}}{\frac{l}{v_c}} \left(= \frac{K_{eq}\, v_c}{\mathcal{D}_\beta}\right) = \frac{\text{adsorption time scale}}{\text{convection time scale}}\,. \tag{D.3}$$

The Damköhler number Da can also be expressed as

$$Da = \frac{K_{eq}\frac{l}{\mathcal{D}_\beta}}{\frac{l}{v_c}} \left(= \frac{K_{eq}}{l} \cdot \frac{v_c\, l}{\mathcal{D}_\beta}\right) = A \cdot Pe \tag{D.4}$$

where $A\left(= \frac{K_{eq}}{l}\right)$ is the diffusion transport based Damköhler number (Eq. (4.42)) and Pe is the cell Péclet number (Eq. (4.28)).

After substituting these variables in Eqs. (4.1-4.5), the dimensionless version of the problem can be summarized as follows:

$$\frac{\partial c_\beta^*}{\partial t_{conv}^*} + \mathbf{v}_\beta^* \cdot \nabla^* c_\beta^* = \frac{1}{Pe}\,\nabla^{*2} c_\beta^* \tag{D.5}$$

$$\text{B.C.1}: \quad -\mathbf{n}_{\beta\sigma} \cdot \nabla^* c_\beta^* = Da\,\frac{\partial c_\beta^*}{\partial t_{conv}^*}, \quad \text{at } A_{\beta\sigma} \tag{D.6}$$

$$0 \quad = \quad -\nabla^* P^* + \nabla^{*2} \mathbf{v}_\beta^* \tag{D.7}$$

$$\nabla^* \cdot \mathbf{v}_\beta^* \quad = \quad 0 \tag{D.8}$$

$$\text{B.C.2:} \quad \mathbf{v}_\beta^* \quad = \quad 0, \quad \text{at } A_{\beta\sigma}. \tag{D.9}$$

Furthermore, the computational domain shown in Fig. D.1 is subjected to the following set of initial and (Dirichlet and Neumann type) boundary conditions:

$$c_\beta^* \quad = \quad 0, \quad \text{when} \quad t_{conv}^* = 0 \tag{D.10a}$$

$$c_\beta^* \quad = \quad 1, \quad \text{at} \quad x^* = 0 \tag{D.10b}$$

$$\frac{\partial c_\beta^*}{\partial x^*} \quad = \quad 0, \quad \text{at} \quad x^* = \frac{L}{l} \tag{D.10c}$$

$$c_\beta^* \left(x^*, \, y^* = 0, \, t_{conv}^* \right) \quad = \quad c_\beta^* \left(x^*, \, y^* = 1, \, t_{conv}^* \right) \tag{D.10d}$$

$$P^* \quad = \quad P_{in}^* \left(= N \right), \quad \text{at} \quad x^* = 0 \tag{D.10e}$$

$$P^* \quad = \quad 0, \quad \text{at} \quad x^* = \frac{L}{l} \tag{D.10f}$$

$$\mathbf{v}_\beta^* \left(x^*, \, y^* = 0, \, t_{conv}^* \right) \quad = \quad \mathbf{v}_\beta^* \left(x^*, \, y^* = 1, \, t_{conv}^* \right) \tag{D.10g}$$

where Eqs. (D.10d) and (D.10g) represent the periodicity boundary conditions applied at the top and bottom of the DNS model, and the pressure differential applied across the domain due to the combination of Eqs. (D.10e) and (D.10f) has an effect such that each unit-cell in Fig. D.1 is subjected to a unitary pressure gradient.

D.2 VAMc and VAMs

For the upscaled model of length L, the characteristic time for convection at the macroscale is given by

$$t_{cL} = \frac{L}{v_c}. \tag{D.11}$$

168

The dimensionless variables needed to nondimensionalize the volume-averaged models (Eqs. (4.23) and (4.27)) are as follows:

$$\nabla_L^* = \nabla_L \, L \,, \ X^* = \frac{x}{L} \,, \ T_{conv}^* = \frac{t \, v_c}{L} \,, \ \mathbf{v}_\beta^* = \frac{\mathbf{v}_\beta}{v_c} \,, \ c_\beta^* = \frac{c_\beta}{c_{in}} \,, \ \text{and} \ A = \frac{a_{\beta\sigma} \, K_{eq}}{\epsilon_\beta} \left(= \frac{K_{eq}}{l} \right) .$$

(D.12)

Here, ∇_L is the differential operator at the length-scale L, ∇_L^* is the dimensionless differential operator at the length-scale L, X^* is the x-direction coordinate nondimensionalized with the length-scale L, and T_{conv}^* is the dimensionless convection time variable corresponding to the length-scale L.

The macroscopic length L is equal to the length of a chain of N square unit cells (see Fig. D.1) each of length l such that $L = N \times l$. Then, on nondimensionalizing Eq. (4.23) using the definitions given in Eq. (D.12) and performing algebraic manipulations, we arrive at the following dimensionless form of VAMc:

$$\frac{\partial \langle c_\beta^* \rangle^\beta}{\partial T_{conv}^*} + \frac{1}{1+A} \, \langle \mathbf{v}_\beta^* \rangle^\beta \cdot \nabla_L^* \langle c_\beta^* \rangle^\beta + \frac{A}{(1+A) \, N} \, \mathbf{u}_\beta \cdot \nabla_L^* \left(\frac{\partial \langle c_\beta^* \rangle^\beta}{\partial T_{conv}^*} \right)$$
$$= \frac{1}{N(1+A) \, Pe} \, \mathbf{D}_\beta^{**} : \nabla_L^* \nabla_L^* \langle c_\beta^* \rangle^\beta . \quad \text{(D.13)}$$

For the macroscopic model considered in this study, the length-scale associated with the spatial variation of $\frac{\partial \langle c_\beta \rangle^\beta}{\partial t}$ is L and the spatial variation in s_β takes place at the microscopic length-scale l. In this case, the dimensionless form of the restraint given in Eq. (4.26) would become

$$\frac{Da}{N} \, \mathbf{v}_\beta^* \quad \ll \quad (1+A) \,, \quad \text{(D.14)}$$

and the mixed derivative term may be dropped from Eq. (D.13). The resulting 1-D nondimensional macroscale equation for VAMs would be

$$\frac{\partial \langle c_\beta^* \rangle^\beta}{\partial T_{conv}^*} + \frac{1}{1+A} \, \langle \mathbf{v}_\beta^* \rangle^\beta \cdot \nabla_L^* \langle c_\beta^* \rangle^\beta = \frac{1}{N(1+A) \, Pe} \, \mathbf{D}_\beta^{**} : \nabla_L^* \nabla_L^* \langle c_\beta^* \rangle^\beta . \quad \text{(D.15)}$$

169

Now, since different length and time scales have been used to nondimensionalize the volume-averaged and the pore-scale models (see Eqs. (D.12) and (D.2), respectively), we need to develop suitable length- and time-scale correlations in order to draw comparisons between the two systems. For this, if a point x in the laboratory frame of reference is to be located in both the coordinate systems, then based on Eqs. (D.12) and (D.2) we deduce the following length-scale relation:

$$\nabla_L^* = N \nabla^* . \tag{D.16}$$

Similarly, in order to study the results at any given time t in the laboratory frame of reference, the following dimensionless time-scale relation should be used:

$$T_{conv}^* = t_{conv}^* / N . \tag{D.17}$$

Also, the relation between the dimensionless convection and diffusion time scales at the pore-scale is as follows:

$$t_{conv}^* = t^* \times Pe \tag{D.18}$$

where $t^* \left(= \frac{t \mathcal{D}_\beta}{l^2} \right)$ is the dimensionless time-scale for diffusion at the pore-scale.

D.3   Validation of Macroscale simulations

In this section we validate the predictions of the volume-averaged models by comparing them with the literature results [166]. To achieve this purpose, a computational domain consisting of 100 in-line unit cells each of side-length l was designed, as shown in Fig. D.1. This model resembles a porous medium made of regularly arranged parallel cylinders with the fluid flow directed perpendicular to the cylinder axis. The nondimensionalized closure problems given by Eqs. ((4.33a-4.34d) and (4.36a-4.36d)) were solved in a unit-cell of the described model to evaluate the effective transfer coefficients $\mathbf{u}_\beta$ (Eq. (4.38)) and $\mathbf{D}_\beta^{**}$
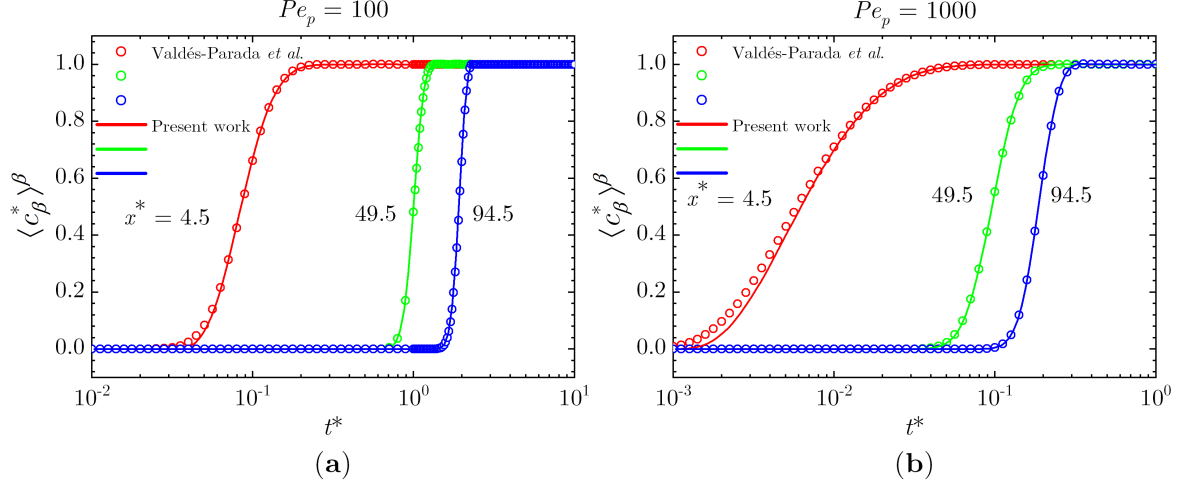
Figure D.2: Comparison of the evolution of the intrinsic phase average concentration between the present work and the literature [166]. Assuming $\epsilon_\beta = 0.8$, case (a) corresponds to $A = 0$, $Pe_p = 100$, and case (b) corresponds to $A = 0$, $Pe_p = 1000$. The dimensionless convection time-scale used in the present work is converted into the dimensionless diffusion time-scale by using Eq. (D.18), which was then used for the comparison of results.

(Eqs. (4.40a-4.40b)). The upscaled equations, Eqs. (D.13) and (D.15), were solved in 1D along a line of unit length.

The simulation codes developed for the upscaled models are validated by comparing the results with that of Valdés Parada et al. [166] under specific circumstances. It can be inferred from ref. [166] that in the absence of heterogeneous first-order chemical reaction, i.e. for the passive dispersion case ($\phi^2 = 0$), the macroscale model given by Eq. (48) of ref. [166] transforms into the standard convection-dispersion transport equation. Analogously, in the present work, the volume-averaged models given by Eqs. (D.13) and (D.15), reduce to that same convection-dispersion form under the no adsorption ($A = 0$) condition. Thus, the data from Figs. 8a and 9a in ref. [166] corresponding to the no-slip boundary condition is used for validation of the code developed for the present work. In this study, the average concentration was tested at the following positions: (a) near the entrance, at $x^* = 4.5$, (b) near the middle, at $x^* = 49.5$, and (c) near the exit, at $x^* = 94.5$, of the computational domain shown in Fig. D.1. It is important to note that the concentration predictions in ref. [166] are made using the model formulations based

on the dimensionless diffusion time-scale. Therefore, in the present work, Eq. (D.18) is used to convert the dimensionless convection time-scale into the dimensionless diffusion time-scale for directly comparing the evolution of the intrinsic average concentration with that in ref. [166].

As reported in Fig. D.2, the concentration predictions made using the current code for both Pe_p of $\mathbf{O}(100)$ and $\mathbf{O}(1000)$ are in excellent agreement with the literature [166], which helps reinforce the accuracy of the proposed convection time-scale based model formulations. The minor divergence observed near the onset of the concentration profiles at position $x^* = 4.5$ maybe due to the use of compound order of magnitude estimate proposed for $\mathbf{b}_\beta$ in ref. [166]. On proceeding farther from the inlet and with increasing time, the difference between the intrinsic phase average concentration predictions occurring due to the above-mentioned estimate and our estimates in Eqs. (4.31) and (4.32) becomes barely noticeable.

Thus, it can be concluded that the convection transport based Damköhler number Da, which signifies the ratio of adsorption to convection time scales, provides an alternative approach to study the mass transport phenomena occurring at the pore-scale in porous water filters.

APPENDIX E

Supplementary Material for Experiments

E.1 Supplementary data for column-flow experiments

As described in Chapter 5, three trials of column-flow experiments were conducted in order to evaluate the performance of functionalized zeolite materal. The experimental data for evolution of the effluent concentration with respect to time is tabulated in Table E.1. The influent concentration in the experiments was as follows: (1) 47.81 mg/L in Trial 1, (2) 51.31 mg/L in Trial 2, and (3) 50.60 mg/L in Trial 3.

We know that artificially prepared materials suffer from numerous imperfections, therefore, it is necessary to conduct multiple experiment trials in order to account for the random sampling errors that might occur during the tests. In our study, for each column-flow experiment, fresh adsorbent material was taken from the same filter bag that was employed in a previous filtration study. Each of the trial experiments was carefully conducted under as identical lab conditions as possible and the effluent concentration readings were taken at stipulated intervals in an accurate manner. For the three given adsorbent samples, the t-test was performed at every measurement time-step in order to estimate the margin of error at that given point in time. An example of the margin of error calculation is as follows. Let us consider the effluent concentration data from the three trials after 405 minutes of elapsed time, i.e., 21.01 mg/L, 10.22 mg/L, and 6.10 mg/L. At this given time, the mean of the effluent concentration is 12.44 mg/L and the standard deviation of the samples is 7.70 mg/L. For a two-tailed t-test with 95% confidence interval, the t-statistic value is 4.303 for $2 (= 3 - 1)$ degrees of freedom. Finally, the margin of error can be calculated by finding the product of t-statistic value

(= 4.303) and the ratio of standard deviation (= 7.70 mg/L) to the square root of the number of samples (= 3). Thus, the margin of error is evaluated to be 19.13 mg/L. Overall, the effluent concentration at this time-step is 12.44 ± 19.13 mg/L. It can be noted that the margin of error exceeds the average concentration value primarily due to the large standard deviation involved at this time-step. The margin of error at other time steps can similarly be calculated.

Table E.1: Evolution of the effluent concentration with respect to time in the column-flow experiments.

| Elapsed time (min)	Effluent concentration (mg/L)		
	Trial 1	Trial 2	Trial 3
15	0.83	1.37	0.20
30	0.66	0.51	-0.20
45	0.83	0.33	-0.20
60	0.66	0.16	0.00
75	0.83	0.33	-0.10
90	0.83	0.51	-0.10
105	1.00	0.33	0.00
120	1.00	0.51	0.00
135	1.17	0.33	-0.10
150	1.34	0.51	0.00
165	1.34	0.16	0.00
180	1.85	0.51	-0.20
195	2.19	0.85	0.40
210	2.70	0.51	0.10
225	3.38	0.51	0.30
240	4.39	0.51	0.80
255	6.09	0.85	0.40
270	7.96	1.20	0.90
285	8.80	1.03	2.30
300	9.82	1.89	1.80
315	12.53	1.89	2.40
330	14.06	2.24	2.70
345	15.59	2.07	6.30
360	17.11	4.32	3.90
375	18.30	5.53	4.70
390	20.33	6.58	5.40
405	21.01	10.22	6.10
420	21.69	5.89	6.90
435	22.03	8.48	7.80
450	23.90	11.95	8.40
465	24.40	10.56	9.30
480	26.52	9.52	10.40

175
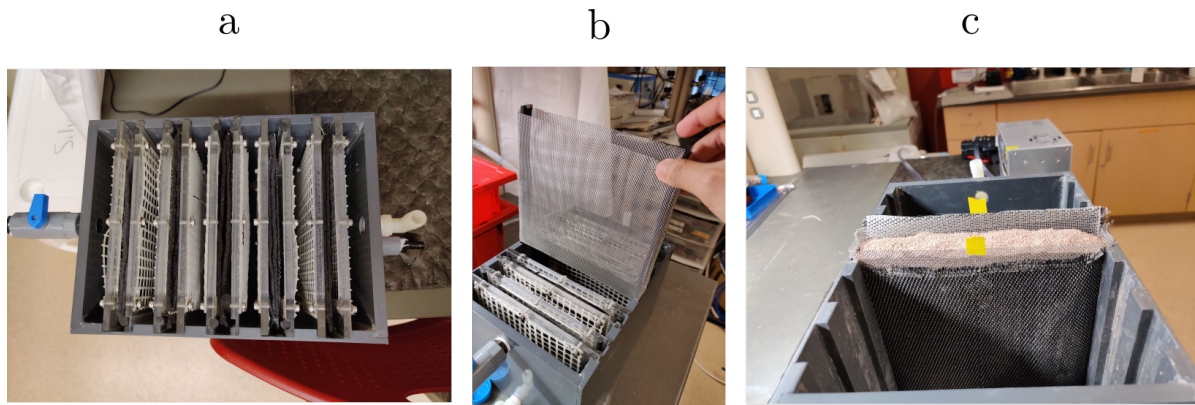
Figure E.1: (a) The lab scale filter box with filter bags, (b) an artificial mesh-case used to store the zeolite material, and (c) the mesh-case positioned into the third slot of the filter box.

E.2   Lab scale filtration experiment

In addition to the column-flow experiments, a lab scale experiment was conducted by using a filtration box designed[1] and built by Kieser & Associates in collaboration with the Silva Lab. This horizontal-flow system, as shown in Fig. E.1a, comprised of a polyethylene plastic box with pipes to collect and store the influent, and combinations of filter bags and holders to filter the contaminated solution. An artificial mesh-case, as shown in Fig. E.1b, constructed out of stiff steel mesh screens of size US 20 mesh was used to store the zeolite material. The use of stiff screens helped in maintaining an even thickness of the case and minimized any structural deformations that occurred during the flow of solution through the adsorbent. The case was inserted into the third slot from the inlet out of the 5 slots in the filter box. Also, an external layer of woven textile cloth was attached to the front and back faces of this mesh box to prevent any finer particles from being washed away during the experiment. The filtration material was poured into the mesh-case and allowed to settle in an uncompacted manner. Due to the deployment of the material in previous field tests, any resultant large chunks were manually crushed before being filled into the holder. The average thickness of the filled up mesh-case was 29.3 ± 1.4 mm. The volumetric porosity of the zeolite filtration material was evaluated

---

[1]Any reproduction of the lab scale filter box photographs herein is prohibited without express consent of the Great Lakes Protection Fund.

Figure E.2: The setup for the lab scale filtration experiment.

to be 49.6%. The characteristic size of the adsorbent particles was 0.72 mm.

A tank of capacity 20 L to store and supply the P spiked solution was continuously refilled at regular intervals. Further, a network of tubes and flow regulator valve reduced the flow rate of 12V DC pump such that the influent from the reservoir was injected into the filter box at a constant flow rate of 3.0 mL/s, as shown in Fig. E.2. The influent concentration for the experiment was 0.21 ± 0.01 mg/L. The effluent samples were taken at 1 inch from the exit face of the mesh-case at the intervals of 15 minutes over a period of 300 minutes. The filtered solution generated over the course of 5-hour experiment was collected in a large reservoir.

2.5 mL aliquot of each effluent sample was analyzed for soluble reactive phosphorus (SRP) by using the UV-VIS Spectrophotometer (Shimadzu UV-2600). For detection of P, the spectrophotometer measured the absorption of light by the sample at 885 nm wavelength. The experimental data for evolution of the effluent concentration with respect to time is tabulated in Table E.2.

Table E.2: Evolution of the effluent concentration with respect to time in the lab scale filtration experiment.

Elapsed time (min)	Effluent concentration (mg/L)
15	0.10
30	0.09
45	0.08
60	0.06
75	0.05
90	0.04
105	0.04
120	0.03
135	0.03
150	0.02
165	0.02
180	0.02
195	0.02
210	0.02
225	0.02
240	0.02
255	0.04
270	0.06
285	0.05
300	0.03
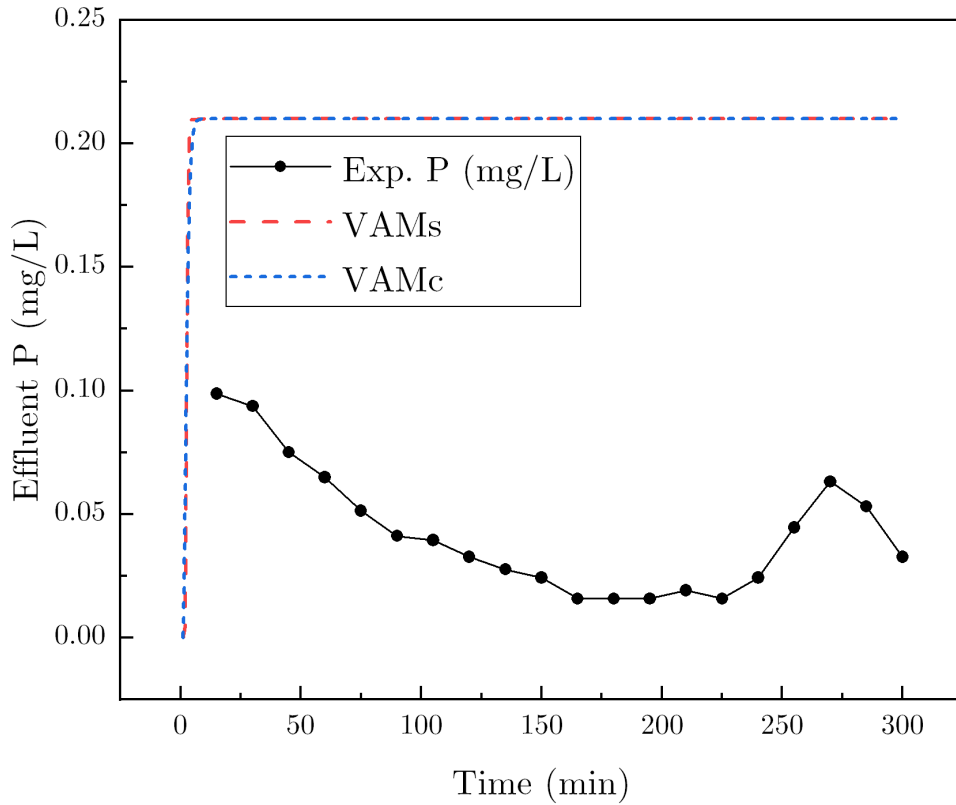
Figure E.3: The effluent concentration data recorded from the lab scale filtration experiment and concentration predictions from the volume-averaged models, VAMs and VAMc.

E.3 Results and discussion

The effluent concentration data plotted in Fig. E.3 shows the experimental values (curve with black solid circles) and concentration predictions from VAMs (red line) and VAMc (blue line) models. As shown in Fig. E.3, the functionalized zeolite was successfully able to remove the majority of phosphorus from the influent for nearly 225 minutes. After this, the number of vacant (or active) adsorption sites in the (previously used) filtration material may have started to decline, which explains the reduction in removal efficiency post 225 minutes.

Similar to the results obtained from the column-flow experiments, the effluent concentration predictions from the volume-averaged models (VAMs and VAMc) show a large difference when compared to the lab scale results. If we closely observe the concentration

179
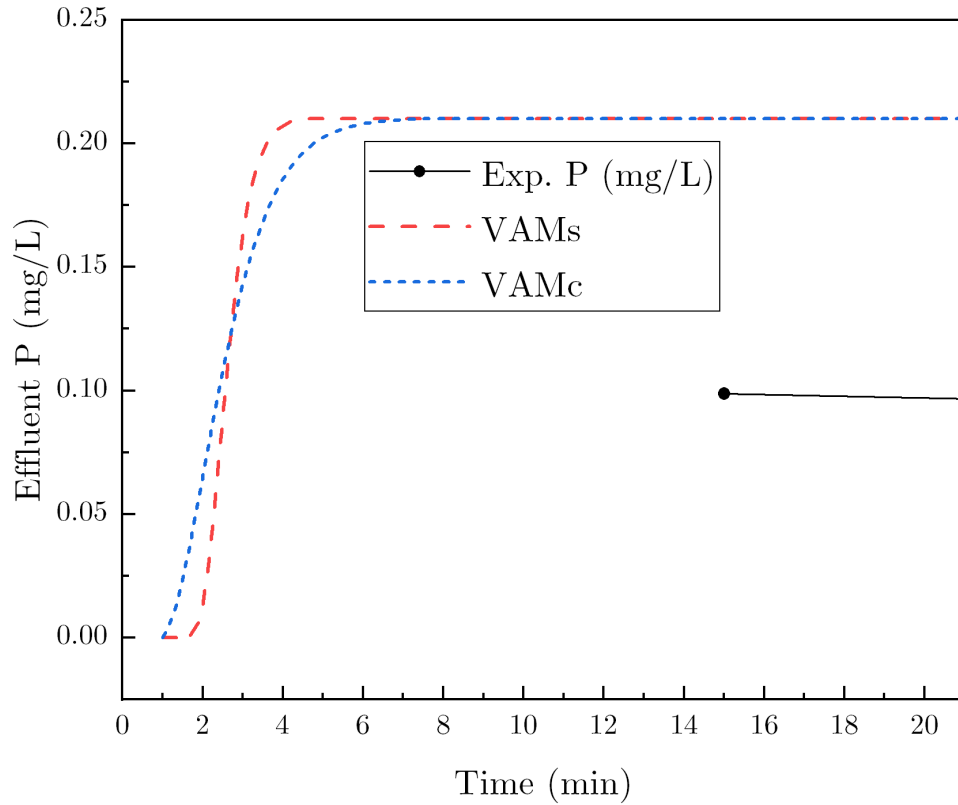
Figure E.4: A closer view of the effluent concentration predictions obtained from the volume-averaged models, VAMs and VAMc.

curves obtained from the upscaled models in Fig. E.4, we again note the following points: (1) the shape of these convection-dispersion equation-based curves is in accordance with those observed in other adsorption studies [13, 14, 175], and (2) even though the VAMc and VAMs curves remain close to each other, they are still distinguishable, which suggests that VAMc does provide some improvement over VAMs in this case.

The major reason behind the discrepancy observed between the experimental results and VAM predictions is the lack of adherence to the time-scale constraint given in Eq. (3.52). An extensive discussion based on this topic is presented in Section 5.4.

180

Bibliography

[1] Jacob Bear. *Dynamics of fluids in porous media*. Courier Corporation, 2013.

[2] Henry Philibert Gaspard Darcy. *Determination of the laws of flow of water through sand*. 1856.

[3] Francis AL Dullien. *Porous media: Fluid Transport and Pore Structure*. Academic press, 2012.

[4] Sauro Succi. *The Lattice Boltzmann Equation: For Fluid Dynamics and Beyond*. Oxford University Press, 2001.

[5] H Brenner and PM Adler. Transport processes in porous media. 1986.

[6] Kambiz Vafai. *Handbook of Porous Media*. CRC Press, 2015.

[7] Thu H Nguyen, Arwa Fraiwan, and Seokheun Choi. Paper-based batteries: A review. *Biosensors and Bioelectronics*, 54:640–649, 2014.

[8] Ruihua Tang, Hui Yang, Yan Gong, Zhi Liu, XiuJun Li, Ting Wen, ZhiGuo Qu, Sufeng Zhang, Qibing Mei, and Feng Xu. Improved Analytical Sensitivity of Lateral Flow Assay Using Sponge for HBV Nucleic Acid Detection. *Scientific reports*, 7(1):1–10, 2017.

[9] MR Rokhforouz and HA Akhlaghi Amiri. Phase-field simulation of counter-current spontaneous imbibition in a fractured heterogeneous porous medium. *Physics of Fluids*, 29(6):062104, 2017.

[10] Suresh G Advani and Kuang-Ting Hsiao. *Manufacturing Techniques for Polymer Matrix Composites (PMCs)*. Elsevier, 2012.

181

[11] Hua Tan and Krishna M Pillai. Effect of fiber-mat anisotropy on 1D mold filling in LCM: A numerical investigation. *Polymer Composites*, 29(8):869–882, 2008.

[12] Subhashini Gunashekar, Krishna M Pillai, Benjamin C Church, and Nidal H Abu-Zahra. Liquid flow in polyurethane foams for filtration applications: a study on their characterization and permeability estimation. *Journal of Porous Materials*, 22(3):749–759, 2015.

[13] Tien Vinh Nguyen, Saravanamuthu Vigneswaran, Huu Hao Ngo, and Jaya Kandasamy. Arsenic removal by iron oxide coated sponge: experimental performance and mathematical models. *Journal of Hazardous Materials*, 182(1-3):723–729, 2010.

[14] Nikolaos P Nikolaidis, Gregory M Dobbs, and Jeffrey A Lackovic. Arsenic removal by zero-valent iron: field, laboratory and modeling studies. *Water Research*, 37(6):1417–1425, 2003.

[15] Soumyadeep Paul, Sumit Roy, Pradyumna Ghosh, Mohammad Amin Faghihi Zarandi, Thomas Cender, and Krishna M Pillai. A Novel Method for Permeability Estimation from Micro-tomographic Images. *Transport in Porous Media*, 127(1):171–190, 2019.

[16] Peyman Mostaghimi, Martin J Blunt, and Branko Bijeljic. Computations of Absolute Permeability on Micro-CT Images. *Mathematical Geosciences*, 45(1):103–125, 2013.

[17] M Amin F Zarandi, Krishna M Pillai, and Bamdad Barari. Flow Along and Across Glass-Fiber Wicks: Testing of Permeability Models Through Experiments and Simulations. *AIChE Journal*, 64(9):3491–3501, 2018.

[18] M Amin F Zarandi, Salvador Arroyo, and Krishna M Pillai. Longitudinal and transverse flows in fiber tows: Evaluation of theoretical permeability models

through numerical predictions and experimental measurements. *Composites Part A: Applied Science and Manufacturing*, 119:73–87, 2019.

[19] JR Weitzenböck, RA Shenoi, and PA Wilson. Measurement of principal permeability with the channel flow experiment. *Polymer Composites*, 20(2):321–335, 1999.

[20] Dara L Woerdeman, Frederick R Phelan Jr, and Richard S Parnas. Interpretation of 3-D permeability measurements for RTM modeling. *Polymer Composites*, 16(6):470–480, 1995.

[21] M Amin F Zarandi, Krishna M Pillai, and Adam S Kimmel. Spontaneous imbibition of liquids in glass-fiber wicks. Part I: Usefulness of a sharp-front approach. *AIChE Journal*, 64(1):294–305, 2018.

[22] M Amin F. Zarandi and Krishna M Pillai. Spontaneous imbibition of liquid in glass fiber wicks, Part II: Validation of a diffuse-front model. *AIChE Journal*, 64(1):306–315, 2018.

[23] Dinesh Mohan and Charles U Pittman Jr. Arsenic removal from water/wastewater using adsorbents—A critical review. *Journal of Hazardous Materials*, 142(1-2):1–53, 2007.

[24] Fayzul Kabir and Shakhawat Chowdhury. Arsenic removal methods for drinking water in the developing countries: Technological developments and research needs. *Environmental Science and Pollution Research*, 24(31):24102–24120, 2017.

[25] Z Alhashmi, MJ Blunt, and B Bijeljic. Predictions of dynamic changes in reaction rates as a consequence of incomplete mixing using pore scale reactive transport modeling on images of porous media. *Journal of Contaminant Hydrology*, 179:171–181, 2015.

[26] Zhiwei Tian and Junye Wang. Lattice Boltzmann simulation of CO2 reactive transport in network fractured media. *Water Resources Research*, 53(8):7366–7381, 2017.

[27] Ilenia Battiato, Daniel O'Malley, Cass T Miller, Pawan S Takhar, Francisco J Valdés-Parada, Brian D Wood, et al. Theory and Applications of Macroscale Models in Porous Media. *Transport in Porous Media*, 130(1):5–76, 2019.

[28] TD Papathanasiou. On the effective permeability of square arrays of permeable fiber tows. *International journal of multiphase flow*, 23(1):81–92, 1997.

[29] Georg Bechtold and Lin Ye. Influence of fibre distribution on the transverse flow permeability in fibre bundles. *Composites Science and Technology*, 63(14):2069–2079, 2003.

[30] A Endruweit, F Gommer, and AC Long. Stochastic analysis of fibre volume fraction and permeability in fibre bundles with random filament arrangement. *Composites Part A: Applied Science and Manufacturing*, 49:109–118, 2013.

[31] B Rikard Gebart. Permeability of unidirectional reinforcements for RTM. *Journal of Composite Materials*, 26(8):1100–1133, 1992.

[32] Z Cai and AL Berdichevsky. An improved self-consistent method for estimating the permeability of a fiber assembly. *Polymer Composites*, 14(4):314–323, 1993.

[33] Parham Soltani, Mohammad Zarrebini, Reyhaneh Laghaei, and Ali Hassanpour. Prediction of permeability of realistic and virtual layered nonwovens using combined application of X-ray μ-CT and computer simulation. *Chemical Engineering Research and Design*, 124:299–312, 2017.

[34] P-C Gervais, N Bardin-Monnier, and D Thomas. Permeability modeling of fibrous media with bimodal fiber size distribution. *Chemical Engineering Science*, 73:239–248, 2012.

184

[35] Aydin Nabovati, Edward W Llewellin, and Antonio CM Sousa. A general model for the permeability of fibrous porous media based on fluid flow simulations using the Lattice Boltzmann Method. *Composites Part A: Applied Science and Manufacturing*, 40(6-7):860–869, 2009.

[36] Mohamad Karaki, Rafic Younes, Francois Trochu, and Pascal Lafon. Progress in experimental and theoretical evaluation methods for textile permeability. *Journal of Composites Science*, 3(3):73, 2019.

[37] Lihwa Fong and SG Advani. Resin Transfer Molding. In *Handbook of Composites*, pages 433–455. Springer, 1998.

[38] MA Ali, R Umer, KA Khan, and WJ Cantwell. Application of X-ray computed tomography for the virtual permeability prediction of fiber reinforcements for Liquid Composite Molding processes: A review. *Composites Science and Technology*, 184:107828, 2019.

[39] M Bodaghi, SV Lomov, P Simacek, NC Correia, and SG Advani. On the variability of permeability induced by reinforcement distortions and dual scale flow in liquid composite moulding: A review. *Composites Part A: Applied Science and Manufacturing*, 120:188–210, 2019.

[40] Spiridon Konstantopoulos, Christian Hueber, Ioannis Antoniadis, John Summerscales, and Ralf Schledjewski. Liquid composite molding reproducibility in real-world production of fiber reinforced polymeric composites: A review of challenges and solutions. *Advanced Manufacturing: Polymer and Composites Science*, 5(3):85–99, 2019.

[41] Da Wu, Ragnar Larsson, and Mohammad S Rouhi. Modeling and Experimental Validation of the VARTM Process for Thin-walled Preforms. *Polymers*, 11(12):2003, 2019.

185

[42] Feifei Zhang, Sébastien Comas-Cardona, and Christophe Binetruy. Statistical modeling of in-plane permeability of non-woven random fibrous reinforcement. *Composites Science and Technology*, 72(12):1368–1379, 2012.

[43] Philip Crosbie Carman. Fluid flow through granular beds. *Trans. Inst. Chem. Eng.*, 15:150–166, 1937.

[44] Sabri Ergun. Fluid flow through packed columns. *Chem. Eng. Prog.*, 48:89–94, 1952.

[45] M V Bruschke and SG Advani. Flow of generalized newtonian fluids across a periodic array of cylinders. *Journal of Rheology*, 37(3):479–498, 1993.

[46] Mohamad Karaki, Ali Hallal, Rafic Younes, Francois Trochu, Pascal Lafon, Amin Hayek, A Kobeissy, and Ahmad Fayad. A Comparative Analytical, Numerical and Experimental Analysis of the Microscopic Permeability of Fiber Bundles in Composite Materials. *Int. J. Compos. Mater*, 7(3):82–102, 2017.

[47] Ali Tamayol and Majid Bahrami. Transverse permeability of fibrous porous media. *Physical Review E*, 83(4):046314, 2011.

[48] S Woudberg. Permeability prediction of an analytical pore-scale model for layered and isotropic fibrous porous media. *Chemical Engineering Science*, 164:232–245, 2017.

[49] A Koponen, D Kandhai, E Hellen, M Alava, A Hoekstra, M Kataja, K Niskanen, Peter Sloot, and J Timonen. Permeability of three-dimensional random fiber webs. *Physical Review Letters*, 80(4):716, 1998.

[50] R C Lam and JL Kardos. The permeability and compressibility of aligned and cross-plied carbon fiber beds during processing of composites. *Polymer Engineering & Science*, 31(14):1064–1070, 1991.

[51] Manolis M Tomadakis and Teri J Robertson. Viscous Permeability of Random Fiber Structures: Comparison of Electrical and Diffusional Estimates with Experimental and Analytical Results. *Journal of Composite Materials*, 39(2):163–188, 2005.

[52] Francisco J Valdes-Parada, J Alberto Ochoa-Tapia, and Jose Alvarez-Ramirez. Validity of the permeability Carman–Kozeny equation: A Volume Averaging Approach. *Physica A: Statistical Mechanics and its Applications*, 388(6):789–798, 2009.

[53] R Arbter, JM Beraud, Christophe Binetruy, L Bizet, J Bréard, Sébastien Comas-Cardona, C Demaria, A Endruweit, Paolo Ermanni, Frank Gommer, et al. Experimental determination of the permeability of textiles: A benchmark exercise. *Composites Part A: Applied Science and Manufacturing*, 42(9):1157–1168, 2011.

[54] C Demaria, Edu Ruiz, and François Trochu. In-plane anisotropic permeability characterization of deformed woven fabrics by unidirectional injection. Part I: Experimental results. *Polymer Composites*, 28(6):797–811, 2007.

[55] Magdi El Messiry. Theoretical analysis of natural fiber volume fraction of reinforced composites. *Alexandria Engineering Journal*, 52(3):301–306, 2013.

[56] JR Weitzenböck, RA Shenoi, and PA Wilson. A unified approach to determine principal permeability of fibrous porous media. *Polymer Composites*, 23(6):1132–1150, 2002.

[57] Darshil U Shah, Peter J Schubel, Peter Licence, and Mike J Clifford. Determining the minimum, critical and maximum fibre content for twisted yarn reinforced plant fibre composites. *Composites Science and Technology*, 72(15):1909–1917, 2012.

[58] Salvatore Federico and Walter Herzog. On the permeability of fibre-reinforced porous materials. *International Journal of Solids and Structures*, 45(7-8):2160–2172, 2008.

[59] Andrew P Vechart, Reza Masoodi, and Krishna M Pillai. Design and evaluation of an idealized porous medium for calibration of permeability measuring devices. *Advanced Composites Letters*, 19(1):096369351001900104, 2010.

[60] Bamdad Barari, Saman Beyhaghi, and Krishna Pillai. Fast and inexpensive 2d-micrograph based method of permeability estimation through micro-macro coupling in porous media. *Journal of Porous Media*, 22(7), 2019.

[61] Saman Beyhaghi and Krishna Pillai. Estimation of tortuosity and effective diffusivity tensors using closure formulation in a sintered polymer wick during transport of a nondilute, multicomponent liquid mixture. *Special Topics & Reviews in Porous Media: An International Journal*, 2(4), 2011.

[62] Arash Rabbani, Saeid Jamshidi, and Saeed Salehi. An automated simple algorithm for realistic pore network extraction from micro-tomography images. *Journal of Petroleum Science and Engineering*, 123:164–171, 2014.

[63] Romain Guibert, Marfa Nazarova, Pierre Horgue, Gérald Hamon, Patrice Creux, and Gérald Debenest. Computational permeability determination from pore-scale imaging: sample size, mesh and method sensitivities. *Transport in Porous Media*, 107(3):641–656, 2015.

[64] JSU Schell, M Deleglise, C Binetruy, P Krawczak, and Paolo Ermanni. Numerical prediction and experimental characterisation of meso-scale-voids in liquid composite moulding. *Composites Part A: Applied Science and Manufacturing*, 38(12):2460–2470, 2007.

[65] AA Zick and GM Homsy. Stokes flow through periodic arrays of spheres. *Journal of Fluid Mechanics*, 115:13–26, 1982.

[66] GO Brown. Henry darcy and the making of a law. *Water Resources Research*, 38(7):11–1, 2002.

[67] Michael C Hegg, Anil Ogale, Ann Mescher, Alexander V Mamishev, and Bob Minaie. Remote Monitoring of Resin Transfer Molding Processes by Distributed Dielectric Sensors. *Journal of Composite Materials*, 39(17):1519–1539, 2005.

[68] Bai-Jian Wei, Yu-Sung Chang, Yuan Yao, and Jun Fang. Online estimation and monitoring of local permeability in resin transfer molding. *Polymer Composites*, 37(4):1249–1258, 2016.

[69] Bai-Jian Wei, Yao-Chen Chuang, Kai-Hong Wang, and Yuan Yao. Model-assisted control of flow front in resin transfer molding based on real-time estimation of permeability/porosity ratio. *Polymers*, 8(9):337, 2016.

[70] Mohammad Karaki, Ali Hallal, Rafic Younes, Francois Trochu, and Pascal Lafon. In-plane permeability prediction model for non-crimp and 3D orthogonal fabrics. *The Journal of The Textile Institute*, 109(8):1110–1126, 2018.

[71] Cheng-Hsien Wu, T James Wang, and L James Lee. Trans-plane fluid permeability measurement and its applications in liquid composite molding. *Polymer Composites*, 15(4):289–298, 1994.

[72] L Trevino, K Rupel, WB Young, Ming J Liou, and L James Lee. Analysis of resin injection molding in molds with preplaced fiber mats. I: Permeability and compressibility measurements. *Polymer Composites*, 12(1):20–29, 1991.

[73] T Bo Anderson and Roy Jackson. Fluid mechanical description of fluidized beds. Equations of motion. *Industrial & Engineering Chemistry Fundamentals*, 6(4):527–539, 1967.

[74] John C Slattery. Flow of viscoelastic fluids through porous media. *AIChE Journal*, 13(6):1066–1071, 1967.

[75] WG Gray and SM Hassanizadeh. Averaging theorems and averaged equations for transport of interface properties in multiphase systems. *International Journal of Multiphase Flow*, 15(1):81–95, 1989.

[76] C Marle. Single-phase flow in a porous medium. In *Review of the French Petroleum Institute and Annals of Liquid Fuels*, volume 22, page 1471. Editions Technip 27 Rue Ginoux, 75737 Paris 15, France, 1967.

[77] Stephen Whitaker. Diffusion and dispersion in porous media. *AIChE Journal*, 13(3):420–427, 1967.

[78] Frederick A Howes and Stephen Whitaker. The spatial averaging theorem revisited. *Chemical engineering science*, 40(8):1387–1392, 1985.

[79] Jin-Hwan Kim, J Alberto Ochoa, and Stephen Whitaker. Diffusion in anisotropic porous media. *Transport in Porous Media*, 2(4):327–356, 1987.

[80] Alec Byron Eidsath. *Flow and dispersion in spatially periodic porous media: A finite element study.* Davis, Calif., 1981.

[81] Jean Barrere, Olivier Gipouloux, and Stephen Whitaker. On the closure problem for Darcy's law. *Transport in Porous Media*, 7(3):209–222, 1992.

[82] Stephen Whitaker. *The Method of Volume Averaging*, volume 13. Springer Science & Business Media, 2013.

[83] Krishna Pillai. Single-phase flows in swelling, liquid-absorbing porous media: A derivation of flow governing equations using the volume averaging method with a nondeterministic, heuristic approach to assessing the effect of solid-phase changes. *Journal of Porous Media*, 17(10), 2014.

[84] Dominique Bernard, Øyvind Nielsen, Luc Salvo, and Peter Cloetens. Permeability assessment by 3D interdendritic flow simulations on microtomography mappings of Al–Cu alloys. *Materials Science and Engineering: A*, 392(1-2):112–120, 2005.

[85] K Yazdchi, S Srivastava, and Stefan Luding. Microstructural effects on the permeability of periodic fibrous porous media. *International Journal of Multiphase Flow*, 37(8):956–966, 2011.

[86] Sinzi Kuwabara. The forces experienced by randomly distributed parallel circular cylinders or spheres in a viscous flow at small Reynolds numbers. *Journal of the Physical Society of Japan*, 14(4):527–532, 1959.

[87] Didier Lasseux, Ali Akbar Abbasian Arani, and A Ahmadi. On the stationary macroscopic inertial effects for one phase flow in ordered and disordered porous media. *Physics of Fluids*, 23(7):073103, 2011.

[88] Yi Wang, Shuyu Sun, and Bo Yu. On full-tensor permeabilities of porous media from numerical solutions of the Navier-Stokes equation. *Advances in Mechanical Engineering*, 5:137086, 2013.

[89] Jean-Baptiste Clavaud, Alexis Maineult, Maria Zamora, Patrick Rasolofosaon, and Camille Schlitter. Permeability anisotropy and its relations with porous medium structure. *Journal of Geophysical Research: Solid Earth*, 113(B1), 2008.

[90] Nicolas Vernet, Edu Ruiz, S Advani, Justin B Alms, Marcel Aubert, Marcin Barburski, Bamdad Barari, Jean Marc Beraud, David Christian Berg, N Correia, et al. Experimental determination of the permeability of engineering textiles: Benchmark II. *Composites Part A: Applied Science and Manufacturing*, 61:172–184, 2014.

[91] Kim Gehle. Arsenic toxicity. Agency for Toxic Substances and Disease Registry: www.atsdr.cdc.gov/csem/csem.asp?csem=1&po=0.

[92] Arundhati Pillai, M Amin F Zarandi, Faten B Hussein, Krishna M Pillai, and Nidal H Abu-Zahra. Towards developing a low-cost gravity-driven arsenic filtration system using iron oxide nanoparticle-loaded PU foam. *Water Quality Research Journal*, 55(3):234–248, 2020.

[93] Hemda Garelick and Huw Jones. *Reviews of Environmental Contamination Volume 197: Arsenic Pollution and Remediation: An International Perspective*, volume 197. Springer Science & Business Media, 2008.

[94] Vedat Batu. *Applied Flow and Solute Transport Modeling in Aquifers: Fundamental Principles and Analytical and Numerical Methods*. CRC Press, 2005.

[95] Jui-Sheng Chen. Analytical model for fully three-dimensional radial dispersion in a finite-thickness aquifer. *Hydrological Processes: An International Journal*, 24(7):934–945, 2010.

[96] Jui-Sheng Chen, Keng-Hsin Lai, Chen-Wuing Liu, and Chuen-Fa Ni. A novel method for analytically solving multi-species advective–dispersive transport equations sequentially coupled with first-order decay reactions. *Journal of Hydrology*, 420:191–204, 2012.

[97] Feike J Leij and Martinus Th Van Genuchten. Analytical modeling of nonaqueous phase liquid dissolution with Green's functions. *Transport in Porous Media*, 38(1):141–166, 2000.

[98] Feike J Leij, Nobuo Toride, and Martinus Th Van Genuchten. Analytical solutions for non-equilibrium solute transport in three-dimensional porous media. *Journal of Hydrology*, 151(2-4):193–228, 1993.

[99] Marco Massabó, Roberto Cianci, and Ombretta Paladino. Some analytical solutions for two-dimensional convection–dispersion equation in cylindrical geometry. *Environmental Modelling & Software*, 21(5):681–688, 2006.

[100] Shaymaa Mustafa, Arifah Bahar, Zainal Abdul Aziz, and Saim Suratman. Modelling contaminant transport for pumping wells in riverbank filtration systems. *Journal of Environmental Management*, 165:159–166, 2016.

[101] Eungyu Park and Hongbin Zhan. Analytical solutions of contaminant transport from finite one-, two-, and three-dimensional sources in a finite-thickness aquifer. *Journal of Contaminant Hydrology*, 53(1-2):41–61, 2001.

[102] Mritunjay Kumar Singh, Shafique Ahamad, and Vijay P Singh. Analytical solution for one-dimensional solute dispersion with time-dependent source concentration along uniform groundwater flow in a homogeneous porous formation. *Journal of engineering mechanics*, 138(8):1045–1056, 2012.

[103] Mritunjay Kumar Singh, Premlata Singh, and Vijay P Singh. Analytical solution for two-dimensional solute transport in finite aquifer with time-dependent source concentration. *Journal of engineering mechanics*, 136(10):1309–1315, 2010.

[104] J Ind Geophys Union. Advection diffusion equation models in near-surface geophysical and environmental sciences. *J. Ind. Geophys. Union (April 2013)*, 17(2):117–127, 2013.

[105] Daniel M Tartakovsky. An analytical solution for two-dimensional contaminant transport during groundwater extraction. *Journal of Contaminant Hydrology*, 42(2-4):273–283, 2000.

[106] RR Yadav and Dilip Kumar Jaiswal. Two-dimensional analytical solutions for point source contaminants transport in semi-infinite homogeneous porous medium. *Journal of Engineering Science and Technology*, 6(4):459–468, 2011.

[107] RR Yadav, Dilip Kumar Jaiswal, Hareesh Kumar Yadav, and GUL Rana. One-dimensional temporally dependent advection-dispersion equation in porous media: analytical solution. *Natural Resource Modeling*, 23(4):521–539, 2010.

[108] Shu-Guang Li, Hua-Sheng Liao, and Chuen-Fa Ni. Stochastic modeling of complex nonstationary groundwater systems. *Advances in Water Resources*, 27(11):1087–1104, 2004.

[109] Gedeon Dagan. Transport in heterogeneous porous formations: Spatial moments, ergodicity, and effective dispersion. *Water Resources Research*, 26(6):1281–1290, 1990.

[110] Aldo Fiori. On the influence of pore-scale dispersion in nonergodic transport in heterogeneous formations. *Transport in Porous Media*, 30(1):57–73, 1998.

[111] Yoram Rubin. *Applied Stochastic Hydrogeology*. Oxford University Press, 2003.

[112] Lynn W Gelhar. Stochastic subsurface hydrology from theory to applications. *Water Resources Research*, 22(9S):135S–145S, 1986.

[113] Gedeon Dagan. *Flow and transport in porous formations*. Springer Science & Business Media, 2012.

[114] John C Slattery. Single-phase flow through porous media. *AIChE Journal*, 15(6):866–872, 1969.

[115] Jacob Bear and Yehuda Bachmat. *Introduction to modeling of transport phenomena in porous media*, volume 4. Springer Science & Business Media, 2012.

[116] William G Gray. A derivation of the equations for multi-phase transport. *Chemical Engineering Science*, 30(2):229–233, 1975.

[117] MA Paine, RG Carbonell, and S Whitaker. Dispersion in pulsed systems—I: Heterogeneous reaction and reversible adsorption in capillary tubes. *Chemical Engineering Science*, 38(11):1781–1793, 1983.

[118] Michel Quintard and Stephen Whitaker. Transport in chemically and mechanically heterogeneous porous media IV: Large-scale mass equilibrium for solute transport with adsorption. *Advances in Water Resources*, 22(1):33–57, 1998.

[119] Azita Ahmadi, Michel Quintard, and Stephen Whitaker. Transport in chemically and mechanically heterogeneous porous media: V. Two-equation model for solute transport with adsorption. *Advances in Water Resources*, 22(1):59–86, 1998.

[120] Brian D Wood, Fabien Cherblanc, Michel Quintard, and Stephen Whitaker. Volume averaging for determining the effective dispersion tensor: Closure using periodic unit cells and comparison with ensemble averaging. *Water Resources Research*, 39(8), 2003.

[121] Fabien Cherblanc, A Ahmadi, and Michel Quintard. Two-medium description of dispersion in heterogeneous porous media: Calculation of macroscopic properties. *Water Resources Research*, 39(6), 2003.

[122] OA Plumb and S Whitaker. Diffusion, adsorption and dispersion in porous media: Small-scale averaging and local volume averaging. *IN: Dynamics of Fluids in Hierarchical Porous Media. Academic Press, Inc., San Diego, California. 1990. p 97-148, 13*, 1990.

[123] S. Whitaker. *Advances in Fluid Mechanics*, volume 13. Southampton Boston: Computational Mechanics, 1997.

[124] Brian D Wood, Karen Radakovich, and Fabrice Golfier. Effective reaction at a fluid–solid interface: Applications to biotransformation in porous media. *Advances in Water Resources*, 30(6-7):1630–1647, 2007.

[125] FJ Valdés-Parada, CG Aguilar-Madera, and J Alvarez-Ramirez. On diffusion, dispersion and reaction in porous media. *Chemical Engineering Science*, 66(10):2177–2190, 2011.

195

[126] Michel Quintard and Stephen Whitaker. Convection, dispersion, and interfacial transport of contaminants: Homogeneous porous media. *Advances in Water Resources*, 17(4):221–239, 1994.

[127] Jianwei Guo, Michel Quintard, and Farid Laouafa. Dispersion in porous media with heterogeneous nonlinear reactions. *Transport in Porous Media*, 109(3):541–570, 2015.

[128] William G Gray and PCY Lee. On the theorems for local volume averaging of multiphase systems. *International Journal of Multiphase Flow*, 3(4):333–340, 1977.

[129] William G Gray, Anton Leijnse, Randall L Kolar, and Cheryl A Blain. *Mathematical tools for changing scale in the analysis of physical systems*. CRC Press, 1993.

[130] Stephen Whitaker. Derivation and application of the Stefan-Maxwell equations. *Revista mexicana de ingeniería química*, 8(3):213–243, 2009.

[131] Jong Soo Cho, Soon Mi Kim, and Ioan Iordache. Analysis of passive remediation of contaminated groundwater with dimensionless numbers. In *2011 International Conference on Environment and Bioscience, IPCBEE*, volume 21, 2011.

[132] David A Edwards, Michael Shapiro, and Howard Brenner. Dispersion and reaction in two-dimensional model porous media. *Physics of Fluids A: Fluid Dynamics*, 5(4):837–848, 1993.

[133] S Bekri, JF Thovert, and PM Adler. Dissolution of porous media. *Chemical Engineering Science*, 50(17):2765–2791, 1995.

[134] Bamdad Barari, Saman Beyhaghi, and Krishna Pillai. Fast and Inexpensive 2D-Micrograph based Method of Permeability Estimation through Micro-macro Coupling in Porous Media. *Journal of Porous Media*, 22(7), 2019.

[135] Saman Beyhaghi and Krishna Pillai. Estimation of tortuosity and effective diffusivity tensors using closure formulation in a sintered polymer wick during transport of a nondilute, multicomponent liquid mixture. *Special Topics & Reviews in Porous Media: An International Journal*, 2(4), 2011.

[136] K Jomova, Z Jenisova, M Feszterova, S Baros, J Liska, D Hudecova, CJ Rhodes, and MJJoatJ Valko. Arsenic: toxicity, oxidative stress and human disease. *Journal of Applied Toxicology*, 31(2):95–107, 2011.

[137] Chenghong Wang, Xinlei Liu, J Paul Chen, and Kang Li. Superior removal of arsenic from water with zirconium metal-organic framework UiO-66. *Scientific reports*, 5(1):1–10, 2015.

[138] Krishna Pillai and Aman Raizada. Modeling Transport and Adsorption of Arsenic Ions in Iron-Oxide Laden Porous Media. Part I: Theoretical Developments. *Water*, 13(6):779, 2021.

[139] Young-Seoub Hong, Ki-Hoon Song, and Jin-Yong Chung. Health effects of chronic arsenic exposure. *Journal of Preventive Medicine and Public Health*, 47(5):245, 2014.

[140] Jérôme Michon, Véronique Deluchat, Raad Al Shukry, Christophe Dagot, and Jean-Claude Bollinger. Optimization of a GFAAS method for determination of total inorganic arsenic in drinking water. *Talanta*, 71(1):479–485, 2007.

[141] Nina Ricci Nicomel, Karen Leus, Karel Folens, Pascal Van Der Voort, and Gijs Du Laing. Technologies for Arsenic Removal from Water: Current Status and Future Perspectives. *International Journal of Environmental Research and Public Health*, 13(1):62, 2016.

[142] Brian G Blackburn, Gunther F Craun, Jonathan S Yoder, Vincent Hill, Rebecca L Calderon, Nora Chen, Sherline H Lee, Deborah A Levy, and Michael J

Beach. Surveillance for waterborne-disease outbreaks associated with drinking water—United States, 2001–2002. *MMWR Surveill Summ*, 53(8):23–45, 2004.

[143] World Health Organization et al. Arsenic and arsenic compounds. In *Arsenic and arsenic compounds (second edition)*, pages 521–521. 2001.

[144] Qinghai Guo, Yaowu Cao, Zuowei Yin, Zhengyan Yu, Qian Zhao, and Zhu Shu. Enhanced removal of arsenic from water by synthetic nanocrystalline iowaite. *Scientific reports*, 7(1):1–10, 2017.

[145] D Kirk Nordstrom. Worldwide occurrences of arsenic in ground water, 2002.

[146] Sahira Joshi, Manobin Sharma, Anshu Kumari, Surendra Shrestha, and Bhanu Shrestha. Arsenic Removal from Water by Adsorption onto Iron Oxide/Nano-Porous Carbon Magnetic Composite. *Applied Sciences*, 9(18):3732, 2019.

[147] Kyle J McDonald, Brandon Reynolds, and KJ Reddy. Intrinsic properties of cupric oxide nanoparticles enable effective filtration of arsenic from water. *Scientific reports*, 5(1):1–10, 2015.

[148] Dionne Dickson, Guangliang Liu, and Yong Cai. Adsorption kinetics and isotherms of arsenite and arsenate on hematite nanoparticles and aggregates. *Journal of Environmental Management*, 186:261–267, 2017.

[149] Tonoy Chowdhury, Lei Zhang, Junqing Zhang, and Srijan Aggarwal. Removal of arsenic (III) from aqueous solution using metal organic framework-graphene oxide nanocomposite. *Nanomaterials*, 8(12):1062, 2018.

[150] Haiyan Yang, Xiaopeng Min, Shangping Xu, and Yin Wang. Lanthanum (III)-coated ceramics as a promising material in point-of-use water treatment for arsenite and arsenate removal. *ACS Sustainable Chemistry & Engineering*, 7(10):9220–9227, 2019.

[151] Atul Kumar, Dilip Kumar Jaiswal, and Naveen Kumar. Analytical solutions of one-dimensional advection-diffusion equation with variable coefficients in a finite domain. *Journal of Earth System Science*, 118(5):539–549, 2009.

[152] William G Gray and Cass T Miller. *Introduction to the thermodynamically constrained averaging theory for porous medium systems*. Springer, 2014.

[153] Jacob Bear and M Yavuz Corapcioglu. *Advances in transport phenomena in porous media*, volume 128. Springer Science & Business Media, 2012.

[154] LE Scriven. Porous media: Geometry and transport by Pierre M. Adler, butterworth-heinemann, stoneham, ma, 1992, 544 pp., 1994.

[155] Jean-Louis Auriault, Claude Boutin, and Christian Geindreau. *Homogenization of coupled phenomena in heterogenous media*, volume 149. John Wiley & Sons, 2010.

[156] Horia I Ene and Dan Poliševski. The homogenization method for the study of fluid flow in porous media. In *Thermal Flows in Porous Media*, pages 3–47. Springer, 1987.

[157] Jongmuk Won, Junghwoon Lee, and Susan E Burns. Upscaling polydispersed particle transport in porous media using pore network model. *Acta Geotechnica*, pages 1–12, 2020.

[158] Marc Prat. Recent advances in pore-scale models for drying of porous media. *Chemical Engineering Journal*, 86(1-2):153–164, 2002.

[159] FJ Valdes-Parada and J Alvarez-Ramirez. On the effective diffusivity under chemical reaction in porous media. *Chemical Engineering Science*, 65(13):4100–4104, 2010.

[160] Xuan Zhang, Koki Urita, Isamu Moriguchi, and Daniel M Tartakovsky. Design of nanoporous materials with optimal sorption capacity. *Journal of Applied Physics*, 117(24):244304, 2015.

[161] Stephen Whitaker. Advances in theory of fluid motion in porous media. *Industrial & Engineering Chemistry*, 61(12):14–28, 1969.

[162] Francisco J Valdés-Parada, Didier Lasseux, and Stephen Whitaker. Diffusion and heterogeneous reaction in porous media: The macroscale model revisited. *International Journal of Chemical Reactor Engineering*, 15(6), 2017.

[163] Michel Quintard and Stephen Whitaker. Transport in ordered and disordered porous media: Volume-averaged equations, closure problems, and comparison with experiment. *Chemical Engineering Science*, 48(14):2537–2564, 1993.

[164] John C Slattery. *Advanced transport phenomena*. Cambridge University Press, 1999.

[165] GH Crapiste, E Rotstein, and S Whitaker. A general closure scheme for the method of volume averaging. *Chemical Engineering Science*, 41(2):227–235, 1986.

[166] Francisco J Valdés-Parada, Didier Lasseux, and Stephen Whitaker. Upscaling Reactive Transport Under Hydrodynamic Slip Conditions in Homogeneous Porous Media. *Water Resources Research*, 56(1):e2019WR025954, 2020.

[167] Jean-Louis Auriault and Jolanta Lewandowska. Diffusion/adsorption/advection macrotransport in soils. *European Journal of Mechanics, A/Solids*, 15(4):681–704, 1996.

[168] RG Carbonell and S Whitaker. Dispersion in pulsed systems—II: Theoretical developments for passive dispersion in porous media. *Chemical Engineering Science*, 38(11):1795–1802, 1983.

[169] DJ Gunn. Axial and radial dispersion in fixed beds. *Chemical Engineering Science*, 42(2):363–373, 1987.

[170] D Buyuktas and WW Wallender. Dispersion in spatially periodic porous media. *Heat and Mass Transfer*, 40(3):261–270, 2004.

[171] I Nozad, RG Carbonell, and S Whitaker. Heat conduction in multiphase systems—I: Theory and experiment for two-phase systems. *Chemical Engineering Science*, 40(5):843–855, 1985.

[172] Maasoud Kaviany. *Principles of heat transfer in porous media*. Springer Science & Business Media, 2012.

[173] Janez Levec and RG Carbonell. Longitudinal and lateral thermal dispersion in packed beds. Part I: Theory. *AIChE journal*, 31(4):581–590, 1985.

[174] William M Moe and Robert L Irvine. Polyurethane foam medium for biofiltration. I: Characterization. *Journal of Environmental Engineering*, 126(9):815–825, 2000.

[175] P Sridhar. Design of affinity membrane bioseparations. *Chemical Engineering & Technology: Industrial Chemistry-Plant Equipment-Process Engineering-Biotechnology*, 19(5):398–404, 1996.

[176] Hai Xu, Hans W Paerl, Boqiang Qin, Guangwei Zhu, and Guang Gaoa. Nitrogen and phosphorus inputs control phytoplankton growth in eutrophic Lake Taihu, China. *Limnology and Oceanography*, 55(1):420–432, 2010.

[177] Patricia M Glibert, Roxane Maranger, Daniel J Sobota, and Lex Bouwman. The Haber Bosch–harmful algal bloom (HB–HAB) link. *Environmental Research Letters*, 9(10):105001, 2014.

[178] Stephen R Carpenter. Eutrophication of aquatic ecosystems: bistability and soil phosphorus. *Proceedings of the National Academy of Sciences*, 102(29):10002–10005, 2005.

[179] Patricia M Glibert. Eutrophication, harmful algae and biodiversity—Challenging paradigms in a world of complex nutrient changes. *Marine Pollution Bulletin*, 124(2):591–606, 2017.

[180] Richard A Vollenweider et al. *Scientific fundamentals of the eutrophication of lakes and flowing waters, with particular reference to nitrogen and phosphorus as factors in eutrophication.* Organisation for economic co-operation and development, 1970.

[181] Donald Scavia, J David Allan, Kristin K Arend, Steven Bartell, Dmitry Beletsky, Nate S Bosch, Stephen B Brandt, Ruth D Briland, Irem Daloğlu, Joseph V DePinto, et al. Assessing and addressing the re-eutrophication of Lake Erie: Central basin hypoxia. *Journal of Great Lakes Research*, 40(2):226–246, 2014.

[182] David W Schindler, Stephen R Carpenter, Steven C Chapra, Robert E Hecky, and Diane M Orihel. Reducing phosphorus to curb lake eutrophication is a success. *Environmental Science & Technology*, 50(17):8923–8929, 2016.

[183] Tetsunori Inoue and Yoshiyuki Nakamura. Response of benthic soluble reactive phosphorus transfer rates to step changes in flow velocity. *Journal of Soils and Sediments*, 12(10):1559–1567, 2012.

[184] Michel Quintard and Stephen Whitaker. Transport in ordered and disordered porous media IV: Computer generated porous media for three-dimensional systems. *Transport in Porous Media*, 15(1):51–70, 1994.

[185] Yohan Davit and Michel Quintard. Technical notes on volume averaging in porous media I: How to choose a spatial averaging operator for periodic and quasiperiodic structures. *Transport in Porous Media*, 119(3):555–584, 2017.

[186] Stephen Whitaker. Levels of simplification: The use of assumptions, restrictions, and constraints in engineering analysis. *Chemical Engineering Education*, 22(2):104–108, 1988.

[187] C Moyne. Two-equation model for a diffusive process in porous media using the volume averaging method with an unsteady-state closure. *Advances in Water Resources*, 20(2-3):63–76, 1997.

[188] Krishna R Reddy, Tao Xie, and Sara Dastgheibi. Removal of heavy metals from urban stormwater runoff using different filter materials. *Journal of Environmental Chemical Engineering*, 2(1):282–292, 2014.

[189] Masato Tanaka, Yoshio Takahashi, Noriko Yamaguchi, Kyoung-Woong Kim, Guodong Zheng, and Mika Sakamitsu. The difference of diffusion coefficients in water for arsenic compounds at various pH and its dominant factors implied by molecular simulations. *Geochimica et Cosmochimica Acta*, 105:360–371, 2013.